Combining Models of Coronal Mass Ejections and Solar Dynamos

Jörn Warnecke

Stockholm
University

Combining Models of Coronal Mass Ejections and Solar Dynamos

Jörn Warnecke

Cover image: Convectively driven dynamo in a spherical shell with realistic differential rotation shedding a coronal ejection of current helicity. The radial velocities at the surface and at the bottom of the convection zone are shown in shades of red on two spherical shells. The meridional cut shows the mean differential rotation profile and the colored ejection on the right contains the two polarities of the current helicity density. This illustration is a composite of two simulations of spherical wedges with coronal envelopes, one with self-consistent convection and the other, with forced turbulence. These simulations has been developed and performed in this thesis. The background image of the Sun was observed by AIA 171 on SDO on the 18th of April 2013.

©Jörn Warnecke, Stockholm 2013

ISBN 978-91-7447-675-0

Printed in Sweden by Universitetsservice, US-AB, Stockholm 2013
Distributor: Department of Astronomy, Stockholm University

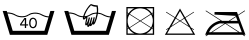

Abstract

Observations show that Coronal Mass Ejections (CMEs) are associated with twisted magnetic flux configurations. Conventionally, CMEs are modeled by shearing and twisting the footpoints of a certain distribution of magnetic flux at the solar surface and letting it evolve at the surface. Of course, the surface velocities and magnetic field patterns should ultimately be obtained from realistic simulations of the solar convection zone where the field is generated by dynamo action. Therefore, a unified treatment of the convection zone and the CMEs is needed. Numerical simulations of turbulent dynamos show that the amplification of magnetic fields can be catastrophically quenched at magnetic Reynolds numbers typical of the interior of the Sun. A strong flux of magnetic helicity leaving the dynamo domain can alleviate this quenching. In this sense, a realistic (magnetic) boundary condition is an important ingredient of a successful solar dynamo model.

Using a two-layer model developed in this thesis, we combine a dynamo-active region with a magnetically inert but highly conducting upper layer which models the solar corona. In four steps we improve this setup from a forced turbulent to a convectively driven dynamo and from an isothermal to a polytropic stratified corona. The simulations show magnetic fields that emerge at the surface of the dynamo region and are ejected into the coronal part of the domain. Their morphological form allows us to associate these events with CMEs. Magnetic helicity is found to change sign in the corona to become consistent with recent helicity measurements in the solar wind. Our convection-driven dynamo model with a coronal envelope has a solar-like differential rotation with radial (spoke-like) contours of constant rotation rate, together with a solar-like meridional circulation and a near-surface shear layer. The spoke-like rotation profile is due to latitudinal entropy gradient which violates the Taylor–Proudman balance through the baroclinic term. We find mean magnetic fields that migrate equatorward in models both with and without the coronal layer. One remarkable result is that the dynamo action benefits substantially from the presence of a corona becoming stronger and more realistic.

The two-layer model represents a new approach to describe the generation of coronal mass ejections in a self-consistent manner. On the other hand, it has important implications for solar dynamo models as it admits many magnetic features observed in the Sun.

List of Papers

The following papers are included in this thesis. They are referred to in the text by their Roman numerals,

I **Warnecke, J.**, & Brandenburg, A.: 2010, "Surface appearance of dynamo-generated large-scale fields", *Astron. Astrophys.*, **523**, A19

II **Warnecke, J.**, Brandenburg, A., & Mitra, D.: 2011, "Dynamo-driven plasmoid ejections above a spherical surface", *Astron. Astrophys.*, **534**, A11

III **Warnecke, J.**, Brandenburg, A., & Mitra, D.: 2012, "Magnetic twist: a source and property of space weather", *J. Spa. Weather Spa. Clim.*, **2**, A11

IV **Warnecke, J.**, Käpylä, P. J., Mantere, M. J., & Brandenburg, A.: 2012, "Emergence of magnetic structures driven by a convective dynamo with differential rotation above a spherical wedge", *Solar Phys.*, **280**, 299-319

V **Warnecke, J.**, Käpylä, P. J., Mantere, M. J., & Brandenburg, A.: 2013, "Solar-like differential rotation in a convective dynamo with a coronal envelope", *Astrophys. J.*, submitted, arXiv: 1301.2248

VI Käpylä, P. J., Mantere, M. J., Cole, E., **Warnecke, J.**, & Brandenburg, A.: 2013, "Effects of strong stratification on equatorward dynamo wave propagation", *Astrophys. J.*, submitted, arXiv: 1301.2595

Reprints were made with permission from the publishers.

My Contribution to the Papers

I Work on this paper started a few weeks after I began my PhD in August 2009. The main idea was developed by my supervisor and myself. I ran all the simulations, did most of the analysis and produced all the plots for the paper. I also did limited work on the implementation of the setup and developed some analysis tools using the PENCIL CODE[1] and IDL. I wrote the major part of the paper.

II In the beginning of the project, I spent time together with one of the co-authors transforming the equations and the setup of the Cartesian model to spherical geometry and implementing this in the PENCIL CODE. I performed the parameter study to identify a regime with stable simulations and performed all of the runs used in the paper. In addition, I coded analysis tools applied in IDL and the PENCIL CODE. I did the analysis and made all the plots used in the paper. The actual writing was done in collaboration with the co-authors, where I contributed a large fraction.

III This paper is based on work presented in **Papers I** and **III**. I performed a deeper analysis of the runs with respect to magnetic helicity and I made most of the analysis and plots in the paper. The writing and discussion was done mainly by myself.

IV On my initiative, I started a collaboration with co-authors Petri J. Käpylä and Maarit J. Mantere, using convective motions to generate magnetic fields in my setup. I developed the new setup involving the implementation of additional physics into the PENCIL CODE. I made a full parameter study to find a stable and efficient setup. I added new diagnostic tools in the PENCIL CODE, as well as in IDL. For the paper, I did all the runs, all the analysis, all the plots and wrote the first complete version of the text. The co-authors contributed to the discussion of the analysis and the text.

V I did all the improvements of a new setup including implementations in the PENCIL CODE. I made a large number of runs to find a stable and sufficient setup. I wrote new diagnostics in the PENCIL CODE and with IDL. I did all the runs related to the paper, all the analysis and plots and I wrote all the text except some suggested additions and comments by the co-authors.

---

[1] `http://pencil-code.googlecode.com`

VI I contributed to the discussion of the setup, the analysis and the writing of the text.

To Atefeh,
The Star in my Universe

Contents

Abstract **v**

List of Papers **vii**

1 The Sun **1**
- 1.1 The convection zone . . . 3
- 1.2 The surface of the Sun . . . 4
- 1.3 The solar corona . . . 6
- 1.4 The solar cycle . . . 7
- 1.5 Space weather . . . 10

2 Solar Convection, Turbulence and Rotation **13**
- 2.1 Convective motions . . . 13
  - 2.1.1 The convective instability . . . 13
  - 2.1.2 Fluid dynamics . . . 16
- 2.2 Turbulence . . . 17
  - 2.2.1 Kolmogorov turbulence . . . 18
  - 2.2.2 Mean-field theory . . . 19
  - 2.2.3 Mixing length theory . . . 20
  - 2.2.4 Turbulent heat transport . . . 21
- 2.3 Rotation . . . 22
- 2.4 Mean-field models of solar differential rotation . . . 23

3 Magnetohydrodynamics **27**
- 3.1 Magnetohydrodynamical equations . . . 27
  - 3.1.1 Alfvén's theorem . . . 29
  - 3.1.2 Force-free fields . . . 29
  - 3.1.3 Magnetic buoyancy . . . 30
- 3.2 Generation of magnetic fields . . . 31
  - 3.2.1 α^2-dynamo . . . 32
  - 3.2.2 α–Ω-dynamo . . . 33
- 3.3 Magnetic helicity . . . 34
  - 3.3.1 Catastrophic quenching of the α–effect and magnetic helicity fluxes . . . 34

4 Solar Dynamo Models 37
4.1 The challenge 37
4.2 Mean-field models 38
4.2.1 Babcock–Leighton dynamo models 40
4.3 Direct numerical simulations 43
4.3.1 Local simulations 43
4.3.2 Global simulations 45

5 Models of Solar Eruptions 49
5.1 Observational constrains 49
5.2 Models and simulations 52

6 A Combined Two-Layer Model 55
6.1 Motivation 55
6.2 Model and setup 57
6.2.1 Step by step 57
6.2.2 A forced turbulent dynamo in a Cartesian box 59
6.2.3 A forced turbulent dynamo in a spherical domain . . . 59
6.2.4 A convective dynamo in a spherical domain 60
6.2.5 A convective dynamo in a spherical domain with a hot corona 61
6.3 Main results of Paper I to V 62
6.3.1 Magnetic field generation 62
6.3.2 Differential rotation 66
6.3.3 Coronal field structure 68
6.3.4 Coronal ejections 69
6.3.5 Magnetic helicity and current helicity 72
6.4 Discussion and conclusions 75

7 Possible Future Developments 79
7.1 Solar dynamo and helicity fluxes 79
7.2 Convection driven coronal mass ejections 79
7.3 Space weather forecasting 80

Acknowledgments lxxxvii

Publications not included in the Thesis lxxxix

Bibliography xci

1. The Sun

Eins, Hier kommt die Sonne
Zwei, Hier kommt die Sonne
Drei, Sie ist der hellste Stern von allen
Vier, Hier kommt die Sonne

Rammstein

Its vicinity to the Earth makes the Sun an object that can be studied in such a precision and resolution than no other star. It reveals a multitude of complex processes and features, where we only know as much as the tip of an iceberg. Although there have been major advances in observing techniques and modeling of solar phenomena in the recent times, fundamental processes as the activity cycle of Sun are ill understood.

Let me start with an introduction to the structure of the Sun. In solar physics, we distinguish the solar interior, containing everything below the visible solar surface, from the solar atmosphere as everything above the solar surface. The solar surface is defined as the layer, where the optical depth at a continuum wavelength is unity. The density stratification from the center of the Sun to its surface varies by about nine orders of magnitudes. The temperature spans from 15 million Kelvin to around 6 thousand Kelvin. The solar interior can be divided into three main parts as shown in Fig. 1.1. In the inner part, the core, nuclear fusion supplies the main source of energy for this star. This energy is outwards transported through the radiative zone by radiation. The radiative zone extends from 0.3 to 0.7 solar radii and rotates as a solid body according to helioseismology. Above the radiative zone, the energy is predominantly transported via convection.

The definition of the solar atmosphere is somewhat ambiguous in the literature. Stix (2002), for example, defines the atmosphere as the photosphere and the chromosphere above. In other work, even the interplanetary space of the heliosphere is included. However, in this work I will define the solar atmosphere as the combination of the photosphere, chromosphere, transition region and solar corona. Near the surface of the Sun, heat is mainly transported as radiation and can leave the Sun freely. The thin surface layer is the lowest part of the solar atmosphere and is called photosphere, because it emits the largest amount of visible light of the total solar luminosity. The lower boundary of the chromosphere is usually defined by the temperature minimum on the

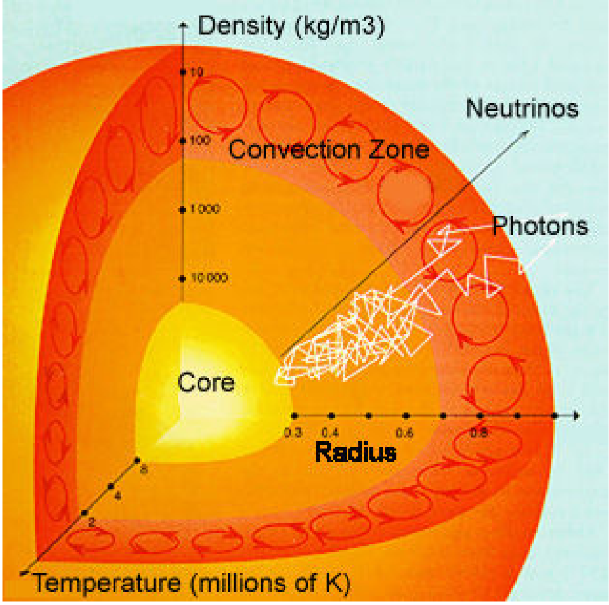

Figure 1.1: A cut-away schematic view of the solar interior, showing the main three parts: core, radiative zone, convection zone. Courtesy of the Center for Science Education of Berkeley, University of California, US.

Sun. The temperature structure of the chromosphere is heavily influenced by complex radiation processes which can only be described by non–equilibrium radiative transfer models. The temperature increases in the chromosphere is caused by one or several of the following heating mechanism; Joule heating, sonic and Alfvén waves. The structure and dynamics of the chromosphere are strongly dependent on the magnetic field and radiative energy transport. The intensity of chromospheric lines, e.g. the cores of Ca H & K, can be used to determine the magnetic activity of other stars than the Sun (see e.g. Noyes et al., 1984; Baliunas et al., 1995; Brandenburg et al., 1998; Saar and Brandenburg, 1999). At a height of around two megameters (Mm), the chromosphere ends and turns into the transition region. There, temperature rises sharply and the density drops by several orders of magnitude. This region represents the transition to solar corona. The corona extends to two to three solar radii, from which the solar wind takes over reaching far out into the interplanetary space.

In the following three sections, I describe these three layers of the Sun in more detail, because they are directly relevant to my work. In the last two sections, I give an overview about the cyclic behavior of magnetic activity of the Sun and the Sun-Earth relation.

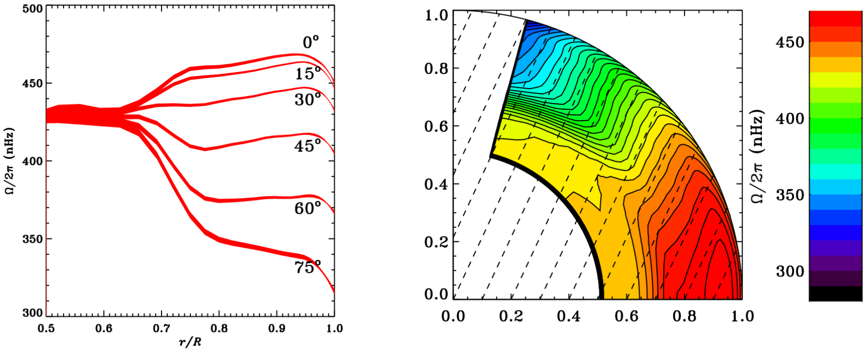

Figure 1.2: The internal differential rotation of the Sun as obtained from helioseismology. The bottom of the convection zone lies at $r = 0.713$ solar radii ($R_\odot$). Image courtesy of GONG.

1.1 The convection zone

In the convection zone, most of the energy is transported to the surface in convection cells, where hotter plasma rises, cools and sinks again; see § 2 for details. Typically, the size of the convection cells depends strongly on the depth due to strong ranging pressure scale height. At the bottom of the convection zone the cells are large, several tens of Mm. At the surface the cells have sizes of about one Mm and are called granules. In the convection zone these motions are highly turbulent. Additionally, the rotation of the Sun acts on the plasma motions as well and causes a differential rotation inside the convection zone. The equator of Sun rotates faster (25 days rotation period) than the poles (30 days). But the exact radial rotation was unknown until the advent of helioseismology. This technique, where one identifies discrete wave modes occurring on the surface of the Sun and invert their properties, allows to measure the velocity and temperature distribution inside the convection zone with a high precision. In Fig. 1.2 the rotation profile obtained by the Global Oscillation Network Group (GONG: Harvey et al., 1996) is shown. It matches the surface observation, where the equator rotates faster than the poles. But the differential rotation has also a radial dependence (see e.g. Thompson et al., 2003). Below the convection zone the radiative zone rotates with constant speed. However, the overlying convection zone has latitudinally dependent rotation and this leads to a region of strong velocity gradients (shear) at the bottom of the convection zone. This region is known as the tachocline (Spiegel and Weiss, 1980). A similar, but thinner region exists close to the surface, which is the Near Surface Shear Layer (NSSL), (see e.g. Thompson et al., 1996; Schou et al., 1998). The overall rotation is clearly not a profile of cylindrical rotation, but the contours of constant rotation are parallel to the rotation axis. In the Sun the contours are *spoke-like*, i.e. they are pointing radially outward. Sunspot proper motions indicate a meridional circulation in the solar convection zone; first found by Tuominen (1941). The flow direction is poleward near the surface and equatorward inside the convection zone. Helioseismology measurements confirm the poleward flow near the surface, but where the equatorward return flow is located is not clear at the moment. There could even exist more than one cell of circulation (Hathaway, 2011).

The dynamics and the structure of the convection zone is an important field of research, because the turbulent motions of the convection together with the differential rotation are able to generate a large-scale magnetic field. The existence of a large-scale magnetic field inside the convection zone is not disputed and can be observed at the surface on the Sun. That there is a mechanism of creating a magnetic field, called solar dynamo is not disputed either. But the location, of the dynamo and how the dynamo works is still under discussion. It is commonly believed that the magnetic field itself back reacts on the turbulent motion and differential rotation as well. At the moment, there is no way to observe magnetic fields below the solar surface. Therefore, we have to rely on simulations of solar dynamo models and constraints from surface observations. In § 4, I present a selection of different solar dynamo models as well as their results.

1.2 The surface of the Sun

The surface of Sun is a region which gives us the most information about the solar interior. We can measure the velocity and the magnetic field with high precision and use the solar oscillations for helioseismology. The convection cells at the surface form a pattern, which is called granulation. The hot plasma flows up in the center of each cell and flows down at its boundaries. The magnetic field occurs at the surface at different scales. The small-scale field is located between the granules in the intergranular lanes. Plage regions, where the magnetic field is stronger than in the quite Sun can cover a region larger than several granules. Hence, the magnetic field is not strong enough to quench the fluid motions, but the granulation is small-scale and obviously disturbed by the magnetic field. The situation is even more extreme in a sunspot. The dark spots on the solar surface, of which the biggest ones can be seen with the naked (protected) eye from the Earth, have strong magnetic field of up to 4000 gauss. The magnetic field is so strong that it suppresses the convective heat transport. This makes the sunspot become 1000 Kelvin cooler than the surface around it, resulting in a dark spot. A beautiful image of a sunspot observed with the

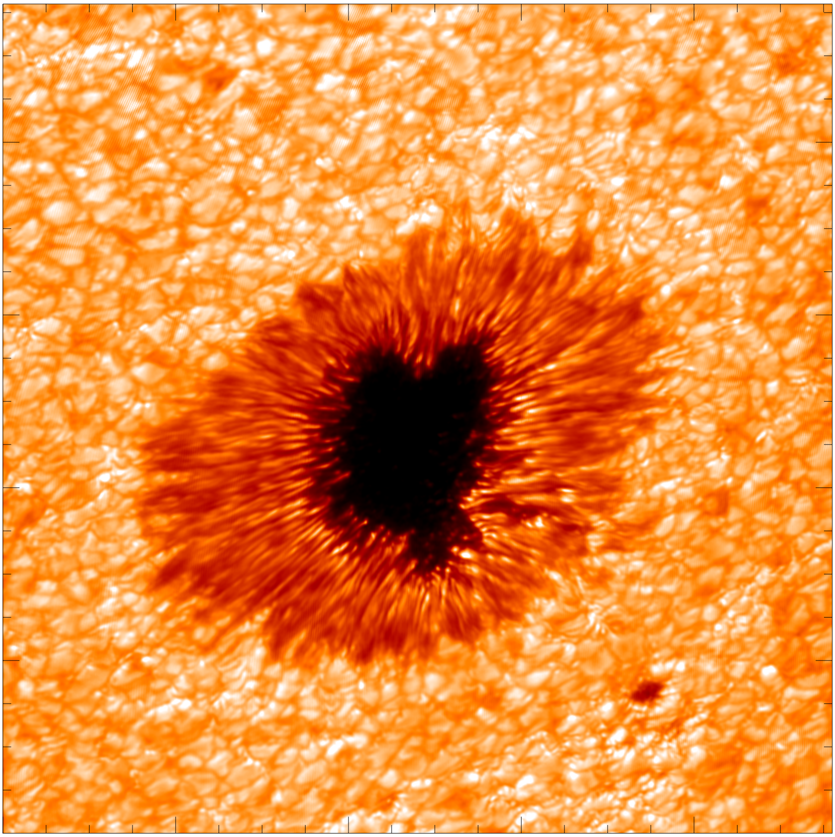

Figure 1.3: Image of a sunspot (AR1591). Observed with CRISP at the Solar Swedish Telescope (SST) on La Palma, Spain at a wavelength of 557.6 nm on 14th of October 2012. Observation and data reduction by Mats Löfdahl, Atefeh Barekat, and Jörn Warnecke.

Swedish 1-meter Solar Telescope can be seen in Fig. 1.3. Sunspots mostly occur as bipolar magnetic concentration with a leading (in terms of rotation) spot and a following spot or plage.

The dynamics and properties at the surface are determined by the radiative cooling of the hot plasma coming from the interior toward the surface. The surface of the Sun is called the photosphere and corresponds to the layer, where the optical depth of the continuum is unity. The strong radiative cooling leads to a strong temperature and therefore density gradient close to the surface.

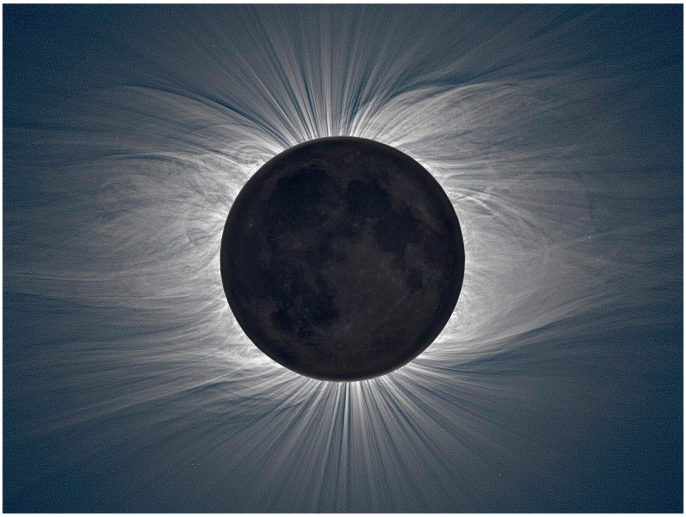

Figure 1.4: White light image of the solar corona during a solar eclipse 2009, observed at Enewetak Atoll, Marshal Islands. Composition of 38 eclipse images. Image processing by Miloslav Druckmüller. Courtesy: Miloslav Druckmüller, Peter Aniol, Vojtech Rusin, Lubomir Klocok, Karel Martisek, Martin Dietzel. `www.zam.fme.vutbr.cz/~druck/Eclipse/index.htm`

1.3 The solar corona

The solar corona is the outer part of the solar atmosphere and reaches out to several solar radii. The temperature in the corona is up to two—in coronal loops even ten—million of Kelvin, which leads to emission lines of highly ionized atoms. But because of the smaller density, which is nine orders of magnitude lower than in the photosphere, it is difficult to observed these lines. They are only observable from Earth during a solar eclipse (as shown in Fig. 1.4) or using a coronagraph, where the photospheric light is covered by an occluding disk. From space, one is able to measure the corona in ultraviolet and X-rays. Due to the low density, the magnetic pressure is stronger than the gas pressure (plasma $\beta = \frac{2\mu_0 p}{B^2} \ll 1$). This means that the resulting Lorentz force dominates inside the corona, and plasma flows along the field lines. Most of the emission comes from the hot plasma moving along magnetic field lines. Therefore the observed plasma structure corresponds directly to the magnetic field structure, as shown in Fig. 1.4. One of the unsolved problems in solar physics is the heating of the corona. The corona is several hundred times hotter than the solar surface and need therefore an additional heating source to sustain this high temperature. Numerical simulations have shown that braid-

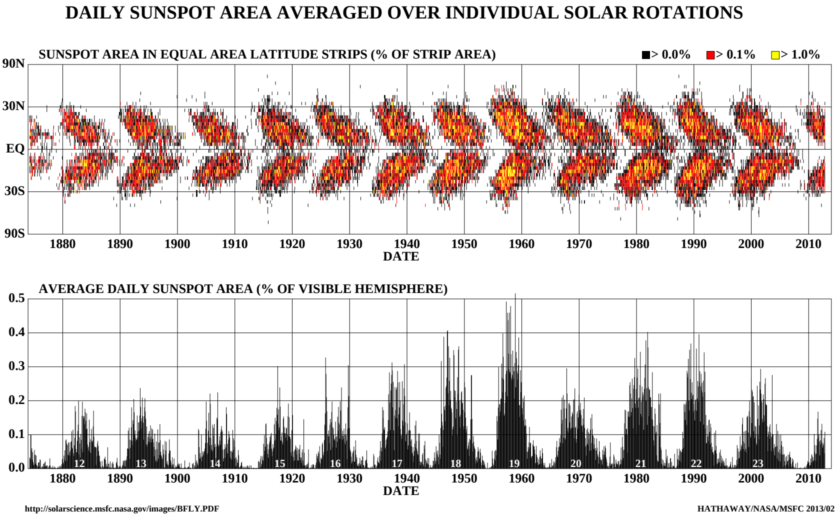

Figure 1.5: Time evolution of the sunspots area. The *upper panel* show the sunspots area in the dependence to the latitude over time. In the *lower panel* the average daily sunspots area is given over time. Graphics and Data courtesy of David Hathaway, NASA Marshall Space Flight center for Solar Physics.

ing of field lines at their footpoints in the photosphere can dissipate enough energy via Ohmic heating to produce coronal temperatures (see e.g. Gudiksen and Nordlund, 2005a; Bingert and Peter, 2011). However, there are other proposed mechanisms which also can lead to such high temperatures: Ohmic heating, sonic and Alfvén waves (see e.g. Aschwanden et al., 2007).

1.4 The solar cycle

Already Galileo Galilei observed sunspots as dark spots on the solar surface, although he thought they were clouds. He counted them and noted their numbers. But only in the 19th century, Schwabe (1844) discovered a cyclic variation with a period of around 10 years. Today we have data of sunspot numbers reaching all the way back to the days Galilei. These data led to an averaged cycle period of the sunspot numbers to be around 11 years (Schwabe's cycle). At solar maximum we can observe several hundred sunspots each month, while

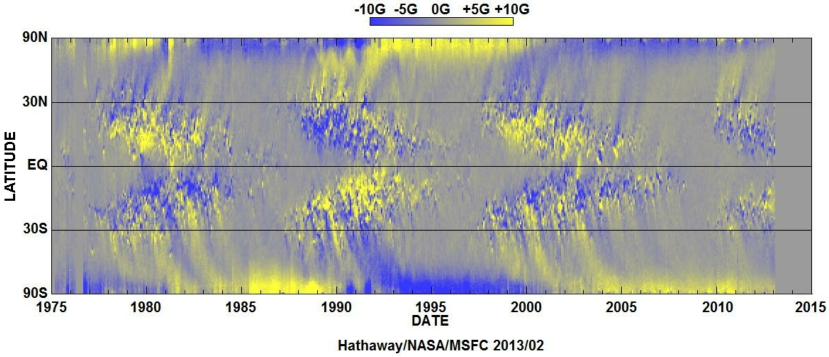

Figure 1.6: Synoptic magnetogram of three and a half solar cycles. Color coded is the radial magnetic field, which is plotted as the averaged magnetograms during the cycles. Graphics and Data courtesy of David Hathaway, NASA Marshall Space Flight center for Solar Physics.

at minimum there may be just a few, or none. In the recent history of the Sun, there have been cycles with just a few sunspots even for a several month during maximum. One prominent example is the Maunder Minimum (1650–1750), where only a few spots even during the maxima were observed. This was the time of the little ice age in Europe. If the Maunder Minimum and the ice age are correlated is highly debated at the moment.

More detailed observations revealed a spatial distribution of the sunspots' occurrence. As shown in Fig. 1.5, at the beginning of each cycle, sunspots emerge preferably at higher latitudes, while at the end of each cycle they emerge at lower latitudes (near the equator). This is often called a *butterfly diagram*, because variation of the latitude of sunspots occurrence with time is reminiscent of the wings of a butterfly. The overall preferred latitudes are between $\pm 30^\circ$. The number of sunspots of each maximum changes with every cycle. Data of hundreds of years of sunspot observation suggest a secondary overlying cycle with a period of around 100 years, which is called the Gleissberg cycle (Gleissberg, 1976). The current cycle is in the decaying phase a Gleissberg cycle, which had its maximum in the middle of last century (see e.g. Feynman and Ruzmaikin, 2011).

Since Hale (1908) and Hale et al. (1919) we know that sunspots correspond to magnetic field concentrations. The cyclic occurrence of the sunspots must be strongly correlated to the magnetic field inside the Sun. Every eleven years the sunspot pairs at the solar surface reverse their magnetic polarity. If observed sunspot pairs on the northern hemisphere have leading positive po-

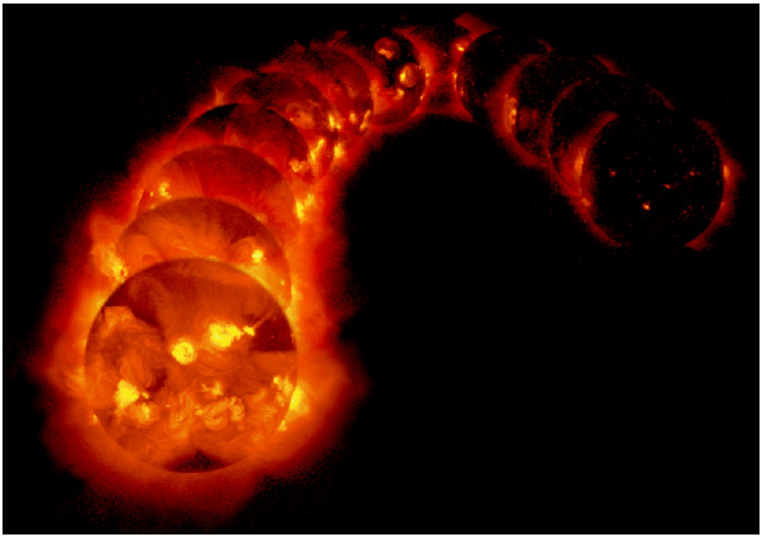

Figure 1.7: Evolution of solar activity in X-rays. The photographs were taken every 90 days by the satellite Yohkoh, a cooperative mission of Japan, the USA, and the UK, in the years 1991–1995.

larity, spot pairs on the southern hemisphere have leading spots with negative polarity. During the next sunspot cycle the leading spots on the northern hemisphere have negative polarity and positive polarity on the southern hemisphere (Hale et al., 1919). This behavior is a manifestation of the 22-year magnetic cycle (Hale's cycle). Synoptic magnetograms such as Fig. 1.6, where magnetograms are averaged in the time-latitude-plane, clearly show the magnetic cycle: the polarity reverses every eleven years. The oscillation and the equatorward migration of the magnetic field is an important observational evidence for a solar dynamo operating below the surface. With a primordial field, which has been amplified in the formation process of the solar system, such a behavior cannot be explained (see e.g. Dicke, 1978; Rosner and Weiss, 1992).

The solar cycle is seen not only at the visible surface. X-ray observation of the solar corona show a strong cyclic dependence, as illustrated in Fig. 1.7. The corona is hotter and more structured during solar maximum (see e.g. Wang and Sheeley, 2003). These variations are manifestations of a close relation between the solar cycle and strong variations in solar activity related to magnetic fields. This includes eruptive events like solar flares and coronal mass ejections, where huge amounts of energy are released. The overall solar irradiation is also cycle dependent (first reported by Willson and Hudson, 1988). Even though sunspots are dark and their coverage of the solar surface is higher at solar maximum (see Fig. 1.5), the solar irradiance is higher, because of the increased amount of bright points, associated with small-scale strong magnetic fields. Also the solar wind changes its structure during the cycle. At solar maximum coronal holes occur more frequently. These holes are often the source of the fast solar wind, which has speeds up to $800\,\mathrm{km s^{-1}}$ (see e.g. Cliver et al., 1996). With a stronger solar wind and higher magnetic field strengths, the solar magnetosphere can shield more effectively cosmic ray particles entering our solar system. This might be related to a modulation of the cloud production in the Earth atmosphere and so influence the climate on Earth (Svensmark and Friis-Christensen, 1997; Lübken et al., 2009).

1.5 Space weather

Space Weather describes the momentary condition of the Sun-Earth interaction, see the right panel of Fig. 1.8 for an artist illustration. A huge amount of energy can be stored in the magnetic field generated by the dynamo in the Sun. This energy can be partially released in violent eruptions. One of the prominent examples are solar flares, where magnetic reconnection releases energy directly via radiation mostly in Hα and the X-ray spectrum. These events are most visible in the solar chromosphere and the corona. The other prominent events are coronal mass ejections (CMEs), where plasma of the solar corona is ejected into the interstellar space. The plasma clouds cause shocks, which can accelerate particles to high velocities. An observed CME is shown in the left panel of Fig. 1.8, where a typical three-part structure (Low, 1999) is clearly visible. It comprises an outer arc-like structure of compressed coronal plasma, which piles up in front of its core. The inner bright core is the original ejected prominence. The third part is the cavity between the two bright structures. For details on solar eruption models see § 5.

These eruptive events can have strong impacts on our daily life. Beside the cultural and touristic influence of aurorae in arctic latitudes, these accelerating particles can endanger human technology and life. The Earth's magnetosphere prevents the main contribution of the particles and from the vicinity of the Earth. Outside the magnetosphere, where for example the solar satellite SOHO is operating, the radiation can be very strong. Microelectronics can be damaged and the particle radiation can endanger the life of astronauts. Flight to the Moon or to Mars is therefore very risky also from this perspective. As an example, between the missions of Apollo 16 and 17 a strong flare erupted in August 1972. It was energetic enough to endanger the life of the astronauts during the Apollo missions, had they been on the way to or on the moon (near-earth orbit doses from the solar flare on August 4, 1972 can be found in Savun and Sladkova, 1976, and estimates of a hypothetical interplanetary crew

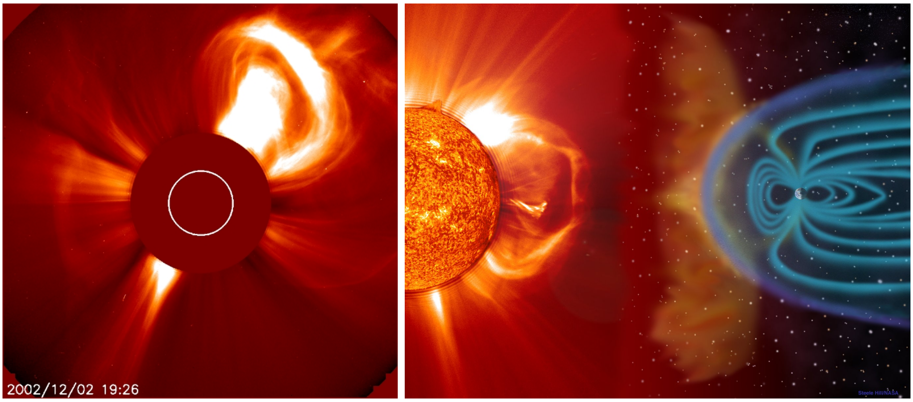

Figure 1.8: *Left panel*: This SOHO LASCO C2 image shows a very large coronal mass ejection (CME) blasting off into space on 2 December 2002. It presents the standard shape of a CME: a large bulbous front with a second, more compact, inner core of hot plasma. This material erupts away from the Sun at speeds of one to two million kilometers per hour. *Right panel*: Artist illustration of Sun-Earth interactions using a disk and a coronal image from SOHO. Image credit NASA.

dose during a strong solar flare in Stephens et al., 2005). Inside the Earth's magnetosphere the damage to microelectronics on satellites on typical near-Earth orbits is small. Strong impacts are caused by the interaction of accelerated particles and magnetic fields of CMEs and the Earth's magnetosphere. Depending on the field polarity, the magnetic field can trigger reconnection event in the Earth's magnetic fields. These events then can cause geomagnetic storms inside the Earth's magnetotail. Geomagnetic storms consist of accelerated energetic particles, which follow the field lines of the Earth's magnetic field toward the polar regions, where they are visible as aurorae. If the energy of the CME is strong enough, the geomagnetic storms can penetrate to lower latitudes, which leads to aurorae also there. The magnetic north pole—which is actually a south pole in the magnetic sense—does not have the same location as the geographical north pole, it is shifted by around 5° toward Alaska. This led to aurorae being visible at lower latitudes on the American continent than in Asia or Europe. Besides the aurorae, the impact of geomagnetic storms can be much more dramatic on the American continent than elsewhere at the same latitudes. There are two main risks to humans, one is primary, the other one is secondary. The primary risk is to be exposed to high radiation doses, for example on polar flights, which can easily exceed the annual safe limit (see e.g. Lantos, 2003). The secondary risk basically is the damage to infrastructure. Due to large geomagnetic induced currents, generators and transformer stations can be destroyed and lead to large power grid failures. In recent history there were several events of such power grid failures. One prominent example is the Quebec blackout in March 1989, where the city was without any power for 9 hours. This geomagnetic storm was so strong that aurorae were seen in Florida and Texas. However, much stronger storms are possible and can cause even larger damages. It is not unrealistic to think of power grid failures that last for several days in a large high populated region. Even in the summer time this would cause a lot of problems. Additionally, telecommunication and navigation systems are disturbed and can stop functioning. Nowadays, our society depends more and more on technologies that are highly vulnerable by solar eruptions.

The name *space weather* also indicates that the time scales of these events are rather short and comparable to those of weather on Earth. A CME needs one to five days to reach the Earth. Because of the strong impact on the Earth, several countries have installed early warning systems to be prepared. Today, we are monitoring the Sun with numerous space and ground based telescopes everyday—even looking with STEREO on the far-side of the Sun—to know, when the next CME will hit the Earth. However, to forecast and predict solar space weather, one should understand two important ingredient in more detail. One is the solar activity cycle. Observations show that solar eruptions happen preferably during solar maximum, i.e. when the magnetic field is relative strong (Schwenn, 2006). Modeling the solar activity cycle with a solar dynamo model will be part of my thesis and involves mostly **Papers V** and **VI**. The other ingredient is the emergence and eruption of magnetic fields from the solar convection zone through the solar atmosphere into the interplanetary space. The generation of magnetic field configurations, which then eventually trigger reconnection and liberation of magnetic energy and plasma, seems to be crucial for CME modeling. My contribution to modeling coronal ejections using an alternative approach also is part of my thesis and is described in **Papers I, II, III** and **IV**.

2. Solar Convection, Turbulence and Rotation

You can check-out any time you like,
But you can never leave!

Eagles

2.1 Convective motions

Convection is an important mechanism to transform thermal energy into kinetic energy. This is of particular interest in astrophysics, because large gradients of temperature together with gravity are often found in astrophysical environment, like in Galaxies, in accretion disks or in the interior of stars. Motions caused by convection are in most astrophysical environment turbulent and can lead to interesting physical phenomena, for instance, enhanced mixing of metals, generation of magnetic fields via a dynamo instability (see § 3.2 and § 4) or the footpoint motion of magnetic fields on the solar surface, leading to coronal heating (see e.g.Gudiksen and Nordlund, 2005a; Bingert and Peter, 2011).

2.1.1 The convective instability

Let us assume a simple explanatory case: We have a very large container of a perfect gas in hydrostatic equilibrium, with the vertical coordinate z. Gravitational acceleration is locally uniform pointing in the negative z direction $\boldsymbol{g} = -g\hat{\boldsymbol{z}}$, which leads to a decrease of density $\rho(z)$ and pressure $p(z)$ with height z. Now, we consider a blob of radius r, which has the same values of density ρ and pressure p as its surrounding medium. We displace the blob a small distance upwards against gravity; in Fig. 2.1 a sketch of the blob is shown. The density ρ' and pressure p' of the surrounding medium have decreased, so that $\rho' < \rho$ and $p' < p$. If the adiabatic time scale is much larger than the diffusion time scale, we can assume that the difference in pressure between the blob and the surrounding will reach a new balance rather quickly and will cause an adiabatic expansion of the blob $r \rightarrow r + \delta r$. But the exchange of heat is comparably slow, which can lead to a difference in temperature and

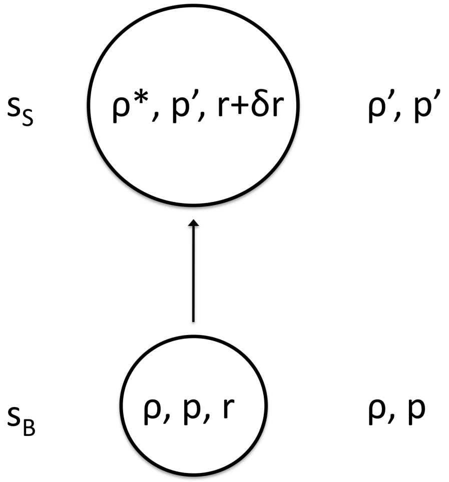

Figure 2.1: Moving a blob of gas upwards in a stratified surrounding.

therefore to a density ρ^* inside the blob which is different from ρ'. If the density inside the blob ρ^* is higher than in its surroundings, it is heavier and moves back downwards; the gas is stable. If the density inside the blob ρ^* is lower than in the surroundings, it moves upwards due to the buoyancy force; the gas is convectively unstable. This can be expressed by looking at the difference in the specific entropy s (i.e entropy per unit mass) of the blob and its surrounding medium. In a perfect gas this change of entropy is given by

$$\Delta s = c_\mathrm{V} \Delta \ln p - c_\mathrm{P} \Delta \ln \rho, \tag{2.1}$$

where c_V is the specific heat at constant volume and c_P is the specific heat at constant pressure. Let us now calculate the density difference $\Delta \ln \rho = \ln \rho^* - \ln \rho'$

$$\Delta \ln \rho = -\frac{1}{c_\mathrm{P}} \Delta s + \frac{1}{\gamma} \Delta \ln p \tag{2.2}$$

where $\gamma = c_\mathrm{P}/c_\mathrm{V}$ is the adiabatic index. The pressure difference balances to zero ($\Delta \ln p = 0$) leading to the expansion of the blob. Because the blob has been displaced adiabatically, its entropy stayed constant and we can express the entropy difference as a gradient over height. We can calculate the density difference as

$$\rho^* - \rho' = \frac{\rho'}{c_\mathrm{P}} \frac{\mathrm{d}s}{\mathrm{d}z} z. \tag{2.3}$$

This equality expresses directly the relation between the dynamics of the blob and the entropy gradient. If the entropy gradient is positive, the blob becomes heavier as it rises and is pulled downward by gravity. If the entropy gradient is negative, the blob becomes lighter as it rises and continues to rise. Solving a simplified momentum equation of the blob, we can express this behavior in terms of a frequency. This frequency N is called *Brunt–Väisälä frequency* and can be deduced from Eq. (2.3) to

$$N = \sqrt{\frac{g}{c_\mathrm{P}} \frac{\mathrm{d}s}{\mathrm{d}z}}, \tag{2.4}$$

where g enters because gravity is the restoring force. If N is a real number, the gas is convectively stable, and the blob will oscillate with the frequency N. If N is imaginary, the gas is convectively unstable, and the blob moves further upward and causes an instability. This is equivalent to the *Schwarzschild instability criterion*

$$\frac{\mathrm{d}\ln T}{\mathrm{d}\ln P} = \nabla > \nabla_\mathrm{ad} = \left(\frac{\mathrm{d}\ln T}{\mathrm{d}\ln P}\right)_s, \tag{2.5}$$

where ∇_ad is the double-logarithmic isentropic temperature gradient. The double-logarithmic temperature gradient ∇ is not to be confused with *nabla operator* $\boldsymbol{\nabla}$ in div, grad, and curl.

For cases, where the adiabatic time scale is comparable or smaller than the typical diffusive one, we need to define a more general criterion. In general, a fluid with a negative entropy gradient can be convectively unstable, if the diffusivities are small enough. There, the instability criterion can be expressed by the non-dimensional *Rayleigh number* (Jeffrey, 1926)

$$\mathrm{Ra} = \frac{gd^4}{\nu\chi}\left(-\frac{1}{c_\mathrm{P}}\frac{\mathrm{d}s}{\mathrm{d}z}\right)_0, \tag{2.6}$$

where d is the height of the domain, ν the kinematic viscosity and χ the heat diffusivity, which is related to the heat conductivity $K = c_\mathrm{P}\chi\rho$. The entropy gradient $\mathrm{d}s/\mathrm{d}z$ is either taken as an average or at a certain location. A meaningful Rayleigh number can only be calculated from the hydrostatic reference solution, which is indicated by the 0. For every system, there exists a critical positive Rayleigh number $\mathrm{Ra}_\mathrm{crit}$, above which the gas is (linearly) convectively unstable.

$$\mathrm{Ra} > \mathrm{Ra}_\mathrm{crit} \Rightarrow \text{unstable} \tag{2.7}$$

For a non-rotating fluid without magnetic field the relation above corresponds to Eq. (2.5). To determine this number analytically is nearly impossible and depends on the boundary conditions. If the Rayleigh number in a system is very large, the gas would likely be convectively unstable.

A more detailed discussion of the derivation and the calculation of the instability criteria can be found in Choudhuri (1998) and Stix (2002).

2.1.2 Fluid dynamics

In many astrophysical systems the mean-free path of particles, like ions and electrons in a plasma, is much smaller than the typical physical length scale. This allows us to use the continuum mechanics for fluid dynamics. For example in the solar convection zone the typical mean-free path of the ions and electrons is of the order of $\lambda = 10^{-8}\,\mathrm{cm}$ and the typical length scale is the pressure scale height $H_P = 10^{10}\,\mathrm{cm}$, which satisfies the fluid dynamic approach. For describing changes and evolutions of fluid quantities, we use typically the Lagrangian or convective derivative, which moves along with the fluid motions

$$\frac{\mathrm{D}}{\mathrm{D}t} = \frac{\partial}{\partial t} + \boldsymbol{u}\cdot\boldsymbol{\nabla}, \tag{2.8}$$

where $\boldsymbol{u}$ is the fluid velocity. The conservation of mass leads to the continuity equation

$$\frac{\mathrm{D}\rho}{\mathrm{D}t} = -\rho\boldsymbol{\nabla}\cdot\boldsymbol{u}, \tag{2.9}$$

which is often rewritten with the logarithmic derivative as

$$\frac{\mathrm{D}\ln\rho}{\mathrm{D}t} = -\boldsymbol{\nabla}\cdot\boldsymbol{u}. \tag{2.10}$$

The conservation of momentum is given by the Navier–Stokes equation

$$\rho\frac{\mathrm{D}\boldsymbol{u}}{\mathrm{D}t} = \rho\boldsymbol{g} - \boldsymbol{\nabla}p + \boldsymbol{\nabla}\cdot 2\nu\rho\mathsf{S} + \boldsymbol{F}, \tag{2.11}$$

which is often also written in terms of the velocity evolution equation

$$\frac{\partial\boldsymbol{u}}{\partial t} = -\left(\boldsymbol{u}\cdot\boldsymbol{\nabla}\right)\boldsymbol{u} + \boldsymbol{g} + \frac{1}{\rho}\left(-\boldsymbol{\nabla}p + \boldsymbol{\nabla}\cdot 2\nu\rho\mathsf{S} + \boldsymbol{F}\right), \tag{2.12}$$

where the traceless rate-of-strain tensor S is given by

$$\mathsf{S}_{ij} = \tfrac{1}{2}(u_{i,j} + u_{j,i}) - \tfrac{1}{3}\delta_{ij}\boldsymbol{\nabla}\cdot\boldsymbol{u}, \tag{2.13}$$

and $\boldsymbol{F}$ includes additional forces originating, for example, from the magnetic field or rotation of the frame; ν is the microphysical kinematic viscosity. The contributions in the momentum equation can be categorized in three parts. There are the terms of forces which are set by the environment or the state of the fluid; the gravitational acceleration $\boldsymbol{g}$ and the pressure gradient $\boldsymbol{\nabla}p$ count to this category. Then there is the diffusion term $\frac{1}{\rho}\boldsymbol{\nabla}\cdot 2\nu\rho\mathsf{S}$, which includes second derivatives and will—as suggested by the name—smooth out strong velocity gradients. The third term $(\boldsymbol{u}\cdot\boldsymbol{\nabla})\,\boldsymbol{u}$ is the advection term and it is non-linear in the velocity $\boldsymbol{u}$. The last one is the most interesting term. Because of its non-linearity it makes analytic descriptions of the fluid difficult. One of the consequences of non-linearity is turbulence, which will be discussed in § 2.2. We can define a meaningful dimensionless number called the Reynolds number by comparing advection and diffusion terms

$$\mathrm{Re} \equiv \frac{\|(\boldsymbol{u} \cdot \boldsymbol{\nabla})\, \boldsymbol{u}\|}{\left\| \frac{1}{\rho} \boldsymbol{\nabla} \cdot 2\nu\rho \mathsf{S} \right\|} \approx \frac{UL}{\nu}. \tag{2.14}$$

U is the typical velocity of the system, L its typical length scale and $\|\cdot\|$ defines a norm, which has to be chosen specifically for the setup. The first term, which represents the exact definition is often called *term-based* Reynolds number. For Reynolds numbers of the order of unity or smaller, diffusion dominates and the flow is laminar; for Reynolds numbers much larger than unity, non-linearities dominate and the flow becomes turbulent. Typical values of the Reynolds number for the solar interior are $\mathrm{Re} \approx 10^{12} \ldots 10^{13}$. Note that the Reynolds number depends on the length scale under consideration; choosing the relevant length scale for a specific setup can be difficult. In **Papers I-VI**, we define the Reynolds number as $\mathrm{Re} = u_{\mathrm{rms}}/k_{\mathrm{f}}\nu$, where k_{f} is the wavenumber of the energy carrying scale and u_{rms} the root-mean-square velocity, see Eq. (2.24). As an example, in one of the simulation setups of **Paper V** $\mathrm{Re} = 50$, but the *term-based* Reynolds number is ≈ 5. The difference of one order of magnitude might be related to our choice of L, which we set to correspond to the depth of the convection zone. Using the pressure scale height near the surface as a more appropriate choice of L leads to an equality of the *term-based* Reynolds number and $\mathrm{Re} = u_{\mathrm{rms}}/k_{\mathrm{f}}\nu$. However, the norm used to determine the *term-based* Reynolds number plays a crucial role.

2.2 Turbulence

Turbulence is often present in astrophysics, but it is actually difficult to define accurately. We can call a flow turbulent, if the Reynolds number is very high and therefore fluid flows non-laminar. Turbulence can be also defined as a flow, in which the correlation length and correlation time become finite. The flow generates structures such as eddies and becomes in general more complex. It is easier to illustrate this with a simple example. Consider a fluid with a certain velocity and viscosity ν that flows around a cylinder; similar to a bridge pillar in a river. Assuming that the viscosity remains constant, we increase slowly the velocity and therefore the Reynolds number. In Fig. 2.2, we show an illustration of this behavior. For Reynolds numbers $\mathrm{Re} < 5$ the flow around the cylinder is fully laminar and without any disturbance, e.g. the flow patter in the front of the cylinder is the same as that behind the cylinder. For Reynolds

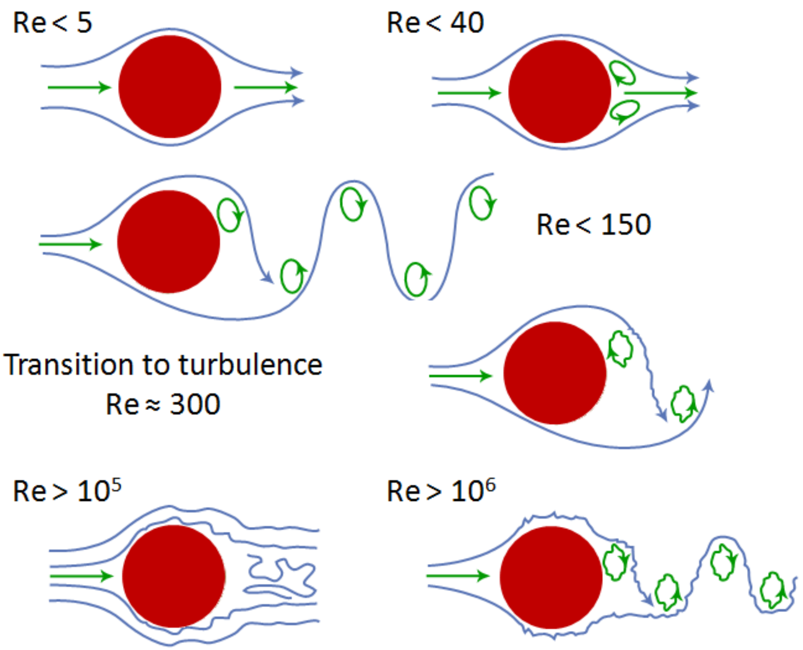

Figure 2.2: Flow past a cylinder for different values of the Reynolds number, from laminar to fully turbulent (Lienhard, 1966). Image courtesy of Koen Kemel.

numbers $\mathrm{Re} < 40$, we find a weak return flow associated with two eddies at the back of the cylinder. When the Reynolds number is increased to $\mathrm{Re} \lesssim 150$, then the eddies are ejected into the flow, which leads to an oscillatory flow pattern behind the cylinder. For even higher Reynolds numbers $\mathrm{Re} \approx 300$, transition to turbulence takes place and the flow pattern becomes very complex. Higher Reynolds numbers make the flow even more distorted and give rise to eddies at a range of different scales.

2.2.1 Kolmogorov turbulence

For isotropic homogeneous turbulence, we can describe some properties with the Kolmogorov theory (see e.g. Frisch, 1995). If we have a fluid in a statistically stationary state and we inject energy at a certain scale to sustain the turbulence, for example by stirring, we can apply this theory. Assuming the energy injection scale is large, then the corresponding wavenumber k is small. The energy spectrum will have a peak at this scale. Kolmogorov's theory predicts that the energy cascades toward smaller length scales with a constant slope as $k^{-5/3}$. At a certain scale for which $\mathrm{Re} = u_{\mathrm{rms}}/k\nu \approx 1$, depending on the viscosity ν, this power law changes to an exponential decrease. This scale is called the dissipative scale. At this scale the kinetic energy of the motions is dissipated to thermal energy via viscous heating.

2.2.2 Mean-field theory

Turbulence is a small-scale phenomenon but can contribute to large scales significantly (see e.g Frisch, 1995). For example, at every airport in the winter time, the wings of the airplanes are cleaned from ice before take-off. Otherwise *icing* can give a rougher wing surface causing turbulent motions along the wing. This leads to a change of the aerodynamic lift of the plane.

Describing the small scales of a fluid as well as its large scales in one consistent theory is very challenging. In addition, in numerical experiments of high Reynolds number turbulent flows, the grid resolution often is too small to resolve sufficiently a large range of scales. Mean-field theory is one way to approach this problem. There, the small-scale physics is modeled or parametrized in terms of mean-field quantities (see e.g. Rüdiger, 1989). A field $\boldsymbol{f}$ can be decomposed into a mean or averaged part $\overline{\boldsymbol{f}}$ and a fluctuation part $\boldsymbol{f}'$

$$\boldsymbol{f} = \overline{\boldsymbol{f}} + \boldsymbol{f}'. \tag{2.15}$$

The definition of the averaging procedure is arbitrary and only needs to satisfy the Reynolds rules,

$$\begin{aligned}
\overline{\boldsymbol{f}'} &= 0 && (2.16)\\
\overline{\boldsymbol{f}+\boldsymbol{h}} &= \overline{\boldsymbol{f}}+\overline{\boldsymbol{h}} && (2.17)\\
\overline{\left(\frac{\partial \boldsymbol{f}}{\partial x_i}\right)} &= \frac{\partial \overline{\boldsymbol{f}}}{\partial x_i} && (2.18)\\
\overline{\overline{\boldsymbol{f}}\boldsymbol{h}} = \ & \overline{\boldsymbol{f}}\,\overline{\boldsymbol{h}} = \overline{\boldsymbol{f}\overline{\boldsymbol{h}}}, && (2.19)\\
\overline{\overline{\boldsymbol{f}}\boldsymbol{h}'} &= 0 && (2.20)
\end{aligned}$$

where $\boldsymbol{h}$ is an arbitrary field and x_i an arbitrary direction including time. Typically the average is over time and/or one spatial direction. We can now rewrite the Navier–Stokes equation (2.12) in terms of mean quantities.

$$\frac{\partial \overline{\boldsymbol{u}}}{\partial t} = -\left(\overline{\boldsymbol{u}}\cdot\boldsymbol{\nabla}\right)\overline{\boldsymbol{u}} + \boldsymbol{g} + \frac{1}{\overline{\rho}}\left(-\boldsymbol{\nabla}\overline{p} + \boldsymbol{\nabla}\overline{\rho}\boldsymbol{\mathsf{Q}} + \boldsymbol{\nabla}\cdot 2\nu\overline{\rho}\overline{\boldsymbol{\mathsf{S}}} + \overline{\boldsymbol{F}}\right), \tag{2.21}$$

where we neglect additional terms involving correlation with fluctuating density ρ'. $\overline{\boldsymbol{F}}$ includes additional forces coming for example from the large-scale and small-scale magnetic field. $\boldsymbol{\mathsf{Q}}$ is the Reynolds stress tensor representing stress contributions due to the small-scale velocities as a second order correlation tensor and can be parametrized in terms of the mean flow. The components of this tensor are given for isotropic turbulence by

$$Q_{ij} = \overline{u_i' u_j'} = -\nu_{\mathrm{t}} \left(\frac{\partial \overline{u}_i}{\partial x_j} + \frac{\partial \overline{u}_j}{\partial x_i} \right) - \zeta_t \delta_{ij} \frac{\partial \overline{u}_k}{\partial x_k}, \tag{2.22}$$

where ν_{t} and ζ_t are the turbulent shear and bulk viscosities. They are parameters, which have to be calculated from the small-scale physics in the system. The Reynolds stresses (2.22) are clearly dissipative and can be interpreted as a representation of energy transfer to smaller non-resolved scales. The term of the Reynolds stresses in the mean Navier–Stokes equation can be combined with its mean diffusive term by adding the turbulent viscosity ν_{t} to the microphysical viscosity ν to give a total viscosity $\nu_{\mathrm{T}} = \nu + \nu_{\mathrm{t}}$. In most astrophysical objects the turbulent viscosity is much higher than the molecular one, therefore $\nu_{\mathrm{T}} \approx \nu_{\mathrm{t}}$.

2.2.3 Mixing length theory

Solving the turbulent hydrodynamic equations for stellar structure models is a complex problem, in particular, because the turbulent aspects of stellar convection are not fully understood. One way to estimate the turbulent viscosity ν_{t} in the solar interior is by using mixing length theory (see e.g. Stix, 2002). To simplify the equations, we can define a specific length scale, the mean-free-path of a convective blob. This length gives the distance, which a convective blob travels before it is completely mixed with the surroundings. This *mixing length* l is related to the typical length scale of the system, the pressure scale height H_P (Vitense, 1953) by,

$$l = \alpha_{\mathrm{MLT}} H_P \quad \text{with} \quad H_P = -\left(\frac{1}{p} \frac{\partial p}{\partial r} \right)^{-1}, \tag{2.23}$$

where α_{MLT} is a free parameter of $\mathcal{O}(1)$. A good estimate of the typical turbulent velocity of a system is given by the root-mean-squared velocity u_{rms}, defined as

$$u_{\mathrm{rms}} = \sqrt{\overline{(\boldsymbol{u}')^2}}. \tag{2.24}$$

The turbulent viscosity ν_{t} is related to the mixing length via (Prandtl, 1926)

$$\nu_{\mathrm{t}} = \tfrac{1}{3} u_{\mathrm{rms}} l = \tfrac{1}{3} \alpha_{\mathrm{MLT}} u_{\mathrm{rms}} H_P. \tag{2.25}$$

Clearly, the rms velocity u_{rms} as well as the pressure scale height H_P are depth dependent. In Table 2.1 the temperature, density, scale height, rms velocity and the turbulent viscosity are shown for different heights z in a solar mixing length model of Spruit (1974).

Table 2.1. The solar mixing length model of Spruit (1974).

z [Mm]	T [K]	ρ [g cm^{-3}]	H_P [Mm]	$u_{\rm rms}$ [m/s]	τ [d]	$\nu_{\rm t}$ [cm^2/s]
24	1.8×10^5	0.004	8	70	1.3	1.5×10^{12}
39	3.0×10^5	0.010	13	56	2.8	2.0×10^{12}
155	1.6×10^6	0.12	48	25	22	3.2×10^{12}
198	2.2×10^6	0.20	56	4	157	0.6×10^{12}

Note. — z is the distance to the solar surface, T the temperature, ρ the density, H_P the pressure scale height and τ is the typical turnover time of a convective cell. $\nu_{\rm t}$ is the calculated turbulent viscosity according to (2.25).

2.2.4 Turbulent heat transport

The heat transport in the convection zone is very complex, because the turbulent convective motions carry a significant amount of the total heat flux. This can be modeled also here by expressing the small-scale correlation properties with mean-field quantities (see e.g. Rüdiger, 1989). The mean convective heat flux reads

$$\boldsymbol{\mathfrak{F}}_{\rm conv} = \overline{(\rho \boldsymbol{u})' c_{\rm P} T'}, \tag{2.26}$$

where $(\rho\boldsymbol{u})'$ is fluctuating mass flux and T' the fluctuating temperature. With the help of mean-field calculations, one can derive the convective heat flux in terms of the mean entropy gradient, see Rüdiger (1989),

$$\boldsymbol{\mathfrak{F}}_{\rm conv} = -\chi_{\rm t}\overline{\rho}\overline{T}\boldsymbol{\nabla}\overline{s}, \tag{2.27}$$

where $\chi_{\rm t}$ is the turbulent heat diffusivity, which can be expressed in terms of the mixing length l

$$\chi_{\rm t} = \tfrac{1}{3}u_{\rm rms}l \tag{2.28}$$

or using the pressure scale height H_P

$$\chi_{\rm t} = \tfrac{1}{3}\alpha_{\rm MLT}u_{\rm rms}H_P. \tag{2.29}$$

The turbulent heat diffusivity is generally speaking not a scalar as in Eq. (2.27), but a tensor

$$\mathfrak{F}_i = -\chi_{ij}\overline{\rho}\overline{T}\partial_j\overline{s}. \tag{2.30}$$

If the heat fluxes and the entropy gradients are known, we can calculate the turbulent heat diffusivities accordingly. A good approximation for the convective heat flux is $|\boldsymbol{\mathfrak{F}}_{\rm conv}| \approx \rho u_{\rm rms}^3$, which was already pointed out by Vitense (1953).

2.3 Rotation

The Sun has a mean rotation period of around $T_{\rm rot} = 27.3\,$days. Compared with other stars, the Sun is considered a slow rotator. The solar rotation can be quantified in terms of the non-dimensional Coriolis number,

$$\mathrm{Co} = \frac{||2\boldsymbol{\Omega}_0 \times \boldsymbol{u}||}{||(\boldsymbol{u}\cdot\boldsymbol{\nabla})\,\boldsymbol{u}||} \approx \frac{2\Omega_0}{u_{\rm rms}k_{\rm f}}, \tag{2.31}$$

where $k_{\rm f}$ is the wavenumber of the inverse length scale of the system and $\boldsymbol{\Omega}_0 = \Omega_0(\cos\theta, -\sin\theta, 0)$ is the rotations vector with Ω_0 the rotation rate of the solar interior (without the convection zone), for which we can assume a solid body rotation. For the case of the Sun, the rotation frequency is $f = 1/T_{\rm rot} = \Omega_0/2\pi \approx 425\,$nHz. The Coriolis number gives the strength of rotation compared with the turbulent motions. For the solar convection zone we often choose (as in e.g. Käpylä et al., 2010, as well as **Papers IV–VI**)

$$k_{\rm f} = \frac{21}{R_\odot} \approx \frac{2\pi}{d}, \tag{2.32}$$

where $d = 0.3R_\odot$ is the thickness of the convection zone and $R_\odot \approx 700\,$Mm the solar radius. In the literature the Rossby number Ro is often used instead of the Coriolis number (following Stix, 2002)

$$\mathrm{Ro} = \frac{u_{\rm rms}}{2\Omega_0 l} \quad \Rightarrow \quad \mathrm{Co} = \frac{2\pi}{\mathrm{Ro}}, \tag{2.33}$$

where $l = 2\pi/k_{\rm f}$. Hence, the Rossby number is the same as the inverse Coriolis number except a factor of 2π. The Coriolis number of the Sun is around 6, when averaged over the convection zone. If we instead take a height dependent rotation profile and a height dependent rms velocity, the Coriolis number shows also a strong height dependence. At the bottom of the convection zone the Coriolis number is around $\mathrm{Co} \approx 60$, while near the surface $\mathrm{Co} \approx 0.06$ (Stix, 2002).

As shown in Fig. 1.2, the Sun rotates in the convection zone non-cylindrically, which is unexpected. Let us consider the simplest case. We have a sphere of fluid rotating about an axis. If there is no turbulence or other forces, the sphere rotates as a solid body. This means, Ω is constant and the rotation speed $u_\phi = \Omega\varpi = \Omega r \sin\theta$ increases linearly with distance from the rotation axis $\varpi = r\sin\theta$. The situation changes, if we consider pressure gradient and gravity acting on the fluid. When the turbulent motions are weak compared with rotation speed ($\mathrm{Co} \gg 1$), the Coriolis force balances with the pressure and the gravity. Then, the *Taylor-Proudman theorem* states, that the contours of constant rotation rate are parallel to the rotation axis; i.e. the local velocity of the fluid is constant along cylindrical surfaces, if the density is constant. In **Paper IV** and **VI**, the differential rotation is constant along cylindrical surfaces, because of the strong rotation rate as implied by the Taylor-Proudman theorem. The Sun is slightly above this limit (Co ≈ 6), and the additional forces acting on the plasma are more important in the convection zone (Kippenhahn, 1963). There, anisotropic turbulent motions and turbulent heat fluxes generated by the convection resulting in a non-zero latitudinal temperature gradients break the Taylor-Proudman balance via the baroclinic term, see Eq. (2.37). In addition the magnetic field also influences the motion of the flow inside the convection zone, but we will introduce this in § 3. These forces are able to transform the rotation of a solid body to a differential rotation with radial contours of constant rotation. In **Paper V** we found a similar differential rotation profile, although the rotation rate is slightly higher (Co ≈ 8), but also there the turbulent stresses and the turbulent heat transport form this rotation profile via the baroclinic term. On the other hand the rotation will influence the convective motions due to the Coriolis and centrifugal forces. The rotation has yet another effect on the fluid motions. It generates a mean flow in the meridional plane, which points polewards at the surface and equatorwards below the surface. This flow is called the *meridional circulation.* It is known since long time, that a slow rotating body as the Sun should have a so-called *Eddington–Sweet circulation* to fulfill conservation of energy (see e.g. Kippenhahn and Weigert, 1990). The meridional circulation can be interpreted as a type of Eddington–Sweet circulation, and it is caused by the inclination of the isobaric relative to the isopycnic surfaces. Isobaric and isopycnic surfaces are the surfaces, where the pressure and the density are constant, respectively. But for the Sun, the time-scale of the Eddington–Sweet circulation is longer than its lifetime.

2.4 Mean-field models of solar differential rotation

The main mechanism causing the differential rotation is the anisotropy of the convective motions (see e.g. Kippenhahn, 1963; Tuominen and Rüdiger, 1989). The Sun is approximately axially symmetric. Therefore we can define mean quantities by averaging over the azimuthal direction ϕ. To investigate this, we look at the conservation of mean angular momentum in spherical coordinates.

$$\frac{\partial\left(\overline{\rho}\overline{\Omega}r^2\sin^2\theta\right)}{\partial t}+\boldsymbol{\nabla}\cdot\left[\overline{\rho}r\sin\theta\left(\overline{\boldsymbol{u}}\overline{u}_\phi+\overline{\boldsymbol{u}'u'_\phi}\right)\right]=0, \tag{2.34}$$

where $\overline{\Omega}=\overline{u}_\phi/r\sin\theta$ is the local rotation rate, $\overline{\boldsymbol{u}'u'_\phi}$ is part of the Reynolds stress tensor $\boldsymbol{Q}$ introduced in Eq. (2.22). Note that we neglect here the magnetic parametrization of the angular momentum transport. First order smoothing calculations reveal an extra term in the components of the Reynolds stress tensor, which is related to the mean rotation

$$Q_{ij} = \Lambda_{ijk}\overline{\Omega}_k - \mathfrak{N}_{ijkl}\overline{u}_{k;l}, \tag{2.35}$$

where the semicolons denote the co-variant derivatives. Comparing Eq. (2.35) with Eq. (2.22), we find that the isotropic part of the turbulent viscosity tensor $\mathfrak{N}_{ijkl}$ can be associated with the turbulent viscosity ν_{t}. The Λ_{ijk} describes the so-called Λ-effect. Using the right parameter for Λ_{ijk} and $\mathfrak{N}_{ijkl}$, it is possible to model the differential rotation of the Sun (see e.g. Tuominen and Rüdiger, 1989; Brandenburg et al., 1992; Kitchatinov and Rüdiger, 1995; Kitchatinov and Rüdiger, 2005).

Differential rotation can be obtained by solving Eq. (2.34) alone while ignoring the meridional circulation. But it will be insufficient, if the rotation period becomes shorter than the time scale of the turbulent viscosity. This is expressed with the Taylor number

$$\mathrm{Ta} = \left(2\Omega_0 R_\odot^2/\nu_{\mathrm{t}}\right)^2. \tag{2.36}$$

For the Sun the Taylor number is around $\mathrm{Ta} \approx 3\times10^7$ (Rüdiger, 1989). The meridional circulation depends on the rotation rate. For low Ta the meridional flow increases with increasing Ta, until it reaches $\mathrm{Ta} \approx 3\times10^5$, then it decreases with increasing Ta; for a rotation rate equal or larger than that of the Sun, the meridional circulation is suppressed by the rotation (Köhler, 1970). This can also be seen from the evolution equation of the mean azimuthal vorticity, which can be derived by taking the curl of $(\boldsymbol{\nabla}\times)$ Eq. (2.21) (e.g. Küker and Stix, 2001)

$$\frac{\partial\overline{\omega}_\phi}{\partial t} = r\sin\theta\,\frac{\partial\overline{\Omega}^2}{\partial z} - \left[\boldsymbol{\nabla}\times\frac{1}{\overline{\rho}}\boldsymbol{\nabla}\left(\overline{\rho}\mathfrak{Q}\right)\right]_\phi + \left(\overline{\boldsymbol{\nabla}T\times\boldsymbol{\nabla}s}\right)_\phi, \tag{2.37}$$

where $\frac{\partial}{\partial z} = \cos\theta\,\frac{\partial}{\partial r} - \frac{1}{r}\sin\theta\,\frac{\partial}{\partial\theta}$ is the derivative along the rotation axis. We neglect here again the Maxwell stresses $\mathfrak{M}$, which can be added by replacing $\overline{\rho}\mathfrak{Q} \Rightarrow \overline{\rho}\mathfrak{Q}+\mathfrak{M}$. The three terms on the right hand side give rise to three different mechanisms to produce meridional circulation. The first is due to the differential rotation, the second due to Reynolds stresses. The third term is the baroclinic term and is probably the most important one for the meridional circulations (Rüdiger, 1989; Kitchatinov and Rüdiger, 2005). As can be seen from Eq. (2.37), baroclinicity is defined as the misalignment of the gradient of temperature and entropy, which gives a contribution to the vorticity evolution. The baroclinic term has two contributions: $\left(\overline{\boldsymbol{\nabla}T\times\boldsymbol{\nabla}s}\right)_\phi = \overline{\partial_r T\,\partial_\theta s} - \overline{\partial_\theta T\,\partial_r s}$.

Radial and latitudinal entropy gradients are comparable, but because the latitudinal temperature gradient is usually much smaller than the radial temperature gradient, the baroclinic term is a manifestation of the result of a latitudinal entropy difference. This implies that the poles are hotter than the equator. Mean-fields models show that just a few Kelvin difference between poles and equator can cause a solar-like meridional circulation (Rüdiger, 1989). In simulations, it frequently turns out that the influence of the Reynolds stresses can be neglected. Assuming now a constant meridional flow, the left hand side of Eq. (2.37) is zero and the two remaining terms on the right hand side must balance. The term $r\sin\theta\frac{\partial\overline{\Omega}^2}{\partial z}$ indicates, to which degree the differential rotation is cylindrical or non-cylindrical. For a cylindrical rotation the term is zero, for differential non-zero. This means that a dominant baroclinic term can reshape the cylindrical differential rotation caused by anisotropic Reynolds stresses to a non-cylindrical one. In **Paper VI** we have used this equation to conclude that the solar-like radial contours of constant rotation are shaped by the a non-zero latitudinal entropy gradient.

3. Magnetohydrodynamics

> *From a long view of history—seen from, say,*
> *ten thousand years from now—there can be little doubt*
> *that the most significant event of the 19th century will be judged*
> *as Maxwell's discovery of the laws of electrodynamics.*
>
> Richard Feynman

For many astrophysical objects magnetic fields are essential. Magnetic fields have a strong influence in the star formation processes occurring in a collapsing nebula. Magnetic fields cause a planetary disk to become turbulent without which planet formation may be impossible. Magnetic fields give stars as our Sun an activity cycle that has a strong impact on the surrounding planets via eruptive events.

3.1 Magnetohydrodynamical equations

In general, the evolution of magnetic fields $\boldsymbol{B}$ and electric fields $\boldsymbol{E}$ are described by the Maxwell equations (Maxwell, 1865)

$$\nabla \cdot \boldsymbol{E} = \frac{\rho_e}{\varepsilon_0} \qquad \text{[Gauss' law]}, \tag{3.1}$$

$$\nabla \cdot \boldsymbol{B} = 0 \qquad \text{[no magnetic monopoles]}, \tag{3.2}$$

$$\nabla \times \boldsymbol{E} = -\frac{\partial \boldsymbol{B}}{\partial t} \qquad \text{[Faraday's law]}, \tag{3.3}$$

$$\nabla \times \boldsymbol{B} = \mu_o \boldsymbol{J} + \mu_o \varepsilon_o \frac{\partial \boldsymbol{E}}{\partial t} \qquad \text{[Ampere's and Maxwell's law]}, \tag{3.4}$$

where ρ_e is the charge density, ε_0 the vacuum permittivity and μ_0 the vacuum permeability. The speed of light is defined via $c = 1/\sqrt{\varepsilon_0 \mu_0}$. To describe magnetic fields in astrophysical objects, we combine the Maxwell equations with the equations of the fluid dynamics introduced in § 2.1.2. To simplify we assume non-relativistic velocities, no electromagnetic waves and high conductivity. Additionally we use Ohm's law and in doing so transform the magnetic and electric fields into the co-moving frame of the fluid. With these conditions, we can derive the evolution equation for the magnetic field, the **induction equation**

$$\frac{\partial \boldsymbol{B}}{\partial t} = \nabla \times (\boldsymbol{u} \times \boldsymbol{B}) - \nabla \times (\eta \nabla \times \boldsymbol{B}), \tag{3.5}$$

where $\eta = 1/\mu_0\sigma$ is the magnetic diffusivity and σ the conductivity. The current density is given by

$$\boldsymbol{J} = \frac{1}{\mu_0}\boldsymbol{\nabla}\times\boldsymbol{B}. \tag{3.6}$$

To form a complete set of equations in magnetohydrodynamics (MHD), we combine the equation above with the **Navier–Stokes equation** (2.12) including the Lorentz force $\boldsymbol{F}_\mathrm{L} = \boldsymbol{J}\times\boldsymbol{B}$,

$$\frac{\partial \boldsymbol{u}}{\partial t} = -\left(\boldsymbol{u}\cdot\boldsymbol{\nabla}\right)\boldsymbol{u} + \boldsymbol{g} + \frac{1}{\rho}\left(\boldsymbol{J}\times\boldsymbol{B} - \boldsymbol{\nabla}p + \boldsymbol{\nabla}\cdot 2\nu\rho\mathsf{S} + \boldsymbol{F}\right) \tag{3.7}$$

and the **continuity equation** as in Eq. (2.10)

$$\frac{\mathrm{D}\ln\rho}{\mathrm{D}t} = -\boldsymbol{\nabla}\cdot\boldsymbol{u}. \tag{3.8}$$

Usually we also include an **energy equation**. Here we take one in the form of the evolution equation of the specific entropy

$$T\frac{\mathrm{D}s}{\mathrm{D}t} = \frac{1}{\rho}\boldsymbol{\nabla}\cdot K\boldsymbol{\nabla}T + 2\nu\mathsf{S}^2 + \frac{\mu_0\eta}{\rho}\boldsymbol{J}^2, \tag{3.9}$$

where K is the heat conductivity, $2\nu\mathsf{S}^2$ is the viscous heating and $\frac{\mu_0\eta}{\rho}\boldsymbol{J}^2$ is the Joule or Ohmic heating. We use these equations with the assumption of a perfect gas obeying the **equation of state**

$$p = \frac{1}{\gamma}c_\mathrm{s}^2\rho, \quad \text{with} \quad c_\mathrm{s}^2 = \frac{1}{c_\mathrm{P}}\left(\gamma-1\right)T, \tag{3.10}$$

where c_s is the speed of sound. The Eqs. (3.5)–(3.10) form a complete set of MHD equations.

In the induction equation, we have, similar to Eq. (2.12), an advection and a diffusion term. Here, we can also define a non-dimensional number to describe the relation of these two terms. Because of the similarity to the Reynolds number, we call it the magnetic Reynolds number, which is defined as

$$\mathrm{Re_M} \equiv \frac{\|\boldsymbol{\nabla}\times(\boldsymbol{u}\times\boldsymbol{B})\|}{\|\boldsymbol{\nabla}\times(\eta\boldsymbol{\nabla}\times\boldsymbol{B})\|} \approx \frac{UL}{\eta}, \tag{3.11}$$

where we used dimensional arguments. U is the typical velocity of the system, and L the typical length scale. For magnetic Reynolds numbers in the order of unity or smaller the diffusion dominates and the magnetic field decays via Ohmic heating, for magnetic Reynolds numbers much higher than the unity magnetic field can be amplified. In the simulations of **Papers I–VI**, we use for the magnetic Reynolds number the definition $\mathrm{Re_M} = u_\mathrm{rms}k_\mathrm{f}/\eta$. Also here, the ratio of the two terms might give a different value than the $\mathrm{Re_M}$ defined above. Before discussing the mechanism of amplifying magnetic fields, we discuss briefly two important applications of the MHD equations.

3.1.1 Alfvén's theorem

When the conductivity σ is high enough, the field is frozen into the fluid. If we consider a bundle of parallel magnetic field lines in a fluid, there exists a well defined magnetic flux through the cross section of the bundle. During the motions of the fluid, the magnetic flux can change in two different ways. A change in the magnetic field can change the magnetic flux and a change in the cross section can change the flux as well. Adding now these two contributions, one can show that the total change of the flux $\mathrm{d}\Phi/\mathrm{d}t$ only depends on the current density $\boldsymbol{J}$ and the conductivity σ (see e.g. Stix, 2002, for a more detailed calculation)

$$\frac{\mathrm{d}\Phi}{\mathrm{d}t} = -\oint_C \frac{\boldsymbol{J}}{\sigma} \cdot \mathrm{d}\boldsymbol{l}, \tag{3.12}$$

where C is boundary of the cross section, $\mathrm{d}\boldsymbol{l}$ is the line element along the boundary. In the limit of $\sigma \to \infty$, the magnetic flux is constant. This theorem can be successfully applied in the solar convection zone and solar corona, where the high temperatures lead to high conductivities. There the flow and the magnetic fields are strongly tied to each other. The plasma-β parameter ($\beta = \frac{2\mu_0 p}{B^2}$) describes, whether the magnetic field or the fluid motion are dominating the other. In the convection zone, the plasma-β is mostly larger than unity and the fluid motion can generate magnetic fields due to this effect. In the corona, the plasma-β is mostly smaller than unity and plasma flows along the magnetic field lines forming coronal loops and prominences. In sunspots, magnetic fields are strong and plasma-β is smaller than unity. This suppresses the fluid motion inside the umbral region and quench the convective heat transport, leading to a dark spot.

3.1.2 Force-free fields

For the solar corona it is common to approximate the magnetic fields by force-free fields. In general, this means that the Lorentz force is zero, which can be achieved by (except the trivial solution $\boldsymbol{B} = \boldsymbol{0}$)

$$\frac{1}{\mu_0}\boldsymbol{\nabla} \times \boldsymbol{B} = \boldsymbol{J} = \alpha_{\mathrm{ff}}\boldsymbol{B}, \tag{3.13}$$

where α_{ff} is a force-free parameter. When $\alpha_{\mathrm{ff}} = 0$, then $\boldsymbol{J} = 0$ and the magnetic field is a potential field $\boldsymbol{B} = \boldsymbol{\nabla}\Phi_{\mathrm{m}}$ with no currents (Schmidt, 1964; Semel and Rayrole, 1968). It can be calculated by solving the Poisson equation for the magnetic potential $\Delta\Phi_{\mathrm{m}} = 0$. A more advanced method consist in using a non-zero α_{ff}. There, the currents $\boldsymbol{J}$ are (anti-)parallel to the magnetic fields $\boldsymbol{B}$. In **Paper I** we have calculated the angle between $\boldsymbol{J}$ and $\boldsymbol{B}$ for one of the simulations, which can give insights about α_{ff}, and we find that in the outer layers of our domain, which correspond to solar corona, the magnetic field is indeed force-free. Similar calculations have been done for more realistic models of the solar corona (Gudiksen and Nordlund, 2005a,b; Bingert and Peter, 2011), where the authors found also force-free fields in their simulated coronae. For describing the magnetic fields inside the corona, force-free extrapolation techniques are commonly used. One possibility is to use magnetograms obtained from high resolution observations of the photosphere and to extrapolate the magnetic field into upper atmospheric regions. There are two extrapolation methods, one is the linear force-free extrapolation, where $\alpha_{\rm ff} = \text{const}$ (Nakagawa and Raadu, 1972; Alissandrakis, 1981; Gary, 1989), the other one is the non-linear force-free extrapolation, where $\alpha_{\rm ff}$ is constant along a field line (Woltjer, 1958; Sakurai, 1981; Wiegelmann, 2004). A more detailed discussion of different methods of force-free extrapolation can be found in Wiegelmann (2008). Neither of these methods work very well. One reason is the chromosphere, which the field has to pass through.

3.1.3 Magnetic buoyancy

In § 2 we have already discussed the buoyancy of fluid elements due to different temperature gradients. Magnetic fields can also lead to buoyancy of fluid elements, this is called magnetic buoyancy. The Lorentz force in Eq. (3.7) can be decomposed into two contributions:

$$\boldsymbol{J} \times \boldsymbol{B} = \frac{1}{\mu_0} (\boldsymbol{B} \cdot \boldsymbol{\nabla}) \boldsymbol{B} - \frac{\boldsymbol{\nabla} \left(\boldsymbol{B}^2\right)}{2\mu_0}, \tag{3.14}$$

where the first term is the magnetic tension along field lines and the second term is the gradient of the magnetic pressure or magnetic energy density $\frac{\boldsymbol{B}^2}{2\mu_0}$. In Eq. (3.7) the magnetic pressure can then be combined with the gas pressure forming a total pressure

$$p_{\rm tot} = p + \frac{\boldsymbol{B}^2}{2\mu_0}. \tag{3.15}$$

If we consider a magnetic flux tube structure in non-magnetic surroundings. In magnetic flux tubes, magnetic field lines are confined to the tube. Then the magnetic field inside the tube leads to enhanced pressure. The pressure will balance in a short time compared to the diffusion time and causes an expansion of the tube. Because the mass inside the tube will not change, the expansion is accompanied by a decrease of density. A density difference with the surrounding medium leads to the buoyancy of the tube. Magnetic buoyancy is believed to be one of the key mechanism that makes magnetic flux tubes rise from the bottom of convection zone to the surface and form bipolar regions.

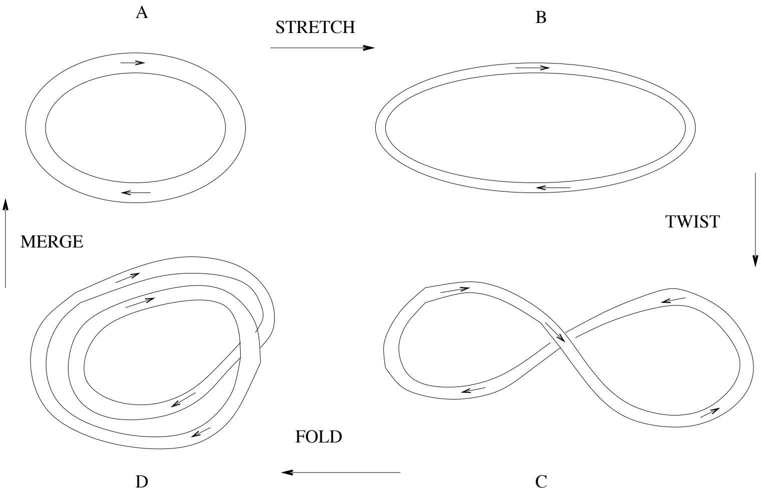

Figure 3.1: A schematic illustration of the stretch-twist-fold-merge dynamo mechanism. Taken from Brandenburg and Subramanian (2005).

3.2 Generation of magnetic fields

We know that the Earth, other planets, the Sun and other stars have magnetic fields. But where do they come from? We could imagine that weak magnetic fields already existed in the interstellar clouds, out of which stars and planets have been formed. In the phase of contraction, also the magnetic fields were concentrated inside the star and this leads to the existence of strong magnetic fields. This is certainly true, but this mechanism alone is not enough to explain the behavior of magnetic fields we observe today. The magnetic field for example of the Earth would have decayed by diffusion away already, if there would not have been a mechanism to regenerate magnetic fields. The fields of the Earth and of the Sun show also another crucial behavior. They reverse and, in the case of the Sun, oscillate. The reversal interval of the Earth's magnetic field is random and shows a range of 0.1 to 50 million years. The magnetic field of the Sun has an averaged period of 22 years. Oscillatory and reversal magnetic field are unexplained by primordial field models; it can only be explained by a dynamo mechanism (Ossendrijver, 2003; Brandenburg and Subramanian, 2005; Charbonneau, 2010).

The dynamo mechanism is a type of instability, which transfers kinetic energy into magnetic energy. But a dynamo mechanism as an instability can never create magnetic fields, it can only amplify small magnetic fields to larger ones. The basic idea can be illustrated by the *stretch-twist-fold-merge-mechanism*, see Vainshtein and Zel'dovich (1972) and Fig. 3.1. Taking a closed flux rope in a incompressible medium and expand it to twice its length (A⇒B). The volume of the rope will be preserved because of the incompressible surroundings. The magnetic field lines are frozen in, see § 3.1.1, and the cross section halves, therefore the magnetic field strength doubles. Now we twist the rope so that we get a figure as an eight (B⇒C). Then we fold the two loops on top of each other (C⇒D). We have now two loops, where the magnetic field points in the same direction and each of them has a magnetic field strength as strong as the original rope. With the help of reconnection, we can merge the two ropes into one rope with the same volume as before, but with twice the magnetic field (D⇒A). To generate a larger magnetic field we use kinetic energy to stretch, twist and fold the rope and a small amount of diffusivity to merge the loops This mechanism illustrates quite well the basic idea of a dynamo operating in the Sun or inside the Earth. In reality it would be hard to imagine a flow, which can reproduce the same deformations as described above. We will discuss now two of the important dynamo mechanisms generating magnetic fields; the first one is the so-called α^2-dynamo and the second one the so-called α-Ω-dynamo.

3.2.1 α^2-dynamo

From direct numerical simulations, we know that turbulence can amplify magnetic fields (see e.g. Brandenburg and Subramanian, 2005). We saw in § 2.2 that mean-field models are a powerful tool to describing turbulence and its influence on physical quantities. To describe turbulent dynamos, we use a mean-field approach. As a first step, we write the mean induction equation, (compare with Eq. (3.5) and see Krause and Rädler, 1980)

$$\frac{\partial \overline{\boldsymbol{B}}}{\partial t} = \boldsymbol{\nabla} \times \left(\overline{\boldsymbol{u}} \times \overline{\boldsymbol{B}}\right) + \boldsymbol{\nabla} \times \left(\overline{\boldsymbol{u}' \times \boldsymbol{B}'}\right) - \boldsymbol{\nabla} \times \left(\eta \boldsymbol{\nabla} \times \overline{\boldsymbol{B}}\right), \tag{3.16}$$

where primes indicate fluctuating quantities and bars mean quantities. The averaging reveals a new term $\boldsymbol{\nabla} \times \left(\overline{\boldsymbol{u}' \times \boldsymbol{B}'}\right)$, which is the correlation of the fluctuating velocity field and the fluctuating magnetic field. This term can be responsible for generating a magnetic field and is called mean electromotive force $\overline{\boldsymbol{\mathcal{E}}} = \overline{\boldsymbol{u}' \times \boldsymbol{B}'}$. Following the mean-field approach, we can express this quantity which rise from the fluctuations, in terms of mean quantities

$$\overline{\boldsymbol{\mathcal{E}}} = \overline{\boldsymbol{u}' \times \boldsymbol{B}'} = \alpha \overline{\boldsymbol{B}} - \eta_{\rm t} \boldsymbol{\nabla} \times \overline{\boldsymbol{B}}, \tag{3.17}$$

where α and the turbulent diffusivity $\eta_{\rm t}$ are in general tensors. Inserting it into Eq. (3.16) and assuming a turbulent flow without any mean velocity ($\overline{\boldsymbol{u}} = \boldsymbol{0}$), we obtain

$$\frac{\partial \overline{\boldsymbol{B}}}{\partial t} = \boldsymbol{\nabla} \times \left(\alpha \overline{\boldsymbol{B}}\right) - \boldsymbol{\nabla} \times \left(\eta_{\rm T} \boldsymbol{\nabla} \times \overline{\boldsymbol{B}}\right), \tag{3.18}$$

where we add the two diffusivities to a total diffusivity $\eta_{\rm T} = \eta_{\rm t} + \eta$. The turbulent diffusivity $\eta_{\rm t}$ in general increases the diffusion of the magnetic field and hence cannot contribute to a dynamo effect, but there can also be exceptions (see e.g. Devlen et al., 2012, where a case with $\eta_{\rm T} < 0$ was found). With a zero mean velocity field, the term $\boldsymbol{\nabla} \times \left(\alpha\overline{\boldsymbol{B}}\right)$, called the α-effect, is the only effect capable of amplifying a magnetic field (Steenbeck et al., 1966). For homogeneous and isotropic turbulence, α can be expressed by (see e.g. Pouquet et al., 1976)

$$\alpha = -\frac{1}{3}\tau_{\rm c}\overline{\boldsymbol{\omega}' \cdot \boldsymbol{u}'} + \frac{1}{3}\frac{\tau_{\rm c}}{\overline{\rho}}\overline{\boldsymbol{J}' \cdot \boldsymbol{B}'} = \alpha_{\rm K} + \alpha_{\rm M}, \tag{3.19}$$

where $\tau_{\rm c}$ is the turbulent correlation time, $\boldsymbol{\omega}' = \boldsymbol{\nabla} \times \boldsymbol{u}'$ is the fluctuating vorticity. $\alpha_{\rm K}$ is the kinetic, and $\alpha_{\rm M}$ the magnetic part of α, which can provide an important feedback of the mean magnetic field on α. If α and η_T are constant in space, we can move them in front of the derivatives. If we additionally assume axisymmetry in spherical coordinates along the ϖ-axis ($\varpi = r\sin\theta$, $\frac{\partial}{\partial\phi} = 0$), we can divide the mean magnetic field in a poloidal and toroidal part $\overline{\boldsymbol{B}} = \overline{\boldsymbol{B}}_{\rm pol} + \overline{\boldsymbol{B}}_{\rm tor}$ with $\overline{\boldsymbol{B}}_{\rm pol} = \left(\overline{B}_r, \overline{B}_\theta, 0\right)$ and $\overline{\boldsymbol{B}}_{\rm tor} = \left(0, 0, \overline{B}_\phi\right)$. Then we can decompose the mean-field induction equation in two separate equations:

$$\frac{\partial\overline{\boldsymbol{B}}_{\rm pol}}{\partial t} = \alpha\boldsymbol{\nabla} \times \overline{\boldsymbol{B}}_{\rm tor} + \eta_{\rm T}\Delta\overline{\boldsymbol{B}}_{\rm pol} \tag{3.20}$$

$$\frac{\partial\overline{\boldsymbol{B}}_{\rm tor}}{\partial t} = \alpha\boldsymbol{\nabla} \times \overline{\boldsymbol{B}}_{\rm pol} + \eta_{\rm T}\Delta\overline{\boldsymbol{B}}_{\rm tor}, \tag{3.21}$$

where we have used Eq. (3.3). Here we can see, why this dynamo is called α^2-dynamo. The toroidal field gets amplified by the α-effect from the poloidal field and the poloidal field gets amplified by the α-effect from the toroidal field.

3.2.2 α–Ω-dynamo

Now we consider an additional mean flow, and Eq. (3.18) will change to

$$\frac{\partial\overline{\boldsymbol{B}}}{\partial t} = \boldsymbol{\nabla} \times \left(\overline{\boldsymbol{u}} \times \overline{\boldsymbol{B}}\right) + \boldsymbol{\nabla} \times \left(\alpha\overline{\boldsymbol{B}}\right) - \boldsymbol{\nabla} \times \left(\eta_{\rm T}\boldsymbol{\nabla} \times \overline{\boldsymbol{B}}\right). \tag{3.22}$$

Applying now a mean flow $\overline{\boldsymbol{u}} = \overline{\boldsymbol{u}}_{\rm tor} = (0, 0, \Omega\varpi)$, which corresponds to a rotation with angular velocity Ω and using similar assumptions as above, we can also write two separate equations

$$\frac{\partial\overline{\boldsymbol{B}}_{\rm pol}}{\partial t} = \alpha\boldsymbol{\nabla} \times \overline{\boldsymbol{B}}_{\rm tor} + \eta_{\rm T}\Delta\overline{\boldsymbol{B}}_{\rm pol} \tag{3.23}$$

$$\frac{\partial\overline{\boldsymbol{B}}_{\rm tor}}{\partial t} = \boldsymbol{\nabla} \times \left(\overline{\boldsymbol{u}}_{\rm tor} \times \overline{\boldsymbol{B}}_{\rm pol}\right) + \alpha\boldsymbol{\nabla} \times \overline{\boldsymbol{B}}_{\rm pol} + \eta_{\rm T}\Delta\overline{\boldsymbol{B}}_{\rm tor}, \tag{3.24}$$

Now, we see that, because of the mean flow in terms of a rotation, the toroidal field gets amplified additionally by a term related to the mean velocity. This kind of dynamo is called α–Ω-dynamo, because the mean velocity is related to the differential rotation. Precisely speaking, this dynamo is called α^2–Ω-dynamo, but since the α-effect generating the toroidal field is typically weaker than the Ω-effect, it can be neglected.

3.3 Magnetic helicity

Magnetic helicity is an important quantity in astrophysics. Not only does it indicate the twist of magnetic fields, it is conserved on a resistive timescale. Magnetic helicity is defined as

$$H = \int_V \boldsymbol{A} \cdot \boldsymbol{B} \, \mathrm{d}V, \tag{3.25}$$

where $\boldsymbol{A}$ is the magnetic vector potential and related via $\boldsymbol{B} = \boldsymbol{\nabla} \times \boldsymbol{A}$ with the magnetic field. The magnetic helicity is in general gauge dependent, but choosing a infinite volume V one can make it independent. Normally, we are using the magnetic helicity density $h = \boldsymbol{A} \cdot \boldsymbol{B}$, which is always gauge dependent. In the following we will apply the Weyl gauge, which satisfies

$$\frac{\partial \boldsymbol{A}}{\partial t} = \boldsymbol{u} \times \boldsymbol{B} - \mu_0 \eta \boldsymbol{J} \tag{3.26}$$

The evolution equation for the magnetic helicity is then given by

$$\frac{\partial}{\partial t} \int_V \boldsymbol{A} \cdot \boldsymbol{B} \, \mathrm{d}V = -2 \int_V \mu_0 \eta \boldsymbol{J} \cdot \boldsymbol{B} \, \mathrm{d}V - \int_V \boldsymbol{\nabla} \cdot \boldsymbol{\mathfrak{F}}_h \, \mathrm{d}V, \tag{3.27}$$

where $\boldsymbol{\mathfrak{F}}_h$ are the helicity fluxes and we have used Eqs. (3.5) and (3.26). If we assume zero fluxes and look at the limit, when the conductivity is going to infinity ($\eta \Rightarrow 0$), then the right hand side of Eq. (3.27) vanishes and magnetic helicity is conserved. With the exception of the flux term $\boldsymbol{\nabla} \cdot \boldsymbol{\mathfrak{F}}_h$, the velocity does not enter, so magnetic helicity is not affected by turbulence diffusion. In the convection zone and the solar corona, the conductivity is high enough to conserve magnetic helicity to a first order, but there, also magnetic helicity fluxes will play an important role.

3.3.1 Catastrophic quenching of the α–effect and magnetic helicity fluxes

One might ask, why does the magnetic helicity have some relation with the α–effect? First of all, α consist of two parts: α_{K} and α_{M} (Pouquet et al., 1976). α_{K} describes the magnetic field amplification in the kinematic regime, i.e. when the magnetic field is weak and does not react back on the flow. In this stage, α_{M} is much smaller than α_{K} and can be neglected. For larger magnetic fields, α_{M} becomes much stronger and contributes with an opposite sign to α. We know from numerical simulations of homogeneous and isotropic turbulence (see e.g. Brandenburg and Subramanian, 2005) that the magnetic field grows first exponentially, which is consistent with linear stability analysis, and then saturates, when the field has become sufficiently strong. Usually, $\overline{\boldsymbol{\omega}' \cdot \boldsymbol{u}'}$ and $\overline{\boldsymbol{J}' \cdot \boldsymbol{B}'}$ have the same sign, let us assume the positive. As we see from Eq. (3.19), α_{M} enters with a plus sign and can balance with the negative α_{K}, if the field is strong enough. For helical magnetic fields, α_{M} can be related to the mean magnetic helicity of the fluctuating fields

$$\alpha_{\mathrm{M}} = \frac{1}{3}\frac{\tau_{\mathrm{c}}}{\rho}\overline{\boldsymbol{J}' \cdot \boldsymbol{B}'} \approx \frac{k_f^2}{3}\frac{\tau_{\mathrm{c}}}{\rho}\overline{\boldsymbol{A}' \cdot \boldsymbol{B}'}, \tag{3.28}$$

where k_f is the typical wavenumber of the fluctuations. Now let us look at the evolution of the mean magnetic helicity. We first consider the mean magnetic helicity of the total field $\overline{h} = \overline{\boldsymbol{A} \cdot \boldsymbol{B}}$, where the evolution equation is given by taking the mean of every term of Eq. (3.27)

$$\frac{\partial}{\partial t}\overline{h} = \frac{\partial}{\partial t}\overline{\boldsymbol{A} \cdot \boldsymbol{B}} = -2\mu_0\eta\overline{\boldsymbol{J} \cdot \boldsymbol{B}} - \boldsymbol{\nabla} \cdot \overline{\boldsymbol{\mathfrak{F}}}_h. \tag{3.29}$$

The mean magnetic helicity $\overline{h}$ has two contributions: one from the mean-fields $\overline{h}_m = \overline{\boldsymbol{A}} \cdot \overline{\boldsymbol{B}}$ and one from the fluctuating fields $\overline{h}_f = \overline{\boldsymbol{A}' \cdot \boldsymbol{B}'}$. In their evolution equations, an additional term appears arising from the electromotive force $\overline{\boldsymbol{\mathcal{E}}} = \overline{\boldsymbol{u}' \times \boldsymbol{B}'}$, see Eq. (3.17),

$$\frac{\partial}{\partial t}\overline{h}_m = \frac{\partial}{\partial t}\overline{\boldsymbol{A}} \cdot \overline{\boldsymbol{B}} = \quad 2\overline{\boldsymbol{u}' \times \boldsymbol{B}'} \cdot \overline{\boldsymbol{B}} - 2\mu_0\eta\overline{\boldsymbol{J}} \cdot \overline{\boldsymbol{B}} - \boldsymbol{\nabla} \cdot \overline{\boldsymbol{\mathfrak{F}}}^m_h, \tag{3.30}$$

$$\frac{\partial}{\partial t}\overline{h}_f = \frac{\partial}{\partial t}\overline{\boldsymbol{A}' \cdot \boldsymbol{B}'} = -2\overline{\boldsymbol{u}' \times \boldsymbol{B}'} \cdot \overline{\boldsymbol{B}} - 2\mu_0\eta\overline{\boldsymbol{J}' \cdot \boldsymbol{B}'} - \boldsymbol{\nabla} \cdot \overline{\boldsymbol{\mathfrak{F}}}^f_h, \tag{3.31}$$

where $\overline{h} = \overline{h}_m + \overline{h}_f$ and $\overline{\boldsymbol{\mathfrak{F}}}_h = \overline{\boldsymbol{\mathfrak{F}}}^m_h + \overline{\boldsymbol{\mathfrak{F}}}^f_h$. Using Eq. (3.28) together with the evolution of $\overline{h}_f$ from Eq. (3.31), we express the evolution of the magnetic α_{M}, see Kleeorin and Ruzmaikin (1982) by

$$\frac{\partial \alpha_{\mathrm{M}}}{\partial t} = -2\eta_t k_f^2 \left(\frac{\overline{\boldsymbol{u}' \times \boldsymbol{B}'} \cdot \overline{\boldsymbol{B}}}{B_{\mathrm{eq}}^2} + \frac{\alpha_{\mathrm{M}}}{\mathrm{Re}_{\mathrm{M}}} \right) - \boldsymbol{\nabla} \cdot \overline{\boldsymbol{\mathfrak{F}}}_{\alpha_{\mathrm{M}}}, \tag{3.32}$$

where the mean flux of α_{M} is related to the mean helicity flux of the fluctuating fields by

$$\overline{\boldsymbol{\mathfrak{F}}}_{\alpha_{\mathrm{M}}} = \frac{\eta_t k_f^2}{B_{\mathrm{eq}}^2}\overline{\boldsymbol{\mathfrak{F}}}^f_h, \tag{3.33}$$

where $B_{\rm eq}$ is the magnetic equipartition field strength, i.e. a magnetic field, whose energy is equal to kinetic energy. The expression (3.32) is also called the dynamical quenching formula and describes an important issue of the dynamo theory. For high magnetic Reynolds numbers $\rm Re_M$, the α-effect is *catastrophically* quenched (see e.g. Vainshtein and Cattaneo, 1992; Cattaneo and Hughes, 1996; Brandenburg and Dobler, 2001). This can be seen by setting the left-hand side of Eq. (3.32) to zero and using $\alpha_{\rm M} = \alpha - \alpha_K$

$$\alpha = \frac{\alpha_{\rm K} + {\rm Re_M}\left(\eta_{\rm t}\overline{\boldsymbol{J}}\cdot\overline{\boldsymbol{B}} - \frac{1}{2}\boldsymbol{\nabla}\cdot\overline{\boldsymbol{\mathcal{F}}}_h^f\right)/B_{\rm eq}^2}{1 + {\rm Re_M}\overline{\boldsymbol{B}}^2/B_{\rm eq}^2} \tag{3.34}$$

For high magnetic Reynolds numbers and vanishing flux, the second term balances with $\alpha_{\rm K}$ to a zero α. However, it is important that the mean magnetic helicity flux also enters into this equation. If $\boldsymbol{\mathcal{F}}_h^f$ is negative and large enough it can suppress the quenching (Blackman and Field, 2000). It has been seen in several numerical simulations of dynamos (Brandenburg and Subramanian, 2005; Mitra et al., 2011; Del Sordo et al., 2013) that if one allows for magnetic helicity fluxes, the catastrophic quenching is suppressed. The behavior is one of the motivations for using a combined model of a convection zone and a corona as in **Papers I** to **V**. An open boundary of a dynamo domain allows magnetic helicity fluxes to escape and alleviates the catastrophic quenching at high Reynolds numbers.

4. Solar Dynamo Models

Die Zukunft wird nicht gemeistert von denen,
die am Vergangenen kleben.

Willy Brandt

In this chapter I will briefly discuss a few of the most important models for the solar dynamo. More detailed discussions of solar dynamo models can be found in reviews by Ossendrijver (2003), Brandenburg and Subramanian (2005), Charbonneau (2010), and Brandenburg et al. (2012) as well as in Stix (2002) and in Charbonneau (2013).

4.1 The challenge

Modeling the solar dynamo is challenging. Not only does there exist a large range of scales, over which a solar dynamo mechanism should operate, there is also a large amount of observed features which a solar dynamo model should reproduce. Let us start with the scales set by the solar environment. The density scale height varies from about tenths of Mm deep in convection zone to 150 km at the surface. The temperature spans from the bottom to the surface the range from two million Kelvin to six thousand Kelvin. The fluid and magnetic Reynolds numbers inside the Sun are high enough to allow for hydromagnetic turbulence (Frisch, 1995). Even developing a hydrodynamical model without any magnetic fields would be challenging as such, see § 2.2. But solving the MHD equations with realistic parameters and resolving the small as well as the large scales in one simulation is at the moment impossible; or more precisely, the computing power is not sufficient to simulate a realistic model even if we run it as long as the age of the universe. Even if we assume the doubling of computing power every two years (Moore's law), it would take over 100 years to have computer powerful enough to solve the solar dynamo realistically.

We have constraints from observations of magnetic fields on the surface and in the solar atmosphere, but unfortunately no information about the magnetic field inside the convection zone. The main properties, a solar dynamo should reproduce, can be divided into global and local phenomena. The global are: an eleven years activity cycle as a result of a 22 years magnetic cycle, where every eleven years the field reverses; equatorward migration of radial and azimuthal magnetic fields being antisymmetric with respect to the equator, as well as a polar migration near the poles, as shown in Fig. 1.6. Additionally, global phenomena include a cyclic behavior with secondary cycles as the Gleissberg cycle and grand minima as the Maunder Minimum. As local phenomena, a solar dynamo model should reproduce flux concentrations in the range from sunspots and their groups to pores and plage fields. The magnetic orientation of the sunspots should be such that the leading and the following spots have the same polarity configuration in one hemisphere, but the opposite one in the other hemisphere. This configuration should remain for eleven years and reverse once every cycle (Hale's law). Further there should be a certain tilt angle of the line between two spots of a pair and the horizontal (Joy's law). We can also include magnetic field configurations, which allow flares and coronal mass ejections to occur. Additionally, there are the ingredients, introduced in the previous Chapters, in particular the effects of turbulent convection (see § 2) causing the solar differential rotation with the tachocline and the NSSL (see § 1.1).

There are different approaches to deal with the constraints mentioned above. Most of the approaches simplify the physical properties of their systems. There are the mean-field models, where the small-scale turbulent quantities are expressed and parametrized by mean quantities, see § 4.2 and Krause and Rädler (1980). These models are often utilized in two dimensional simulations. A subclass of these models are the kinematic models, where the backreaction of the magnetic field on the flow is neglected or just included in a rudimentary form. One example are the Babcock–Leighton dynamo models, see § 4.2.1. In contrast to the mean-field models are the direct numerical simulations (DNS) of solar dynamos, see § 4.3. There the fluid and magnetic Reynolds numbers are chosen above the limit of numerical diffusion and stability of the numerical setup. These values are orders of magnitude smaller than the realistic solar ones. Here, two additional simplifications are used. Instead of simulating the full spherical shell of the solar convection zone, often Cartesian boxes are used to simulate a region of interest as a part of the convection zone, see § 4.3.1. Also instead of self-consistent convective motion, random forcing is applied to generate turbulent motions. Groups doing local as well as global simulations (§ 4.3.2) use approximations for the fluid dynamics as incompressible or anelastic flows.

4.2 Mean-field models

In the mean-field models, we use the mean-field equations for the velocity field, the magnetic field and the density, see Eqs. (2.21) and (3.16) and Krause and Rädler (1980). Additionally the mean energy equation is solved using expressions for the convective flux similar to Eq. (2.27) or Eq. (2.30). The main difficulty of these models is to find good values and profiles for turbulent viscosity ν_t, turbulent diffusivity η_t as well as for α and Λ (see § 2.4). For this we can use mixing length theory, see § 2.2.3, or they can be determined from direct numerical simulations by using a technique like the test-field method (Schrinner et al., 2007).

One issue for mean-field models is the implementation of the magnetic backreaction on the flow. In many models the Lorentz force in the momentum equation is either ignored (kinematic) or the time evolution of the fluid is not even solved and instead the flow field prescribed and used in the mean induction equation (see e.g. Dikpati and Charbonneau, 1999; Ossendrijver, 2003). Other models use algebraic quenching formulae for α, as in Käpylä et al. (2006b)

$$\alpha = \frac{\alpha_0}{1 + \overline{\boldsymbol{B}}^2 / B_{\rm eq}^2}, \tag{4.1}$$

which is the same as neglecting the mean helicity flux and the mean current density ($\boldsymbol{\nabla} \cdot \overline{\boldsymbol{\mathcal{F}}}_h^f = \overline{\boldsymbol{J}} = 0$) in Eq. (3.34), or solve an explicit evolution equation for α as Eq. (3.32). In general, models where the meridional circulation is able to transport the flux and is dominant over the turbulent diffusion are often called *flux-transport dynamo models*, when the toroidal magnetic field is produced at the bottom of the convection zone and leads to equatorward migration of mean magnetic field at the surface (see e.g. Dikpati and Charbonneau, 1999). Most of the models solve the equations of the α-Ω-dynamo model, where the differential rotation obtained by helioseismology enters as an input parameter. Mean-field models were able to reproduce successfully many observed features, as in Rüdiger and Brandenburg (1995), Dikpati and Charbonneau (1999), Ossendrijver (2003), Käpylä et al. (2006b), and Kitchatinov and Olemskoy (2012).

Transition between the differential rotation in the convection zone to the rigid rotation in the core leads to a region of strong shear below the convection zone, the tachocline (Spiegel and Weiss, 1980). Strong shear results in a strong Ω-effect and can amplify the toroidal field to large values. However, how large these values are, is debated (Brandenburg, 2005). But, because of the quenching of α in dependence on the equipartition field strength $B_{\rm eq}$, see Eq. (4.1), having the α-effect localized in the same region is difficult. Parker (1993) proposed an interface dynamo, where α is strong above the tachocline to avoid the strong quenching effects, see for example the approaches by MacGregor and Charbonneau (1997). In other approaches, like those of Rüdiger and Brandenburg (1995) and Käpylä et al. (2006b), α was calculated more sophisticatedly. As an example we show in Fig. 4.1 a butterfly diagram from

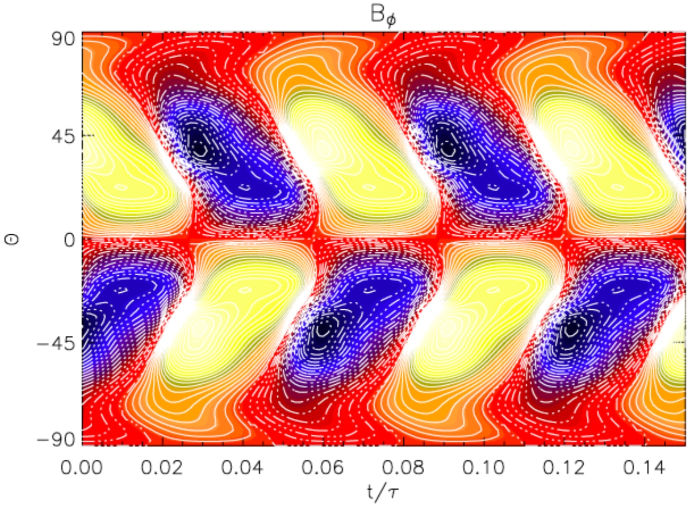

Figure 4.1: Butterfly diagram of mean azimuthal magnetic field $\overline{B}_{\rm phi}$ plotted over resistive time t/τ and latitude θ near the surface of the convection zone $r = 0.99 R_\odot$ for a mean-field α-Ω dynamo model (from Käpylä et al., 2006b).

Käpylä et al. (2006b), where a meridional circulation of $u_{\rm m} = 10\,{\rm m\,s^{-1}}$ is used. Additionally the authors include the effect of the NSSL (Brandenburg, 2005) as well as turbulent pumping (see e.g. Ossendrijver et al., 2002; Käpylä et al., 2006a), where anisotropies in the α-tensor lead to advection of mean magnetic fields. The new approach of this work was that the transport coefficients were obtained from local three dimensional calculations of convection. As seen from Fig. 4.1, the mean-magnetic field migrates equatorwards at lower latitudes and polewards near the poles. Additionally the field is antisymmetric over the equator. This is precisely the behavior of the solar magnetic field. In these models, the mean-fields are defined by averaging in azimuthal direction and therefore are not capable of resolving the small-scales or describing flux concentrations as observed in sunspots. Describing these phenomena needs an additional model for forming flux concentrations, for which there have been different proposals (see e.g. Kitchatinov and Mazur, 2000; Brandenburg et al., 2011a; Stein and Nordlund, 2012).

4.2.1 Babcock–Leighton dynamo models

A different approach is to include the process of sunspot formation and their decay into a solar dynamo model. It is broadly believed that sunspots are formed by strong magnetic flux tubes emerging from the tachocline to the so-

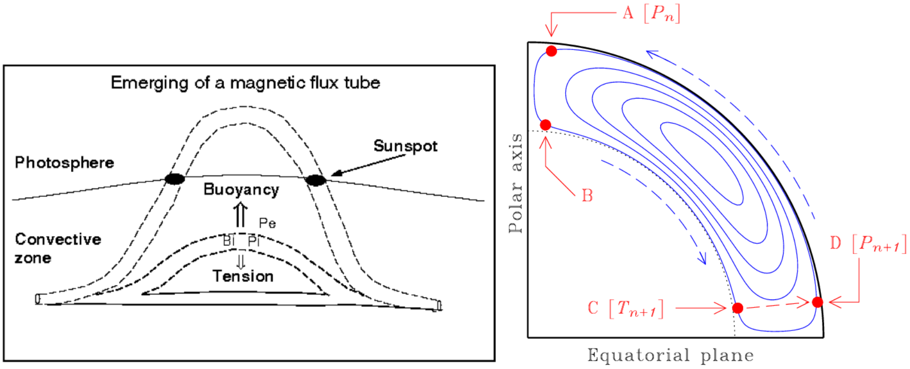

Figure 4.2: *Left panel:* A schematic sketch of an emerging magnetic flux tube. Due to magnetic buoyancy the flux tube rises from the bottom of the convection zone to the solar atmosphere. When it breaches through the photosphere it forms features like sunspots (After Parker, 1955, and Caligari et al., 1995). *Right panel:* Operation of a solar cycle model based on the Babcock–Leighton mechanism. The diagram is drawn in a meridional quadrant of the Sun, with streamlines of meridional circulation plotted in blue. Poloidal field having accumulated in the surface polar regions (A) at cycle n must first be advected down to the core–envelope interface (dotted line) before the production of the toroidal field for cycle $n+1$ can take place (B⇒C). Buoyant rise of flux ropes to the surface (C⇒D) is a process taking place on a much shorter timescale. From Charbonneau (2010).

lar surface and breaching as bipolar regions through the photosphere (see e.g. Ossendrijver, 2003; Charbonneau, 2010). I will first introduce the mechanism before discussing its results and criticism at the end of this section. It is known that strong shear in the tachocline can produce strong magnetic fields. If these fields get concentrated into flux tubes, they might rise due to the magnetic buoyancy effect, see § 3.1.3 for the description of the effect and an illustration in the left panel of Fig. 4.2. During its rise the tube might form a loop with an Ω shape, where the two *legs* breach through the solar surface and form the typical pattern of a bipolar region. This idea was already proposed by Parker (1955) and demonstrated in numerical models by Caligari et al. (1995). Numerical simulations of near surface loop emergence by Cheung et al. (2008) were able to reproduce observed features of sunspot emergence.

Babcock (1961) and Leighton (1964) introduced a new mechanism, which can be used for solar dynamo models. As described in § 1.4, sunspot pairs have a leading and a following spot (in respect with rotation) with opposite polarity. On average the leading spot emerges at lower latitudes than the following spot (Joy's law). Because of the differential rotation the spots will lose their cohesiveness. Eventually the leading spot will decay by coalescing with another sunspot of opposite sign from the other hemisphere. The following spot will be advected by meridional circulation toward the poles, where it forms together with other decaying sunspots a polar field of the sign of the former following sunspot. Flux tubes rising to the surface will be deflected by the Coriolis force resulting in twisted tubes and the tilt angle of the sunspot pairs following Joy's law. This effect is actually an α-effect operating on larger scales as the turbulence, but in comparison to the large-scale magnetic field of Sun, these scales are still small. Therefore, the Babcock–Leighton effect is nothing else than a local α-effect represented in Eq. (3.16) operating on larger scales than the turbulence and being confined to the near surface region. For the Babcock–Leighton mechanism, we need a meridional circulation and a differential rotation as a input for the flow. This is a kinematic flux-transport dynamo model, where the magnetic backreaction on the flow is completely neglected. Because the problem is axisymmetric and one hemisphere is independent of the other, it can be calculated as a two dimensional model with toroidal and poloidal fields in one hemisphere. The two amplification mechanisms (Ω and Babcock–Leighton) are separated in location and are only connected by the meridional circulation. In the right panel of Fig. 4.2, the scheme of the Babcock–Leighton-Model is shown. Starting at point A, the poloidal magnetic field of cycle n is transported by the meridional circulation downwards to the tachocline ($\mathsf{A} \Rightarrow \mathsf{B}$). There the field is transformed into a strong toroidal field due to the differential rotation and is transported towards the equator by the meridional circulation ($\mathsf{B} \Rightarrow \mathsf{C}$). The strong toroidal field rises to the surface due to magnetic buoyancy and generates sunspots of cycle $n+1$ ($\mathsf{C} \Rightarrow \mathsf{D}$). Then the sunspots decay and form a new reverse polar field ($\mathsf{D} \Rightarrow \mathsf{A}$).

The success of these models emerges from the good agreement with observations. With Babcock–Leighton models many observed features can be reproduced (see e.g. Dikpati and Charbonneau, 1999, Charbonneau, 2010, and reference therein), including grand minima in the solar cycle (see e.g. Karak, 2010). But this model is also strongly criticized, because of its simplifications (see e.g. Brandenburg, 2005). First of all, the formation of sunspots via emerging flux tubes is not well verified. If a flux tube emerges via magnetic buoyancy, also its volume expands and the magnetic field decreases. Therefore the generated magnetic field at the tachocline has to be large (100 kilo-gauss, see Choudhuri and Gilman, 1987), maybe too large to be generated by a dynamo mechanism (see e.g. Guerrero and Käpylä, 2011). Whether a flux tube survives the journey to the surface through violent turbulent convection depends crucially on the amount of magnetic twist in the tube (see e.g. Fang et al., 2010). The advection of the following spot of a sunspot pair to the poles implies that the spots in the pair loose their cohesiveness. These are strong simplifications, which are in contradiction with the effects of magnetic tension and pressure within the spots as well as the anchoring of the spots in the underlying azimuthal magnet field. One of the important assumptions of these models is the one-cell meridional circulation and Joy's law. The one-cell meridional circulation have been recently questioned by improved observations by Hathaway (2011) and simulations by Miesch et al. (2012). As one might think, Joy's law is an observationally determined law. But the tilde angle between the line between the two sunspots in a pair and the horizontal line is not always the same. It turn out, that detailed measurements show a large scatter range of the angle, which can be even negative at some occasions (Kosovichev and Stenflo, 2008; Stenflo and Kosovichev, 2012). Therefore, the generality of Joy's law is not always given. In all, the Babcock–Leighton dynamo model suffers from a strong lack of verifiable physical properties of the solar environment. With the use of fine-tuned parameters, this model is capable of modeling a lot of observed features without providing understanding of their real origin.

4.3 Direct numerical simulations

Instead of simplifying or parameterizing the MHD equations, one can also solve directly by using viscosities and diffusivities far above the solar values. The advantage of these models is that effects like turbulent heat transport or the α-effect, which arise from magnetohydrodynamical turbulence, do not have to be included artificially. The results of these simulations are in general more reliable than mean-field models, because no fine tuning of turbulent coefficients is possible. On the other hand analyzing and describing their results in terms of physical quantities might be more difficult.

4.3.1 Local simulations

Solar dynamo simulations of a small region of the Sun are used to study local phenomena or general properties of dynamos. Simulating only a part of the convection zone allows us to reach higher fluid and magnetic Reynolds numbers. In simulations of turbulent dynamo models it is common to use random forcing in the momentum equation to mimic turbulent convective motions, without actually solving the energy equation. In the work by e.g. Pouquet et al. (1976), Käpylä et al. (2006a) and Hubbard et al. (2009), local direct numerical simulation with forced turbulence are used to estimate transport coefficients as α, where the test field method (Schrinner et al., 2007) may be employed in determining the transport coefficients. For details I refer to Brandenburg et al. (2010) and references therein.

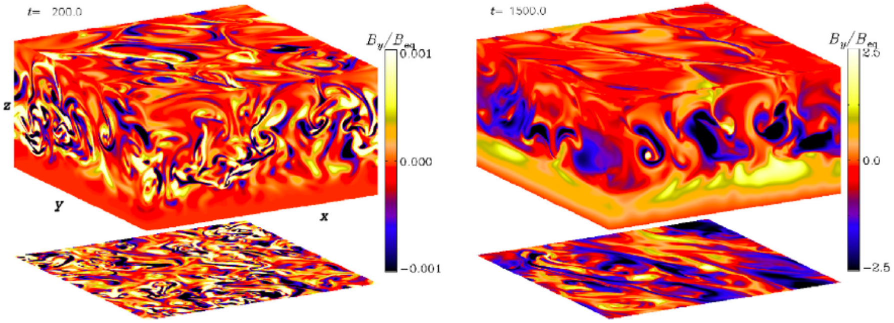

Figure 4.3: Large-scale magnetic field from a simulation of turbulent convection with shear in a Cartesian box. In the left panel the early phase is shown, where the magnetic field is weak and has the same as the convection or smaller one. In the right panel the saturated state is shown. The magnetic field is more than two times larger than $B_{\rm eq}$. The sides of the box show the periphery of the domain whereas the top and bottom slices show B_y at bottom and the top of the domain, respectively (taken from Käpylä et al., 2008).

Local convective simulations generating the turbulent motions self-consistently started with Meneguzzi and Pouquet (1989) and Nordlund et al. (1992), who showed that the turbulent pumping effects lead to a downdraft of magnetic fields. Later as shown by Käpylä et al. (2008), it was possible to generate for the first time large-scale magnetic fields generated by turbulent convection using shear. Recently, local simulations have been used to estimate the possibility of creating flux tubes with convection and shear (Guerrero and Käpylä, 2011). But the maximum magnetic field strength obtained by their simulations is $\sim 6\, B_{\rm eq}$. Some of the flux tubes are even able to rise up to the surface, but they always lose their initial coherence.

Assuming that the Babcock–Leighton mechanism is the right one to describe the large-scale fields and the sunspot emergence, the question remains, where the magnetic field of smaller or intermediate strength come from. One proposed mechanism is a small-scale dynamo operating in the surface layer of the Sun, driven by the small-scale turbulent motion of the granulation. These ideas are investigated in local dynamo simulations (see e.g. Cattaneo, 1999; Vögler and Schüssler, 2007). It is possible to excite a small-scale dynamo just by the turbulent motions without any rotation and shear, for details see the review by Stein (2012). Concerns, the magnetic Prandtl number ($\mathrm{Pr_M} = \mathrm{Re_M}/\mathrm{Re}$) is with $\mathrm{Pr_M} \ll 1$ too small for a small-scale dynamo to operate, was resolved by Brandenburg (2011). In **Paper I** we also use a local model of a solar dynamo driven by random forcing. In the following papers, we expand the domain to global simulations.

4.3.2 Global simulations

Global simulations of solar dynamos are in most cases still utilizing a model describing only a part of the Sun. Describing the physics of the convection zone is sufficient. In some cases, polar regions are omitted to avoid the coordinate singularity at the axis, so instead of the whole sphere just a spherical wedge is used (see e.g. Käpylä et al., 2010; Mitra et al., 2010b, and **Papers II–VI**). In other models the whole convective spherical shell was modeled by using the anelastic approximation $\boldsymbol{\nabla} \cdot (\rho \boldsymbol{u}) = 0$, thus filtering out sound waves (see e.g. Brun et al., 2004).

The first global numerical simulations of solar dynamo models by Gilman and Miller (1981), Gilman (1983) and Glatzmaier (1985) were already able to produce remarkable results. The mean magnetic field showed an oscillating behavior, but it migrated polewards. Due to larger computing power in the last 30 years, more realistic global simulations were possible. Even though their luminosity and rotation rate are similar to those in the Sun, their fluid and magnetic Reynolds numbers are still several orders of magnitude lower than the solar ones. One way of dealing with this issue is to use large-eddy simulations (LES), where small-scale turbulence effect are added to the direct numerical simulations. These models were used to simulate successfully large-scale magnetic fields generated self-consistently by convection in spherical shells (see e.g. Brun et al., 2004; Brown et al., 2008). For rotation rates larger than solar, large-scale active so-called wreaths of non-oscillatory magnetic field were found (Brown et al., 2010). The azimuthal field concentrated at lower latitudes and is organized in loosely bundled flux tubes. More recently, using these models, also oscillating large-scale magnetic fields were found (Brown et al., 2011; Nelson et al., 2013, and references therein), but these oscillating patterns are far from solar-like regular patterns. The azimuthal magnetic field consist of strong wreath, which change their polarity irregularly and with no significant correlation in the two hemispheres. These wreaths migrate from time to time polewards but never equatorwards. For solar rotation rates, Brun et al. (2004) failed to produce large-scale magnetic fields. Using grid methods instead of spherical harmonics, Ghizaru et al. (2010) and Racine et al. (2011) were able to produce oscillatory large scale magnetic fields, but without any clear migration.

Approaches, where instead of a full sphere a spherical wedge is used, have been successful in generating large-scale migrating magnetic fields. With random forcing of helical transversal waves, Mitra et al. (2010b) could produce an oscillatory magnetic field with equatorward migration. In this case the migra-

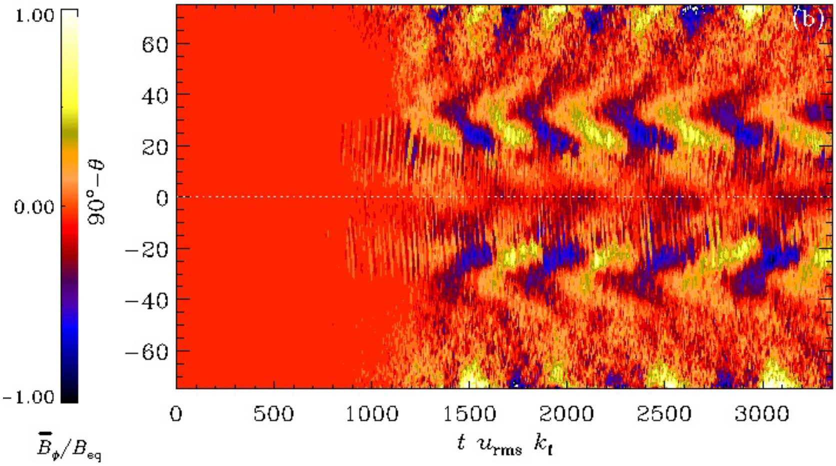

Figure 4.4: Butterfly diagram for the mean azimuthal magnetic field $\overline{B}_\phi$ near the surface of the convection $r = 0.98R_\odot$ as a function of latitude $90° - \theta$ for $\mathrm{Co} = 7.6$. The white dotted line denotes $90° - \theta = 0$ (taken from Käpylä et al., 2012, and **Paper VI**).

tion can be explained by a sign change of α across the equator. In this model no rotation is applied, but the sign of the kinetic helicity are reversed across the equator, which mimics the effect of the solar rotation. The same effect has been seen in the model of **Paper II**. Simulations of self-consistent convective dynamos in spherical wedges were at first unable to reproduce oscillatory magnetic fields (see e.g. Käpylä et al., 2010, and **Paper IV**). But recently, with the implementation of an LES approach for the turbulent heat conductivity $\chi_{\rm t}$ (Käpylä et al., 2011b) and a black body boundary condition for the temperature, Käpylä et al. (2012) were able to produce an equatorward migration of the large-scale magnetic field. In Fig. 4.4 the butterfly diagram of the mean azimuthal magnetic field is shown. There exists a clear equatorward migration of the field between latitudes of 40° and 60°, which has a cycle period of 33 years, clearly longer than the solar magnetic cycle. Near the pole, there exists a poleward migrating branch, which is similar to the observed pattern as seen in Fig. 1.6. **Paper VI** is a follow-up work of Käpylä et al. (2012), where we investigate mainly how the density stratification influences the equatorward migration of the mean field as shown in Fig. 4.4. The magnetic field is again generated by self-consistent convection in a rotating spherical wedge. The mean azimuthal magnetic field shows poleward migration for all runs in the beginning of the simulations, when the magnetic field is weak. For high enough stratification (density contrast above 25) this pattern is overcome by equatorward migration. For a slight increase of magnetic and fluid Reynolds number the pattern does not change significantly. As in Käpylä et al. (2012), the Coriolis numbers in these runs are around slightly higher than that in the Sun. At the moment the work of Käpylä et al. (2012) and its followup work of **Paper VI** are the state of the art of equatorward migration of self-consistent convective dynamos. In **Paper V** we find a similar pattern, but the higher latitudes show strong equatorward migrations instead of poleward. Unfortunately the mechanism for the equatorward migration behavior is still unclear and need more investigation. In § 6, I will discuss the difference in the setup as well as the results in more detail.

An important result of the global convection simulations is that the magnetic field is distributed over the whole convection zone. Although Nelson et al. (2013) detect even flux tubes, there are no clear signs of their formation in the tachocline, from where they should rise and contribute to the solar cycle. In this sense, the direct numerical simulations of the global solar dynamo support the distributed dynamo model of Brandenburg (2005).

Let me also make a note about the differential rotation in solar dynamo models. The differential rotation in direct numerical simulations is normally not an input quantity as in the mean-field and flux-transport models: it emerges instead from the simulations. Kitchatinov and Rüdiger (2005), Miesch et al. (2006) and Brun et al. (2011) use only hydrodynamical models to be able to reproduce solar-like differential rotation. This can be misleading, because Maxwell stresses as well as suppression of turbulent heat fluxes due to magnetic fields (e.g. Käpylä et al., 2004) can influence the differential rotation. Solar dynamo models were able to generate an equator rotating faster than the poles for higher than solar rotation rates (e.g. Nelson et al., 2013, and **Paper VI**), but spoke-like rotation contours as in Fig. 1.2 or in mean-field hydrodynamical models by Brandenburg et al. (1992) and Kitchatinov and Rüdiger (2005) have only been achieved in hydro-LES by imposing a latitudinal entropy gradient at the bottom of the convection zone (Miesch et al., 2006) or with a stably stratified layer below the convection zone, which mimic the radiative interior (Brun et al., 2011). The only MHD DNS models of self-consistent convection reproducing spoke-like rotation are those with a coronal envelope of **Paper V**. I will present and discuss its results in § 6 in more detail.

5. Models of Solar Eruptions

Explosions are not comfortable.

Yevgeny Zamyatin

In this chapter, I want to give a short overview about the different models of solar eruptions. First I present some observational constrains of solar eruptions and then the models of these eruptions. More detailed information can be found in the reviews by Chen (2011) and by Shibata and Magara (2011), whereas observations of coronal mass ejections (CMEs) are summarized by Webb and Howard (2012). Solar eruptions can be categorizes into two main groups of phenomena. One are the solar flares, which are impulsive emissions of radiation accompanied by a sudden increase of brightness and particle showers. The other one are coronal mass ejections (CMEs), where plasma of the corona gets ejected out into the interplanetary space. Often and in particular for strong events, these two phenomena are connected (see e.g. Harrison, 1995). The energy released in such events have been stored before inside the magnetic field.

5.1 Observational constrains

On the first day of September 1859, Carrington (1859) and Hodgson (1859) observed the first flare in the continuum light on the photosphere. In the left panel of Fig. 5.1, a sketch of the sunspot region is shown, from which this flare emerged. The flare and the associated CME led to a strong geomagnetic storm, which is know as the Carrington event. It was the largest ever recorded solar storm, which resulted in aurorae in the Caribbean and telegraph failures in the US and Europe. More detailed observation of flares and CMEs are possible since space telescopes are monitoring the Sun. Flares are hard to observe from the ground, because either they are emitted only in this part of the spectrum, which is absorbed by the Earth's atmosphere, or the coronal emissions are much weaker than the photospheric ones. After the first mission, of the NASA space station Skylab, the Sun was monitored permanently by the SOlar and Heliospheric Observatory (SOHO: Domingo et al., 1995) built by ESA and NASA. With the instruments on SOHO, the photosphere, the chromosphere and the solar corona can be observed simultaneously 24 hours a day. Additionally there were two white light coronagraphs (LASCO) on board, which

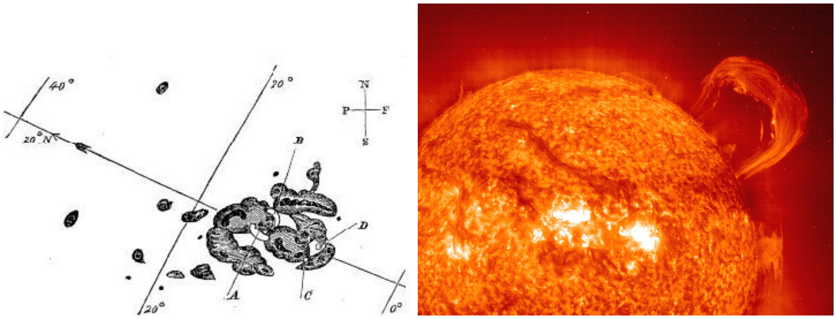

Figure 5.1: *Left panel:* Sketch from the first observed and noted sunspot formation, which lead to a solar flare. The British astronomer Richard Carrington had done this drawing of the Sun at the 1st of September 1859, after he had observed a solar flare for the first time. The white regions among the black and gray sunspots represent the Doppler ribbons (A and B) of the white flare which emerge suddenly amid the sunspots (Carrington, 1859). *Right panel:* Solar prominence observed with EIT on SOHO in the He II/Si XI 304 Å line band. Image courtesy of NASA/ESA.

are able to observe the shapes of CMEs as shown in Fig. 5.2. Nowadays, the Dynamic Solar Observatory (SDO: Pesnell et al., 2012) gives us remarkable pictures and data of solar flares and coronal mass ejections. With the twin spacecrafts Solar TErrestrial RElations Observatory (STEREO: Kaiser et al., 2008) CMEs can be observed three-dimensionally, which gives important insights of the structure and evolution of CMEs.

Flares have a power law energy distribution, which range from weak nanoflares, releasing energies of about 10^{19} J, to white flares, releasing energies of about 10^{24} J. Nanoflares are believed to contribute to the heating process in the solar corona (e.g. Bingert and Peter, 2011, 2013). White flares are strong flares and can cause major impacts on the Earth. Because of the observation of even stronger flares on other solar-type stars, Maehara et al. (2012) suggested that superflares, which are hundred times more powerful than white light flares, are also able to occur on the Sun. Typically the flare is first visible as two ribbons in Hα emitted from the chromosphere, as see in left panel of Fig. 5.1. Later, strong X-ray and UV emissions follow from X-loops in the corona.

Coronal mass ejections (CMEs) can be divided into two main categories. There are jet-like ejections, the narrow CMEs and there are the cone-like ejections, the normal CMEs. In the following I will focus on the normal type of CMEs. Normal CMEs are basically prominences, which are ejected into the interplanetary space (House et al., 1981). In the right panel of Fig. 5.1, an example of a prominence observed with EIT on SOHO, is shown. Hot plasma can

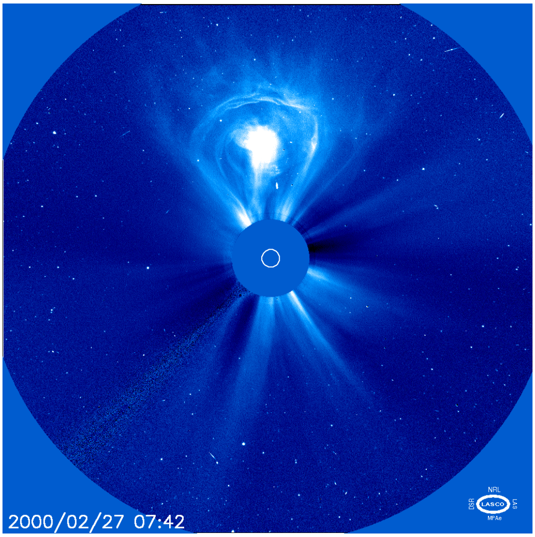

Figure 5.2: This SOHO LASCO C1 image shows a very large coronal mass ejection (CME) blasting off into space on 27 February 2000. It presents the standard shape of a CME: a large bulbous front with a second, more compact, inner core of hot plasma. This material erupts away from the Sun at speeds of one to two million kilometers per hour. Image credit ESA and NASA.

only flow along the magnetic field lines for example of a coronal loop and can be trapped there. If field lines reconnect underneath this prominence and release sufficient magnetic energy to push the prominence out, a CME happens. The hot and dense prominence will show up as a bright bubble in projected white light image, as in Fig. 5.2. In front of this emerging bubble the coronal plasma will pile up and form a bright arc. The bright bubble, the cavity in between and the bright arc form the characteristic three-part structure of CMEs (see e.g. Illing and Hundhausen, 1985; Low, 1996). Ahead of the arc, the CME causes shocks, which can accelerate particles to high velocities. These particles can then penetrate the Earth's atmosphere. The plasma, which is carried out with the CME is often called magnetic cloud (Rust, 1994). This plasma has a typical mass of 10^{11} to 10^{13} kg (see e.g. Hudson et al., 1996) and can reach a velocity of 1000 km/s. Coronal mass ejections are believed to carry a large amount of magnetic helicity out of the Sun, (e.g. Low, 1994, 2001; Plunkett et al., 2000; Régnier et al., 2002; Thompson et al., 2012). Magnetic clouds can form bipolar magnetic field, just due to their rotation and inclination (see e.g. Li et al., 2011, where they use in-situ measurements of two satellites). More measurements of current helicity, which can serve as a proxy for magnetic helicity, and magnetic twist could be important for dynamo theory. Blackman and Brandenburg (2003) suggested CMEs to be a major contributor to magnetic helicity transport out of the Sun and so to prevent catastrophic quenching of the α-effect, see § 3.3.1.

5.2 Models and simulations

For powering CMEs and flares, one needs a large amount of energy (10^{25} J). In the solar atmosphere only the magnetic field can supply this amount of energy. As calculated in Stix (2002), a volume of $10^{23}\,\mathrm{m}^3$, with a field strength of a hundred gauss have a magnetic energy of around 4×10^{24} J, which is of the same order as the flare energies of 10^{25} J. The thermal and kinetic energy are much lower, and not sufficient to store this amount of energy. As a basic step, modeling flares and CMEs starts by modeling the storage of energy in the magnetic field. Observations suggest strong shearing motions localized near strong magnetic field gradients in active regions before a flare or CME erupts. Sturrock (1980) and Antiochos et al. (1999) use shearing motions to model magnetic storage in the corona. Also Warnecke (2009) found indications that granulation motion is capable of twisting and shearing the magnetic field to store sufficient energy for a flare or CME.

For studying the mechanism of eruptive events, it is often sufficient to use two dimensional models. For example Forbes and Priest (1995) and Priest and Forbes (2000) are able to reproduce the spread of Hα ribbons and X-loop structures in the after-flare phase by using a two dimensional force-free reconnection model. Simplified flux rope models can be used to generate a current sheet and trigger the ejection of flux ropes.

In three dimensions, there are two different types of models commonly used. The first one is the break-out model (see e.g. Antiochos et al., 1999). There, a multi-flux system of coronal fields is used to form complex magnetic topologies in the corona. To trigger the eruption, they use an observed photospheric magnetogram and impose velocities similar to the observed ones. The shearing motions lead to reconnection of the coronal field, which then causes the eruption. Here, the coronal field topology is crucial for eruptions to happen, and the storage of energy is comparable to the one needed to release CMEs. The second type of model are the three-dimensional flux rope-models. There, a twisted flux rope (configuration see Titov and Démoulin, 1999) is placed into a simulation model, where to bottom represents the photosphere. Shearing the footpoints of this rope breaks its stability and causes a rise and twist of the rope. This have been studied intensively by Török et al. (2004) and Török and Kliem (2005), where they were able to reproduce a rising and twisting prominence similar as in observed ones on the Sun as shown in Fig. 5.3. In their simulation they solved the ideal MHD equations, where no reconnection can

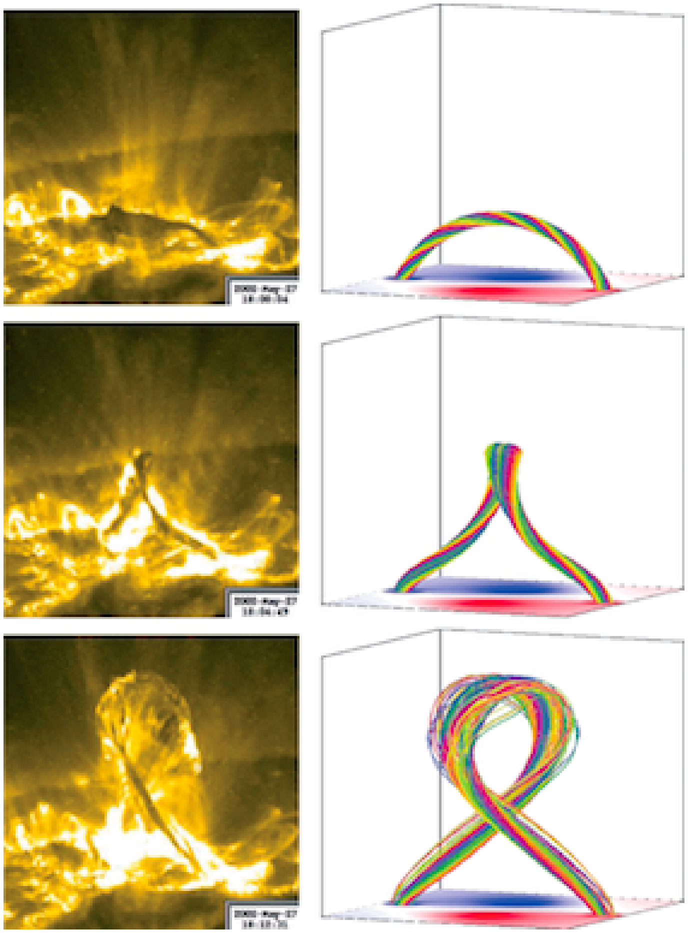

Figure 5.3: Comparison of observations and simulations, time is evolving from top to bottom: *Left panel*: TRACE 195 Å images of the confined filament eruption on 27th May 2002. *Right panel*: Colored magnetic field lines outlining the core of the kink-unstable flux rope with starting points lie in the bottom plane. The magnetogram of the vertical magnetic field is shown color coded at the bottom of the box (taken from Török and Kliem, 2005).

happen, this prohibited the flux rope from ejecting. A slightly different approach has been conducted by Fan and Gibson (2004, 2007), where a twisted flux rope emerges into a prescribed coronal field configuration. It becomes unstable and ejected depending crucial on the amount of twist. With this model they were able to reproduce X-ray observation of intense current layers of inverse-S-shapes on the northern hemisphere. Similar simulation have been also performed by Roussev et al. (2003) to find suitable trigger mechanism.

For other models using the flux emerging and shearing motions to trigger an erupting flux rope see e.g. Amari et al. (2000). Similar flux-rope models are used to simulate the formations of CME shocks (see e.g. Pomoell et al., 2008). These shocks are of particular interest, because they can accelerate particles to high speeds penetrating the Earth's atmosphere and lead to high doses of radiation.

At the moment, in all models of erupting events, the initial condition are prescribed. The magnetic field at the bottom of the domain is either taken from two-dimensional observations of the photospheric magnetic fields or set by hand. The overall magnetic field is the extrapolated from the bottom field or also completely set by hand as by including a flux rope configuration. Twisted magnetic field has to be included artificially or by implying strong shearing motions at the footpoints. Observing horizontal velocity field is only possible with a low accuracy and low resolution, and they are not even sufficient to actually trigger the ejections (see e.g. Baumann et al., 2012). That the magnetic field configuration and the velocity field are connected to magneto–convection and a dynamo process below the surface, is often neglected. In § 6 I will therefore describe a different approach, where we combine the dynamo process below the surface to trigger coronal ejections, see also **Paper I - IV**.

6. A Combined Two-Layer Model

Das Studium und allgemein das Streben
nach Wahrheit und Schönheit ist ein Gebiet,
auf dem wir das ganze Leben lang
Kinder bleiben dürfen.

Albert Einstein

6.1 Motivation

The main purpose of this thesis is to develop a two-layer model combining the solar convection zone and the solar corona. There are basically two motivations for the combined two-layer model. One path originates from modeling coronal mass ejections and flux emergence. As described in § 1.5, coronal mass ejections and solar flares are contributing to the space weather, which has a strong impact on the life on Earth. Despite this importance, a reliable prediction of space weather events and in particular solar storms is currently not possible. After the detection of solar eruptions on the solar surface using space telescopes, it takes about one to five days for them to reach the Earth. This time interval is currently the maximum advance warning time we have. Predictions about the strength and velocity of the ejection can be only made during this interval. There have recently been major advances in simulating and observing coronal mass ejections and solar flares, see § 5. However, the mechanism leading to eruptions is not yet fully understood. Whether an active region is likely to erupt, can often only be answered using statistical arguments rather than physical understanding (see e.g. Schwenn, 2006). It is generally agreed that the solar magnetic field not only supplies the energy source, but it also triggers the eruptive events. On the Sun, however, the magnetic field is only observable in the photosphere and above; information about magnetic fields in the interior of the Sun is not accessible. This is one of the reasons, why most of the models of solar eruptions use photospheric magnetic fields as lower boundary condition, see § 5. The surface magnetic field is the only observable field, which is useful to include in an eruptive event model. One might believe that this is the most realistic boundary condition, but this is actually misleading. If twisted magnetic fields and other complex topologies are projected onto a two-dimensional plane at the solar surface, the regaining magnetic field information from this projection will be insufficient and possibly wrong. But these complex topologies and twisted fields might be one of the important ingredients missing in the eruption models. To generate twisted magnetic fields in these models, either strong shearing motions are applied at the bottom of their domain, representing the photosphere or twisted magnetic fields are just imposed in the domain as initial conditions. The fact that the magnetic field structures and the photospheric motions are coupled together in terms of magneto-convection or dynamo action is often neglected. The combined two-layer model developed in this thesis connects the fluid motions below the surface of the Sun with the fluid on and above the surface directly, as well as the magnetic field below and above the surface. In eruptive models, the twist of the magnetic field plays an important role and can also be found in observed coronal mass ejections (see e.g. Thompson et al., 2012). Instead of imposing twisted fields or generating them by at least partially artificial photospheric motions, another possibility is that these twisted fields are generated by dynamo action below the surface. Differential rotation and convection is capable of producing helical magnetic fields, which contain a large amount of twist. Our combined two-layer model allows twisted magnetic fields, which have been generated below the surface, to emerge and to contribute to CMEs.

The other motivation starts from dynamo theory. As described in §§ 3.2 and 4, magnetic helicity and magnetic helicity fluxes are important quantities in dynamo theory and solar dynamo models. Dynamo action can be catastrophically quenched for high magnetic Reynolds numbers (see e.g. Brandenburg and Subramanian, 2005, and § 3.3.1). The only loophole is via magnetic helicity fluxes, which are capable of preventing catastrophic quenching of the α-effect (Blackman and Field, 2000; Brandenburg et al., 2009). From this point of view, an appropriate boundary condition for the magnetic field is crucial for the performance of the dynamo. Numerical simulations have shown that a dynamo can be more efficient with open (vertical field) boundaries than with closed (perfect conductor) ones (Brandenburg and Sandin, 2004). In the Sun, the convection zone has no closed boundaries at the surface. Magnetic fields can emerge through the surface and can be eventually ejected. We know that the Sun has a powerful dynamo operating inside the convection zone. If the dynamo theory of quenching the α-effect (see § 3.3.1) is reliable, the Sun has to transport large amounts of magnetic helicity out of the convection zone. Possible candidates for the transport are the solar wind and coronal mass ejections (Blackman and Brandenburg, 2003). Coronal mass ejections are a good candidate, because they are believed to carry magnetic helicity outwards (see e.g. Thompson et al., 2012).

Observations of magnetic helicity on the solar surface are difficult to perform. Magnetic helicity is not a gauge-invariant quantity and is therefore impossible to be determined unambiguously, but there are mechanisms to determine the relative helicity or proxies for the magnetic helicity such as the current helicity (Pariat et al., 2005; Thalmann et al., 2011; Valori et al., 2012). But even the gauge invariant current helicity can only partly be observed and measured, because the horizontal components of the current density are not accessible.

The combined two-layer model can be used to create a realistic boundary condition for the solar dynamo, similar to the solar photosphere. We can determine if such a boundary condition supports a dynamo below the surface and can be even more efficient than without giving the possibility of ejections of magnetic helicity. We can investigate the interplay between the solar convection zone and the solar corona in terms of dynamo-driven ejections as well as magnetic helicity fluxes with this model.

6.2 Model and setup

The model consists of two layers, where the lower one represents the solar convection zone and the upper one the solar corona. In the lower layer we use turbulent motions to amplify a weak Gaussian-distributed seed magnetic field. There are no imposed or initial magnetic fields in the upper layer. Magnetic fields are only able to emerge from the lower layer into the upper layer in order to have magnetic field in the upper layer. One of the important features of the combined two-layer model is that there are no numerical boundaries between the two layers. The different dynamics of the two layers are controlled in the used equations by a choosing suitable profile function multiplying terms on the right hand side of the MHD equations, see § 3. This allows a flux of magnetic helicity and magnetic fields between the two layers. For the numerical computations, we use the PENCIL CODE with sixth-order centered finite differences in space and a third-order accurate Runge–Kutta scheme in time. For the extension of the PENCIL CODE to spherical coordinates see Mitra et al. (2009).

6.2.1 Step by step

The combined two-layer model is simple at the starting point and has been improved step by step. In every step, we include more realistic physical features leading to new useful insights and results. Using a step-by-step method allows us to adjust the model, where improvements are important and needed. It also allow us to compare the results of every step with the former ones.

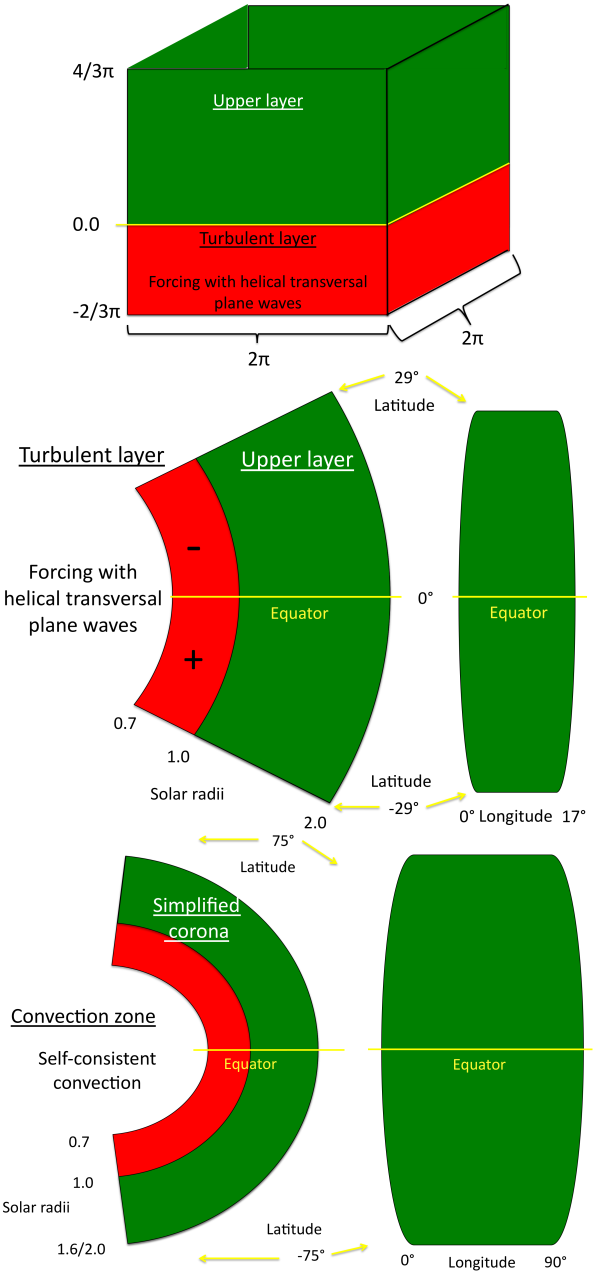
4/3π
Upper layer
0.0
Turbulent layer
Forcing with helical transversal plane waves
-2/3π
2π
2π
29°
Latitude
Turbulent layer
Upper layer
-
Forcing with helical transversal plane waves
Equator
0°
Equator
+
0.7
1.0
Solar radii
Latitude
-29°
2.0
0° Longitude 17°
75°
Latitude
Simplified corona
Convection zone
Self-consistent convection
Equator
Equator
0.7
1.0
Solar radii
1.6/2.0
Latitude
-75°
0°
Longitude
90°

Figure 6.1: Schematic sketch of the model setup of **Paper I** (top), **Paper II** (middle) and **Papers IV** and **V** (bottom).

6.2.2 A forced turbulent dynamo in a Cartesian box

As a first step we use a model in a Cartesian box, see top panel of Fig. 6.1. This model is used in **Papers I** and **III**. The lower layer, which is about one third of the total domain, mimics the convection zone and the upper layer represents the solar corona. In the lower layer, we impose a forcing function in the momentum equation which injects random helical transverse waves in the domain. Profile functions arrange for a smooth transition from the forced momentum equation in the lower layer to a non-forced one in the upper layer. The forcing is used to mimic convective turbulent motions and its helical part represents the influence of rotation and stratification on these motions. We neglect gravity and solve the continuity equation only in the lower layer supporting the turbulent motions. We omit the energy equation and apply instead a constant temperature in the whole domain. This leads to so-called force-free model in the coronal layer, which has been used to model properties of the solar corona as well as plasmoid ejections, which fits well with observations of coronal fields (see e.g. Mikic et al., 1988; Ortolani and Schnack, 1993; Warnecke, 2009). It implies that processes like magnetic buoyancy are not captured. The boundary conditions are periodic in the x and y directions. In the z direction, we use a stress-free boundary condition for the velocity field. For the magnetic field we employ a perfect conductor at the bottom boundary and a vertical field condition ($B_x = B_y = 0$) on the upper boundary. The vertical field condition is chosen, because in the solar corona the solar wind pushes the field lines radially at a distance of around $r \approx 2 \ldots 2.5 R_\odot$ (see e.g. Levine et al., 1982; Schrijver and De Rosa, 2003).

6.2.3 A forced turbulent dynamo in a spherical domain

As a second step, we transform the setup from Cartesian to spherical coordinates. We now model a major part of the Sun, as shown in the middle panel of Fig. 6.1 using a spherical wedge, which extends from the bottom of the convection zone at $r = 0.7 R_\odot$ to the upper solar corona at $r = 1.6 \ldots 2 R_\odot$. In the latitudinal (θ) direction we omit the poles and limit ourselves to latitudes of ± 0.5 radians (corresponding to $\pm 29^\circ$). The wedge has a 17° extent in the azimuthal (ϕ) direction for simplicity. This model is used in **Papers II** and **III**. Besides the use of spherical coordinates, there are two main improvements added to the model. As the first one, we include gravity, which is much weaker than in the Sun, and solve the continuity equation in the whole domain. This leads to a radial density stratification covering in most of the simulations, around one or two orders of magnitude, while in the Sun, the density contrast is around 14 orders of magnitude. Secondly, we apply a latitudinally dependent forcing function. The kinetic helicity density $\boldsymbol{u} \cdot \boldsymbol{\omega}$ imposed in terms of the helical forcing, is largely negative in the northern hemisphere and positive in the southern hemisphere. This mimics the different sign of the kinetic helicity in both hemispheres due to solar rotation, which is omitted in this model. As in the Cartesian model, we omit the energy equation and use a constant temperature. The boundary conditions are periodic in the ϕ-direction while in the radial direction they are similar to those of the z-direction in the Cartesian model. On the θ-boundaries, we employ stress-free velocity and perfect conductor boundary conditions for the magnetic field. We prevent a flux of mass at the outer radial boundary of the full domain, because an open boundary allows a Parker wind to develop. A Parker wind for this low gravitation is too strong and would push all the magnetic field out of the domain in a short time.

6.2.4 A convective dynamo in a spherical domain

As a third step we use self-consistent convection to generate a large-scale magnetic field. This model is used in **Paper IV**, where we combine a setup used by Käpylä et al. (2010, 2011b) for the convection zone with the isothermal coronal model of **Paper II**. We extend the domain to latitudes of ± 1.3 radians (corresponding to $\pm 75^\circ$) and to longitudes of $\pi/2$ radians (90°), see lower panel of Fig. 6.1. As one of the improvements, we solve the energy equation in terms of the entropy, see Eq. (3.9) and use a cooling function to keep the temperature at the surface of the convection zone and in the corona constant. We impose a with radius decreasing profile for the heat conductivity and an initial temperature profile of a polytropic atmosphere with an index of $m = 1$ to generate an convectively unstable stratification in the convection zone. Additionally, we switch to a rotating frame, by adding the Coriolis force in the momentum equation, but we neglect the centrifugal force (see discussion in Dobler et al., 2006). This leads to the generation of differential rotation and helical motions inside the convection zone. The density contrast is now around four in the convection zone and forty in the whole domain, i.e. higher than in **Paper II**, but still not much closer to the solar density stratification. Due to the low density in the corona, the Coriolis force is there unrealistically strong compared to the Lorentz force[1]. This leads to strong velocity gradients and possible artefacts such as the magneto-rotational instability. That is why we employ a damping term in the momentum equation to reduce the mean velocities in the corona, see details in Section 2.2 of **Paper IV**, but actually the damping violates Galilean invariance. The boundary conditions are very similar to those of the model of **Paper II**. However, for the temperature, we use a constant heat flux at the bottom and constant temperature at the top boundary.

---

[1] In Eq. (2.12), the Coriolis force would enter on the rhs as $-\boldsymbol{\Omega}_0 \times \boldsymbol{u}$, the Lorentz force as $\frac{1}{\rho}\boldsymbol{J} \times \boldsymbol{B}$.

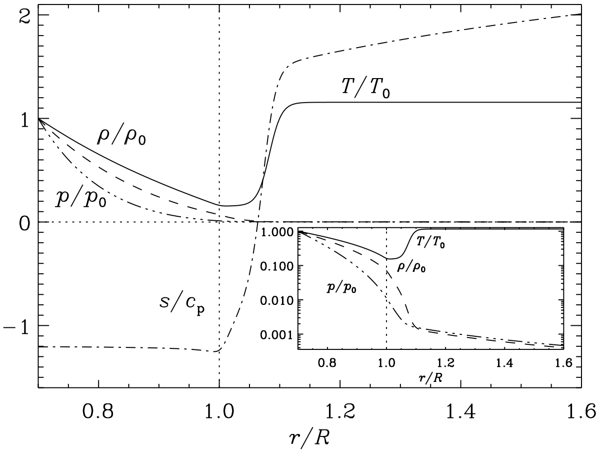

Figure 6.2: Mean radial profiles of stratification for one representing run of **Paper V** in the equilibrated state. The normalized density ρ/ρ_0 (dashed lines), pressure p/p_0 (dash-triple-dotted), and temperature T/T_0 (solid) are plotted together with the specific entropy s/c_P (dash-dotted) over the radius. The inset shows the same profiles in logarithmic representation to emphasize the steep decrease of the pressure and density in the lower coronal layer. The index 0 represents the value at the bottom of the convection zone.

At the latitudinal boundaries the entropy and the density have zero gradients to avoid heat fluxes in and out of the domain.

6.2.5 A convective dynamo in a spherical domain with a hot corona

In a forth step, performed in **Paper V**, we improve our model in two aspects. We use a more advanced convection zone model similar to Käpylä et al. (2011a, 2012) (also employed in **Paper VI**), where the decrease of the heat conductivity with radius is stronger in the convection zone and a turbulent heat conductivity χ_t is introduced. The latter resembles the unresolved convective heat flux, see § 2.2.4 and is in this sense an LES feature. This leads to a much higher convective flux than in **Paper IV**. The energy equation then reads (compare with Eq. (3.9) and Equation (4) in **Paper V**)

$$T\frac{\mathrm{D}s}{\mathrm{D}t} = \frac{1}{\rho}\boldsymbol{\nabla}\cdot\left(K\boldsymbol{\nabla}T + \chi_t\rho T\boldsymbol{\nabla}s\right) + 2\nu\mathbf{S}^2 + \frac{\mu_0\eta}{\rho}\boldsymbol{J}^2 - \Gamma_{\mathrm{cool}}(r). \qquad (6.1)$$

There, $\Gamma_{\mathrm{cool}}(r)$ is a radially dependent cooling function, which is also improved compared with the one in **Paper IV**. We impose a cooling profile which causes a higher temperature in the corona than at the bottom of the convection zone.

In Fig. 6.2, an overview of the mean radial profiles of density, pressure and temperature is plotted for the model used in **Paper V**. Using this type of temperature profile allow us to achieve much higher density contrasts than in the models of **Papers II** and **IV**. The density contrast in the convection zone is now around fifteen, whereas in the whole domain it is about two thousand. We apply the same boundary conditions as in **Paper IV**. It turns out that the velocity damping used in the model of **Paper IV** could be better realized by a viscosity profile than an actually damping term in the momentum equation. The viscosity increases to an about twenty times higher value in the corona than in the convection zone. This is sufficient to damp high velocities in the corona, at least in the first stage, when the magnetic field is still weak. Also, because of the stronger stratification the Coriolis forces are not that strong as in **Paper IV**.

More detailed descriptions of the model setups can be found from the model sections of **Papers I, II, IV** and **V**. To summarize, the convection zone of our two-layer model has been evolved from a simple local isothermal layer, where random helical forcing generated a magnetic field to a global layer with self-consistent convection, self-generated differential rotation and a magnetic field generated by the turbulent convective motions. Likewise, the coronal layer develops from an isothermal, zero-gravity force-free model to a realistic corona, where the temperature is high and the density low.

6.3 Main results of Paper I to V

In the following I present the main results of **Papers I–V** as well some unpublished additional results. The order follows rather the result topics than the publishing chronology.

6.3.1 Magnetic field generation

In all papers a large-scale magnetic field is generated by turbulent motions in the lower layer representing the convection zone. In **Paper I** the saturated magnetic field is bipolar, where its alignment direction is a random choice of the system. The vertical component of the field varies sinusoidally in one of horizontal directions and is essentially constant in the other. The field pattern is stationary, but can move slowly in one of the directions, see Figs. 7 and 9 of **Paper I**. In the model of **Paper II** the saturated magnetic field shows an equatorward migration due to an α-effect, which changes sign across the equator, similar to Mitra et al. (2010b). In Fig. 6.3, we show the equatorward migration of the radial magnetic field at the surface of the lower layer. Two polarities of opposite sign are generated at the poles and move toward the equator,

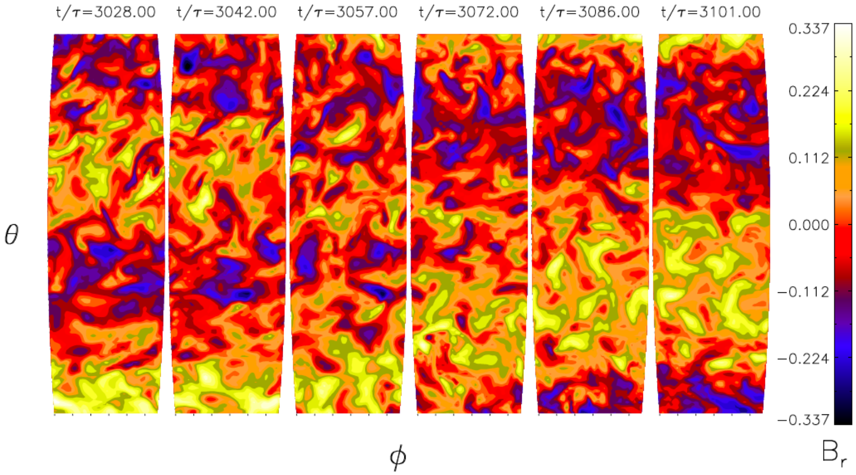

Figure 6.3: Equatorward migration, as seen in visualizations of the normalized radial magnetic field $B_r/B_{\rm eq}$ at the surface ($r = R_\odot$) over a horizontal extent of $\Delta\theta = 58°$ and $\Delta\phi = 17°$ for six different time snapshots. $\tau = 1/u_{\rm rms}k_{\rm f}$ indicates the turnover time of the turbulent motions (taken from **Paper II**).

where they annihilate. At the same time the polarities in each hemisphere have changed and new magnetic fields move equatorward, see Fig. 5 in **Paper II**.

The model used in **Paper IV** shows no clear sign of equatorward migration (Figs. 10 and 11 of **Paper IV**). The mean (azimuthal averaged) magnetic field seems to be stationary and forms "wreaths" of strong fields, similar as in Brun et al. (2004), Brown et al. (2008) and Nelson et al. (2013). The field shows no sign of polarity change, but some changes in strength. They are in phase with velocity changes, similar as in **Paper II**; the field is strong, when the velocity is weak, and vice versa, see Fig. 5 of **Paper II** as well as Fig. 9 of **Paper IV**. In the model used in **Paper V**, the magnetic field is clearly oscillatory and shows indications of equatorward migration of the mean magnetic field. In Fig. 6.4, the butterfly diagram of the mean radial field is shown close to the surface of the convection zone ($r = 0.97R_\odot$). During the first hundred turnover times the magnetic field is weak and a poleward migration is visible. But at later times the equatorward migration is strong and penetrates again down to the equator. After around $t/\tau = 1500$ the dynamo seems to change its mode and the equatorward migration vanishes or becomes less clear, but at $t/\tau = 2300$ it reoccurs and penetrates to the equator. The magnetic cycle period is around $t/\tau = 150$ turn over times. Assuming a typical turnover time for convective motion in bulk of the solar convection zone of a month, this cycle would cor-

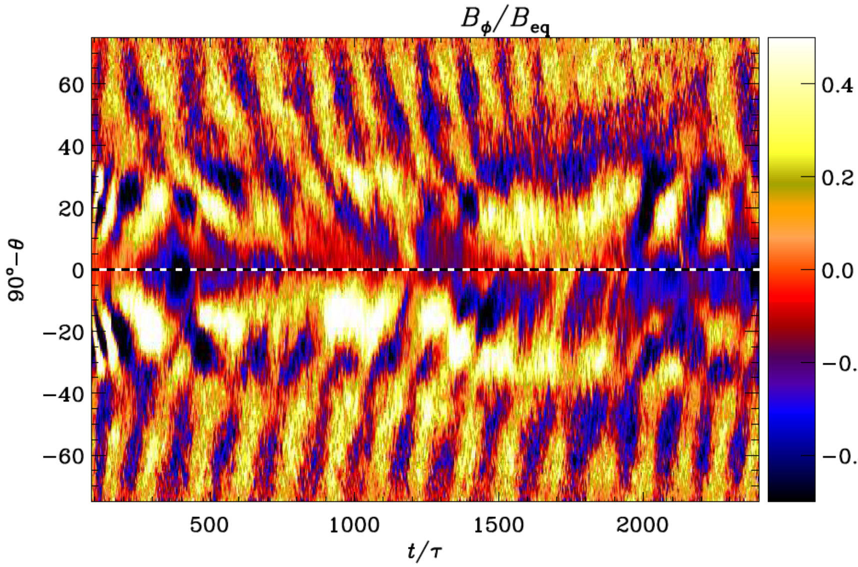

Figure 6.4: Time evolution of the mean radial magnetic field $\overline{B}_r$ in the convection zone at $r = 0.97\,R_\odot$. The dashed horizontal lines show the location of the equator at $\theta = \pi/2$. The magnetic field is normalized by its equipartition value $B_{\rm eq}$. Overbars indicate azimuthal averages (taken from **Paper V**).

respond to around 12 years, which is very close to the 22 years of the solar magnetic cycle. Besides the work by Käpylä et al. (2012) and **Papers V** and **VI**, equatorward migration was not previously reproduced in direct numerical simulations, see § 4. Brown et al. (2011) and Nelson et al. (2013) were able to produce an oscillatory magnetic field with highly irregular cycles and poleward migration. In the work by Racine et al. (2011), the authors found regular oscillatory mean magnetic fields, but no clear equatorward migration. One reason for the success of Käpylä et al. (2012) might be the use of a new developed thermal boundary condition at the surface of the convection zone following a black-body boundary condition, which lets the temperature vary in time and space. This not only allows us to measure the irradiance variation due to the magnetic cycle as done in **Paper VI**, it is less restrictive than forcing the temperature or the entropy gradient to be a constant at the boundary as e.g. in Brun et al. (2004, 2011) and Miesch et al. (2006). In the model of **Paper V**, the coronal layer serves as an even less restrictive boundary condition. The cause of the equatorward migration can be only clearly revealed, if one determines the transport coefficients. Racine et al. (2011) used a rudimentary way to calculate the α-tensor while neglecting the turbulent diffusivity tensor,

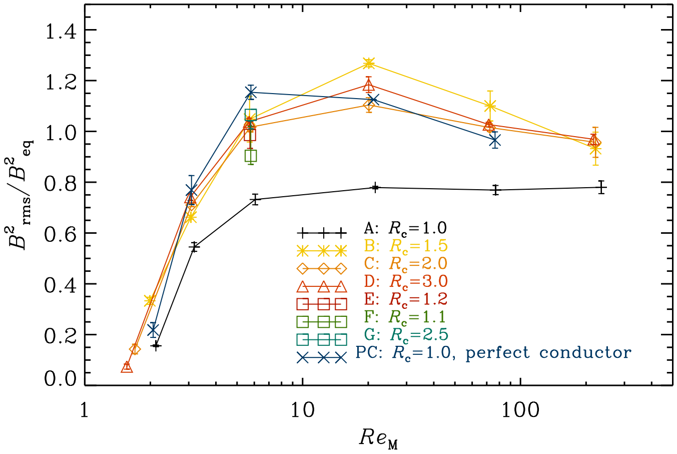

Figure 6.5: Dependence of magnetic field energy normalized by the equipartition value $B^2_{\rm rms}/B^2_{\rm eq}$ with coronal radial extent $\mathrm{R_C}$ and magnetic Reynolds number $\mathrm{Re_M}$. The solid black line indicates the dynamo region without any corona, the other colors have coronal radial extents of $1.1\,R_\odot$, $1.2\,R_\odot$, $1.5\,R_\odot$, $2.0\,R_\odot$, $2.5\,R_\odot$, and $3.0\,R_\odot$. The blue line represents simulations with a perfect conductor boundary condition at top boundary in radial direction ($r = \mathrm{R_C}$) (taken from Warnecke et al. 2013b, in preparation).

which limits their results fundamentally. A more accurate and reliable way to determine the transport coefficients including the turbulent diffusivity tensor is the test-field method, developed by Schrinner et al. (2007), which is at the moment not implemented in spherical coordinates.

The magnetic field pattern in Fig. 12 of **Paper V** (compare also with the other panels of Fig. 12 and 13 of **Paper V**) is different from that in Fig. 1.6 of the Sun and Fig. 4.4 of Käpylä et al. (2012) and **Paper VI**. In **Paper V** the equatorward migration exists to high latitudes and is there also more stable than at lower latitudes. In the Sun and in the work by Käpylä et al. (2012) as well as in **Paper VI**, there exists a polar branch, where the field migrates towards the while, and the equatorward migration is stronger at low latitudes. However, the parameters in both of the simulations show also some difference. For example, the runs of **Paper VI**, which produce equatorward migration have a stronger stratification, i.e. the density contrast in the convection zone is 14 in **Paper V** while being ≥ 25 in **Paper VI**.

The model of **Paper II** is well suited for testing, whether a coronal layer supports a dynamo in the lower layer. As shown in Fig. 6.5, the magnetic field strength in terms of $B^2_{\rm rms}/B^2_{\rm eq}$ is significantly higher for models with a corona than for models without. This is a remarkable result, taking into account that in

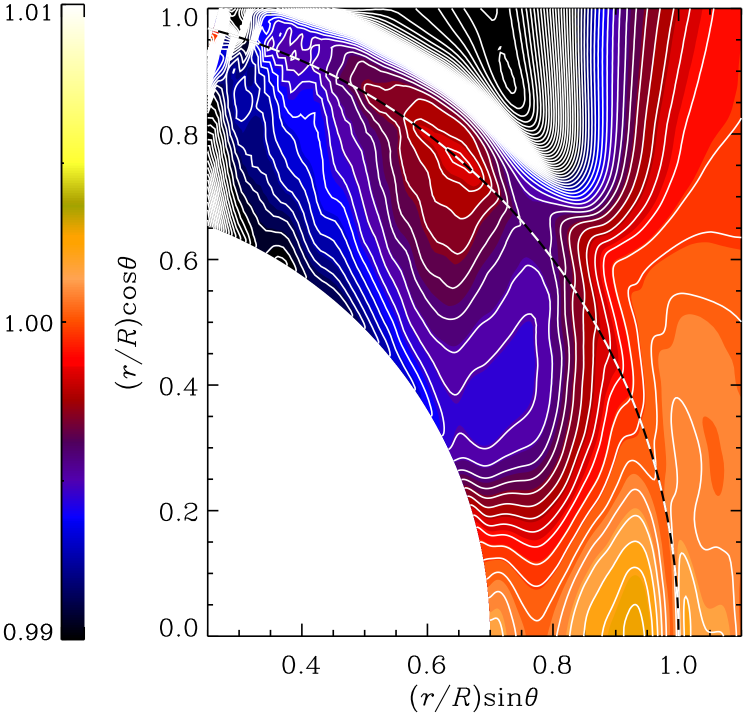

Figure 6.6: Differential rotation in the convection zone in the northern hemisphere. The mean rotation profile $\overline{\Omega}(r,\theta)/\Omega_0$ is shown color coded and with white contours. The white-black dashed line indicates the surface ($r = R_\odot$). Overbars indicate azimuthal averages (taken from **Paper V**).

the simulations without a corona, a vertical field condition is applied at the upper boundary. A combined two-layer model is capable of supporting dynamo action in addition to the helicity fluxes allowed by the vertical field condition. The vertical field condition might be too restrictive as it forces the magnetic field into a certain configuration, which has a lower dynamo saturation value, see also § 6.4.

6.3.2 Differential rotation

Differential rotation plays a role only in **Papers IV** and **V**, because in the other ones no rotation is included. In the model of **Paper IV**, the stratification is weak and the convective flux is not as strong as the radiative flux. This causes that the Taylor–Proudman balance is not broken and the rotation profile is cylindrical in the convection zone as well as in the corona, see Fig. 6 of **Pa-**

per IV. The model of **Paper V** is more suitable for investigating the differential rotation. We found the new and interesting result of a solar-like differential rotation profile. As described in § 2.4 and § 4.3.2, direct numerical simulations of global convective dynamos in spherical shells were not able to reproduce a solar-like differential rotation pattern. In pure hydrodynamic simulations this can be accomplished only by imposing a latitudinal entropy gradient at the bottom of the convection zone (Miesch et al., 2006) or by including a stably stratified layer below the convection zone (Brun et al., 2011). As shown in Fig. 6.6, the equator rotates in our model faster than the poles, which has also been achieved in other DNS and LES models (e.g. Käpylä et al., 2011b, 2012; Nelson et al., 2013, and **Paper VI**). The important features are the roughly radial contour lines of constant rotation in the convection zone. This is generated for the first time self-consistently in a direct magnetohydrodynamical numerical simulation. We find out that the Taylor–Proudman balance is broken by the baroclinic term in the mean azimuthal vorticity equation, see Eq. (2.37) and Fig. 5 of **Paper V**. This is related to a 8% higher temperature at higher latitudes than at the equator. It is still puzzling, that we do not see any similar spoke-like differential profiles in the runs without any corona of **Paper VI**. One of the reasons might be, that the transition region containing large temperature and density gradients provides an isolation between the convection zone and the corona. However, a realistic description of the upper thermal boundary as an open boundary might be crucial also in this sense. The results of Brun et al. (2011) show, that a more realistic treatment of the lower thermal and velocity boundary can also lead to a realistic differential rotation profile including the generation of a tachocline. See the details of this discussion in Section 3.1 and 3.2 of **Paper V**.

Additionally, the differential rotation profiles obtained in the model of **Paper V** show a near-surface-shear layer (NSSL), at low latitudes. This is a promising result, because we know from mean-field simulations, that the NSSL plays an important part for the solar dynamo, generating a solar-like oscillation pattern and migration direction of the mean magnetic field, (see Käpylä et al., 2008, and § 4). In the LES model of Brun et al. (2011), the differential rotation is similar to the rotation profile obtained by helioseismology (see e.g. Thompson et al., 2003), but no NSSL was found by the authors, also because the near-surface stratification was not included in these models. This leads to the conclusion, that a corona supports the generation of an NSSL, due to less restrictive boundary also for the velocity field.

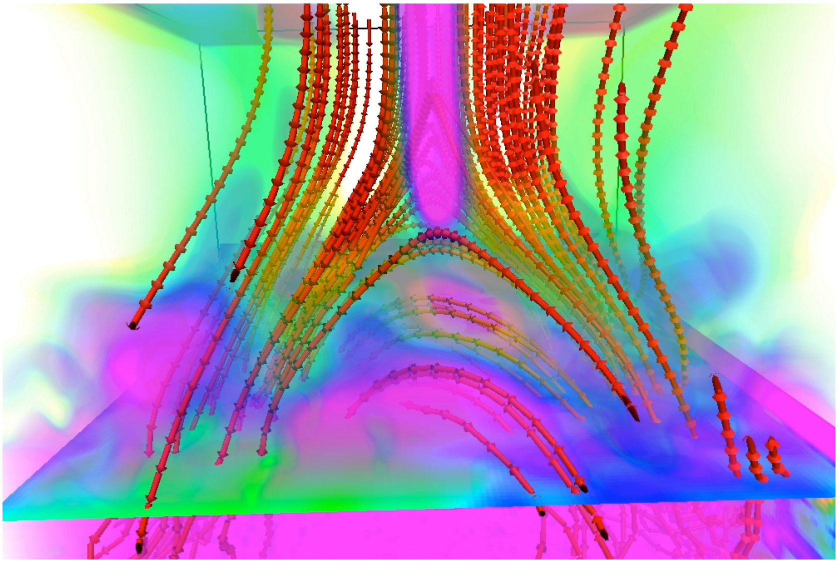

Figure 6.7: Magnetic field structure in the upper layer of the domain. Field lines are shown in red and the modulus of the current density is shown in pink with semi-transparent opacity. Note the formation of a vertical current sheet above the arcade (taken from **Paper I**).

6.3.3 Coronal field structure

The model of **Paper I** shows a significant magnetic structure in the coronal layer. Confined by the bipolar field and the vertical field boundary condition, an arcade of magnetic field lines is formed. In Fig. 6.7 we show a three dimensional visualization of this structure. Magnetic field lines form closed loops between opposite polarities on the surface as well as open field lines which connect to the upper boundary. At the interface between them an inverted Y-point is formed. Such a point is basically the lower end of an extended X-point. As plotted in Fig. 6.7, the location of the Y-point coincides with the formation of a current sheet. In a more realistic simulation, this current sheet would correspond to a region of strong Ohmic heating and energy dissipation. This energy could be released as a flare. In the model of **Paper II**, the magnetic field in the corona forms a structure similar to magnetic clouds, which are ejected recurrently. A deeper discussion on this will follow in § 6.3.4. Besides the coronal ejection, the coronal magnetic fields influence the rotation in the models of **Papers IV** and **V**. As shown in Fig. 2 of **Paper V**, the rms velocity averaged over the whole domain decreases due to the growing magnetic field. After the coronal magnetic field reaches a certain strength, the rotation

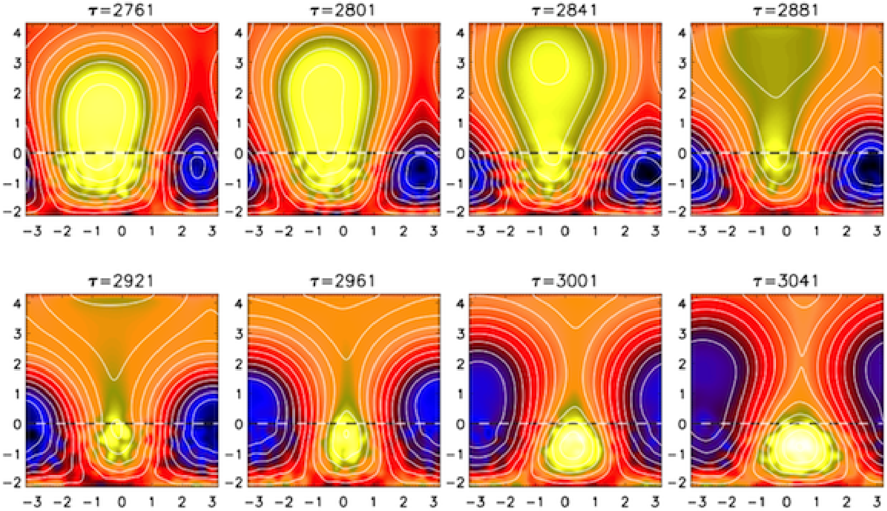

Figure 6.8: Time series of the formation of a plasmoid ejection. Projections of field lines of $\langle \boldsymbol{B} \rangle_x$ in the yz plane are shown together with a color-scale representation of $\langle B_x \rangle_x$; blue stands for negative and yellow for positive values. The dotted horizontal lines show the location of the surface at $z = 0$. τ indicates here the time normalized to the turnover time. The angle brackets represent averages in the direction of the subscript (taken from **Paper I**).

in the corona is quenched essentially to the same level as the turbulent motion inside the convection zone. This is an important numerical result. Until now, the rotation of the solar corona is not clearly determined by observations, see Section 2.2 in **Paper IV**.

6.3.4 Coronal ejections

In **Papers I–IV**, the detection of coronal ejections can be reported. However, in the model of **Paper V**, we see indication of ejections (not yet published), but in **Paper V** we focus on the physical properties of the convection zone. Using the model of **Paper I**, we produce ejections of magnetic field structures and current helicity density $\boldsymbol{J} \cdot \boldsymbol{B}$. Looking at lines of the magnetic field averaged in the x direction, we find plasmoids recurrently getting ejected from the coronal layer out of the domain. In Fig. 6.8, a positive B_x concentration is lifted up and emerges through the top boundary. Between the third and fourth panels in the second row of Fig. 6.8, a reconnection event happens, similar to what is shown in Fig. 6.7. After the positive flux concentration has been erupted, a new negative flux concentration has emerged and will be erupted shortly after

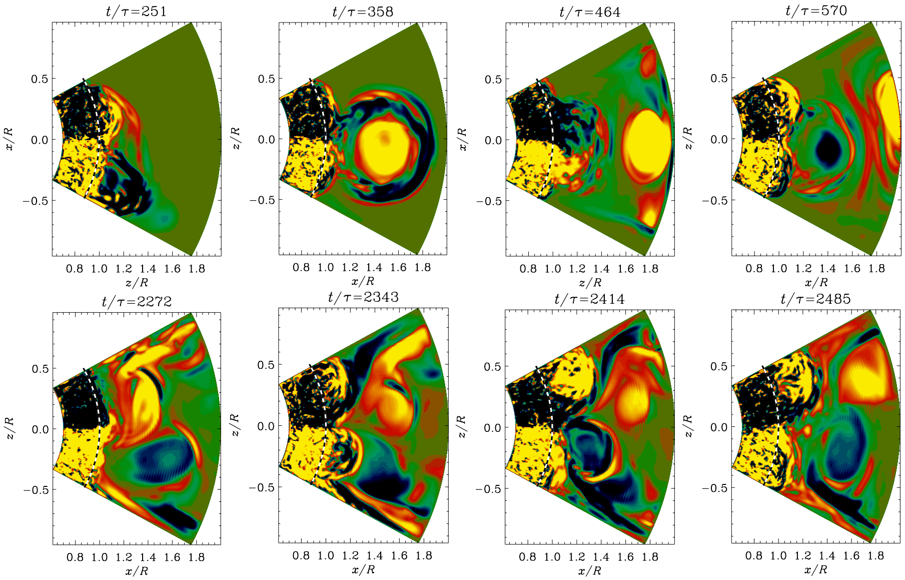

Figure 6.9: Time series of coronal ejections in a spherical wedge. The normalized current helicity, $\mu_0 R\overline{\boldsymbol{J}\cdot\boldsymbol{B}}/\langle\overline{\boldsymbol{B}^2}\rangle_t$, is shown in a color-scale representation for different times; dark/blue stands for negative and light/yellow for positive values. The dashed lines show the location of the surface at $r^2 = x^2 + z^2 = R^2 = R_\odot^2$. Overbars indicate azimuthal averages (taken from **Paper III**).

that. Looking at a time-height diagram of current helicity, as in Fig. 3 of **Paper III**, one notices that the ejections happen regularly and carry a substantial amount of current helicity out of the domain. Here it is notable that magnetic buoyancy is not the dominant force, at least in our simulations. Therefore, the emergence and ejection of magnetic field structures must be due to the Lorentz force that is basically due to the twists of the fields. Twisted magnetic fields tend to untwist, because of the magnetic tension as part of the Lorentz force, see Eq. (3.14). The most important way to untwist in this setup is to emerge to the coronal layer or out of the domain through the top boundary. The model we used in **Paper II** is able to produce coronal ejections of similar shape as observed in coronal mass ejections. In Fig. 6.9, we show a time series of coronal ejections by plotting the normalized current helicity $\mu_0 R_\odot\overline{\boldsymbol{J}\cdot\boldsymbol{B}}/\langle\overline{\boldsymbol{B}^2}\rangle_t$ for different times. In the upper row a strong ejection has emerged close to the equator and is pushed out of the domain. The ejection consists of a bubble-like structure in the center and a bow in the front, which is very similar to the three-part structure in observed coronal mass ejection on the Sun (see e.g Illing and Hundhausen, 1985; Low, 1996, and § 5). The bow seems to have always the opposite sign of current helicity than the bubble, which can be re-

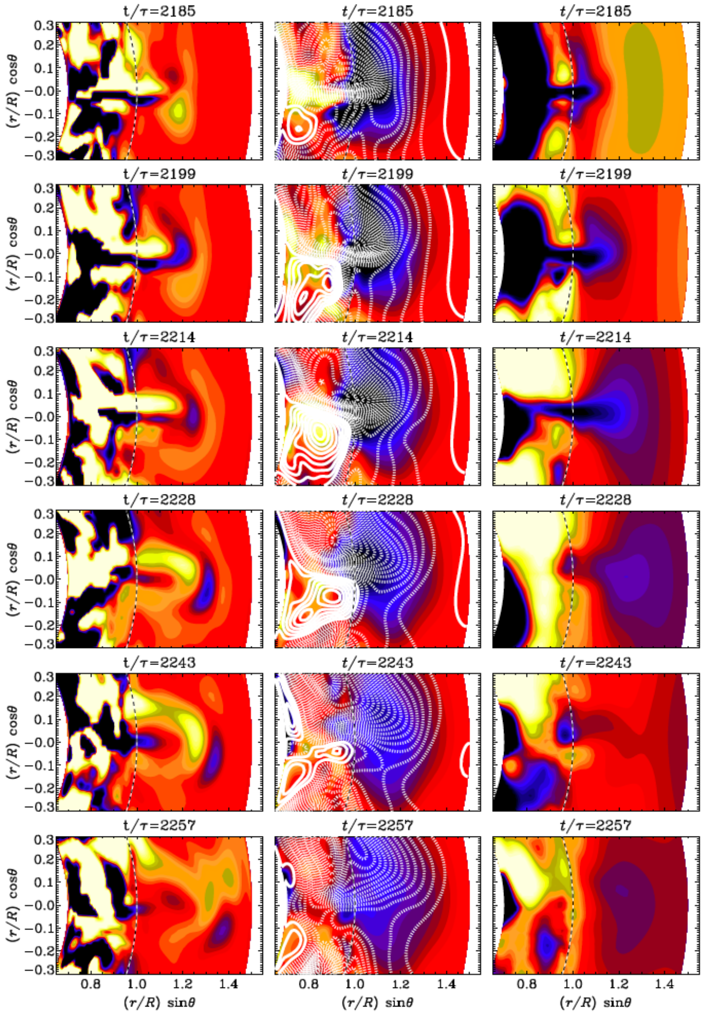

Figure 6.10: Time series of a coronal ejection zoomed into the region of the ejection near the equator ($\theta = \pi/2$), taken from Run A5 of **Paper IV**, where turbulence is driven by convection. The dashed curved vertical lines show the location of the surface $r = R = R_\odot$. *Left column*: normalized current helicity, $\mu_0 R \overline{\boldsymbol{J} \cdot \boldsymbol{B}} / \langle \overline{\boldsymbol{B}^2} \rangle_t$. *Middle column*: magnetic field, field lines of $\overline{\boldsymbol{B}}$ projected into the r,θ plane, where solid lines represent clockwise magnetic field lines and the dashed ones counter-clockwise are shown together with a color-scale representation of $\overline{B}_\phi$. *Right column:* density fluctuations $\Delta\overline{\rho(t)} = \overline{\rho(t)} - \langle \overline{\rho} \rangle_t$. For all plots, the color-scale represents negative as dark blue and positive as light yellow (taken from **Paper IV**.)

lated to a bipolar magnetic structure. Such bipolar magnetic structures have been observed in magnetic clouds (see e.g. Li et al., 2011). The occurrence of ejections is not always close to the equator. However, their emergence seems often to coincide with the annihilation of the magnetic field polarities at the equator, as described in § 6.3.1. Also in our model, magnetic buoyancy is not dominant, because the field generated by a forced turbulent dynamo is not concentrated enough to couple efficiently to the pressure distribution as our simulations show. Therefore the emergence and ejection of the magnetic field can be explained by the untwisting of helical structures. Looking here also at the time-height current helicity diagram, one finds recurrences, similar to those in the Cartesian model of **Paper I**. The pattern of recurrence depends on the fluid and magnetic Reynolds numbers (Re, $\mathrm{Re_M}$); see Fig. 12 of **Paper II** for lower Re and $\mathrm{Re_M}$ and Fig. 6 of **Paper III** for higher Re and $\mathrm{Re_M}$.

In the model of **Paper IV**, ejections are not that easy to detect as in the previous models. The magnetic field is weaker and less helical. Additionally, the ejections are smaller and hence more difficult to find in a larger domain. We have performed many more runs than those mentioned in **Paper IV**, but only in a few of them, we could detect ejections. These isolated structures can be found best by plotting the current helicity density. In Fig. 6.10 we show the time series of the current helicity density, the magnetic field and the density disturbance of such an isolated structure. In the current helicity density, we found a bipolar structure similar to those in **Paper II**, but much smaller and less pronounced. This is correlated with strong radial magnetic field concentrations near the surface. The density disturbance indicates the emergence of a magnetic flux tube, whose density is lowered due to magnetic pressure. Because of the low stratification inside our model, the tube stays less dense than its surroundings and does not carry mass into the corona. Unfortunately, the resolution of this isolated structure is not that high, because it is a global simulations. A detailed analysis of this ejection shows a clear bipolar structure in the current helicity represented by two current sheets and a strong radial magnetic field, see Fig. 16 of **Paper IV**. The recurrence of the events is not as regular as in **Papers I** and **II**, but we can detect several events happening during the simulated time.

6.3.5 Magnetic helicity and current helicity

Already in the model of **Paper I**, we found a different sign of current helicity in the coronal layer than in the dynamo layer, see Fig. 3 of **Paper III**. The current helicity is positive in the lower layer, where the dynamo is operating and negative in the upper layer, representing the corona. In the spherical model of **Paper II**, the reversal of sign is even more pronounced. In Fig. 6.9, the current

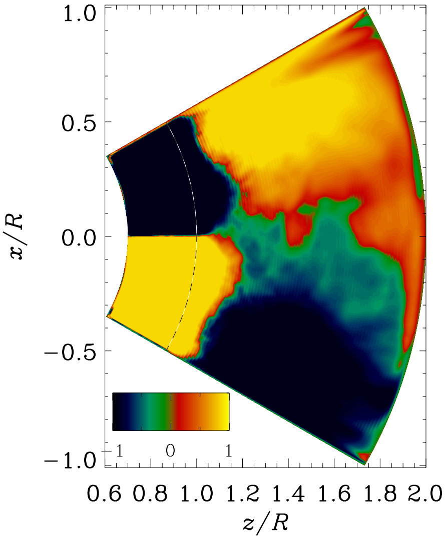

Figure 6.11: Time averaged current helicity $\mu_0 R_\odot \langle\overline{\boldsymbol{J}\cdot\boldsymbol{B}}\rangle_t/\langle\overline{\boldsymbol{B}^2}\rangle_t$. Dark/blue corresponds to negative values, while light/yellow corresponds to positive values, as in Fig. 6.9. The dashed line shows the location of the surface at $r^2 = x^2 + z^2 = R^2 = R_\odot^2$ (taken from one of the runs of **Paper III**).

helicity in the convection zone has a negative sign in the northern hemisphere and a positive sign in the southern hemisphere. This is a result of the sign of the helical forcing applied in this part of the domain. In the corona, we notice that (in particular in the second row of Fig. 6.9) the current helicity carried by the ejections has opposite signs as in the corresponding part in the convection zone of each hemisphere: they are positive (yellow) in the northern hemisphere and negative (blue) in the southern hemisphere. This can be seen even more clearly in a time-averaged plot, as shown in Fig. 6.11. There we have averaged over nearly 4000 turnover times, and see that the sign of current helicity changes in the outer atmosphere. This behavior has been confirmed by *Ulysses* spacecraft observations of the magnetic helicity (Brandenburg et al., 2011b). This satellite measures the magnetic field far from the ecliptic which allows us to compute the magnetic helicity using the Taylor hypothesis, see Matthaeus et al. (1982) and Brandenburg et al. (2011b) for details. In the latter paper, it was found that the magnetic helicity in the solar wind changes its sign at a certain distance from the Sun, similar to the results found in our simulations. In **Paper III**, we use a simple analytical model to explain this sign reversal. The current helicity is related to the magnetic helicity of the fluctuating field, see Eq. (3.28). Therefore, we can use Eq. (3.31) with Eq. (3.17), neglecting

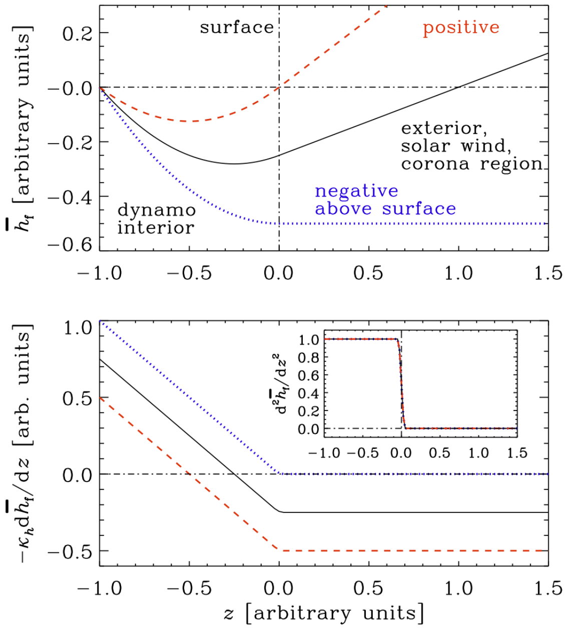

Figure 6.12: Sketch showing possible solutions of Eq. (6.3) for the mean helicity density of the fluctuating fields $\overline{h}_f(z)$ with $S = \text{const} = -1$ in $z < 0$ and $S = 0$ in $z > 0$ (upper panel). The red (dashed) and black (solid) lines show solutions for which the magnetic helicity flux ($-\kappa_h \mathrm{d}\overline{h}_f/\mathrm{d}z$, see lower panel) is negative in the exterior. This corresponds to the case observed in the Sun. The blue (dotted) lines show the case, where the magnetic helicity flux is zero above the surface and therefore does not reverse the sign of $\overline{h}_f(z)$ in the exterior (taken from **Paper III**).

the molecular diffusivity η and assuming a steady state, to derive the equation

$$\boldsymbol{\nabla}\cdot\overline{\boldsymbol{\mathfrak{F}}}_h^f = -2\alpha\overline{\boldsymbol{B}}^2 + 2\eta_\mathrm{t}\mu_0\overline{\boldsymbol{J}}\cdot\overline{\boldsymbol{B}}. \tag{6.2}$$

With a Fickian diffusion approach, $\overline{\boldsymbol{\mathfrak{F}}}_h^f = -\kappa_h\boldsymbol{\nabla}\overline{h}_f$, we can construct a one dimensional model of the helicity distribution

$$-\kappa_h\frac{\mathrm{d}^2\overline{h}_f}{\mathrm{d}z^2} = S(z), \tag{6.3}$$

with the source term $S(z) \equiv -2\alpha\overline{\boldsymbol{B}}^2 + 2\eta_\mathrm{t}\mu_0\overline{\boldsymbol{J}}\cdot\overline{\boldsymbol{B}}$. Here κ_h is the magnetic helicity diffusion coefficient (assumed constant), which is expected to be around $0.3\,\eta_\mathrm{t}$ (Hubbard and Brandenburg, 2010; Mitra et al., 2010a, and **Paper II**). In Fig. 6.12, we plot three different solutions for $\overline{h}_f$, where the source term is $S(z) = -1$ in the interior and zero outside (using arbitrary units). Depending on the slope, which depends on κ and the boundary conditions, and the size of the domain, the helicity changes sign at different locations in the outer part. This is why in some dynamo models, we can observe a sign change, but not in all of them. In the model of **Papers IV** and **V** no clear indication of helicity sign reversal has been found. This could be related to the lower amount of magnetic helicity produce by less helical (as convective instead of forced) motions.

6.4 Discussion and conclusions

The results of **Papers I–V** show that we were able to reproduce important features of the Sun's magnetic field as well as its differential rotation with a simplified two-layer model. Combining the convection zone, where a dynamo is operating, with an overlying corona gives useful and remarkable insights about dynamo theory, the mechanism of coronal mass ejections and the magnetic helicity distribution in the Sun. We found that the dynamo is stronger in the present of the corona and shows equatorward migration. The coronal layer does not only influence the convection zone as it represents a more realistic boundary condition for the magnetic field, it also seems to promote the generation of spoke-like differential rotation. We are able to generate coronal ejections and flux emergence just by the untwisting of helical fields. We additionally show that even with kinetic helicity which is less for the convective dynamo than for a force turbulent one, coronal ejections occur. The shape of these ejections is similar to those observed in real coronal mass ejections. Most of these results have been found for the first time and suggest that they are only reproducible using a combined two-layer model.

One issue with using direct numerical simulations to model astrophysical bodies is the question, whether these models are realistic enough; and if they are not, why we should bother using them. Currently, direct numerical simulations are unable to reach realistic values of the magnetic diffusivity and fluid viscosity. Therefore, every direct simulation of a solar dynamo model is per se unrealistic. But, we can still learn a lot from these simulations. In particular, we can run them for a series of different values of magnetic and fluid Reynolds numbers and try to extrapolate the results to solar values. On the other hand, our scope is not to reproduce every little detail of the Sun with our model; we are more interested in specific models, and investigate their outcome. If we understand the results of these simplified and concededly unrealistic simulations in a proper way, it will yield great contributions to the understanding of the Sun's dynamics.

Beside the Reynolds numbers, what about the other quantities, are they consistent with solar values? The density contrast is order of magnitudes lower than in the considered region of the Sun, which includes the entire convection zone and the corona to a large extent. The solar density changes over fourteen orders of magnitude, which is currently impossible to model in direct numerical simulations. Using tools such as non-equidistant grids might extend the contrast, but not to solar values. After all, we have improved the density contrast in our models from unity to over two thousand. Applying non-solar-like values for the density stratification in our models influences the results. In the model of **Papers I** and **II**, the density is either constant or does not play an important role in producing ejections of current helicity density. But in the models of **Papers IV** and **V**, the low stratification has a strong influence on the results. For example in **Paper IV**, the ejected flux tube shows a lower density than the surrounding plasma because of the low stratification. We expect that with a higher stratification this tube would have a higher density than the surrounding plasma in the corona, similar to observed CMEs. Also, in **Paper VI** the equatorward migration pattern depends crucial on the strength of the stratification. The luminosity, we choose in the models of **Papers IV** and **V** is much higher than the solar one. Using this, we try to compensate for the low Reynolds number regime, which make convection harder to excite. A similar argument we employ for the use of rotation rates higher than the Sun. Although the Sun might have slower convective motions than expected (Hanasoge et al., 2012), which would increase the solar Coriolis number, the Coriolis numbers we use in our models are only slightly higher than those in the Sun, although the rotation rate is three times higher. With lower magnetic Reynolds numbers and a solar-like rotation rates it is in general more difficult to excite a solar dynamo, therefore, we increase the rotation rate to compensate for the too low magnetic Reynolds number. Additionally, higher rotation rate might be not applicable to the Sun, but to other stars, where the magnetic fields are also observable.

In our combined two-layer model, we use strong simplifications to implement the combination of a convection zone and a corona in a single model. We found that there exists a dynamo solution which shows equatorward migration even in the low Reynolds number regime. The fact that a coronal layer has a strong influence on the properties inside the convection zone, may have been overestimated by the lack of realistic stratification and Reynolds numbers, but it should be taken into account in future simulations of stellar dynamo models. Helical magnetic fields can emerge, build up structures similar to CMEs, and get eventually ejected. The untwisting of magnetic fields as an alternative way to the emergence of structures should be studied further and can in the Sun also have significant importance.

Researchers, who model coronal mass ejections might criticize the lack of coronal properties in our model. The value of the plasma-β, which determines,

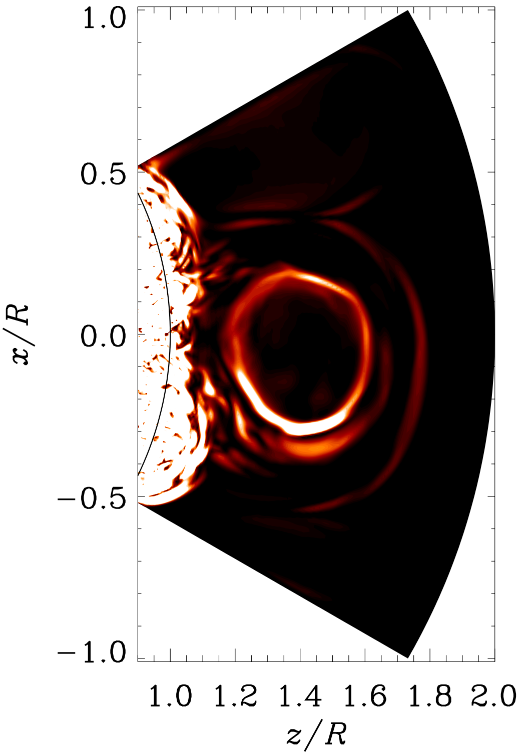

Figure 6.13: Coronal ejection plotted in terms of the Ohmic heating $\mu_0\eta\overline{\boldsymbol{J}^2}$ of the model of **Papers II** and **III**. This ejection is the same as in the second panel of Fig. 6.9. Bright colors correspond to large values and dark to small ones. The solid black line show the location of the surface at $r^2 = x^2 + z^2 = R^2 = R_\odot^2$. Overbars indicate azimuthal averages.

whether the magnetic field follows the plasma, is not very low in our corona. In the models of **Papers II** and **IV** our corona is isothermal and has therefore a high value of plasma-β. This is a valid criticism, but not for our scope, which is to describe the magnetic properties and the magnetic structures emerging into the corona. Because the plasma-β is low in the solar corona, the magnetic structures are the important features. We do not claim to describe the fluid and plasma properties of these ejections realistically. We are interested to study the emergence of ejections of magnetic field and current helicity. In future models similar to those in **Paper V**, we will see, if a lower plasma-β changes the main magnetic properties of the ejections. Additionally, we also do not claim to describe the coronal ejections realistically, as we are more interested in the mechanism of the emergence and its connection with dynamo action.

In **Papers II** and **III**, we compare plots of current helicity density and white light images of observed CMEs and conclude that the shape of our ejections are similar to them. White light emission and current helicity are not the same quantities and comparing these two can be misleading. However, in this work, as mentioned before, we are mostly interested in CMEs as magnetic phenomena. The current helicity concentrations are emerging from the surface of our convection zone, carrying some mass with it. In a realistic simulation with high enough density stratification, the shape of the current helicity ejections would directly correspond to density enhancement and therefore emissivity. In Fig. 6.13, we plot Ohmic heating for one of the prominent ejections of the model of **Paper II**. The revealed shape shows clear similarities with the observed one of real coronal mass ejections. We claim, that the Ohmic heating can be related to the emissivity of the CMEs shown in Figs. 1.8 and 5.2.

For another aspect it is shown that a coronal layer as an upper boundary condition is important for the dynamo. Comparing Fig. 4.4 with Fig. 6.4, the evolution of the mean magnetic field shows a different behavior in cases with and without a coronal layer. Beside the different patterns of the equatorward migration in the saturated stage, the excitation times are significantly different. In the simulation without a coronal layer (Fig. 4.4), the mean magnetic field is visible after around $t/\tau = 1000$, whereas in the case with a coronal layer (Fig. 6.4), it is already visible in the very beginning of the simulation. The input parameters of the simulations are not that different leading to a similar estimation for the turnover time τ (see **Papers V** and **VI**). Additionally, the simulation without a corona have been started from a equilibrated hydrodynamical run, where the convective motions has reached a saturated state. In the model with a corona the simulations have been started from the hydrostatic reference solution without any convective motions. This fact together with the similarity of the input parameters suggest that the coronal layer has a strong influence on the excitation of the large-scale dynamo. To express it in a different way: the radial field boundary condition at the surface of the convection zone is very restrictive and can change the dynamo evolution in the convection zone significantly. However, to have clear evidence for this, we have to perform more simulations both with and without a coronal later, whereas the other parameters are held exactly the same.

Overall, this two-layer model is an excellent model to study the corona-dynamo interaction as well as the ejection of magnetic helicity and mass from the convection zone through the corona into the interstellar space.

7. Possible Future Developments

> *My goal is simple.*
> *It is a complete understanding of the universe,*
> *why it is as it is and why it exists at all.*
>
> Stephen Hawkins

This combined two-layer model as described in § 6 is a rich model, which can be used in many ways for many different purposes. Let me outline here a few possibilities.

7.1 Solar dynamo and helicity fluxes

Measuring and modeling magnetic helicity fluxes is an important element in understanding the solar dynamo. The combined two-layer model provides a straightforward approach to quantify how much magnetic helicity flux is needed for the solar dynamo. It would be important to determine its influence on the equatorward migration of the mean magnetic field found in the model of Käpylä et al. (2012). This would involve a study of magnetic helicity fluxes and mean magnetic fields generated by a convective dynamo using mono- and bi-layer models. In this context, investigating also the differential rotation in these simulations would be beneficial. However, a general understanding of the dynamo and convection mechanism generating equatorward migration and spoke-like differential rotation will only be possible by calculating the transport coefficients of the mean-flow and mean magnetic field by using approaches like the test-field method (Schrinner et al., 2007). Although rudimentary approaches have already been used (Racine et al., 2011), but their outcome is limited by neglecting the turbulent diffusivity tensor. The obtained transport coefficients can then be used in mean-field models of the solar dynamo. The predictive power of those models and their Reynolds number dependence will first be compared with DNS and those models will then be applied to magnetic Reynolds numbers closer to those of the Sun.

7.2 Convection driven coronal mass ejections

In the work of **Papers I, II** and **IV**, we could show that a dynamo below the surface can drive coronal ejections, which have a similar shape as observed

CMEs and magnetic clouds. But these models have been performed using strong simplifications, in particular in describing the coronal layer. The coronal temperature, for example, is set to the value of the surface by applying a prescribed cooling function. This led to a much higher plasma-β in our modeled corona, than in the solar one. It would be a good project to develop a realistic coronal stratification in a bi-layer model of dynamo-driven coronal mass ejection. This includes a realistic treatment of density and temperature profiles, a self-consistent coronal heating mechanism, background coronal field structures as well as solar wind interactions. Step by step, one can include more improvements in describing the coronal layer, starting with steeper temperature and density profiles. One step would be including a realistic treatment of heat conductivity similar as in the work by Bingert and Peter (2011), where it leads to self-consistently generated coronal heating due to field line braiding at the footpoints. Already these improvements will give important insights about comparing self-consistent granulation motions with granulation velocity drivers as used by Bingert and Peter (2011). Additionally, one can investigate in what extend the coronal heating is affected by ejections. As a third step one can impose coronal background fields and investigate, how the ejection are influenced or even triggered by this field as shown by, e.g. Fan and Gibson (2004). Due to numerical reasons, in the models of **Papers I, II** and **IV**, we apply closed radial boundaries, i.e. no mass flux can leave the domain. Therefore a Parker solution of the solar wind is prohibited. To study the interaction of the solar wind and coronal ejections would be a useful extension on the model. A Cartesian bi-layer will give useful insights about driven coronal mass ejections. However, this model can be extended to a global spherical model to study the coronal mass ejections as well as their interplay with the global coronal field. There, the Parker wind has a solution and can be generated self-consistently.

7.3 Space weather forecasting

A CME takes about one to five days to reach the Earth, see § 1.5 and § 5. This time interval defines the maximum advance warning time for magnetic storm events to happen. The prediction time could be extended using more realistic models and new methods. The idea is to use the data assimilation technique to forecast space weather. This is similar to weather forecast on Earth where measurements of certain quantities at stations around the world are included into the model. Each time new data are read in, the parameters of the model will be adjusted. By running an ensemble of models with different parameters, one is able to give probabilities of the resulting outcomes. Recently, there were attempts to use these methods for the forecast of the solar activity cycle (see, e.g., Dikpati and Anderson, 2012). It would be very interesting to apply the data assimilation and forecast techniques to my dynamo-driven coronal ejection model to develop a solar space weather forecast. This will involve the improvement of the ejection model, including solar wind fluctuations as well as low plasma β effects. Additionally, time should be spend on collecting observational data of ejections and preparing them to be accessible for the model. Pinning down the crucial parameters of the ejection model with observed data will be a first step. In a second step the actual forecasting can be done.

Sammanfattning

Observationer visar att koronamassutkastningar är förknippade med vridna magnetfältskonfigurationer. Koronamassutkastningar brukar vanligtvis modelleras genom att man skjuvar och vrider fotpunkterna för en viss distribution av magnetiskt flöde vid solytan och sedan låter den tidsutvecklas på ytan. Ythastigheterna och de magnetiska fältmönstren borde naturligtvis i första hand erhållas från realistiska simuleringar av solens konvektionszon där fältet genereras genom dynamoverkan. Därför behövs en enhetlig hantering av konvektionszonen och koronamassutkastningar. Numeriska simuleringar av turbulenta dynamos visar att förstärkningen av magnetfält kan dämpas genom s.k. "catastrophic quenching" vid magnetiska Reynoldstal som är typiska för solens inre. Ett starkt flöde av magnetisk helicitet från dynamoområdet can mildra denna dämpning. I denna mening är ett realistiskt (magnetiskt) randvillkor en viktig ingrediens för en framgångsrik soldynamomodell.

Med hjälp av den tvålagermodell som utvecklas i avhandlingen kombinerar vi en dynamoaktiv område med ett magnetiskt “passivt” men effektivt ledande övre lager som modellerar solens korona. I fyra steg förbättras denna uppställning från en tvingad turbulent till en konvektivt driven dynamo och från en isoterm till en polytropt stratifierad korona. Simuleringarna uppvisar magnetiska fält som uppstår vid dynamo områdes yta och sedan kastas in i domänens korona. Deras morfologi låter oss associera sådana händelser med koronamassutkastningar. Den magnetiska heliciteten visar sig ändra tecken i koronan och är förenlig med nyligen utförda helicitetsmätningar i solvinden. Vår konvektionsdrivna dynamomodell med en yttre korona har en sol-liknande differentiell rotation med radiella (eker-lika) konturer av konstant rotationshastighet, samt en sol-lik meridionell cirkulation och ett ytnära skjuvningslager. Den eker-lika rotationsprofilen härrör från en longitudinell entropigradient som bryter Taylor-Proudmanbalansen genom den barokliniska termen. Vi observerar genomsnittliga magnetiska fält som migrerar mot ekvatorn både i modeller med och utan koronalagret. Ett anmärkningsvärt resultat är att dynamoverkan gynnas avsevärt av närvaron av en korona som är starkare och mer realistisk.

Tvålagermodellen representerar en ny ansats för att på ett självkonsistent sätt beskriva hur koronamassutkastningarna skapas. Dessutom har den en stor betydelse för soldynamomodeller eftersom den återger många magnetiska företeelser som observerats i solen.

Zusammenfassung

Beobachtungen zeigen, dass koronale Massenauswürfe mit verdrillten magnetische Flußkonfigurationen verbunden sind. Üblicherweise werden koronale Massenauswürfe mit Hilfe von Scherung und Verdrillung von Fußpunkten einer vorgebenen magnetischen Flußverteilung und deren Entwicklung an der Oberfläche modelliert. Letztlich sollten jedoch die Oberflächengeschwindigkeiten und die Magnetfeldstrukturen aus realitischen Sonnenkonvektionssimulationen entnommen werden, in denen das Feld von einem Dynamoprozess erzeugt wird. Deshalb bedarf es einer vereinheitlichten Behandlung der Konvektionszone der Sonne and koronaler Massenauswürfe. Numerische Simulationen turbulenter Dynamos zeigen, dass die Verstärkung von Magnetfeldern für sonnentypische magnetische Reynoldszahlen drastisch unterdrückt wird. Ein starker magnetischer Helizitätsfluß, der das Dynamogebiet verlässt, kann diese Unterdrückung abmildern. In diesem Sinne is eine realistische (magnetische) Randbedingung ein sehr wichtiger Bestandteil eines erfolgreichen Modells für den Sonnendynamo.

Das in dieser Doktorarbeit entwickelte zweischichtige Modell, verbindet eine dynamoaktive Schicht mit einer darüber liegenden Schicht, die zwar dynamoinaktiv, aber stark leitfähig ist, sie imitiert die Korona der Sonne. In vier Schritten vervollkommnen wir den Simulationsaufbau von einem erzwungen turbulenten zu einem von Konvektion getriebenen Dynamo und von einer isothermen zu einer polytrop geschichteten Korona. Die Simulationen bringen Magnetfelder hervor, die aus dem Dynamogebiet aufsteigen und aus dem koronalen Teil des Simulationsgebiets ausgestoßen werden. Wegen deren morphologischer Form interpretieren wir diese Ereignisse als koronale Masseauswürfe. Im Ergebnis zeigt sich, dass die magnetische Helizität ihr Vorzeichen in der Korona ändert und daher mit kürzlich gemessenen Helizitätswerten aus dem Sonnenwind übereinstimmt. Unser von Konvektion getriebenes Dynamomodel mit koronaler Hülle besitzt eine sonnenähliche differentielle Rotation mit radialen (speichenähnlichen) Isolinien konstanter Winkelgeschwindigkeit sowie eine sonnenähnliche meridionale Zirkulation und einer oberflächennahen Scherschicht. Das speichenähnliche Profil der Rotation lässt sich auf den latitudinalen Entropiegradienten zurückführen, der mit Hilfe der Baroklinität das Taylor–Proudman–Gleichgewicht verletzt. Sowohl in Modellen mit als auch ohne koronaler Schicht finden wir ein mittleres Magnetfeld, das zum Äquator wandert. Ein beachtenswertes Ergebnis ist, dass der Dynamoprozess

durch das Vorhandensein der Korona erheblich begünstig und somit stärker und realistischer wird.

Das zweischichtige Modell stellt einen neuen Ansatz dar, die Erzeugung koronaler Massenauswürfe in einer selbstkonsistenten Weise zu beschreiben. Auf der anderen Seite hat es wichtige Konsequenzen für Sonnendynamomodelle, da es viele magnetische Phänomene, die auf der Sonne beobachtet werden, wiedergibt.

Acknowledgments

The first thanks is dedicated to my supervisor **Axel Brandenburg**, the most efficient person I have ever met. I learned from him the broadness and deepness of astrophysics, and that only deepness will give you broadness. He encouraged me to fulfill my own ideas, which then often resulted in collaborations and publications. I am very thankful for his intensive support and supervision to help me to become a good scientist, including BBQs and nitrogen ice cream. I also would like to give a big thanks to my close collaborators **Petri J. Käpylä** and **Maarit J. Mantere**. I enjoyed the visits to Helsinki, the long (not entirely) scientific discussions via Skype and the Sauna parties. I want to thank **Dhrubaditya Mitra** for his collaboration and supervision during my time in Nordita. I like his way of tackling scientific problems and his ability to explain them in such a way that his own daughter could understand it. I would like to give a thanks to **Matthias Rheinhardt**, whose knowledge in mean-field dynamos and numerics is as enormous as in human history. I enjoyed long and interesting discussions about German politics and non-equidistant grids. A big thanks is also deserved by my second supervisor **Göran Scharmer**. He not only supported me and my PhD project by, for example, forwarding every new article about CMEs, but he also made it possible for me to go to La Palma and observe sunspots with the SST. I think he is one of the great solar physicists of our time, and I thank him for being part of my supervision. I would also like to thank my mentor **Claes-Ingvar Björnsson** in taking care for me having a smooth sailing, and **Garrelt Mellema** of being a mindful director for graduate studies.

I am grateful to all the people in the **Astrophysics Group** and **Nordita** in general for establishing a productive and supportive scientific environment. This includes persons such as **Hans**, who helps with computer problems, Swedish translations and all the little things no one thinks about. I would like to thank the **Astronomy Department** especially **Göran Östlin** and **Sandra** for creating such a nice and warm atmosphere for my PhD studies.

A special thanks goes to my three *Roomies*, **Koen**, **Simon** and **Fabio**, who unfortunately left me alone this March. I was very happy to be able to share my office and trips through North America, South America, Asia and Europe with you guys. And remember: *the wine is too pink*! At this point, I would also acknowledge all the nice conferences (Krakow, Nice, Naxos, Ventura, Teistungen, Rhodes, Mendoza and Beijing), including travel grants supported by the International Astronomy Union as well as the C F Liljevalchs Foundation, the K&A Wallenberg Foundation, and the High Performance Computing-

EUROPA2 Project.

There have been many people in and around Nordita and the Department of Astronomy, whose presence I enjoyed very much. They are (without any preferential order): **Oliver, Sarah, Gianni, Illa, Cecilia, Gustavo, Piyali, Hiva, Saghar, Vasco, Jaime, Hannes, Andreas, Florent, Emanuel, Thørger, Lucia, Genoeva, Katia, Fernanda, Alessandro, Francesco, Gautam, Mikael** and **Laia**. Others have already left, but are still important friends, like **Javier&Claire, Martina, Nuria&Antonio** and **Angela&Arjan**. Thanks to **Sidney, Leili** and **Elliot Maxwell**, as my family in Stockholm.

A grateful thanks deserves my Family in Germany, my parents **Reinhard und Gabi** with their unconditional support and love, as well as **Lars und Steffi** and my grandparents **Hannelore und Gerd** and **Anni und Lothar** for they unappeasable interest in my life and my work.

At last, but most important, I wish thank to **Atefeh**. Your love, your kindness and your naturalness have made my last two and a half years the best of my life. Doset Daram, Atijunam!

At the end, I would also like to thank all my friends in Stockholm, in Germany and all around the World. *Tack! Danke! Thank you!*

Publications not included in the Thesis

Conference proceedings

I **Warnecke, J.**, & Brandenburg, A.: 2011, "Recurrent flux emergence from dynamo-generated fields", in *Astrophysical Dynamics: from Stars to Galaxies*, ed. N. Brummell, A. S. Brun, M. S. Miesch, & Y. Ponty, Proc. IAU Symp., **Vol. 271**, pp. 407-408

II **Warnecke, J.**, & Brandenburg, A.: 2011, "Dynamo generated field emergence through recurrent plasmoid ejections", in *Physics of Sun and Star Spots*, ed. D. P. Choudhary & K. G. Strassmeier, Proc. IAU Symp., **Vol. 273**, pp. 256-260

III **Warnecke, J.**, Brandenburg, A., & Mitra, D.: 2011, "Plasmoid ejections driven by dynamo action underneath a spherical surface", in *Advances in Plasma Astrophysics*, ed. A. Bonanno, E. de Gouveia dal Pino, & A. Kosovichev, Proc. IAU Symp., **Vol. 274**, pp. 306-309

IV **Warnecke, J.**, Käpylä, P. J., Mantere, M. J., & Brandenburg, A.: 2012, "Coronal ejections from convective spherical shell dynamos", in *Comparative Magnetic Minima: Characterizing quiet times in the Sun and stars*, ed. C. H. Mandrini & D. F. Webb, Proc. IAU Symp., **Vol. 286**, pp. 154-158

V **Warnecke, J.**, Käpylä, P. J., P. J., Mantere, M. J., & Brandenburg, A.: 2012, "Solar-like differential rotation and equatorward migration in a convective dynamo with a coronal envelope", in *Solar and astrophysical dynamos and magnetic activity*, ed. A. Kosovichev, Proc. IAU Symp., **Vol. 294**, in press

Bibliography

C. E. Alissandrakis. On the computation of constant alpha force-free magnetic field. *Astron. Astrophys.*, 100:197–200, 1981. 30

T. Amari, J.F. Luciani, Z. Mikić, and J. Linker. A twisted flux rope model for coronal mass ejections and two-ribbon flares. *Astrophys. J. Lett.*, 529:L49–L52, 2000. 54

S. K. Antiochos, C. R. DeVore, and J. A. Klimchuk. A Model for Solar Coronal Mass Ejections. *Astrophys. J.*, 510:485–493, 1999. 52

M. J. Aschwanden, A. Winebarger, D. Tsiklauri, and H. Peter. The coronal heating paradox. *Astrophys. J.*, 659:1673–1681, 2007. 7

H.W. Babcock. The topology of the sun's magnetic field and the 22-year cycle. *Astrophys. J.*, 133:572–589, 1961. 41

S. L. Baliunas, R. A. Donahue, W. H. Soon, J. H. Horne, J. Frazer, L. Woodard-Eklund, M. Bradford, L. M. Rao, O. C. Wilson, Q. Zhang, W. Bennett, J. Briggs, S. M. Carroll, D. K. Duncan, D. Figueroa, H. H. Lanning, T. Misch, J. Mueller, R. W. Noyes, D. Poppe, A. C. Porter, C. R. Robinson, J. Russell, J. C. Shelton, T. Soyumer, A. H. Vaughan, and J. H. Whitney. Chromospheric variations in main-sequence stars. *Astrophys. J.*, 438:269–287, 1995. 2

G. Baumann, K. Galsgaard, and Å. Nordlund. 3D Solar Null Point Reconnection MHD Simulations. *Solar Phys.*, page 291, 2012. 54

S. Bingert and H. Peter. Intermittent heating in the solar corona employing a 3D MHD model. *Astron. Astrophys.*, 530:A112, 2011. 7, 13, 30, 50, 80

S. Bingert and H. Peter. Nanoflare statistics in an active region 3D MHD coronal model. *Astron. Astrophys.*, 550:A30, 2013. 50

E. G. Blackman and A. Brandenburg. Doubly Helical Coronal Ejections from Dynamos and Their Role in Sustaining the Solar Cycle. *Astrophys. J. Lett.*, 584:L99–L102, 2003. 51, 56

E. G. Blackman and G. B. Field. Constraints on the Magnitude of α in Dynamo Theory. *Astrophys. J.*, 534:984–988, 2000. 36, 56

A. Brandenburg. The Case for a Distributed Solar Dynamo Shaped by Near-Surface Shear. *Astrophys. J.*, 625:539–547, 2005. 39, 40, 42, 47

A. Brandenburg. Nonlinear Small-scale Dynamos at Low Magnetic Prandtl Numbers. *Astrophys. J.*, 741:92, 2011. 44

A. Brandenburg and W. Dobler. Large scale dynamos with helicity loss through boundaries. *Astron. Astrophys.*, 369:329–338, 2001. 36

A. Brandenburg and C. Sandin. Catastrophic alpha quenching alleviated by helicity flux and shear. *Astron. Astrophys.*, 427:13–21, 2004. 56

A. Brandenburg and K. Subramanian. Astrophysical magnetic fieds and nonlinear dynamo theory. *Physics Reports*, 417:1–209, 2005. 31, 32, 35, 36, 37, 56

A. Brandenburg, D. Moss, and I. Tuominen. Stratification and thermodynamics in mean-field dynamos. *Astron. Astrophys.*, 265:328–344, 1992. 24, 47

A. Brandenburg, S. H. Saar, and C. R. Turpin. Time Evolution of the Magnetic Activity Cycle Period. *Astrophys. J. Lett.*, 498:L51, 1998. 2

A. Brandenburg, S. Candelaresi, and P. Chatterjee. Small-scale magnetic helicity losses from a mean-field dynamo. *Month. Not. Roy. Astron. Soc.*, 398:1414–1422, 2009. 56

A. Brandenburg, P. Chatterjee, F. Del Sordo, A. Hubbard, P. J. Käpylä, and M. Rheinhardt. Turbulent transport in hydromagnetic flows. *Physica Scripta Volume T*, 142: 014028, 2010. 43

A. Brandenburg, K. Kemel, N. Kleeorin, D. Mitra, and I. Rogachevskii. Detection of Negative Effective Magnetic Pressure Instability in Turbulence Simulations. *Astrophys. J. Lett.*, 740:L50, 2011a. 40

A. Brandenburg, K. Subramanian, A. Balogh, and M. L. Goldstein. Scale Dependence of Magnetic Helicity in the Solar Wind. *Astrophys. J.*, 734:9, 2011b. 73

A. Brandenburg, D. Sokoloff, and K. Subramanian. Current Status of Turbulent Dynamo Theory. From Large-Scale to Small-Scale Dynamos. *Spa. Sci. Rev.*, 169: 123–157, 2012. 37

B. P. Brown, M. K. Browning, A. S. Brun, M. S. Miesch, and J. Toomre. Rapidly Rotating Suns and Active Nests of Convection. *Astrophys. J.*, 689:1354–1372, 2008. 45, 63

B. P. Brown, M. K. Browning, A. S. Brun, M. S. Miesch, and J. Toomre. Persistent Magnetic Wreaths in a Rapidly Rotating Sun. *Astrophys. J.*, 711:424–438, 2010. 45

B. P. Brown, M. S. Miesch, M. K. Browning, A. S. Brun, and J. Toomre. Magnetic Cycles in a Convective Dynamo Simulation of a Young Solar-type Star. *Astrophys. J.*, 731:69, 2011. 45, 64

A. S. Brun, M. S. Miesch, and J. Toomre. Global-Scale Turbulent Convection and Magnetic Dynamo Action in the Solar Envelope. *Astrophys. J.*, 614:1073–1098, 2004. 45, 63, 64

A. S. Brun, M. S. Miesch, and J. Toomre. Modeling the Dynamical Coupling of Solar Convection with the Radiative Interior. *Astrophys. J.*, 742:79, 2011. 47, 64, 67

P. Caligari, F. Moreno-Insertis, and M. Schussler. Emerging flux tubes in the solar convection zone. 1: Asymmetry, tilt, and emergence latitude. *Astrophys. J.*, 441: 886–902, 1995. 41

R. C. Carrington. Description of a Singular Appearance seen in the Sun on September 1, 1859. *Month. Not. Roy. Astron. Soc.*, 20:13–15, 1859. 49, 50

F. Cattaneo. On the origin of magnetic fields in the quiet photosphere. *Astrophys. J. Lett.*, 515:L39–L42, 1999. 44

F. Cattaneo and D. W. Hughes. Nonlinear saturation of the turbulent α effect. *Phys. Rev. Lett. E*, 54:4532, 1996. 36

P. Charbonneau. Dynamo Models of the Solar Cycle. *Living Reviews in Solar Physics*, 7:3, 2010. 31, 37, 41, 42

P. Charbonneau. *Solar and Stellar Dynamos*. Springer-Verlag Berlin Heidelberg, 2013. 37

P. F. Chen. Coronal Mass Ejections: Models and Their Observational Basis. *Living Reviews in Solar Physics*, 8:1, 2011. 49

M. C. M. Cheung, M. Schüssler, T. D. Tarbell, and A. M. Title. Solar Surface Emerging Flux Regions: A Comparative Study of Radiative MHD Modeling and Hinode SOT Observations. *Astrophys. J.*, 687:1373–1387, 2008. 41

A. R. Choudhuri. *The Physics of Fluids and Plasmas : An Introduction for Astrophysicists*. Cambridge University Press, 1998. 15

A. R. Choudhuri and P. A. Gilman. The influence of the Coriolis force on flux tubes rising through the solar convection zone. *Astrophys. J.*, 316:788–800, 1987. 42

E. W. Cliver, V. Boriakoff, and K. H. Bounar. The 22-year cycle of geomagnetic and solar wind activity. *J. Geophys. Res.*, 101:27091–27110, 1996. 10

F. Del Sordo, G. Guerrero, and A. Brandenburg. Turbulent dynamos with advective magnetic helicity flux. *Month. Not. Roy. Astron. Soc.*, 429:1686–1694, 2013. 36

E. Devlen, A. Brandenburg, and D. Mitra. A mean field dynamo from negative eddy diffusivity. *ArXiv:1212.2626*, 2012. 33

R. H. Dicke. Is there a chronometer hidden deep in the sun. *Nature*, 276:676–680, 1978. 9

M. Dikpati and J. L. Anderson. Evaluating Potential for Data Assimilation in a Flux-transport Dynamo Model by Assessing Sensitivity and Response to Meridional Flow Variation. *Astrophys. J.*, 756:20, 2012. 80

M. Dikpati and P. Charbonneau. A Babcock-Leighton Flux Transport Dynamo with Solar-like Differential Rotation. *Astrophys. J.*, 518:508–520, 1999. 39, 42

W. Dobler, M. Stix, and A. Brandenburg. Magnetic Field Generation in Fully Convective Rotating Spheres. *Astrophys. J.*, 638:336–347, 2006. 60

V. Domingo, B. Fleck, and A. I. Poland. The SOHO Mission: an Overview. *Solar Phys.*, 162:1–37, 1995. 49

Y. Fan and S. E. Gibson. Numerical Simulations of Three-dimensional Coronal Magnetic Fields Resulting from the Emergence of Twisted Magnetic Flux Tubes. *Astrophys. J.*, 609:1123–1133, 2004. 53, 80

Y. Fan and S. E. Gibson. Onset of Coronal Mass Ejections Due to Loss of Confinement of Coronal Flux Ropes. *Astrophys. J.*, 668:1232–1245, 2007. 53

F. Fang, W. Manchester, W. P. Abbett, and B. van der Holst. Simulation of Flux Emergence from the Convection Zone to the Corona. *Astrophys. J.*, 714:1649–1657, 2010. 42

J. Feynman and A. Ruzmaikin. The Sun's Strange Behavior: Maunder Minimum or Gleissberg Cycle? *Solar Phys.*, 272:351–363, 2011. 8

T. G. Forbes and E. R. Priest. Photospheric Magnetic Field Evolution and Eruptive Flares. *Astrophys. J.*, 446:377, 1995. 52

U. Frisch. *Turbulence. The legacy of A. N. Kolmogorov.* Cambridge University Press, 1995. 18, 19, 37

G. A. Gary. Linear force-free magnetic fields for solar extrapolation and interpretation. *Astrophys. J. Suppl.*, 69:323–348, 1989. 30

M. Ghizaru, P. Charbonneau, and P. K. Smolarkiewicz. Magnetic Cycles in Global Large-eddy Simulations of Solar Convection. *Astrophys. J. Lett.*, 715:L133–L137, 2010. 45

P. A. Gilman. Dynamically consistent nonlinear dynamos driven by convection in a rotating spherical shell. II - Dynamos with cycles and strong feedbacks. *Astrophys. J. Suppl.*, 53:243–268, 1983. 45

P. A. Gilman and J. Miller. Dynamically consistent nonlinear dynamos driven by convection in a rotating spherical shell. *Astrophys. J. Suppl.*, 46:211–238, 1981. 45

G. A. Glatzmaier. Numerical simulations of stellar convective dynamos. II - Field propagation in the convection zone. *Astrophys. J.*, 291:300–307, 1985. 45

W. Gleissberg. The recent maximum of the 80-year sunspot cycle. *Kleinheubacher Berichte*, 19:661–664, 1976. 8

B. Gudiksen and Å. Nordlund. An ab initio approach to the solar coronal heating problem. *Astrophys. J.*, 618:1020–1030, 2005a. 7, 13, 30

B. Gudiksen and Å. Nordlund. An ab initio approach to solar coronal loops. *Astrophys. J.*, 618:1031–1038, 2005b. 30

G. Guerrero and P. J. Käpylä. Dynamo action and magnetic buoyancy in convection simulations with vertical shear. *Astron. Astrophys.*, 533:A40, 2011. 42, 44

G. E. Hale. On the Probable Existence of a Magnetic Field in Sun-Spots. *Astrophys. J.*, 28:315, 1908. 8

G. E. Hale, F. Ellerman, S. B. Nicholson, and A. H. Joy. The Magnetic Polarity of Sun-Spots. *Astrophys. J.*, 49:153, 1919. 8, 9

S. M. Hanasoge, T. L. Duvall, and K. R. Sreenivasan. Anomalously weak solar convection. *Proceedings of the National Academy of Science*, 109:11928–11932, 2012. 76

R.A. Harrison. The nature of solar flares associated with coronal mass ejection. *Astron. Astrophys.*, 304:585, 1995. 49

J. W. Harvey, F. Hill, R. P. Hubbard, J. R. Kennedy, J. W. Leibacher, J. A. Pintar, P. A. Gilman, R. W. Noyes, A. M. Title, J. Toomre, R. K. Ulrich, A. Bhatnagar, J. A. Kennewell, W. Marquette, J. Patron, O. Saa, and E. Yasukawa. The Global Oscillation Network Group (GONG) Project. *Science*, 272:1284–1286, 1996. 3

D. H. Hathaway. The Sun's Shallow Meridional Circulation. *arXiv:1103.1561*, 2011. 4, 43

R. Hodgson. On a curious Appearance seen in the Sun. *Month. Not. Roy. Astron. Soc.*, 20:15–16, 1859. 49

L.L. House, W.J. Wagner, E. Hildner, C. Sawyer, and H.U. Schmidt. Studies of the corona with the solar maximum mission coronagraph/polarimeter. *Astrophys. J. Lett.*, 244:L117–L121, 1981. 50

A. Hubbard and A. Brandenburg. Magnetic helicity fluxes in an $\alpha 2$ dynamo embedded in a halo. *Geophysical and Astrophysical Fluid Dynamics*, 104:577–590, 2010. 74

A. Hubbard, F. Del Sordo, P. J. Käpylä, and A. Brandenburg. The α effect with imposed and dynamo-generated magnetic fields. *Month. Not. Roy. Astron. Soc.*, 398:1891–1899, 2009. 43

H.S. Hudson, L.W. Acton, and S.L. Freeland. A long-duration solar flare with mass ejection and global consequences. *Astrophys. J.*, 470:629, 1996. 51

R.M.E. Illing and A.J. Hundhausen. Observation of a coronal transient from 1.2 to 6 solar radii. *J. Geophys. Res.*, 90:275–282, 1985. 51, 70

H. Jeffrey. The stability of a layer of fluid heated below. *Phil. Mag.*, 2:833–844, 1926. 15

M. L. Kaiser, T. A. Kucera, J. M. Davila, O. C. St. Cyr, M. Guhathakurta, and E. Christian. The STEREO Mission: An Introduction. *Spa. Sci. Rev.*, 136:5–16, 2008. 50

P. J. Käpylä, M. J. Korpi, and I. Tuominen. Local models of stellar convection:. Reynolds stresses and turbulent heat transport. *Astron. Astrophys.*, 422:793–816, 2004. 47

P. J. Käpylä, M. J. Korpi, M. Ossendrijver, and M. Stix. Magnetoconvection and dynamo coefficients. III. α-effect and magnetic pumping in the rapid rotation regime. *Astron. Astrophys.*, 455:401–412, 2006a. 40, 43

P. J. Käpylä, M. J. Korpi, and I. Tuominen. Solar dynamo models with α-effect and turbulent pumping from local 3D convection calculations. *Astron. Nachr.*, 327:884, 2006b. 39, 40

P. J. Käpylä, M. J. Korpi, and A. Brandenburg. Large-scale dynamos in turbulent convection with shear. *Astron. Astrophys.*, 491:353–362, 2008. 44, 67

P. J. Käpylä, M. J. Korpi, A. Brandenburg, D. Mitra, and R. Tavakol. Convective dynamos in spherical wedge geometry. *Astron. Nachr.*, 331:73, 2010. 22, 45, 46, 60

P. J. Käpylä, M. J. Mantere, and A. Brandenburg. Effects of stratification in spherical shell convection. *Astron. Nachr.*, 332:883, 2011a. 61

P. J. Käpylä, M. J. Mantere, G. Guerrero, A. Brandenburg, and P. Chatterjee. Reynolds stress and heat flux in spherical shell convection. *Astron. Astrophys.*, 531:A162, 2011b. 46, 60, 67

P. J. Käpylä, M. J. Mantere, and A. Brandenburg. Cyclic Magnetic Activity due to Turbulent Convection in Spherical Wedge Geometry. *Astrophys. J. Lett.*, 755:L22, 2012. 46, 47, 61, 64, 65, 67, 79

B. B. Karak. Importance of Meridional Circulation in Flux Transport Dynamo: The Possibility of a Maunder-like Grand Minimum. *Astrophys. J.*, 724:1021–1029, 2010. 42

R. Kippenhahn. Differential Rotation in Stars with Convective Envelopes. *Astrophys. J.*, 137:664, 1963. 23

R. Kippenhahn and A. Weigert. *Stellar Structure and Evolution*. 1990. 23

L. L. Kitchatinov and M. V. Mazur. Stability and equilibrium of emerged magnetic flux. *Solar Phys.*, 191:325–340, 2000. 40

L. L. Kitchatinov and S. V. Olemskoy. Solar Dynamo Model with Diamagnetic Pumping and Nonlocal α-Effect. *Solar Phys.*, 276:3–17, 2012. 39

L. L. Kitchatinov and G. Rüdiger. Differential rotation in solar-type stars: revisiting the Taylor-number puzzle. *Astron. Astrophys.*, 299:446, 1995. 24

L. L. Kitchatinov and G. Rüdiger. Differential rotation and meridional flow in the solar convection zone and beneath. *Astron. Nachr.*, 326:379–385, 2005. 24, 47

N. I. Kleeorin and A. A. Ruzmaikin. Dynamics of the average turbulent helicity in a magnetic field. *Magnetohydrodynamics*, 18:116, 1982. 35

H. Köhler. Differential Rotation Caused by Anisotropic Turbulent Viscosity. *Solar Phys.*, 13:3–18, 1970. 24

A. G. Kosovichev and J. O. Stenflo. Tilt of emerging bipolar magnetic regions on the Sun. *Astrophys. J. Lett.*, 688:L115–L118, 2008. 43

F. Krause and K.-H. Rädler. *Mean-field Magnetohydrodynamics and Dynamo Theory*. Pergamon Press, Oxford, 1980. 32, 38

M. Küker and M. Stix. Differential rotation of the present and the pre-main-sequence Sun. *Astron. Astrophys.*, 366:668–675, 2001. 24

P. Lantos. Radiation doses received on-board aeroplanes during large solar flares. *Hvar Observatory Bulletin*, 27:171–178, 2003. 11

R.B. Leighton. Transport of magnetic fields on the sun. *Astrophys. J.*, 140:1547–1562, 1964. 41

R. H. Levine, M. Schulz, and E. N. Frazier. Simulation of the magnetic structure of the inner heliosphere by means of a non-spherical source surface. *Solar Phys.*, 77: 363–392, 1982. 59

Y. Li, J. G. Luhmann, B. J. Lynch, and E. K. J. Kilpua. Cyclic Reversal of Magnetic Cloud Poloidal Field. *Solar Phys.*, 270:331–346, 2011. 51, 72

J. H. Lienhard. *Synopsis of lift, drag, and vortex frequency data for rigid circular cylinders.* Washington State University, 1966. 18

B. C. Low. Coronal mass ejections and magnetic helicity. In J. J. Hunt, editor, *Solar Dynamic Phenomena and Solar Wind Consequences, the Third SOHO Workshop*, volume 373 of *ESA Special Publication*, page 123, 1994. 51

B. C. Low. Solar activity and the corona. *Solar Phys.*, 167:217–265, 1996. 51, 70

B. C. Low. Coronal mass ejections, flares, and prominences. In S. R. Habbal, R. Esser, J. V. Hollweg, and P. H. Isenberg, editors, *Solar Wind 9*, page 109. AIP CP471, 1999. 10

B. C. Low. Coronal mass ejections, magnetic flux ropes, and solar magnetism. *J. Geophys. Res.*, 106:25141–25164, 2001. 51

F.-J. Lübken, U. Berger, and G. Baumgarten. Stratospheric and solar cycle effects on long-term variability of mesospheric ice clouds. *J. Geophys. Res.*, 114:A11, 2009. 10

K.B. MacGregor and P. Charbonneau. Solar interface dynamos. i. linear, kinematic models in cartesian geometry. *Astrophys. J.*, 486:484–501, 1997. 39

H. Maehara, T. Shibayama, S. Notsu, Y. Notsu, T. Nagao, S. Kusaba, S. Honda, D. Nogami, and K. Shibata. Superflares on solar-type stars. *Nature*, 485:478–481, 2012. 50

W. H. Matthaeus, M. L. Goldstein, and C. Smith. Evaluation of magnetic helicity in homogeneous turbulence. *Phys. Rev. Lett.*, 48:1256–1259, 1982. 73

J. C. Maxwell. A dynamical theory of the electromagnetic field. *Royal Society Transactions*, 155:459–512, 1865. 27

M. Meneguzzi and A. Pouquet. Turbulent dynamos driven by convection. *Journal of Fluid Mechanics*, 205:297–318, 1989. 44

M. S. Miesch, A. S. Brun, and J. Toomre. Solar Differential Rotation Influenced by Latitudinal Entropy Variations in the Tachocline. *Astrophys. J.*, 641:618–625, 2006. 47, 64, 67

M. S. Miesch, N. A. Featherstone, M. Rempel, and R. Trampedach. On the Amplitude of Convective Velocities in the Deep Solar Interior. *Astrophys. J.*, 757:128, 2012. 43

Z. Mikic, D. C. Barnes, and D. D. Schnack. Dynamical evolution of a solar coronal magnetic field arcade. *Astrophys. J.*, 328:830–847, 1988. 59

D. Mitra, R. Tavakol, A. Brandenburg, and D. Moss. Turbulent Dynamos in Spherical Shell Segments of Varying Geometrical Extent. *Astrophys. J.*, 697:923–933, 2009. 57

D. Mitra, S. Candelaresi, P. Chatterjee, R. Tavakol, and A. Brandenburg. Equatorial magnetic helicity flux in simulations with different gauges. *Astron. Nachr.*, 331: 130, 2010a. 74

D. Mitra, R. Tavakol, P. J. Käpylä, and A. Brandenburg. Oscillatory Migrating Magnetic Fields in Helical Turbulence in Spherical Domains. *Astrophys. J. Lett.*, 719: L1–L4, 2010b. 45, 62

D. Mitra, D. Moss, R. Tavakol, and A. Brandenburg. Alleviating α quenching by solar wind and meridional flows. *Astron. Astrophys.*, 526:A138, 2011. 36

Y. Nakagawa and M. A. Raadu. On Practical Representation of Magnetic Field. *Solar Phys.*, 25:127–135, 1972. 30

N. J. Nelson, B. P. Brown, A. S. Brun, M. S. Miesch, and J. Toomre. Magnetic Wreaths and Cycles in Convective Dynamos. *Astrophys. J.*, 762:73, 2013. 45, 47, 63, 64, 67

Å. Nordlund, A. Brandenburg, R. L. Jennings, M. Rieutord, J. Ruokolainen, R. F. Stein, and I. Tuominen. Dynamo action in stratified convection with overshoot. *Astrophys. J.*, 392:647–652, 1992. 44

R. W. Noyes, L. W. Hartmann, S. L. Baliunas, D. K. Duncan, and A. H. Vaughan. Rotation, convection, and magnetic activity in lower main-sequence stars. *Astrophys. J.*, 279:763–777, 1984. 2

S. Ortolani and D. D. Schnack. *Magnetohydrodynamics of Plasma Relaxation*. World Scientific, 1993. 59

M. Ossendrijver. The solar dynamo. *Astron. Astrophys. Rev*, 11:287–367, 2003. 31, 37, 39, 41

M. Ossendrijver, M. Stix, A. Brandenburg, and G. Rüdiger. Magnetoconvection and dynamo coefficients. II. Field-direction dependent pumping of magnetic field. *Astron. Astrophys.*, 394:735–745, 2002. 40

E. Pariat, P. Démoulin, and M. A. Berger. Photospheric flux density of magnetic helicity. *Astron. Astrophys.*, 439:1191–1203, 2005. 57

E. N. Parker. Hydromagnetic Dynamo Models. *Astrophys. J.*, 122:293, 1955. 41

E.N. Parker. A solar dynamo surface wave at the interface between convection and nonuniform rotation. *Astrophys. J.*, 408:707–719, 1993. 39

W. D. Pesnell, B. J. Thompson, and P. C. Chamberlin. The Solar Dynamics Observatory (SDO). *Solar Phys.*, 275:3–15, 2012. 50

S. P. Plunkett, A. Vourlidas, S. Šimberová, M. Karlický, P. Kotrč, P. Heinzel, Y. A. Kupryakov, W. P. Guo, and S. T. Wu. Simultaneous SOHO and Ground-Based Observations of a Large Eruptive Prominence and Coronal Mass Ejection. *Solar Phys.*, 194:371–391, 2000. 51

J. Pomoell, R. Vainio, and R. Kissmann. MHD Modeling of Coronal Large-Amplitude Waves Related to CME Lift-off. *Solar Phys.*, 253:249–261, 2008. 54

A. Pouquet, U. Frisch, and J. Leorat. Strong MHD helical turbulence and the nonlinear dynamo effect. *Journal of Fluid Mechanics*, 77:321–354, 1976. 33, 34, 43

L. Prandtl. Aufgaben der Strömungsforschung. *Naturwissenschaften*, 14:335–338, 1926. 20

E. R. Priest and T. Forbes. *Magnetic reconnection: MHD theory and applications*. Cambridge University Press, 2000. 52

É. Racine, P. Charbonneau, M. Ghizaru, A. Bouchat, and P. K. Smolarkiewicz. On the Mode of Dynamo Action in a Global Large-eddy Simulation of Solar Convection. *Astrophys. J.*, 735:46, 2011. 45, 64, 79

S. Régnier, T. Amari, and E. Kersalé. 3D Coronal magnetic field from vector magnetograms: non-constant-alpha force-free configuration of the active region NOAA 8151. *Astron. Astrophys.*, 392:1119–1127, 2002. 51

R. Rosner and N. O. Weiss. The Origin of the Solar Cycle. In K. L. Harvey, editor, *The Solar Cycle*, volume 27 of *Astronomical Society of the Pacific Conference Series*, page 511, 1992. 9

I. I. Roussev, T. G. Forbes, T. I. Gombosi, I. V. Sokolov, D. L. DeZeeuw, and J. Birn. A Three-dimensional Flux Rope Model for Coronal Mass Ejections Based on a Loss of Equilibrium. *Astrophys. J. Lett.*, 588:L45–L48, 2003. 53

G. Rüdiger. *Differential Rotation and Stellar Convection. Sun and Solar-type Stars*. Akademie Verlag, Berlin, 1989. 19, 21, 24, 25

G. Rüdiger and A. Brandenburg. A solar dynamo in the overshoot layer: cycle period and butterfly diagram. *Astron. Astrophys.*, 296:557–566, 1995. 39

D. M. Rust. Spawning and shedding helical magnetic fields in the solar atmosphere. *Geophys. Res. Lett.*, 21:241–244, 1994. 51

S. H. Saar and A. Brandenburg. Time Evolution of the Magnetic Activity Cycle Period. II. Results for an Expanded Stellar Sample. *Astrophys. J.*, 524:295–310, 1999. 2

T. Sakurai. Calculation of force-free magnetic field with non-constant α. *Solar Phys.*, 69:343–359, 1981. 30

O. I. Savun and A. I. Sladkova. Calculation of the radiation doses absorbed from the solar flare of August 4, 1972 in a near-earth orbit. *Cosmic Research*, 14:422–426, 1976. 10

H. U. Schmidt. On the Observable Effects of Magnetic Energy Storage and Release Connected With Solar Flares. *NASA Special Publication*, 50:107, 1964. 29

J. Schou, H. M. Antia, S. Basu, R. S. Bogart, R. I. Bush, S. M. Chitre, J. Christensen-Dalsgaard, M. P. di Mauro, W. A. Dziembowski, A. Eff-Darwich, D. O. Gough, D. A. Haber, J. T. Hoeksema, R. Howe, S. G. Korzennik, A. G. Kosovichev, R. M. Larsen, F. P. Pijpers, P. H. Scherrer, T. Sekii, T. D. Tarbell, A. M. Title, M. J. Thompson, and J. Toomre. Helioseismic Studies of Differential Rotation in the Solar Envelope by the Solar Oscillations Investigation Using the Michelson Doppler Imager. *Astrophys. J.*, 505:390–417, 1998. 3

C. J. Schrijver and M. L. De Rosa. Photospheric and heliospheric magnetic fields. *Solar Phys.*, 212:165–200, 2003. 59

M. Schrinner, K.-H. Rädler, D. Schmitt, M. Rheinhardt, and U. R. Christensen. Mean-field concept and direct numerical simulations of rotating magnetoconvection and the geodynamo. *Geophys. Astrophys. Fluid Dyn.*, 101:81–116, 2007. 39, 43, 65, 79

M. Schwabe. Sonnenbeobachtungen im Jahre 1843. Von Herrn Hofrath Schwabe in Dessau. *Astron. Nachr.*, 21:233, 1844. 7

R. Schwenn. Space Weather: The Solar Perspective. *Living Reviews in Solar Physics*, 3:2, 2006. 12, 55

M. Semel and J. Rayrole. Étude Critique d'un Champ Current-Free dans l'Atmosphère Solaire. In K. O. Kiepenheuer, editor, *Structure and Development of Solar Active Regions*, volume 35 of *IAU Symposium*, page 134, 1968. 29

K. Shibata and T. Magara. Solar Flares: Magnetohydrodynamic Processes. *Living Reviews in Solar Physics*, 8:6, 2011. 49

E. A. Spiegel and N. O. Weiss. Magnetic activity and variations in solar luminosity. *Nature*, 287:616, 1980. 3, 39

H. C. Spruit. A model of the solar convection zone. *Solar Phys.*, 34:277–290, 1974. 20, 21

M. Steenbeck, F. Krause, and K.-H. Rädler. Berechnung der mittleren Lorentz-Feldstärke für ein elektrisch leitendes Medium in turbulenter, durch Coriolis-Kräfte beeinflußter Bewegung. *Zeitschrift Naturforschung Teil A*, 21:369, 1966. 33

R. F. Stein. Solar Surface Magneto-Convection. *Living Reviews in Solar Physics*, 9: 4, 2012. 44

R. F. Stein and Å. Nordlund. On the Formation of Active Regions. *Astrophys. J. Lett.*, 753:L13, 2012. 40

J. O. Stenflo and A. G. Kosovichev. Bipolar magnetic regions on the Sun: global analysis of the SOHO/MDI data set. *Astrophys. J.*, 745:129, 2012. 43

D. L. Stephens, Jr., L. W. Townsend, and J. L. Hoff. Interplanetary crew dose estimates for worst case solar particle events based on historical data for the Carrington flare of 1859. *Acta Astronautica*, 56:969–974, 2005. 11

M. Stix. *The sun: an introduction*. Springer, Berlin, 2002. 1, 15, 20, 22, 29, 37, 52

P. A. Sturrock. *Solar Flares*. Colorado Associated University Press, Boulder, 1980. 52

H. Svensmark and E. Friis-Christensen. Variation of cosmic ray flux and global cloud coverage-a missing link in solar-climate relationships. *Journal of Atmospheric and Solar-Terrestrial Physics*, 59:1225–1232, 1997. 10

J. K. Thalmann, B. Inhester, and T. Wiegelmann. Estimating the Relative Helicity of Coronal Magnetic Fields. *Solar Phys.*, 272:243–255, 2011. 57

M. J. Thompson, J. Toomre, E. R. Anderson, H. M. Antia, G. Berthomieu, D. Burtonclay, S. M. Chitre, J. Christensen-Dalsgaard, T. Corbard, M. De Rosa, C. R. Genovese, D. O. Gough, D. A. Haber, J. W. Harvey, F. Hill, R. Howe, S. G. Korzennik, A. G. Kosovichev, J. W. Leibacher, F. P. Pijpers, J. Provost, E. J. Rhodes, Jr., J. Schou, T. Sekii, P. B. Stark, and P. R. Wilson. Differential Rotation and Dynamics of the Solar Interior. *Science*, 272:1300–1305, 1996. 3

M. J. Thompson, J. Christensen-Dalsgaard, M. S. Miesch, and J. Toomre. The Internal Rotation of the Sun. *Ann. Rev. Astron. Astrophys.*, 41:599–643, 2003. 3, 67

W. T. Thompson, B. Kliem, and T. Török. 3D Reconstruction of a Rotating Erupting Prominence. *Solar Phys.*, 276:241–259, 2012. 51, 56

V. S. Titov and P. Démoulin. Basic topology of twisted magnetic configurations in solar flares. *Astron. Astrophys.*, 351:707–720, 1999. 52

T. Török and B. Kliem. Confined and Ejective Eruptions of Kink-unstable Flux Ropes. *Astrophys. J. Lett.*, 630:L97–L100, 2005. 52, 53

T. Török, B. Kliem, and V. S. Titov. Ideal kink instability of a magnetic loop equilibrium. *Astron. Astrophys.*, 413:L27–L30, 2004. 52

I. Tuominen and G. Rüdiger. Solar differential rotation as a multiparameter turbulence problem. *Astron. Astrophys.*, 217:217–228, 1989. 23, 24

J. Tuominen. On Stellar Envelopes. *Annals of the New York Academy of Sciences*, 41: 61–76, 1941. 4

S. I. Vainshtein and F. Cattaneo. Nonlinear restrictions on dynamo action. *Astrophys. J.*, 393:165–171, 1992. 36

S. I. Vainshtein and Y. B. Zel'dovich. Reviews of Topical Problems: Origin of Magnetic Fields in Astrophysics (Turbulent "Dynamo" Mechanisms). *Soviet Physics Uspekhi*, 15:159–172, 1972. 31

G. Valori, P. Démoulin, and E. Pariat. Comparing Values of the Relative Magnetic Helicity in Finite Volumes. *Solar Phys.*, 278:347–366, 2012. 57

E. Vitense. Die Wasserstoffkonvektionszone der Sonne. *Zeitschr. f. Astrophys.*, 32: 135, 1953. 20, 21

A. Vögler and M. Schüssler. A solar surface dynamo. *Astron. Astrophys.*, 465:L43–L46, 2007. 44

Y.-M. Wang and N. R. Sheeley, Jr. On the Topological Evolution of the Coronal Magnetic Field During the Solar Cycle. *Astrophys. J.*, 599:1404–1417, 2003. 9

J. Warnecke. Einfluss photosphärischer Bewegungen auf die Struktur der solaren Korona. *Master Thesis*, 2009. 52, 59

D. F. Webb and T. A. Howard. Coronal Mass Ejections: Observations. *Living Reviews in Solar Physics*, 9:3, 2012. 49

T. Wiegelmann. Optimization code with weighting function for the reconstruction of coronal magnetic fields. *Solar Phys.*, 219:87–108, 2004. 30

T. Wiegelmann. Nonlinear force-free modeling of the solar coronal magnetic field. *J. Geophys. Res.*, 113:A12, 2008. 30

R. C. Willson and H. S. Hudson. Solar luminosity variations in solar cycle 21. *Nature*, 332:810–812, 1988. 9

L. Woltjer. A Theorem on Force-Free Magnetic Fields. *Proceedings of the National Academy of Sciences of the United States of America*, 44:489–491, 1958. 30

I

A&A 523, A19 (2010)
DOI: 10.1051/0004-6361/201014287
© ESO 2010

Astronomy
&
Astrophysics

Surface appearance of dynamo-generated large-scale fields

J. Warnecke[1,2] and A. Brandenburg[1,2]

[1] Nordita, AlbaNova University Center, Roslagstullsbacken 23, 10691 Stockholm, Sweden
e-mail: `joern@nordita.org`
[2] Department of Astronomy, AlbaNova University Center, Stockholm University, 10691 Stockholm, Sweden

Received 19 February 2010 / Accepted 11 August 2010

ABSTRACT

Aims. Twisted magnetic fields are frequently seen to emerge above the visible surface of the Sun. This emergence is usually associated with the rise of buoyant magnetic flux structures. Here we ask how magnetic fields from a turbulent large-scale dynamo appear above the surface if there is no magnetic buoyancy.

Methods. The computational domain is split into two parts. In the lower part, which we refer to as the turbulence zone, the flow is driven by an assumed helical forcing function leading to dynamo action. Above this region, which we refer to as the exterior, a nearly force-free magnetic field is computed at each time step using the stress-and-relax method.

Results. Twisted arcade-like field structures are found to emerge in the exterior above the turbulence zone. Strong current sheets tend to form above the neutral line, where the vertical field component vanishes. Time series of the magnetic field structure show recurrent plasmoid ejections. The degree to which the exterior field is force free is estimated as the ratio of the dot product of current density and magnetic field strength to their respective rms values. This ratio reaches values of up to 95% in the exterior. A weak outward flow is driven by the residual Lorentz force.

Key words. magnetohydrodynamics (MHD) – turbulence – stars: magnetic field – Sun: dynamo –
Sun: coronal mass ejections (CMEs)

1. Introduction

The magnetic field at the visible surface of the Sun is known to take the form of bipolar regions. Above these magnetic concentrations the field continues in an arch-like fashion. These formations appear usually as twisted loop-like structures. These loops can be thought of as a continuation of more concentrated flux ropes in the bulk of the solar convection zone. However, this interpretation is problematic because we cannot be certain that the magnetic field in the Sun is generated in the form of flux ropes. Indeed, simulations of successful large-scale dynamos suggest that concentrated tube-like structures are more typical of the early kinematic stage, but in the final nonlinear stage the field becomes more space-filling (Brandenburg 2005; Käpylä et al. 2008). The idea that the dynamics of such tubes is governed by magnetic buoyancy is problematic too, because the solar convection zone is strongly stratified with concentrated downdrafts and broader upwellings. This leads to efficient downward pumping of magnetic field toward the bottom of the convection zone (Nordlund et al. 1992; Tobias et al. 1998). This downward pumping is generally found to dominate over magnetic buoyancy. The question then emerges whether magnetic buoyancy can still be invoked as the main mechanism for causing magnetic flux emergence at the solar surface. Another possible mechanism for the emergence of magnetic field at the solar surface might simply be the relaxation of a strongly twisted magnetic field in the bulk of the convection zone. Twisted magnetic fields are produced by a large-scale dynamo mechanism that is generally believed to be the motor of solar activity (Parker 1979). One such dynamo mechanism is the α effect that produces a large-scale poloidal magnetic field from a toroidal one. However, this mechanism is known to produce magnetic fields of opposite helicity (Seehafer 1996; Ji 1999). This magnetic helicity of opposite sign is an unwanted by-product, because it quenches the dynamo effect (Pouquet et al. 1976). A commonly discussed remedy is therefore to allow the helicity of small-scale field to leave the domain, possibly in the form of coronal mass ejections (Blackman & Brandenburg 2003).

In order to study the emergence of helical magnetic fields from a dynamo, we consider a model that combines a direct simulation of a turbulent large-scale dynamo with a simple treatment of the evolution of nearly force-free magnetic fields above the surface of the dynamo. An additional benefit of such a study is that it alleviates the need for adopting a boundary condition for the magnetic field at the top of the dynamo region. This is important, because it is known that the properties of the generated large-scale magnetic field strongly depend on boundary conditions. A common choice for the outer boundary condition is to assume that the magnetic field can be matched smoothly to a potential field. Such a condition is relatively easily implemented in calculations employing spherical harmonic functions (see, e.g., Krause & Rädler 1980). A more realistic boundary condition might be an extrapolation to a force-free magnetic field where the Lorentz force vanishes in the exterior. This means that the current density is proportional to the local magnetic field, but the constant of proportionality depends generally on the magnetic field itself. This renders the magnetic boundary condition nonlinear, which is therefore not easy to implement. Moreover, a perfectly force-free magnetic field is not completely realistic either. Instead, we know that above the solar surface, magnetic fields drive flares and coronal mass ejections through the Lorentz force. A more comprehensive approach would be to include in the calculations the exterior regions above the solar or stellar surface. This can be computationally prohibitive and a realistic treatment of that region may not even be necessary. It may therefore make sense to look for simplifying alternatives. One possibility is therefore to attempt an iteration toward a nearly force-free magnetic field such that the field can deviate from a force-free state locally in regions where the field cannot easily be made force-free. This could be done by solving the induction equation with an additional ambipolar diffusion term, which implies the presence of an effective velocity correction proportional to the local Lorentz force. This is sometimes called the magneto-frictional method and has been introduced by Yang et al. (1986) and Klimchuk & Sturrock (1992). In this approach the electromotive force attains not only a term in the direction of $\boldsymbol{B}$, but also a term in the direction of $\boldsymbol{J}$ (Brandenburg & Zweibel 1994). The latter corresponds to a diffusion term, which explains the diffusive aspects of this effect. However, the resulting ambipolar diffusivity coefficient is proportional to $\boldsymbol{B}^2$ and can locally become so large that the computational time step becomes significantly reduced. This is a typical problem of parabolic equations. A better method is therefore to turn the problem into a hyperbolic one and to solve an additional evolution equation for the velocity correction where the driving force is the Lorentz force. This approach is sometimes called the "force-free model" (FFM), even though the field in this model is never exactly force-free anywhere (Mikić et al. 1988; Ortolani & Schnack 1993). In the context of force-free magnetic field extrapolations this method is also known as the stress-and-relax method (Valori et al. 2005).

2. Equations for the force-free model

The equation for the velocity correction in the force-free model (FFM) is similar to the usual momentum equation, except that there is no pressure, gravity, or other driving forces on the right-hand side. Thus, we just have

$$\frac{\mathrm{D}\boldsymbol{U}}{\mathrm{D}t} = \boldsymbol{J}\times\boldsymbol{B}/\rho + \boldsymbol{F}_{\rm visc}, \qquad (1)$$

where $\boldsymbol{J}\times\boldsymbol{B}$ is the Lorentz force, $\boldsymbol{J} = \boldsymbol{\nabla}\times\boldsymbol{B}/\mu_0$ is the current density, μ_0 is the vacuum permeability, $\boldsymbol{F}_{\rm visc}$ is the viscous force, and ρ is here treated as a constant corresponding to a prescribed density. Equation (1) is solved together with the induction equation. In order to preserve $\boldsymbol{\nabla}\cdot\boldsymbol{B} = 0$, we write $\boldsymbol{B} = \boldsymbol{\nabla}\times\boldsymbol{A}$ in terms of the vector potential $\boldsymbol{A}$ and solve the induction equation in the form

$$\frac{\partial\boldsymbol{A}}{\partial t} = \boldsymbol{U}\times\boldsymbol{B} + \eta\nabla^2\boldsymbol{A}, \qquad (2)$$

where we have adopted the so-called resistive gauge in which the electrostatic potential is equal to $-\eta\boldsymbol{\nabla}\cdot\boldsymbol{A}$ and the magnetic diffusivity η is assumed constant. The value of η will be given in terms of the magnetic Reynolds number, whose value will be specified below. No continuity equation for ρ is solved in this part of the domain, because there is no pressure gradient in the momentum equation.

In the following we couple such a model for the magnetic field above the solar photosphere to a simulation of a large-scale dynamo. In order to keep matters simple, we restrict ourselves to the case of an isothermal equation of state with constant sound speed $c_{\rm s}$. Our goal is then to analyze the appearance of the resulting magnetic field above the surface of the dynamo and to study also the effects on the dynamo itself.

3. The model

The idea is to combine the evolution equations for the dynamo interior with those of the region above by simply turning off those terms that are not to be included in the upper part of the domain. We do this with error function profiles of the form

$$\theta_w(z) = \tfrac{1}{2}\left(1 - \mathrm{erf}\frac{z}{w}\right), \qquad (3)$$

where w is the width of the transition. Thus, the momentum equation is assumed to take the form

$$\frac{\mathrm{D}\boldsymbol{U}}{\mathrm{D}t} = \theta_w(z)\,(-\boldsymbol{\nabla}h + \boldsymbol{f}) + \boldsymbol{J}\times\boldsymbol{B}/\rho + \boldsymbol{F}_{\rm visc}, \qquad (4)$$

where $\boldsymbol{F}_{\rm visc} = \rho^{-1}\boldsymbol{\nabla}\cdot(2\rho\nu\mathsf{S})$ is the viscous force, $\mathsf{S}_{ij} = \frac{1}{2}(U_{i,j} + U_{j,i}) - \frac{1}{3}\delta_{ij}\boldsymbol{\nabla}\cdot\boldsymbol{U}$ is the traceless rate-of-strain tensor, commas denote partial differentiation, $h = c_{\rm s}^2\ln\rho$ is the specific pseudo-enthalpy, $c_{\rm s}$ = const is the isothermal sound speed, and $\boldsymbol{f}$ is a forcing function that drives turbulence in the interior. The pseudo-enthalpy term emerges from the fact that for an isothermal equation of state the pressure is given by $p = c_{\rm s}^2\rho$, so the pressure gradient force is given by $\rho^{-1}\boldsymbol{\nabla}p = c_{\rm s}^2\boldsymbol{\nabla}\ln\rho = \boldsymbol{\nabla}h$. The continuity equation can either be written in terms of h

$$\frac{\mathrm{D}h}{\mathrm{D}t} = -c_{\rm s}^2\theta_w(z)\boldsymbol{\nabla}\cdot\boldsymbol{U}, \qquad (5)$$

where we have inserted the $\theta_w(z)$ factor to terminate the evolution of h in the exterior, or in terms of ρ,

$$\frac{\partial\rho}{\partial t} = -\boldsymbol{\nabla}\cdot\left[\theta_w(z)\,\rho\boldsymbol{U}\right], \qquad (6)$$

which serves the same purpose, but also preserves total mass. Most of the runs presented below are carried out using Eq. (5), but comparisons using Eq. (6) resulted in rather similar behavior.

The forcing function consists of random plane helical transversal waves with wavenumbers that lie in a band around an average forcing wavenumber $k_{\rm f}$. These waves are maximally helical with $\boldsymbol{\nabla}\times\boldsymbol{f} \approx k_{\rm f}\boldsymbol{f}$, so the helicity is positive. This type of forcing was also adopted in Brandenburg (2001) and many other recent papers. The profile function $\theta_w(z)$ in front of the forcing term restricts the occurrence of turbulence mostly to the dynamo region, $z < 0$. The forcing amplitude is chosen such that the rms velocity in this region, $u_{\rm rms}$, is about 4% of the sound speed.

We adopt non-dimensional units by measuring density in units of the initially constant density ρ_0, velocity in units of $c_{\rm s}$, and length in units of k_1^{-1}, where $k_1 = 2\pi/L_x$ is the minimal wavenumber in the x direction with an extent L_x. In most of the cases reported below, the vertical extent is $L_{z1} \leq z \leq L_{z2}$ with $L_{z1} = -L_x/3$ and $L_{z2} = 2L_x/3$. In a few cases we shall consider larger domains where the domain is two or four times larger in the z direction than in the horizontal directions. The extent of the domain in the y direction is $L_y = L_x$. We adopt periodic boundary conditions in the x and y directions. For the velocity we employ stress-free boundary conditions at top and bottom, i.e.

$$U_{x,z} = U_{y,z} = U_z = 0 \quad \text{on} \quad z = L_{z1}, L_{z2}, \qquad (7)$$

for the magnetic field we adopt perfect conductor boundary conditions at the bottom, which corresponds to

$$A_x = A_y = A_{z,z} = 0 \quad \text{on} \quad z = L_{z1}, \qquad (8)$$

and vertical-field or pseudo-vacuum conditions at the top, i.e.,

$$A_{x,z} = A_{y,z} = A_z = 0 \quad \text{on} \quad z = L_{z2}. \qquad (9)$$

Note that no mass is allowed to escape at the top. Although this restriction does not seem to affect the results of our simulations significantly, it might be useful to adopt in future applications outflow boundary conditions instead.

Our model is characterized by several dimensionless parameters. Of particular importance is the magnetic Reynolds number,

$$\mathrm{Re_M} = u_{\rm rms}/\eta k_{\rm f}, \tag{10}$$

where $k_{\rm f}$ is the wavenumber of the energy-carrying eddies. The ratio of viscosity to magnetic diffusivity is the magnetic Prandtl number, $\mathrm{Pr_M} = \nu/\eta$. In most of our simulations we use $\mathrm{Pr_M} = 1$. The typical forcing wavenumber, expressed in units of the box wavenumber, $k_{\rm f}/k_1$, is another important input parameter. In our simulations this value is 10. For the profile functions we take a transition width w with $k_1 w = 0.1$ in most of the runs, but in some cases it is 0.2. The magnetic field is expressed in terms of the equipartition value, $B_{\rm eq}$, where $B_{\rm eq}^2 = \mu_0\langle\rho\boldsymbol{u}^2\rangle$, and the average is taken over the turbulence zone. We measure time in non-dimensional units $\tau = t u_{\rm rms} k_{\rm f}$, which is the time normalized to the eddy turnover time of the turbulence. As initial condition we choose a hydrostatic state, $\boldsymbol{U} = \boldsymbol{0}$, with constant density $\rho = \rho_0$, and the components of the magnetic vector potential are random white noise in space with Gaussian statistics and low amplitude (10^{-4} below equipartition).

In this paper we present both direct numerical simulations and mean-field calculations. In both cases we use the Pencil Code[1], which is a modular high-order code (sixth order in space and third-order in time) for solving a large range of different partial differential equations.

4. Results

We begin by considering first hydrodynamic and hydromagnetic properties of the model. In the turbulence zone the velocity reaches quickly a statistically steady value, while in the exterior it takes about 1000 turnover times before a statistically steady state is reached. This is seen in Fig. 1, where we show $u_{\rm rms}(z)$ at different times. In the following we discuss the properties of the magnetic field that is generated by the turbulence.

4.1. Dynamo saturation

Dynamo action is possible when $\mathrm{Re_M}$ reaches a critical value $\mathrm{Re_M^{crit}}$ that is about 0.5 in our case. The situation is only slightly modified compared with dynamo saturation in a periodic domain. For not too large values of $\mathrm{Re_M}$ the dynamo saturates relatively swiftly, but for larger values of $\mathrm{Re_M}$ the magnetic field strength may decline with increasing value of $\mathrm{Re_M}$ (Brandenburg & Subramanian 2005). An example of the saturation behavior is shown in Fig. 2, where $\mathrm{Re_M} \approx 3.4$. The initial saturation phase ($100 \le \tau \le 500$) is suggestive of the resistively slow saturation found for periodic domains (Brandenburg 2001), but then the field declines somewhat. Such a decline is not normally seen in periodic domains, but is typical of dynamo action in domains with open boundaries or an external halo (see Fig. 5 of Hubbard & Brandenburg 2010a). The field strength is about 78% of the equipartition field strength, $B_{\rm eq}$.

In all cases the magnetic field is strongest in the turbulence zone, but it always shows a systematic variation in one of the two horizontal directions. It is a matter of chance whether this variation is in the x or in the y direction. Comparison of different runs shows that both directions are about equally possible (see below). Also, the magnetic field pattern shows sometimes a slow horizontal migration, but this too seems to be a matter of chance, as will be discussed below.

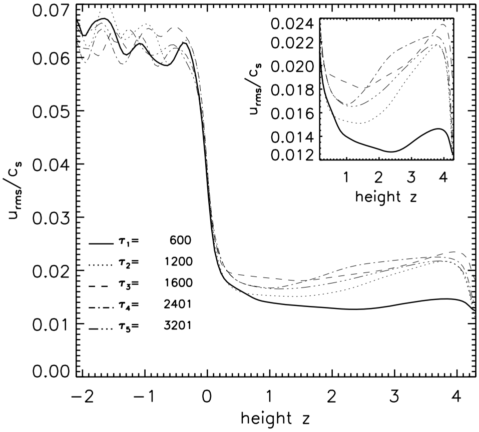

Fig. 1. Vertical dependence of the rms velocity at different times. Note the drop of $u_{\rm rms}(z)$ from the turbulence zone to the exterior by a factor of about 3−5. The inset shows $u_{\rm rms}(z)$ in the exterior at different times.

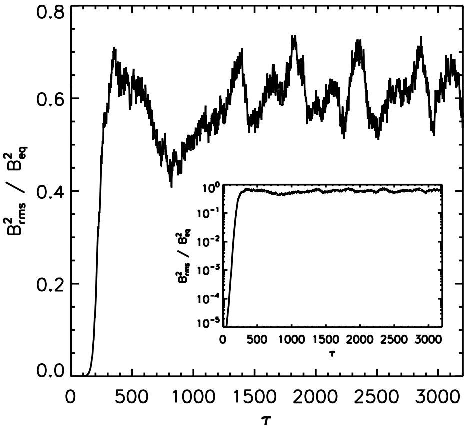

Fig. 2. Initial exponential growth and subsequent saturation behavior of the magnetic field in the interior for forced turbulence with dynamo action.

4.2. Arcade formation

After some time the magnetic field extends well into the exterior regions where it tends to produce an arcade-like structure, as seen in Figs. 3 and 4. The arcade opens up in the middle above the line where the vertical field component vanishes at the surface. This leads to the formation of anti-aligned field lines with a current sheet in the middle; see Figs. 3 and 4. The dynamical evolution is seen clearly in a sequence of field line images

---

[1] `http://pencil-code.googlecode.com`

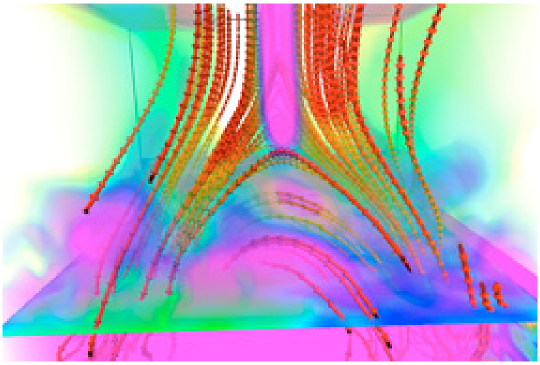

Fig. 3. Magnetic field structure in the dynamo exterior at $\tau = 1601$. Field lines are shown in red and the modulus of the current density is shown in pink with semi-transparent opacity. Note the formation of a vertical current sheet above the arcade.

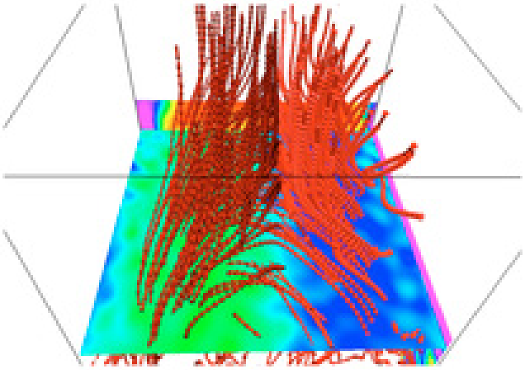

Fig. 4. Structure of magnetic field lines in the exterior, together with a representation of the normal component of the field at the interface at $z = 0$ between turbulence zone and exterior at $\tau = 1601$. Green represents a positive and blue a negative value of B_z.

in Fig. 5 where anti-aligned vertical field lines reconnect above the neutral line and form a closed arch with plasmoid ejection above. This arch then changes its connectivity at the foot points in the sideways direction (here the y direction), making the field lines bulge upward to produce a new reconnection site with anti-aligned field lines some distance above the surface. Note that this sideways motion takes the form of a slowly propagating wave. However, it is a matter of chance whether this wave propagates in the positive or negative coordinate direction, as will be shown below in Sect. 4.4.

Field line reconnection is best seen for two-dimensional magnetic fields, because it is then possible to compute a flux function whose contours correspond to field lines in the corresponding plane. In the present case the magnetic field varies only little in the x direction, so it makes sense to visualize the field averaged in the x direction. Since the averaging commutes with the curl operator, we can also average the x component of the magnetic vector potential, i.e. we compute $\langle A_x\rangle_x$, where the second subscript indicates averaging along the x direction. This function corresponds then to the flux function of the magnetic field in the yz plane and averaged along the x direction. In Fig. 6 we plot contours of $\langle A_x\rangle_x$, which correspond to poloidal field lines of $\langle \boldsymbol{B}\rangle_x$ in the yz plane. This figure shows clearly the recurrent reconnection events with subsequent plasmoid ejection. We also compare with a color/grey scale representation of the x component of the x-averaged magnetic field, $\langle B_x\rangle_x$. Note that in the exterior the contours of $\langle B_x\rangle_x$ trace nearly perfectly those of $\langle A_x\rangle_x$. This suggests that the x-averaged magnetic field has nearly maximal magnetic helicity in the exterior. This is also in agreement with other indicators that will be considered below.

4.3. Averaged field properties

The magnetic field is largely confined to the turbulence zone where it shows a periodic, nearly sinusoidal variation in the y direction. Away from the turbulence zone the field falls off, as can be seen from the vertical slice shown in Fig. 7. Near the top boundary, some components of the field become stronger again, but this is probably an artifact of the vertical field condition employed in this particular case.

In order to describe the vertical variation of the magnetic field in an effective manner, it is appropriate to Fourier-decompose the field in the two horizontal directions and to define a complex-valued mean field as

$$\overline{B}_i^{lm}(z,t) = \int\!\!\int \frac{\mathrm{d}x\,\mathrm{d}y}{L_x\,L_y}\boldsymbol{B}(x,y,z,t)\,\mathrm{e}^{2\pi\mathrm{i}(lx/L_x+my/L_y)}, \tag{11}$$

where superscripts l and m indicate a suitable Fourier mode. In Fig. 8 we plot absolute values of the three components of $\overline{\boldsymbol{B}}^{01}(z,t)$ as a function of z for a time representing the final saturated state. This figure shows quite clearly a relatively rapid decline of $|\overline{B}_y|$ with z, while $|\overline{B}_x|$ and $|\overline{B}_z|$ level off at values that are still about 40% of that in the turbulence zone. This suggests that our model is suitable to describe the evolution of magnetic fields in the dynamo exterior. Earlier simulations of coronal loops and coronal heating (Gudiksen & Nordlund 2002, 2005; Peter et al. 2004) demonstrate that the dynamics of such fields is controlled by the velocity properties at their footpoints, which is here the interface between the turbulence zone and the dynamo exterior.

4.4. Force-free versus current free

Already the straightforward inspection of magnetic field lines viewed from the top suggests that the magnetic field is twisted and forms a left-handed spiral; see Fig. 9. This is indeed the orientation expected for turbulence with positive kinetic helicity, producing a negative α effect and hence magnetic spirals with negative helicity at the scale of the domain.

We expect the magnetic field in the dynamo exterior to be nearly force free, i.e., we expect $\langle(\boldsymbol{J}\times\boldsymbol{B})^2\rangle_\mathrm{H}$ to be small compared with $\langle\boldsymbol{B}^2\rangle_\mathrm{H}\langle\boldsymbol{J}^2\rangle_\mathrm{H}$. Here, $\langle\cdot\rangle_\mathrm{H}$ denotes an xy average. In order to characterize the degree to which this is the case, we define the quantities

$$k_{J\times B}^2 = \mu_0^2\frac{\langle(\boldsymbol{J}\times\boldsymbol{B})^2\rangle_\mathrm{H}}{\langle\boldsymbol{B}^4\rangle_\mathrm{H}}, \quad k_{J\cdot B}^2 = \mu_0^2\frac{\langle(\boldsymbol{J}\cdot\boldsymbol{B})^2\rangle_\mathrm{H}}{\langle\boldsymbol{B}^4\rangle_\mathrm{H}}, \tag{12}$$

and note that

$$\frac{k_{J\times B}^2}{k_{JB}^2} + \frac{k_{J\cdot B}^2}{k_{JB}^2} = 1, \tag{13}$$

with $k_{JB}^2 = \mu_0^2\langle\boldsymbol{J}^2\rangle_\mathrm{H}/\langle\boldsymbol{B}^2\rangle_\mathrm{H}$. In Fig. 10 we show $k_{J\times B}^2$ and $k_{J\cdot B}^2$ as functions of z. Given that $k_{J\times B}^2/k_{JB}^2$ has values below 0.1, it is

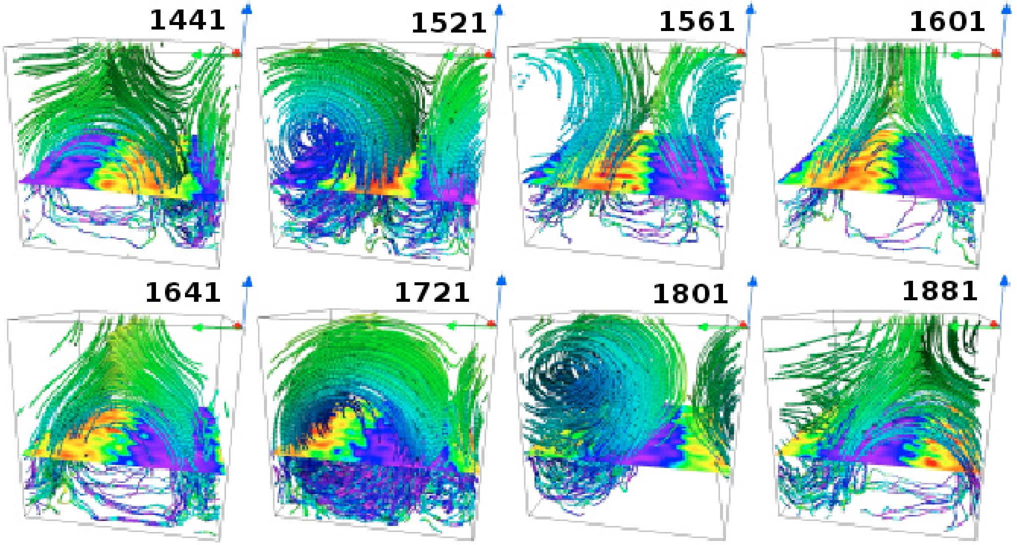

Fig. 5. Time series of arcade formation and decay. Field lines are colored by their local field strength which increases from pink to green. The plane shows B_z increasing from red (positive) to pink (negative). The normalized time τ is giving in each panel.

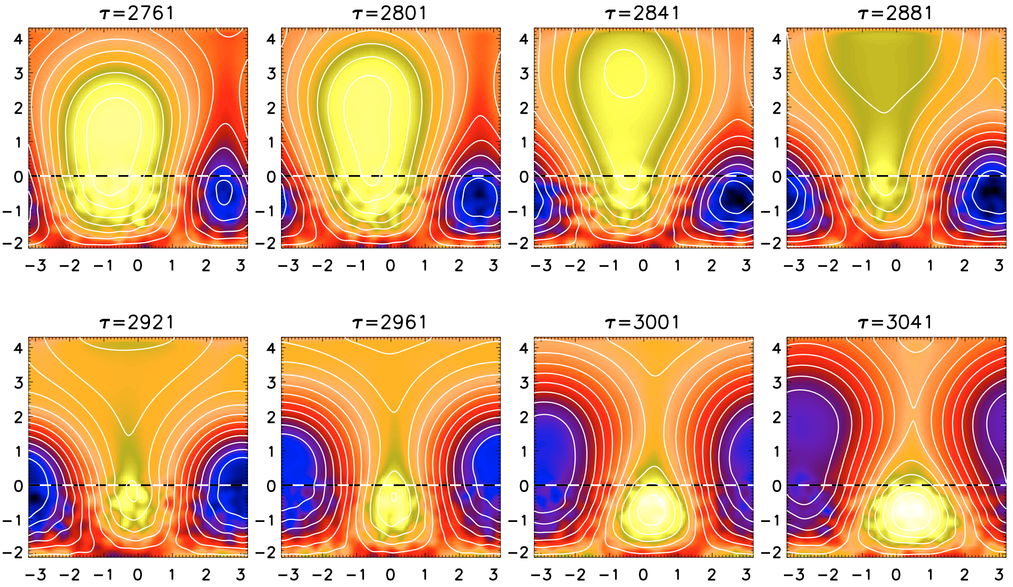

Fig. 6. Time series of the formation of a plasmoid ejection. Contours of $\langle A_x\rangle_x$ are shown together with a color-scale representation of $\langle B_x\rangle_x$; dark blue stands for negative and red for positive values. The contours of $\langle A_x\rangle_x$ correspond to field lines of $\langle \boldsymbol{B}\rangle_x$ in the yz plane. The dotted horizontal lines show the location of the surface at $z = 0$.

evident that the field is indeed nearly force free in the exterior. In the turbulence zone, on the other hand, the Lorentz force is quite significant.

To prove the existence of a force-free structure, it is convenient to calculate the angle χ between $\boldsymbol{J}$ and $\boldsymbol{B}$. We expect χ to be 0 or π for an ideal force-free environment. In Fig. 11 we show the distribution of values of χ plotted over the height z. One sees that, in the exterior, the angle χ is close to π, but it drops to $\pi/2$ at the very upper part, where the normal field condition enforces that $\boldsymbol{J}$ and $\boldsymbol{B}$ are at right angles to each other.

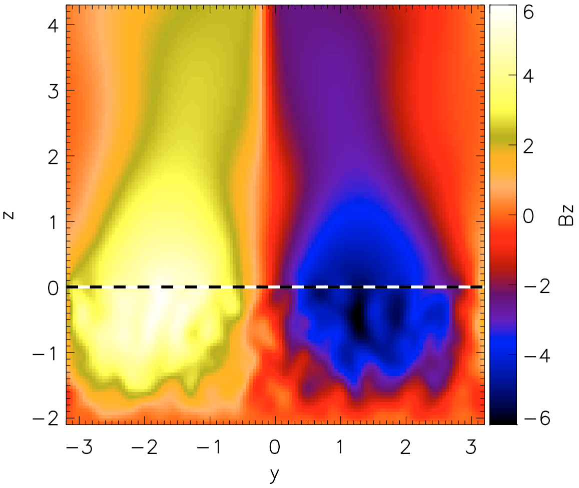

Fig. 7. Slice of B_z through an arbitrarily chosen cross-section x = const. Note the periodicity with nearly sinusoidal variation in the y direction, and the more nearly monotonous fall-off in the z direction.

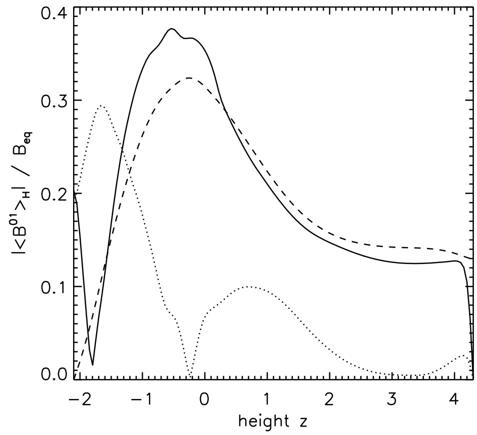

Fig. 8. Vertical dependence of the moduli of the components of $\overline{\boldsymbol{B}}$, as defined in Eq. (11).

In order to demonstrate that plasmoid ejection is a recurrent phenomenon, it is convenient to look at the evolution of the ratio $\langle \boldsymbol{J} \cdot \boldsymbol{B} \rangle_{\mathrm{H}} / \langle \boldsymbol{B}^2 \rangle_{\mathrm{H}}$ versus τ and z. This is done in Fig. 12 for $L_z = 6.4$ and $\mathrm{Re_M} = 3.4$ (Run A) and in Fig. 13 for $L_z = 8\pi$ and $\mathrm{Re_M} = 6.7$ (Run B1). It turns out that in both cases the typical speed of plasmoid ejecta is about 1/2 of the rms velocity of the turbulence in the interior region. However, the time interval $\delta\tau$ between plasmoid ejections increases from ≈250 to ≈570 turnover times as we increase the kinetic and magnetic Reynolds numbers. At higher magnetic Reynolds numbers, the length of the interval increases to ≈800 turnover times. A summary of all runs is given in Table 1. Here we also give the l and m values of the leading mode of the mean field in Eq. (11) and indicate explicitly whether the large-scale magnetic field varies in the x or the y direction. Indeed, both directions are possible, confirming that it is a matter of chance. In most cases the magnetic field pattern shows a slow horizontal migration, whose direction appears

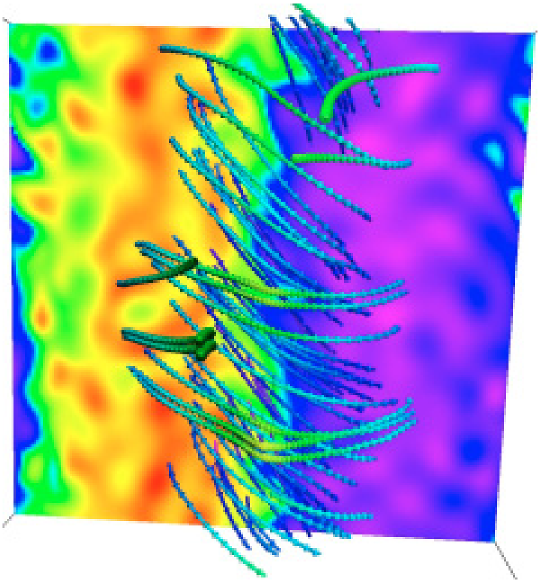

Fig. 9. Three-dimensional visualization of the magnetic field viewed from above. The vertical magnetic field component is color-coded (yellow pointing upward and blue pointing downward). Note that the field lines form a left-handed spiral over the scale of the domain, as expected for turbulence with positive helicity at small scales.

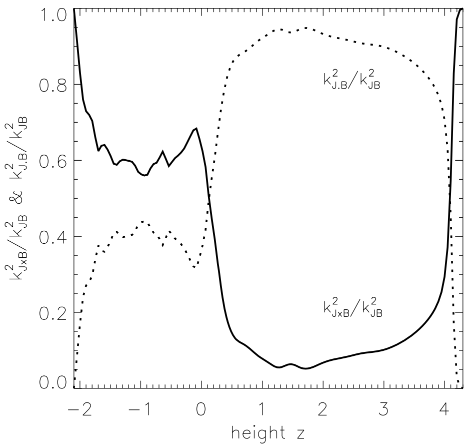

Fig. 10. Vertical dependence of $k_{J\times B}^2/k_{JB}^2$ and $k_{J\cdot B}^2/k_{JB}^2$. Note the decline of the normalized Lorentz force from more than 60% in the turbulence zone to less than 10% in the exterior.

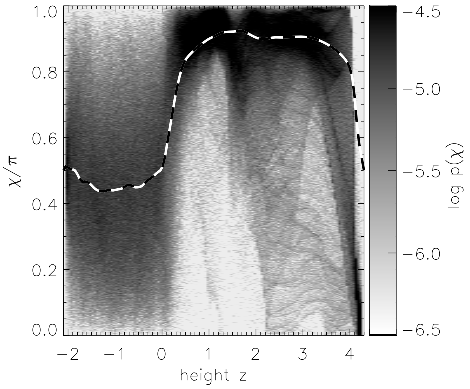

Fig. 11. Two-dimensional histogram of the distribution of angles, $p(\chi)$, where $\chi = \arccos(\boldsymbol{J} \cdot \boldsymbol{B})$ is the angle between $\boldsymbol{J}$ and $\boldsymbol{B}$ at different heights. $p(\chi)$ is normalized such that $\int p(\chi)\mathrm{d}\chi = 1$. The dashed line gives the location of the maximum position of the distribution.

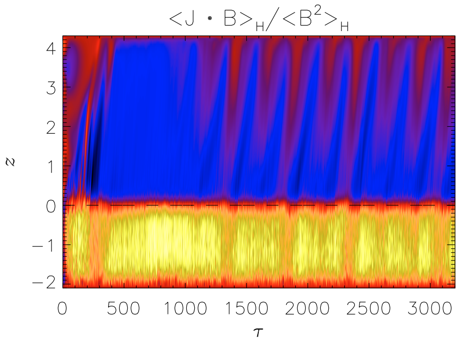

Fig. 12. Dependence of $\langle \boldsymbol{J} \cdot \boldsymbol{B}\rangle_{\rm H}/\langle \boldsymbol{B}^2\rangle_{\rm H}$ versus time τ and height z for $L_z = 6.4$ with $\mathrm{Re_M} = 3.4$ (Run A).

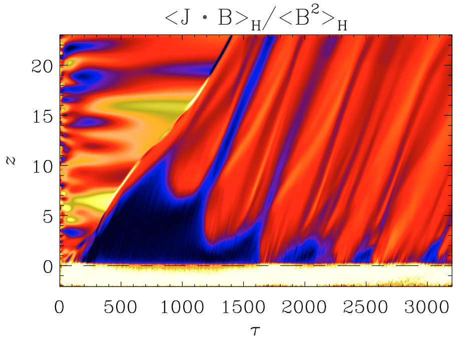

Fig. 13. Similar to Fig. 12, but for $L_z = 8\pi$ and $\mathrm{Re_M} = 6.7$ (Run B1).

to be random. The sign in the table indicates whether the wave migrates in the positive or negative coordinate direction.

4.5. Interpretation in terms of a mean-field model

The magnetic field found in the simulations displays a clear large-scale structure. One may have expected that the magnetic field varies mainly in the z direction, because this is also the direction in which the various profile functions vary. However, this is not the case. Instead, the main variation is in one of the horizontal directions (see Fig. 7, where the field varies mainly in the y direction). The magnetic field does of course also vary in the z direction, but this happens without sign change in $\overline{B}_z$. Above the surface at $z = 0$, the field gradually decays and retains only rather smooth variations.

In order to compare with dynamo theory, we now solve the usual set of mean-field equations for the mean magnetic vector potential $\overline{\boldsymbol{A}}$, where $\overline{\boldsymbol{B}} = \boldsymbol{\nabla} \times \overline{\boldsymbol{A}}$ is the mean magnetic field and $\overline{\boldsymbol{J}} = \boldsymbol{\nabla} \times \overline{\boldsymbol{B}}/\mu_0$ is the mean current density,

$$\frac{\partial \overline{\boldsymbol{A}}}{\partial t} = \alpha \overline{\boldsymbol{B}} - (\eta_{\rm t} + \eta)\mu_0 \overline{\boldsymbol{J}}. \tag{14}$$

We recall that $\eta =$ const is the microscopic magnetic diffusivity, which is not negligible, even though it is usually much smaller than $\eta_{\rm t}$. We consider first the kinematic regime where α and $\eta_{\rm t}$ are independent of $\overline{\boldsymbol{B}}$. In order to account for the fact that there is no turbulence above the turbulence zone, we adopt the profile $\theta_w(z)$ for α and $\eta_{\rm t}$, i.e., we write

$$\alpha(z) = \alpha_0\theta_w(z), \quad \eta_{\rm t}(z) = \eta_{\rm t0}\theta_w(z), \tag{15}$$

where α_0 and $\eta_{\rm t0}$ are constants, and for w we take the same value as for the other profile functions used in the direct simulations. The excitation condition for the dynamo can be quantified in terms of a dynamo number that we define here as

$$C_\alpha = \alpha_0/\eta_{\rm T0}k_1, \tag{16}$$

where $\eta_{\rm T0} = \eta_{\rm t0} + \eta$ is the total magnetic diffusivity and k_1 was defined in Sect. 3 as the smallest horizontal wavenumber that fits into the domain. If the turbulence zone were homogeneous and periodic in the z direction, the critical value of C_α is unity, but now the domain is open in the z direction, so one expects the dynamo to be harder to excite. In the models presented below we therefore adopt the value $C_\alpha = 2.5$, which is also compatible with estimates of the critical value from the simulations, if we write $\alpha \approx u_{\rm rms}/3$ and $\eta_{\rm t} \approx u_{\rm rms}/3k_{\rm f}$.

Next, we consider the nonlinear regime by employing the dynamical quenching model (Kleeorin & Ruzmaikin 1982; Blackman & Brandenburg 2002). We assume that $\alpha = \alpha_{\rm K} + \alpha_{\rm M}$, where now $\alpha_{\rm K}(z) = \alpha_0\theta_w(z)$ is the kinetic α effect profile used earlier in the solution to the kinematic equations, and $\alpha_{\rm M}$ is the solution to the dynamical quenching equation,

$$\frac{\partial \alpha_M}{\partial t} = -2\eta_{\rm t}k_{\rm f}^2 \frac{\overline{\boldsymbol{\mathcal{E}}} \cdot \overline{\boldsymbol{B}}}{B_{\rm eq}^2} - 2\eta k_{\rm f}^2 \alpha_{\rm M}, \tag{17}$$

where $\overline{\boldsymbol{\mathcal{E}}} = \alpha\overline{\boldsymbol{B}} - \eta_{\rm t}\mu_0\overline{\boldsymbol{J}}$ is the mean electromotive force. Note that we have here ignored the possibility of magnetic helicity fluxes that must become important at larger values of $\mathrm{Re_M}$.

In Fig. 14 we compare the resulting magnetic field geometry with that of the direct simulations. In both cases the horizontal

Table 1. Summary of runs.

Run	Re	Re_M	Pr_M	$k_1 w$	$B^2_\mathrm{rms}/B^2_\mathrm{eq}$	$\overline{B}^2_{i,\mathrm{rms}}/B^2_\mathrm{eq}$	lm	direction	$\Delta\tau$	$V_\mathrm{eject}/u_\mathrm{rms}$
A	3.4	3.4	1	0.1	0.3–0.4	0.11	01	$+y$	250	0.45
B1	6.7	6.7	1	0.2	1.0–1.2	0.52	01	$-y$	530	0.55
B2	6.7	13	2	0.2	0.9–1.2	0.45	10	$+x$	570	0.63
B3	6.7	67	10	0.2	0.9–1.0	0.28	01	$\pm y$	800	0.55
B4	6.7	133	20	0.2	0.9	0.27	01	$-y$	?	?
B5	15.0	15	1	0.2	0.7–1.0	0.29	10	$+x$	370	0.52

Notes. Run A is for a cubic domain while Runs B1 to B5 are for taller domains at different values of Re_M. Note that the nondimensional interval length $\delta\tau$ as well as the ejection speeds cannot be determined accurately for most of the runs, but the values suggests that there is no systematic dependence on the value of Re_M. The column "lm" gives the l and m values of the leading mode of the mean field in Eq. (11) and the columns "direction" gives the direction of propagation of this mean field, confirming that it is a matter of chance.

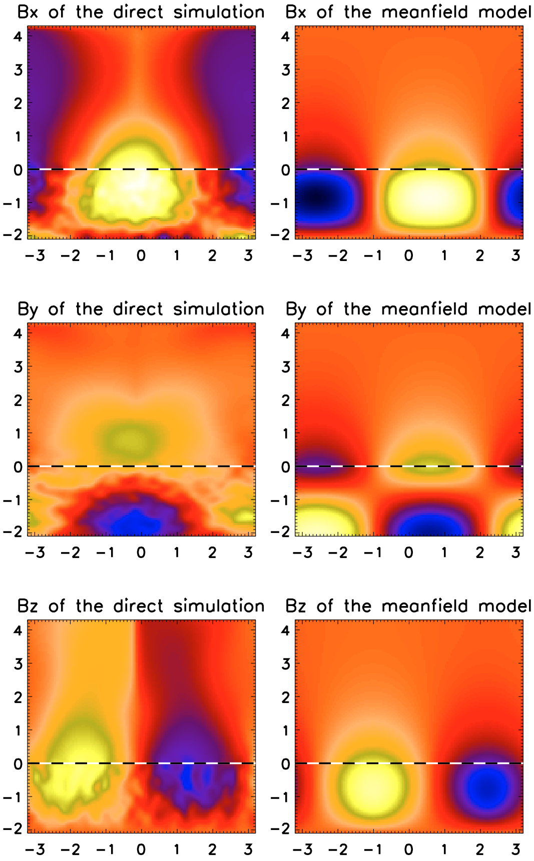
Bx of the direct simulation
Bx of the meanfield model
By of the direct simulation
By of the meanfield model
Bz of the direct simulation
Bz of the meanfield model

Fig. 14. Comparing the average in the x direction of the magnetic field with the 2D mean-field model. The structures are very similar.

variation of the field is similar. However, in the direct simulations the field extends more freely into the exterior. This is probably caused by a vertical upward flow that appears to be driven by the magnetic field. In Fig. 15 we see the vertical dependence of an upward flow, which soon reaches a statistically steady state.

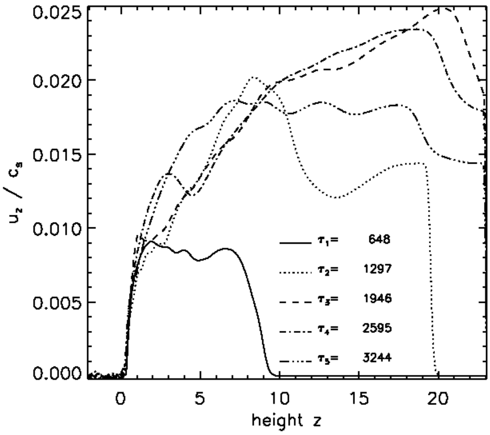

Fig. 15. Horizontally averaged rms velocity field as a function of height z for 5 different times for a run with $L_z = 8\pi$. Note the development of a statistically steady state after about 1000 turnover times.

5. Conclusions

Our first results are promising in that the dynamics of the magnetic field in the exterior is indeed found to mimic open boundary conditions at the interface between the turbulence zone and the exterior at $z = 0$. In particular, it turns out that a twisted magnetic field generated by a helical dynamo beneath the surface is able to produce flux emergence in ways that are reminiscent of that found in the Sun.

Some of the important questions that still remain open include the presence and magnitude of magnetic helicity fluxes. In the present model we expect there to be diffusive magnetic helicity fluxes associated with the vertical gradient of magnetic helicity density. A related question concerns the dependence on the magnetic Reynolds number. One expects magnetic helicity fluxes to become more important at large values of Re_M.

One of the future extensions of this model includes the addition of shear. In that case one might expect there to be strong magnetic helicity fluxes associated with the Vishniac & Cho (2001) mechanism that may transports magnetic helicity along the lines of constant shear, although more recent considerations now cast doubt on this possibility (Hubbard & Brandenburg 2010b). One should also keep in mind that the magnetic field cannot really be expected to be fully helical, as was assumed here in order to promote large-scale dynamo action under relatively simple conditions. Reducing the degree of helicity makes the dynamo harder to excite. On the other hand, shear helps to lower the excitation conditions, making it again feasible to obtain large-scale dynamo action even at low relative helicity of the driving. Another promising extension would be to move to a more global geometry, including the effects of curvature and gravity. This would allow for the emergence of a Parker-like wind that turns into a supersonic flow at sufficiently large radii. This would also facilitate the removal of magnetic field through the sonic point.

Acknowledgements. We thank Jaime de la Cruz Rodriguez, Gustavo Guerrero, and Göran Scharmer for discussions at the early stages of this work. We acknowledge the allocation of computing resources provided by the Swedish National Allocations Committee at the Center for Parallel Computers at the Royal Institute of Technology in Stockholm and the National Supercomputer Centers in Linköping. This work was supported in part by the European Research Council under the AstroDyn Research Project 227952 and the Swedish Research Council grant 621-2007-4064.

References

Blackman, E. G., & Brandenburg, A. 2002, ApJ, 579, 359
Blackman, E. G., & Brandenburg, A. 2003, ApJ, 584, L99
Brandenburg, A. 2001, ApJ, 550, 824
Brandenburg, A. 2005, ApJ, 625, 539
Brandenburg, A., & Subramanian, K. 2005, Astron. Nachr., 326, 400
Brandenburg, A., & Zweibel, E. G. 1994, ApJ, 427, L91
Gudiksen, B. V., & Nordlund, Å. 2002, ApJ, 572, L113
Gudiksen, B. V., & Nordlund, Å. 2005, ApJ, 618, 1031
Hubbard, A., & Brandenburg, A. 2010a, Geophys. Astrophys. Fluid Dyn., in print [`arXiv:1004.4591`]
Hubbard, A., & Brandenburg, A. 2010b, ApJ, submitted [`arXiv:1006.3549`]
Ji, H. 1999, Phys. Rev. Lett., 83, 3198
Käpylä, P. J., Korpi, M. J., & Brandenburg, A. 2008, A&A, 491, 353
Kleeorin, N. I., & Ruzmaikin, A. A. 1982, Magnetohydrodynamics, 18, 116
Klimchuk, J. A., & Sturrock, P. A. 1992, ApJ, 385, 344
Krause, F., & Rädler, K.-H. 1980, Mean-field magnetohydrodynamics and dynamo theory (Oxford: Pergamon Press)
Mikić, Z., Barnes, D. C., & Schnack, D. D. 1988, ApJ, 328, 830
Nordlund, Å., Brandenburg, A., Jennings, R. L., et al. 1992, ApJ, 392, 647
Ortolani, S., & Schnack, D. D. 1993, Magnetohydrodynamics of plasma relaxation (Singapore: World Scientific)
Parker, E. N. 1979, Cosmical magnetic fields (Oxford: Clarendon Press)
Peter, H., Gudiksen, B. V., & Nordlund, Å. 2004, ApJ, 617, L85
Pouquet, A., Frisch, U., & Léorat, J. 1976, J. Fluid Mech., 77, 321
Seehafer, N. 1996, Phys. Rev. E, 53, 1283
Tobias, S. M., Brummell, N. H., Clune, T. L., & Toomre, J. 1998, ApJ, 502, L177
Valori, G., Kliem, B., & Keppens, R. 2005, A&A, 433, 335
Vishniac, E. T., & Cho, J. 2001, ApJ, 550, 752
Yang, W. H., Sturrock, P. A., & Antiochos, S. K. 1986, ApJ, 309, 383

II

A&A 534, A11 (2011)
DOI: 10.1051/0004-6361/201117023
© ESO 2011

Astronomy & Astrophysics

Dynamo-driven plasmoid ejections above a spherical surface[⋆]

J. Warnecke[1,2], A. Brandenburg[1,2], and D. Mitra[1]

[1] Nordita, AlbaNova University Center, Roslagstullsbacken 23, 10691 Stockholm, Sweden
e-mail: `joern@nordita.org`
[2] Department of Astronomy, AlbaNova University Center, Stockholm University, 10691 Stockholm, Sweden

Received 4 April 2011 / Accepted 26 July 2011

ABSTRACT

Aims. We extend earlier models of turbulent dynamos with an upper, nearly force-free exterior to spherical geometry, and study how flux emerges from lower layers to the upper ones without being driven by magnetic buoyancy. We also study how this affects the possibility of plasmoid ejection.

Methods. A spherical wedge is used that includes northern and southern hemispheres up to mid-latitudes and a certain range in longitude of the Sun. In radius, we cover both the region that corresponds to the convection zone in the Sun and the immediate exterior up to twice the radius of the Sun. Turbulence is driven with a helical forcing function in the interior, where the sign changes at the equator between the two hemispheres.

Results. An oscillatory large-scale dynamo with equatorward migration is found to operate in the turbulence zone. Plasmoid ejections occur in regular intervals, similar to what is seen in earlier Cartesian models. These plasmoid ejections are tentatively associated with coronal mass ejections (CMEs). The magnetic helicity is found to change sign outside the turbulence zone, which is in agreement with recent findings for the solar wind.

Key words. magnetohydrodynamics (MHD) – turbulence – Sun: dynamo – Sun: coronal mass ejections (CMEs) – stars: magnetic field

1. Introduction

Observations show that the Sun sheds mass through twisted magnetic flux configurations (Démoulin et al. 2002). Remarkable examples of such helical ejections can be seen in the movies produced by the SOHO and SDO missions[1]. Such events may be important for the solar dynamo (Blackman & Brandenburg 2003). They are generally referred to as coronal mass ejections (CMEs). Conventionally, CMEs are modeled by adopting a given distribution of magnetic flux at the solar surface and letting it evolve by shearing and twisting the magnetic field at its footpoints at the surface (Antiochos et al. 1999; Török & Kliem 2003). This approach is also used to model coronal heating (Gudiksen & Nordlund 2005; Bingert & Peter 2011). The success of this method depends crucially on the ability to synthesize the velocity and magnetic field patterns at the surface. Of course, ultimately such velocity and magnetic field patterns must come from a realistic simulation of the Sun's convection zone, where the field is generated by dynamo action. In other words, we need a unified treatment of the convection zone and the CMEs. The difficulty here is the large range of time scales, from the 11-year dynamo cycle to the time scales of hours and even minutes on which CMEs develop. Such a large range of time scales is related to the strong density stratification in the Sun, as can be seen from the following argument. In the bulk of the convection zone, the dynamo is controlled by rather slow motions with turnover times of days and months. The typical velocity depends on the convective flux via $F_{\rm conv} \approx \overline{\rho} u_{\rm rms}^3$, where $\overline{\rho}$ is the mean density and $u_{\rm rms}$ is the rms velocity of the turbulent convection. The dynamo cycle time can even be several hundred times the turnover time. In the corona, on the other hand, the typical time scale depends on the Alfvén time, $L/v_{\rm A}$, where L is the typical scale of magnetic structures and $v_{\rm A} = B/\sqrt{\mu_0\overline{\rho}}$ is the Alfvén speed for a given magnetic field strength B. Here, μ_0 is the vacuum permeability.

In a recent paper, Warnecke & Brandenburg (2010) attempted a new approach of a unified treatment by combining a dynamo-generated field in the convection zone with a nearly force-free coronal part, albeit in a local Cartesian geometry. In this paper, we go a step further by performing direct numerical simulations (DNS) in spherical geometry. We also include density stratification due to gravity, but with a density contrast between the dynamo interior and the outer parts of the simulation domain that is much less (about 20) than in the Sun (around 14 orders of magnitude). This low density contrast is achieved by using an isothermal configuration with constant sound speed $c_{\rm s}$. Hence, the average density depends only on the gravitational potential and is given by $\ln\rho(r) \approx GM/rc_{\rm s}^2$, where G is Newton's gravitational constant, M is the central mass, and r is the distance from the center. As convection is not possible in such an isothermal setup, we drive turbulence by an imposed helical forcing that vanishes outside the convection zone. This also helps achieving a strong large-scale magnetic field. The helicity of the forcing is negative (positive) in the northern (southern) hemisphere and smoothly changes sign across the equator. Such a forcing gives rise to an α^2 dynamo with periodic oscillations and equatorward migration of magnetic activity (Mitra et al. 2010a). We ignore differential rotation, so there is no systematic shearing in

---

[⋆] Movie is available in electronic form at `http://www.aanda.org`

[1] `http://sohowww.nascom.nasa.gov/bestofsoho/Movies/10th/transcut_sm.mpg` and `http://www.youtube.com/watch?v=CvRj6Uykois&feature=player_embedded`

latitude. The only twisting comes then from the same motions that also sustain the dynamo-generated magnetic field. Note that in our model the mechanism of transport of the magnetic field to the surface is not magnetic buoyancy. Instead, we expect that, twisted magnetic fields will expel themselves to the outer regions by the Lorentz force.

Our aim in this paper is not to provide a model as close to reality as possible, but to show that it is possible to capture the phenomenon of CMEs (or, more generally, plasmoid ejections) within a minimalistic model that treats the convection zone and the outer parts of the Sun in a self-consistent manner. That is, the magnetic field in the convection zone is dynamically generated by dynamo action and the motions are not prescribed by hand, but they emerge as a solution of the momentum equation and include magnetic backreaction from the Lorentz force.

Given that gravity decreases with radius, there is in principle the possibility of a radial wind with a critical point at $r_* = GM/2c_{\rm s}^2$ (Choudhuri 1998). However, as we use stress-free boundary conditions with no mass flux in the radial direction, no such wind can be generated in our simulations. Nevertheless, we observe radially outward propagation of helical magnetic field structures without mass flux. Furthermore, our results for the flux of magnetic helicity compare well with recent measurements of the same in the solar wind (Brandenburg et al. 2011). Our approach might therefore provide new insights not only for CMEs and dynamo theory, but also for solar wind turbulence.

2. The model

We use spherical polar coordinates, (r, θ, ϕ). As in earlier work of Mitra et al. (2009, 2010a), our simulation domain is a spherical wedge. The results of Mitra et al. (2009) for such a wedge are consistent with those of Livermore et al. (2010) for a full spherical shell, both of which ignored the effects of an equator, which was included in the work of Mitra et al. (2010a). Our model is a bi-layer in the radial direction. The inner layer is forced with random helical forcing functions which have different signs of helicity in the two hemispheres. This models the helical aspects of convection in the Sun. We shall often call the inner layer "turbulence zone". The radius separating the two layers corresponds to the solar radius, $r = R$. This length scale is used as our unit of length. The inner layer models some aspects of the convection zone ($0.7R \le r \le R$) without however having any real convection, and the outer layer ($R \le r \le 2R$) models the solar corona. We consider the range $\pi/3 \le \theta \le 2\pi/3$, corresponding to ±30° latitude, and $0 < \phi < 0.3$, corresponding to a longitudinal extent of 17°. Here, θ is the polar angle and ϕ the azimuth. At the solar surface at $R = 700$ Mm, this would correspond to an area of about $730 \times 210\,{\rm Mm}^2$, which could encompass several active regions in the Sun. In our model the momentum equation is

$$\frac{\mathrm{D}\boldsymbol{U}}{\mathrm{D}t} = -\boldsymbol{\nabla}h + \boldsymbol{g} + \boldsymbol{J}\times\boldsymbol{B}/\rho + \boldsymbol{F}_{\rm for} + \boldsymbol{F}_{\rm visc}, \tag{1}$$

where $\boldsymbol{F}_{\rm visc} = \rho^{-1}\boldsymbol{\nabla}\cdot(2\rho\nu\mathsf{S})$ is the viscous force, ν is the kinematic viscosity, $\mathsf{S}_{ij} = \frac{1}{2}(U_{i;j} + U_{j;i}) - \frac{1}{3}\delta_{ij}\boldsymbol{\nabla}\cdot\boldsymbol{U}$ is the traceless rate-of-strain tensor, semicolons denote covariant differentiation, $h = c_{\rm s}^2\ln\rho$ is the specific pseudo-enthalpy, $c_{\rm s} = {\rm const.}$ is the isothermal sound speed, and $\boldsymbol{g} = -GM\boldsymbol{r}/r^3$ is the gravitational acceleration. We choose $GM/Rc_{\rm s}^2 = 3$, so $r_* = 1.5R$ lies within our domain. This value is rather close to the surface and would lead to significant mass loss if there was a wind, but this is suppressed by using impenetrative outer boundaries.

The forcing function $\boldsymbol{F}_{\rm for}$ is given as the product of two parts,

$$\boldsymbol{F}_{\rm for}(r,\theta,\phi,t) = \Theta_w(r-R)\,\boldsymbol{f}(r,\theta,\phi,t;-\cos\theta), \tag{2}$$

where $\Theta_w(r) = \frac{1}{2}\,[1-{\rm erf}(r/w)]$ is a profile function connecting the two layers and w is the width of the transition at the border between the two layers ($r = R$). In other words, we choose the external force to be zero in the outer layer, $r > R$. The function $\boldsymbol{f}$ consists of random plane helical transverse waves with relative helicity $\sigma = (\boldsymbol{f}\cdot\boldsymbol{\nabla}\times\boldsymbol{f})/k_{\rm f}\boldsymbol{f}^2$ and wavenumbers that lie in a band around an average forcing wavenumber of $k_{\rm f}R \approx 63$. This value should be compared with the normalized wavenumber k_1R, corresponding to the thickness of the shell ΔR, which yields $k_1R = 2\pi R/\Delta R \approx 21$, so the effective scale separation ratio, $k_{\rm f}/k_1$, is about 3.

In Eq. (2) the last argument of $\boldsymbol{f}(r,\theta,\phi,t;\sigma)$ denotes a parametric dependence on the helicity which is here chosen to be $\sigma = -\cos\theta$ such that the kinetic helicity of the turbulence is negative in the northern hemisphere and positive in the southern. Specifically, $\boldsymbol{f}$ is given by (Haugen et al. 2003)

$$\boldsymbol{f}(\boldsymbol{x},t) = A_{\rm f}N{\rm Re}\{\boldsymbol{f}_{\boldsymbol{k}(t)}\exp[{\rm i}\boldsymbol{k}(t)\cdot\boldsymbol{x} + {\rm i}\phi(t)]\}, \tag{3}$$

where $A_{\rm f}$ is a nondimensional forcing amplitude, and $\boldsymbol{x}$ is the position vector. The wavevector $\boldsymbol{k}(t)$ and the random phase $-\pi < \phi(t) \le \pi$ change at every time step, so $\boldsymbol{f}(\boldsymbol{x},t)$ is δ-correlated in time. The normalization factor N is chosen on dimensional grounds to be $N = c_{\rm s}(|\boldsymbol{k}|c_{\rm s}/\delta t)^{1/2}$. At each timestep we select randomly one of many possible wavevectors in a certain range around a given forcing wavenumber. The average wavenumber is referred to as $k_{\rm f}$. We ignore curvature effects in the expression for the forcing function and thus force the system with what would correspond to transverse helical waves in a Cartesian coordinate system, i.e.,

$$\boldsymbol{f}_{\boldsymbol{k}} = \mathsf{R}\cdot\boldsymbol{f}_{\boldsymbol{k}}^{\rm (nohel)} \quad \text{with} \quad \mathsf{R}_{ij} = \frac{\delta_{ij} - {\rm i}\sigma\epsilon_{ijk}\hat{k}_k}{\sqrt{1+\sigma^2}}, \tag{4}$$

where $-1 \le \sigma \le 1$ is the helicity parameter of the forcing function,

$$\boldsymbol{f}_{\boldsymbol{k}}^{\rm (nohel)} = (\boldsymbol{k}\times\hat{\boldsymbol{e}})\,/\,\sqrt{\boldsymbol{k}^2 - (\boldsymbol{k}\cdot\hat{\boldsymbol{e}})^2}, \tag{5}$$

is a non-helical forcing function, and $\hat{\boldsymbol{e}}$ is an arbitrary unit vector not aligned with $\boldsymbol{k}$; note that $|\boldsymbol{f}_{\boldsymbol{k}}|^2 = 1$.

The pseudo-enthalpy term in Eq. (1) emerges from the fact that for an isothermal equation of state the pressure is given by $p = c_{\rm s}^2\rho$, so the pressure gradient force is given by $\rho^{-1}\boldsymbol{\nabla}p = c_{\rm s}^2\boldsymbol{\nabla}\ln\rho = \boldsymbol{\nabla}h$. The continuity equation is then written in terms of h as

$$\frac{\mathrm{D}h}{\mathrm{D}t} = -c_{\rm s}^2\boldsymbol{\nabla}\cdot\boldsymbol{U}. \tag{6}$$

Equations (1) and (6) are solved together with the uncurled induction equation for the vector potential $\boldsymbol{A}$ in the resistive gauge (Candelaresi et al. 2011),

$$\frac{\partial\boldsymbol{A}}{\partial t} = \boldsymbol{U}\times\boldsymbol{B} + \eta\nabla^2\boldsymbol{A}, \tag{7}$$

where η is the (constant) magnetic diffusivity, so the magnetic field is given by $\boldsymbol{B} = \boldsymbol{\nabla}\times\boldsymbol{A}$ and thus obeys $\boldsymbol{\nabla}\cdot\boldsymbol{B} = 0$ at all times. The gauge can in principle become important when calculating the magnetic helicity density $\boldsymbol{A}\cdot\boldsymbol{B}$, although the part resulting from the small-scale fields is expected to be independent of the gauge (Subramanian & Brandenburg 2006; Hubbard & Brandenburg 2010), while that of the large-scale fields is not.

Our wedge is periodic in the azimuthal direction. For the velocity, we use stress-free boundary conditions on all other boundaries. For the magnetic field we employ vertical field conditions on $r = 2R$ and perfect conductor conditions on both $r = 0.7R$ and the two θ boundaries. Time is expressed in units of $\tau = (u_{\rm rms}k_{\rm f})^{-1}$, which is the eddy turnover time in the turbulence zone, and $u_{\rm rms}$ is the rms velocity in $r < R$. Density is given in units of the mean density in the turbulence zone, $\rho_0 = \overline{\rho}$. The magnetic field is expressed in units of the mean equipartition value, $B_{\rm eq}$, defined via $B_{\rm eq}^2 = \mu_0\overline{\rho \boldsymbol{u}^2}$. We use a magnetic diffusivity that is constant in space and time and its value is given in terms of the magnetic Reynolds number, defined as

$$R_{\rm m} = u_{\rm rms}/\eta k_{\rm f}, \tag{8}$$

where $k_{\rm f}$ is the characteristic scale of the external force, defined above. This also turns out to be the energy containing scale of the fluid. In the following analysis, we use ϕ averages, defined as $\overline{F}(r,\theta,t) = \int F(r,\theta,\phi,t)\,{\rm d}\phi/2\pi$. Occasionally we also use time averages denoted by $\langle . \rangle_t$. We perform DNS with the P C[2], which is a modular high-order code (sixth order in space and third-order in time, by default) for solving a large range of partial differential equations, including the ones relevant in the present context.

3. Results

3.1. Dynamo in the turbulence zone

We start our DNS with seed magnetic field everywhere in the domain. Owing to the helical forcing in the turbulent layer, a large-scale magnetic field is produced by dynamo action. The dynamo is cyclic with equatorward migration of magnetic fields. This dynamo was studied by DNS in Mitra et al. (2010a) and has been interpreted as an α^2 dynamo. The possibility of oscillating α^2 dynamos was known since the early papers of Baryshnikova & Shukurov (1987) and Rädler & Bräuer (1987), who showed that a necessary condition for oscillations is that the α effect must change sign in the domain.

The dynamo first grows exponentially and then saturates after around 300 turnover times, see Fig. 1. After saturation the dynamo produces a large-scale magnetic field with opposite polarities in the northern and southern hemispheres. In Fig. 2 we plot the radial magnetic field at the surface of the dynamo region at $r = R$. This layer would correspond to the solar photosphere if we had a more realistic solar model, which would include higher stratification as well as cooling and radiation effects. The six wedges represent different times and show clearly an equatorward migration of the radial magnetic field with polarity reversal every half cycle. The other components of the magnetic field (not plotted) also shows the same behavior. Comparing the first ($t/\tau = 3028$) and the last ($t/\tau = 3101$) panel, the polarity has changed sign in a time interval $\Delta t/\tau \approx 100$. The oscillatory and migratory properties of the dynamo is also seen in the butterfly diagram of Fig. 3 for $\langle \overline{B}_\phi \rangle_r$ and $\langle \overline{B}_r \rangle_r$. In Fig. 1 one can also verify that the oscillation period is around 200 turnover times, corresponding to a non-dimensional dynamo cycle frequency of $\tau\omega_{\rm cyc} = 0.032$ and the field strength in the turbulent layer varies between 1.2 and 1.6 of the equipartition field strength. This value of the cycle frequency is roughly consistent with an estimate of Mitra et al. (2010b) that $\omega_{\rm cyc} = 0.5\eta_{\rm t}k_{\rm m}^2$, where $k_{\rm m}$ is the relevant wavenumber of the mean field. Using $\eta_{\rm t} \approx \eta_{\rm t0} \equiv u_{\rm rms}/3k_{\rm f}$ (Sur et al. 2008), we find $\tau\omega_{\rm cyc} \approx 0.2(k_{\rm m}/k_{\rm f})^2 \approx 0.02$, where we have assumed $k_{\rm m} \approx 2\pi/0.3R \approx 20k_1$ and $k_{\rm f} \approx 60k_1$. The estimate of

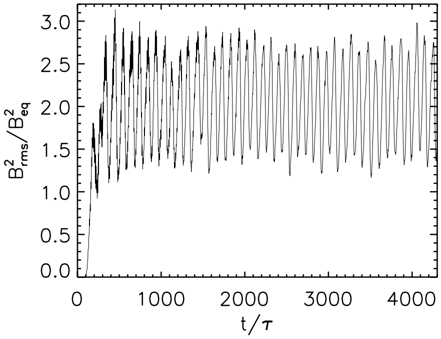

Fig. 1. Initial exponential growth and subsequent saturation behavior of the magnetic field in the interior for forced turbulence with dynamo action for Run A. The magnetic field strength is oscillating with twice the dynamo frequency $2\omega_{\rm cyc}$.

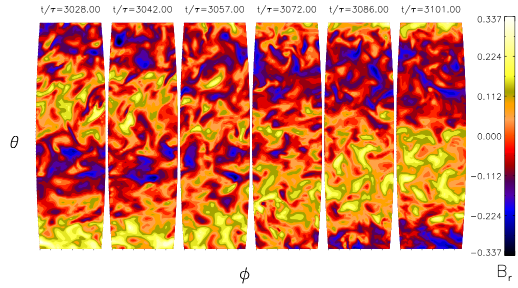

Fig. 2. Equatorward migration, as seen in visualizations of B_r for Run D at $r = R$ over a horizontal extent $\Delta\theta = 58°$ and $\Delta\phi = 17°$.

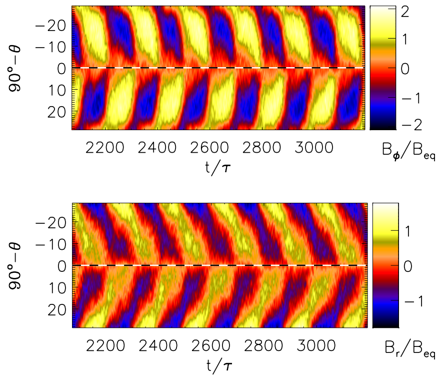

Fig. 3. Periodic variation of $\langle \overline{B}_\phi \rangle_r$ and $\langle \overline{B}_r \rangle_r$ in the turbulence zone. Dark blue stands for negative and light yellow for positive values. The dotted horizontal lines show the location of the equator at $\theta = \pi/2$. The magnetic field is normalized by the equipartition value. Taken from Run A.

---

[2] `http://pencil-code.googlecode.com`

Table 1. Summary of runs discussed in this paper.

Run	A_f	R_m	P_m	$B^2_\mathrm{rms}/B^2_\mathrm{eq}$	$\tau\omega_\mathrm{cyc}$	$\Delta t/\tau$	$V_\mathrm{ej}/u_\mathrm{rms}$
A	0.20	1.5	1	1.2–2.7	0.032	100	0.482
B	0.20	5	1	1.5–3.5	0.029	110	0.409
C	0.20	9	1	2.1–5.5	0.022	130	0.455
D	0.20	18	1	2.0–5.0	0.019	140	0.409
D1	0.10	11	1	2.0–5.0	0.018	140	0.455
D2	0.15	15	1	2.0–5.0	0.016	130	0.482
D3	0.25	20	1	1.0–3.0	0.023	130	0.293
E	0.20	22	1	1.5–4.5	0.017	220	0.205
F	0.20	28	1	1.2–4.2	0.015	280	0.273
G	0.20	44	1	1.7–3.5	0.015	285	0.409

Notes. A_f is the forcing amplitude defined in Eq. (3), R_m is the magnetic Reynolds number defined in Eq. (8) and $P_\mathrm{m} = \nu/\eta$ is the magnetic Prandtl number. $\omega_\mathrm{cyc} = 2\pi/T_\mathrm{cyc}$ stands for the frequency of the oscillating dynamo, where T_cyc is the cycle period. $\Delta t/\tau$ is the typical interval of plasmoid ejections, whose typical speed is V_ej. For the runs D1 to D3, the forcing amplitude A_f is changed, while η and ν have the same value as for run D. The rms velocities in the turbulence zone change accordingly and affect therefore the Reynolds number and the turnover times τ.

Mitra et al. (2010b) applies to perfectly conducting outer boundary conditions, which might explain the remaining discrepancy.

A summary of all runs is given in Table 1, where the amplitudes of the magnetic field show a weak non-monotonous dependence on the magnetic Reynolds number R_m. For larger values of R_m, the magnetic field strength decreases slightly with increasing R_m, but it is weaker than in some earlier α^2 dynamos with open boundaries (Brandenburg & Dobler 2001). This could be due to two reasons. Firstly, our simulations are far from the asymptotic limit of large magnetic Reynolds numbers, in which the results of Brandenburg & Dobler (2001) are applicable. The maximum value R_m is in our simulations approximately 15 times the critical R_m. The second reason could be that we have expulsion of magnetic helicity from our domain which was not present in (Brandenburg & Dobler 2001). We find the peak of the R_m dependency at $R_\mathrm{m} = 9$, corresponding to Run C. The dynamo cycle frequency shows a weak decrease (by a factor of 2) as the magnetic Reynolds number increases (by a factor of 30).

3.2. Phase relation between radial and azimuthal fields

Although our dynamo model does not include important features of the Sun such as differential rotation, some comparison may still be appropriate. For the Sun, one measures the mean radial field by averaging the line-of-sight magnetic field from synoptic magnetograms. The azimuthal field is not directly observed, but its sign can normally be read off by looking at the magnetic field orientation of sunspot pairs. Existing data suggest that radial and azimuthal fields are approximately in out-of-phase (Yoshimura 1976). This is reasonably well reproduced by $\alpha\Omega$ dynamos models, where the radial field lags behind the azimuthal one by 0.75π (Stix 1976). However, in the present work, radial and azimuthal fields are approximately in phase with a phase difference of 0.3π inside the dynamo region; see Fig. 4. Future studies will include the near-surface shear layer, which has been suspected to play an important role in producing equatorward migration (Brandenburg 2005). This would also help reproducing the observed phase relation.

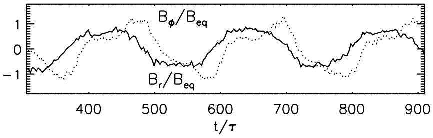

Fig. 4. Time evolution of the radial magnetic field B_r (solid line) and the azimuthal magnetic field B_ϕ (dotted line) in the dynamo region averaged over the radius r and azimuth at $\theta = \pm 7°$. To improve the statistics, we calculate the components of the magnetic field as the antisymmetric part in latitude, i.e., $B_i = \left(B_i^\mathrm{N} - B_i^\mathrm{S}\right)/2$ for $i = r, \phi$.

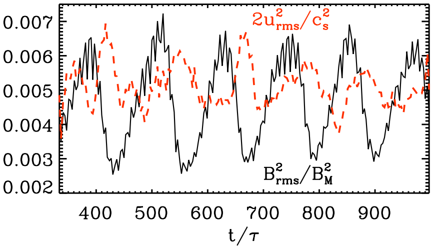

Fig. 5. Phase relations between the magnetic field and the velocity in the dynamo region. The magnetic field is plotted as B^2_rms, normalized with the equipartition field of the sound speed, B^2_M ($=\mu_0\rho c_\mathrm{s}^2$) as a solid and black line. The rms velocity, normalized by the sound speed c_s, is plotted as a dashed red line, and has been smoothed over 5 neighboring data points to make it more legible. Taken from Run A.

3.3. Relation between kinetic and magnetic energies

Next we investigate the relation between the rms values of the magnetic field and the velocity. Both quantities are oscillating in time with a typical period of 200 turnover times. In Fig. 5 we compare the time evolution of the magnetic field strength and the rms velocity. The magnetic field is calculated in the dynamo region and normalized to the thermal equipartition field strength. The phase difference between the two is slightly less than π within the dynamo region. This basically shows that the magnetic field quenches the turbulence.

3.4. Density variations

The density is stratified in radius and varies by over an order of magnitude. For all the runs listed in Table 1 the density fluctuates about the hydrostatic equilibrium value, $\rho \approx \rho_0 \exp(GM/rc_\mathrm{s}^2)$. The relative fluctuations are of comparable strength at all radii; see Fig. 6.

3.5. Magnetic field outside the turbulence zone

The magnetic field averaged over the entire domain is more than 5 times smaller than in the turbulence zone. In Fig. 7 we show that the magnetic field is concentrated to the turbulence zone and $\boldsymbol{B}^2$ drops approximately exponentially with a scale height of about $0.23R$ in the outer parts for $r > R$. The toroidal component of the magnetic field is dominant in the turbulence layer, but does not play a significant role in the outer part. By contrast, the radial field is weak in the inner parts and dominates in the outer.

Magnetic structures emerge through the surface and create field line concentrations that reconnect, separate, and rise to the outer boundary of the simulation domain. This dynamical

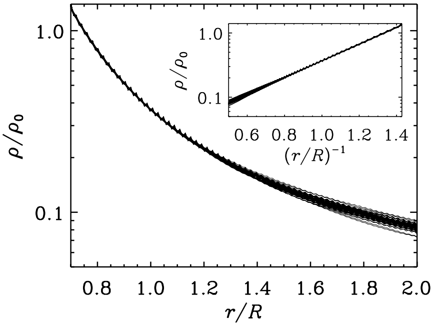

Fig. 6. Radial dependence of density overplotted at different times. In the inset is the linear behavior of the logarithmic density $\log \rho/\rho_0$ to the inverse of the radius shown. Taken from Run A.

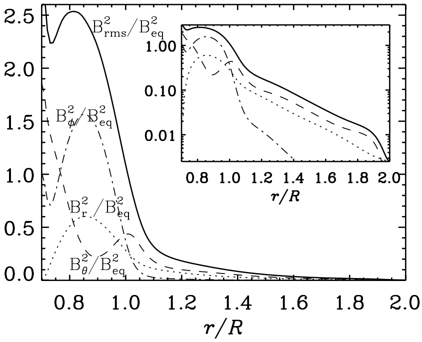

Fig. 7. Radial dependence of the mean squared magnetic field, $B^2_{\rm rms}$ (solid line), compared with those of B_r (dotted), B_θ (dashed), and B_ϕ (dash-dotted). All quantities are averaged over 13 dynamo cycles. The inset shows the same quantities in a logarithmic representation. Taken from Run A.

evolution is seen in a sequence of field line images in Fig. 8, where field lines of the mean field are shown as contours of $r\sin\theta\overline{A}_\phi$ and colors represent $\overline{B}_\phi$. Prior to a plasmoid ejection we see a convergence of antiparallel radial field lines, which then reconnect such that the newly reconnected field lines move away from the reconnection site. The actual reconnection seems to happen much faster than the subsequent ejection.

In the outer layers, the magnetic field emerges as large structures that correlate with reconnection events of magnetic fields. In Rust (1994) such phenomena have been described as *magnetic clouds*. We find recurrent ejections of magnetic field lines with concentrations and reconnection events, but the occurrence of structures such as magnetic clouds does not happen completely regularly, i.e., these structured events would be difficult to predict.

In Fig. 9 we show a close-up of the magnetic field. A configuration resembling a reconnection event is clearly seen. Here, the contours represent magnetic field lines with solid and dashed lines denoting counter-clockwise and clockwise orientations, respectively. The solid antiparallel field lines reconnect around $r = 0.9R$ and separate to the left and to the right. On the right-hand side, a plasmoid has formed, which is eventually ejected. This plasmoid appears as a CME-like ejection in the first panel of Fig. 11. These plasmoids, as seen more clearly in Figs. 8 and 10, appear as a concentration of field lines that propagate outwards. The fact that reconnection happens predominantly in the upper parts of the turbulence zone suggests that turbulence is needed to enable fast reconnection (Lazarian & Vishniac 1999).

Additionally, we find reconnection as a result of the interaction between ejections. As plotted in Fig. 10, the field lines of two subsequent events have the opposite field line direction, which can then interact in the outer layers. Comparison with the first panel of Fig. 11 shows that the current helicity has a correlation with the separatrices of the two polarities of the field lines. We also find that in the interaction region the field lines have high density and are more strongly concentrated.

3.6. Current helicity

The current helicity ($\boldsymbol{J} \cdot \boldsymbol{B}$) is often used as a useful proxy for the magnetic helicity ($\boldsymbol{A} \cdot \boldsymbol{B}$) at small scales, because, unlike magnetic helicity, it is gauge-independent. Current helicity has also been observed in the Sun (Seehafer 1990) and it has been obtained from mean-field dynamo models (Dikpati & Gilman 2001). In the present paper we are particularly interested in the current helicity outside the Sun. We normalize it by the r-dependent time-averaged mean squared field to compensate for the radial decrease of $\overline{\boldsymbol{J} \cdot \boldsymbol{B}}$. In Fig. 12, we have also averaged in latitude from 20° to 28°. In the turbulence zone the sign of $\overline{\boldsymbol{J} \cdot \boldsymbol{B}}/\langle\overline{\boldsymbol{B}^2}\rangle_t$ is the same as that of kinetic helicity which, in turn, has the same sign as the helicity of the external forcing, i.e. of σ; see Figs. 11 and 12.

However, to our surprise, above the surface, and separately for each hemisphere, the signs of current helicity tend to be opposite to those in the turbulence zone; see Fig. 11 for the panels of $t/\tau = 1669$ and $t/\tau = 1740$. To demonstrate that plasmoid ejections are recurrent phenomena, we look at the evolution of $\overline{\boldsymbol{J} \cdot \boldsymbol{B}}/\langle\overline{\boldsymbol{B}^2}\rangle_t$ as a function of t and r. This is done in Fig. 12 for Run A. It turns out that the speed of plasmoid ejecta is about 0.45 of the rms velocity of the turbulence in the interior region for Reynolds numbers up to 15 and about 0.3 up to 30. To compare with the Sun, we estimate the rms velocity of the turbulence in terms of the convective energy flux via $F \approx \rho u^3_{\rm rms}$. The density of the corona is $\rho_{\rm cor} \approx 10^{-12}\,{\rm kg\,m^{-3}}$, so our estimate would suggest $V_{\rm ej} \approx 0.3(F/\rho_{\rm cor})^{1/3} \approx 1200\,{\rm km\,s^{-1}}$, which is somewhat above the observed speeds of 400–1000 $\rm km\,s^{-1}$. The time interval between subsequent ejections is around $100\,\tau$ for Run A. As seen from Table 1, the ejection interval is independent of the forcing amplitude $A_{\rm f}$ and increases weakly with magnetic Reynolds number, but it seems to be still comparable to half the dynamo cycle period, i.e., $\Delta\tau \approx T_{\rm cyc}/2$. This means that plasmoid ejections happen about twice each cycle. It is therefore not clear whether such a result can be extrapolated to the real Sun.

In our simulations, we find the ejections to have the shape of the characteristic three-part structure that is observed in real CMEs. This is particularly clear in Fig. 11, where the ejections seem to contain three different parts. In the center we find a ball-shaped structure consisting of one polarity of current helicity, where at the front of the ejection a bow of opposite polarity had formed. In between these two structures the current helicity is close to zero and appears as a cavity. These three parts (prominence, cavity, and front) are described by Low (1996) for CMEs and are generally referred to as "three-part structure". The basic shape of the ejection is independent of the used forcing amplitudes and the kinetic and magnetic Reynolds numbers. It should, however, be noted that the three-part structure of the ejections becomes clearer at magnetic higher Reynolds numbers

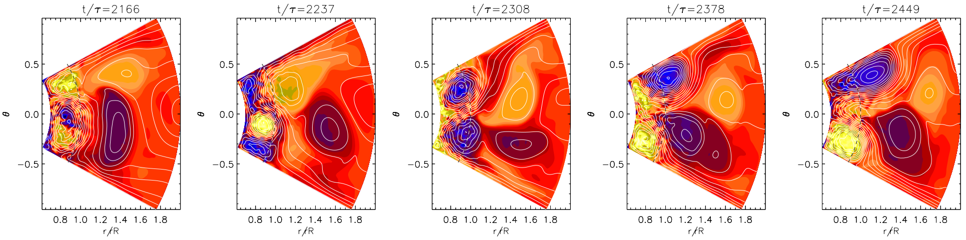

Fig. 8. Time series of formation of plasmoid ejections in spherical coordinates. Contours of $r \sin\theta \overline{A}_\phi$ are shown together with a color-scale representation of $\overline{B}_\phi$; dark blue stands for negative and light yellow for positive values. The contours of $r \sin\theta \overline{A}_\phi$ correspond to field lines of $\overline{\boldsymbol{B}}$ in the $r\theta$ plane. The dashed horizontal lines show the location of the surface at $r = R$. Taken from Run D.

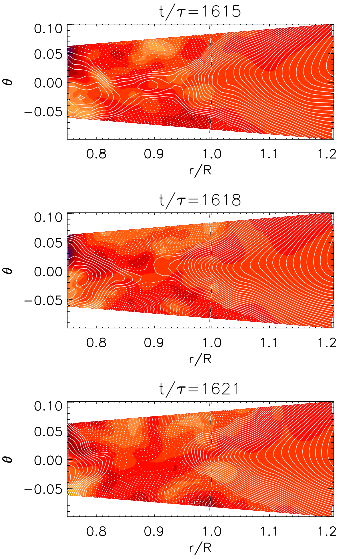

Fig. 9. Time series of a reconnection event in an X-point as a close-up view. Contours of $r \sin\theta \overline{A}_\phi$ are shown together with a color-scale representation of $\overline{B}_\phi$; dark blue stands for negative and light yellow for positive values. The contours of $r \sin\theta \overline{A}_\phi$ correspond to field lines of $\overline{\boldsymbol{B}}$ in the $r\theta$ plane, where solid lines represent counter-clockwise magnetic field lines and the dash ones clockwise. The dashed vertical lines show the location of the surface at $r = R$. Taken from Run D.

(e.g., for Runs D and G compared with Run A, for example). In the Sun, the plasma is confined to loops of magnetic field with flows along field lines due to the low plasma beta in the solar corona. This is also seen in our simulations displayed in Fig. 11, where the ejections follow field lines and appear to create loop-like structures. An animation of the detailed time evolution of the CME-like structures emerging recurrently into the solar corona is available in the on-line edition (see Fig. 11)[3]. However, since our choice of boundary conditions does not allow mass flux at the outer boundary, no plasma can actually leave the domain. The recurrent nature of the plasmoid ejections found here and in Warnecke & Brandenburg (2010) is not yet well understood. In contrast to Warnecke & Brandenburg (2010), where there are no strong oscillations present, here the ejections seem to correlate with the dynamo cycle. In each hemisphere of the turbulence zone a magnetic field is created with different polarity. After they have migrated to the equator, they merge and produce an ejection. However, comparing with the results of Warnecke & Brandenburg (2010), which are similar to those in the present paper, the oscillation cannot be the only explanation for the recurrence of the ejections. As we have seen in Fig. 12, these events export magnetic helicity out of the domain. For the dynamo, on the other hand, magnetic helicity losses play a role only in the nonlinear stage. It is therefore conceivable that the regular occurrence of plasmoid ejections is connected with nonlinear relaxation oscillations rather than with the dynamo cycle which is essentially a linear phenomenon. This is also suggested by the results of Warnecke & Brandenburg (2010), where recurrent ejections occur without oscillations of the large-scale field.

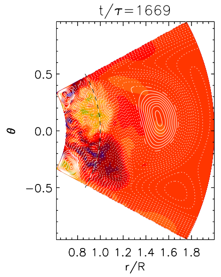

Fig. 10. Magnetic field configuration at the time of a ejection. Contours of $r \sin\theta \overline{A}_\phi$ are shown together with a color-scale representation of $\overline{B}_\phi$; dark blue stands for negative and light yellow for positive values. The contours of $r \sin\theta \overline{A}_\phi$ correspond to field lines of $\overline{\boldsymbol{B}}$ in the $r\theta$ plane, where the solid lines represent counter-clockwise magnetic field lines and the dash ones clockwise. The dashed vertical lines show the location of the surface at $r = R$. Taken from Run D.

From Figs. 11 and 12 we conclude that in each hemisphere the sign of current helicity outside the turbulence zone is mostly opposite to that inside the turbulence zone. A stronger trend is shown in the cumulative mean of current helicity over time. This is shown in Fig. 13, where we plot the time evolution of the ϕ averaged current helicity at $r = 1.5\,R$ and 28° latitude, which is a safe distance away from the outer r and θ boundaries so as not to perturb our results, which should thus give a reasonable representation of the outer layers. For the northern hemisphere the current helicity (solid black line) and the cumulative mean (solid red line) show positive values and for the southern hemisphere (dotted lines) negative values. This agrees with results of

---

[3] The movie is also available at `http://www.youtube.com/watch?v=aR-PgxQyP24`.

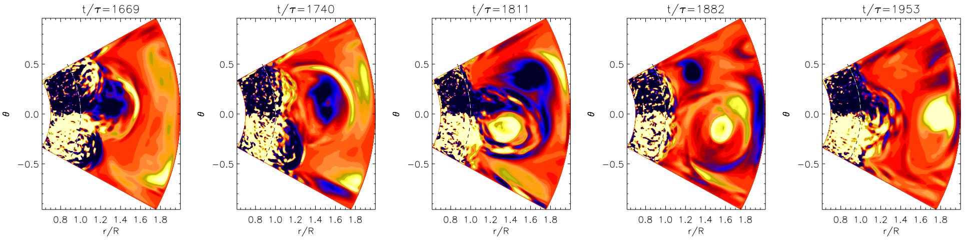

Fig. 11. Time series of coronal ejections in spherical coordinates. The normalized current helicity, $\mu_0 R\overline{\boldsymbol{J}\cdot\boldsymbol{B}}/\langle\overline{\boldsymbol{B}}^2\rangle_t$, is shown in a color-scale representation for different times; dark blue stands for negative and light yellow for positive values. The dashed horizontal lines show the location of the surface at $r = R$. Taken from Run D. The temporal evolution is shown in a movie available as online material.

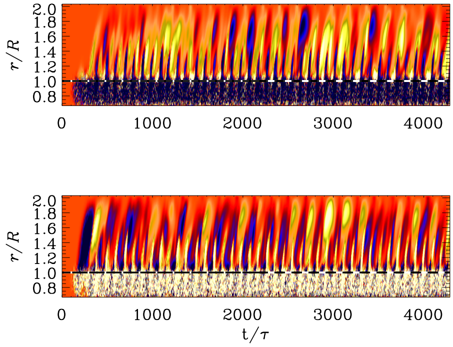

Fig. 12. Dependence of the dimensionless ratio $\mu_0 R\overline{\boldsymbol{J}\cdot\boldsymbol{B}}/\langle\overline{\boldsymbol{B}}^2\rangle_t$ on time t/τ and radius r in terms of the solar radius. The *top panel* shows a narrow band in θ in the northern hemisphere and the *bottom* one a thin band in the southern hemisphere. In both plots we have also averaged in latitude from 20° to 28°. Dark blue stands for negative and light yellow for positive values. The dotted horizontal lines show the location of the surface at $r = R$.

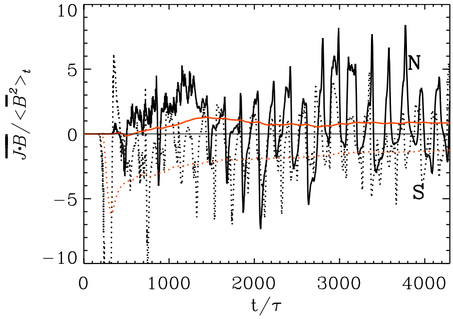

Fig. 13. Dependence of the dimensionless ratio $\mu_0 R\overline{\boldsymbol{J}\cdot\boldsymbol{B}}/\langle\overline{\boldsymbol{B}}^2\rangle_t$ on time t/τ at radius $r = 1.5\,R$ and 28° latitude. The solid line stands for the northern hemisphere and the dotted for the southern hemisphere. The red lines represent the cumulative mean for each hemisphere.

Brandenburg et al. (2009), where the magnetic helicity of the field in the exterior has the opposite sign than in the interior.

To investigate whether the sign of the current helicity in the turbulence zone is different from that and in the outer parts, we show in Fig. 14 the azimuthally and time-averaged current helicity as a function of radius and colatitude. It turns out that,

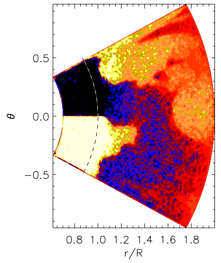

Fig. 14. Current helicity averaged over 3900 turnover times. Legend is the same as in Fig. 11. Dark blue corresponds to negative values, while the light yellow corresponds to positive value. Taken from Run D.

even though we have averaged the result over several thousand turnover times, the hemispheric sign rule of current helicity is still only approximately obeyed in the outer layers – even though it is nearly perfectly obeyed in the turbulence zone. There remains substantial uncertainty, especially near the equator. This suggests that meaningful statements about magnetic and current helicities in the solar wind can only be made after averaging over sufficiently long stretches of time.

3.7. Magnetic helicity fluxes

In view of astrophysical dynamo theory it is important to understand the amount of magnetic helicity that can be exported from the system. Of particular interest here is the magnetic helicity associated with the small-scale magnetic field. Under the assumption of scale separation, this quantity is gauge-independent (Subramanian & Brandenburg 2006), so we can express it in any gauge. This has been verified in simulations both with an equator (Mitra et al. 2010b) and without (Hubbard & Brandenburg 2010). Here, we compute the magnetic helicity flux associated with the small-scale field by subtracting that of the azimuthally averaged field from that of the total field, i.e.,

$$\overline{\boldsymbol{e}\times\boldsymbol{a}} = \overline{\boldsymbol{E}\times\boldsymbol{A}} - \overline{\boldsymbol{E}}\times\overline{\boldsymbol{A}}, \tag{9}$$

where $\boldsymbol{E} = \mu_0\eta\boldsymbol{J} - \boldsymbol{U}\times\boldsymbol{B}$ is the electric field. This is also the way how the magnetic helicity flux from the small-scale field was computed in Hubbard & Brandenburg (2010), where the magnetic helicity flux from the total and large-scale fields was found to be gauge-dependent, but that from the small-scale field was not. In Fig. 16 we compare the flux of magnetic helicity of the small-scale field across the outer surfaces in the northern and southern hemispheres with that through the equator. It turns

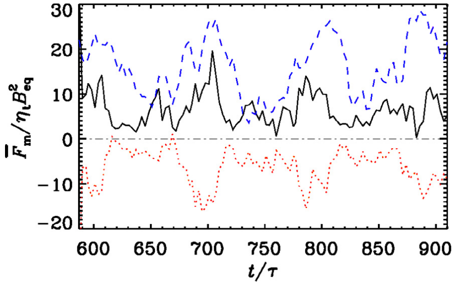

Fig. 15. Time evolution of the magnetic helicity flux of the large-scale field, smooth over two data points. Here, the mean of magnetic helicity flux out through the surface of the northern hemisphere (black) is shown, together with that through the southern hemisphere (dotted red), and the equator (dashed blue).

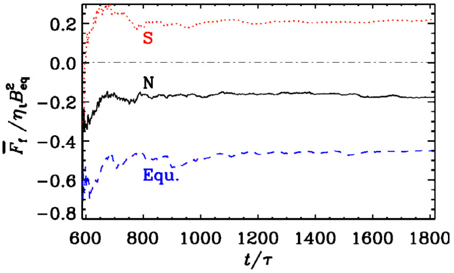

Fig. 16. Cumulative mean of the time evolution of the magnetic helicity flux of the small-scale field, $\overline{\boldsymbol{F}}_{\rm f} = \overline{\boldsymbol{e}\times\boldsymbol{a}}$, normalized by $\eta_{\rm t}B_{\rm eq}^2$, where $\eta_{\rm t} \approx \eta_{t0} \equiv u_{\rm rms}/3k_{\rm f}$ was defined in Sect. 3.1. Here, the mean of magnetic helicity flux out through the surface of the northern hemisphere (black) is shown, together with that through the southern hemisphere (dotted red), and the equator (dashed blue).

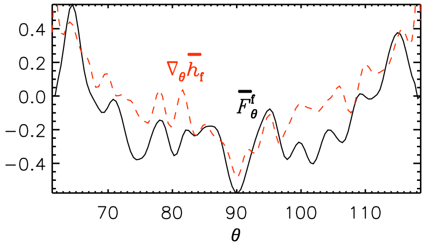

Fig. 17. Dependence of the latitudinal component of the magnetic helicity flux, $\overline{F}_\theta^{\rm f}$, compared with the latitudinal gradient of the magnetic helicity density of the small-scale field, $\boldsymbol{\nabla}_\theta\overline{h}_{\rm f}$, at $r/R = 0.85$. The large-scale variation of the latter agrees with that of the former if the gradient is multiplied by an effective diffusion coefficient for magnetic helicity of $\kappa_{\rm t} \approx 3\eta_{t0}$.

out that a major part of the flux goes through the equator. The part of the magnetic helicity flux that goes through the surface is about 20% of $\eta_{\rm t}B_{\rm eq}^2$. However, the magnetic helicity flux should primarily depend on $\overline{\boldsymbol{B}}$ rather than $B_{\rm eq}$. In the present simulations, where the dynamo works with a fully helical field, the two are comparable. This is not the case in the Sun, where the estimated field strength is expected to be about 300 G (Brandenburg 2009). Thus, to compare with the Sun, a more reasonable guess for the magnetic helicity flux would be about 20% of $\eta_{\rm t}\overline{\boldsymbol{B}}^2$. Integrating this over one hemisphere and multiplying this with the 11 year cycle time, we find the total magnetic helicity loss to be $2\pi R^2\eta_{\rm t}\overline{\boldsymbol{B}}^2T_{\rm cyc}$, which corresponds to $5\times10^{47}\,{\rm Mx}^2$ if we use $\eta_{\rm t} = 3\times10^{12}\,{\rm cm}^2\,{\rm s}^{-1}$. This value exceeds the estimated upper limit for the solar dynamo of about $10^{46}\,{\rm Mx}^2$ per cycle given by Brandenburg (2009). However the estimate by Brandenburg (2009) is based on an $\alpha\Omega$ dynamo model with α effect and shear that yield a period comparable with the 11 year period of the Sun. Therefore, the discrepancy with the present model, where shear plays no role, should not be surprising. Instead, it tells us that a dynamo without shear has to shed even more magnetic helicity than one with shear.

The magnetic helicity flux of the large-scale field may not a priori be gauge-invariant. However, the system is in a statistically steady state and, in addition, the magnetic helicity integrated over each cycle is constant. In that case the divergence of the magnetic helicity flux is also gauge-invariant. Furthermore, the shell-integrated magnetic helicity cannot have a rotational component and is therefore uniquely defined. In Fig. 15 we plot this flux and see that its maxima tend to occur about 50 turnover times after magnetic field maxima; see Figs. 4 and 5. The helicity flux of the small-scale field does not show a clear behavior. Since the ejections appear to be related to the magnetic field strength in this way, one might conclude that the magnetic helicity flux of the large-scale field is transported through these ejections. This result is somewhat unexpected and deserves to be reexamined more thoroughly in future simulations where cycle and ejection frequencies are clearly different from each other.

Next, let us look at the magnetic helicity flux of the small-scale field. On earlier occasions, Mitra et al. (2010b) and Hubbard & Brandenburg (2010) have been able to describe the resulting magnetic helicity flux by a Fickian diffusion ansatz of the form $\overline{\boldsymbol{F}}_{\rm f} = -\kappa_{\rm h}\boldsymbol{\nabla}\overline{h}_{\rm f}$, where $\kappa_{\rm h}/\eta_{t0}$ was found to be 0.3 and 0.1, respectively. In Fig. 17 we show that the present data allow a similar representation, although the uncertainty is large. It turns out that $\kappa_{\rm h}/\eta_{t0}$ is about 3, suggesting thus that turbulent magnetic helicity exchange across the equator can be rather efficient. Such an efficient transport of magnetic helicity out of the dynamo region is known to be beneficial for the dynamo in that it alleviates catastrophic quenching (Blackman & Brandenburg 2003). In this sense, the inclusion of CME-like phenomena is not only interesting in its own right, but it has important beneficial consequences for the dynamo itself in that it models a more realistic outer boundary condition.

3.8. Comparison with solar wind data

Our results suggest a reversal of the sign of magnetic helicity between the inner and outer parts of the computational domain. This is in fact in agreement with recent attempts to measure magnetic helicity in the solar wind (Brandenburg et al. 2011). They used the Taylor hypothesis to relate temporal fluctuations of the magnetic field to spatial variations by using the fact that the turbulence is swept past the space craft with the mean solar wind. This idea can in principle also be applied to the present simulations, provided we use the obtained mean ejection speed $V_{\rm ej}$ (see Table 1) for translating temporal variations (in t) into spatial ones (in r) via $r = r_0 - V_{\rm ej}t$. Under the assumption of homogeneity, one can then estimate the magnetic helicity spectrum as $H(k) = 4\,{\rm Im}(\hat{B}_\theta\hat{B}_\phi^\star)/k$; see Matthaeus et al. (1982) and Eq. (9) of

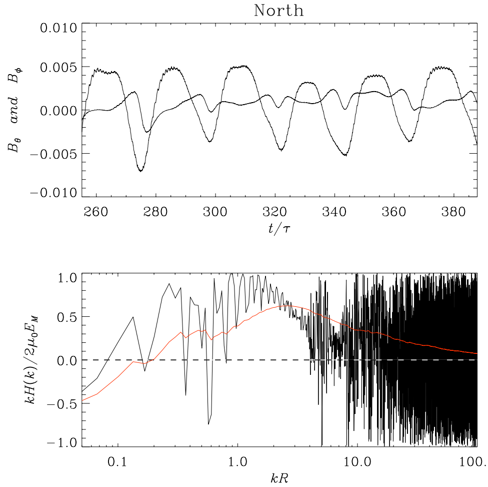

Fig. 18. Helicity in the northern outer atmosphere. The values are written out at the point, $r = 1.5\,R$, $90^\circ - \theta = 17^\circ$, and $\phi = 9^\circ$. *Top panel*: phase relation between the toroidal B_ϕ and poloidal B_θ field, plotted over time t/τ. *Bottom panel*: helicity $H(k)$ is plotted over normalized wave number kR. The helicity is calculated with the Taylor hypothesis using the Fourier transformation of the poloidal and toroidal field.

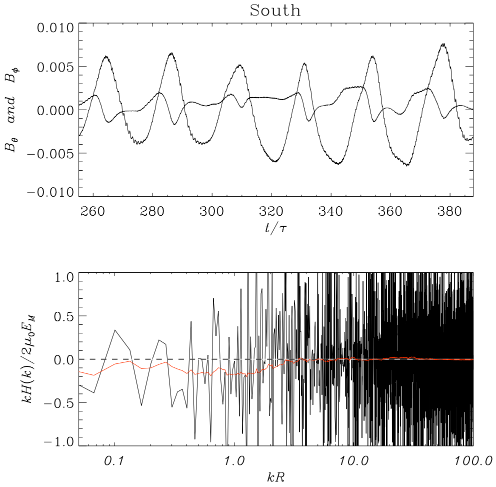

Fig. 19. Helicity in the southern outer atmosphere. The values are written out at the point, $r = 1.5\,R$, $90^\circ - \theta = -17^\circ$ and $\phi = 8.6^\circ$. *Top panel*: phase relation between the toroidal B_ϕ and poloidal B_θ field, plotted over time t/τ. *Bottom panel*: helicity $H(k)$ is plotted over normalized wave number kR. The helicity is calculated with the Taylor hypothesis using the Fourier transformation of the poloidal and toroidal field.

Brandenburg et al. (2011). Here, hats indicate Fourier transforms and the asterisk denotes complex conjugation.

In Figs. 18 and 19 we show the results for the northern and southern hemispheres, as well as time series of the two relevant components B_θ and B_ϕ. The resulting magnetic helicity spectra, normalized by $2\mu_0 E_\mathrm{M}/k$, where E_M is the magnetic energy spectrum, give a quantity that is between -1 and $+1$. Note that the time traces are governed by a low frequency component of fairly large amplitude. In addition, there are also other components of higher frequency, but they are harder to see. The results suggest positive magnetic helicity in the north and negative in the south, which would be indicative of the helicities of the solar wind at smaller length scale. It also agrees with the current helicities determined using explicit evaluation in real space. On the other hand, the Parker spiral (Parker 1958) might be responsible for the magnetic helicity at large scales (Bieber et al. 1987a,b).

4. Conclusions

In the present work we have demonstrated that CME-like phenomena are ubiquitous in simulations that include both a helicity-driven dynamo and a nearly force-free exterior above it. This was first shown in Cartesian geometry (Warnecke & Brandenburg 2010) and is now also verified for spherical geometry. A feature common to both models is that the helical driving is confined to what we call the turbulence zone, which would correspond to the convection zone in the Sun. In contrast to the earlier work, we have now used a helical forcing for which the kinetic helicity changes sign across the equator. This makes the dynamo oscillatory and displays equatorward migration of magnetic field (Mitra et al. 2010a). More importantly, unlike our earlier work where the gas pressure was neglected in the outer parts, it is fully retained here, because it does automatically become small away from the surface due to the effect of gravity that is here included too, but was neglected in the earlier Cartesian model. The solutions shown here and those of Warnecke & Brandenburg (2010) demonstrate that this new approach of combining a self-consistent dynamo with a corona-like exterior is a viable one and can model successfully features that are similar to those in the Sun. However, our model is still not sophisticated enough for direct quantitative comparisons.

Of particular interest is the sign change of magnetic and current helicities with radius. Although similar behavior has also been seen in other Cartesian models of Brandenburg et al. (2009), its relevance for the Sun was unknown until evidence for similar sign properties emerged from solar wind data (Brandenburg et al. 2011). In the present case we were also able to corroborate similar findings by using the Taylor hypothesis based on the plasmoid ejection speed. It is remarkable that this appears to be sufficient for relating spatial and temporal fluctuations to each other.

There are many ways in which the present model can be extended and made more realistic. On the one hand, the assumption of isothermal stratification could be relaxed and the increase of temperature in the corona together with the solar wind could be modeled in a reasonably realistic way. On the other hand, the dynamo model could be modified to include the effects of convection and of latitudinal differential rotation. Among other things, differential rotation would lead to the Parker spiral (Parker 1958), which is known to produce magnetic helicity of its own (Bieber et al. 1987a,b). It would then be interesting to see how this affects the magnetic helicity distribution seen in the present model.

Acknowledgements. We thank the anonymous referee for useful suggestions and Matthias Rheinhardt for help with the implementation. We acknowledge the allocation of computing resources provided by the Swedish National Allocations Committee at the Center for Parallel Computers at the Royal Institute of Technology in Stockholm, the National Supercomputer Centers in Linköping and the High Performance Computing Center North. This work was supported in part by the European Research Council under the AstroDyn Research Project

No. 227952 and the Swedish Research Council Grant No. 621-2007-4064, and the National Science Foundation under Grant No. NSF PHY05-51164.

References

Antiochos, S. K., De Vore, C. R., & Klimchuk, J. A. 1999, ApJ, 510, 485
Baryshnikova, Y., & Shukurov, A. M. 1987, Astron. Nachr., 308, 89
Bieber, J. W., Evenson, P. A., & Matthaeus, W. H. 1987a, ApJ, 315, 700
Bieber, J. W., Evenson, P. A., & Matthaeus, W. H. 1987b, J. Geophys. Res., 14, 864
Bingert, S., & Peter, H. 2011, A&A, 530, A112
Blackman, E. G., & Brandenburg, A. 2003, ApJ, 584, L99
Brandenburg, A. 2005, ApJ, 625, 539
Brandenburg, A. 2009, Plasma Phys. Control. Fusion, 51, 124043
Brandenburg, A., & Dobler, W. 2001, A&A, 369, 329
Brandenburg, A., Candelaresi, S., & Chatterjee, P. 2009, MNRAS, 398, 1414
Brandenburg, A., Subramanian, K., Balogh, A., & Goldstein, M. L. 2011, ApJ, 734, 9
Candelaresi, S., Hubbard, A., Brandenburg, A., & Mitra, D. 2011, Phys. Plasmas, 18, 012903
Choudhuri, A. R. 1998, The Physics of Fluids and Plasmas (Cambridge University Press)
Démoulin, P., Mandrini, C. H., van Driel-Gesztelyi, L., et al. 2002, ApJ, 382, 650
Dikpati, M., & Gilman, P. A. 2001, ApJ, 559, 428
Gudiksen, B. V., & Nordlund, Å. 2005, ApJ, 618, 1031
Haugen, N. E. L., Brandenburg, A., & Dobler, W. 2004, Phys. Rev. E, 70, 016308
Hubbard, A., & Brandenburg, A. 2010, Geophys. Astrophys. Fluid Dyn., 104, 577
Käpylä, P. J., & Brandenburg, A. 2009, ApJ, 699, 1059
Krause, F., & Rädler, K.-H. 1980, Mean-field magnetohydrodynamics and dynamo theory (Oxford: Pergamon Press)
Lazarian, A., & Vishniac, E. T. 1999, ApJ, 517, 700
Low, B. C. 1996, Sol. Phys., 167, 217
Livermore, P. W., Hughes, D. W., & Tobias, S. M. 2010, Phys. Fluids, 22, 037101
Matthaeus, W. H., Goldstein, M. L., & Smith, C. 1982, Phys. Rev. Lett., 48, 1256
Mitra, D., Tavakol, R., Brandenburg, A., & Moss, D. 2009, ApJ, 697, 923
Mitra, D., Tavakol, R., Käpylä, P. J., & Brandenburg, A. 2010a, ApJ, 719, L1
Mitra, D., Candelaresi, S., Chatterjee, P., Tavakol, R., & Brandenburg, A. 2010b, Astron. Nachr., 331, 130
Parker, E. N. 1958, ApJ, 128, 664
Rädler, K.-H., & Bräuer, H.-J. 1987, Astron. Nachr., 308, 101
Rust, D. M. 1994, Geophys. Res. Lett., 21, 241
Seehafer, N. 1990, Sol. Phys., 125, 219
Stix, M. 1976, A&A, 47, 243
Subramanian, K., & Brandenburg, A. 2006, ApJ, 648, L71
Sur, S., Subramanian, K., & Brandenburg, A. 2007, MNRAS, 376, 1238
Török, T., & Kliem, B. 2003, A&A, 406, 1043
Warnecke, J., & Brandenburg, A. 2010, A&A, 523, A19
Yoshimura, H. 1976, Sol. Phys., 50, 3

III

J. Space Weather Space Clim. **2** (2012) A11
DOI: 10.1051/swsc/2012011
© Owned by the authors, Published by EDP Sciences 2012

Magnetic twist: a source and property of space weather

Jörn Warnecke[1,2,*], Axel Brandenburg[1,2], and Dhrubaditya Mitra[1]

[1] Nordita, AlbaNova University Center, Roslagstullsbacken 23, SE-10691 Stockholm, Sweden
[2] Department of Astronomy, AlbaNova University Center, Stockholm University, SE-10691 Stockholm, Sweden
*corresponding author: e-mail: `joern@nordita.org`

Received 5 March 2012 / Accepted 10 July 2012

ABSTRACT

Aims: We present evidence for finite magnetic helicity density in the heliosphere and numerical models thereof, and relate it to the magnetic field properties of the dynamo in the solar convection zone.
Methods: We use simulations and solar wind data to compute magnetic helicity either directly from the simulations or indirectly using time series of the skew-symmetric components of the magnetic correlation tensor.
Results: We find that the solar dynamo produces negative magnetic helicity at small scales and positive at large scales. However, in the heliosphere these properties are reversed and the magnetic helicity is now positive at small scales and negative at large scales. We explain this by the fact that a negative diffusive magnetic helicity flux corresponds to a positive gradient of magnetic helicity, which leads to a change of sign from negative to positive values at some radius in the northern hemisphere.

Key words. MHD – turbulence – solar activity – coronal mass ejection (CME) – solar wind

1. Introduction

The magnetic field in the heliosphere is a direct consequence of the solar dynamo converting kinetic energy of the convection zone into magnetic energy. The magnetic field is cyclic with a period of 22 years on average, but has also significant fluctuations on top of this. These fluctuations can be large enough to suppress the number of sunspots to minimum levels for decades, for example during the Maunder minimum. This minimum has been associated with the little ice age in the early 17th century, although the solar activity to Earth climate relation remains ill understood. Of particular interest for space weather are strong variations caused by coronal mass ejections (CMEs). These events are believed to be a result of footpoint motions of the magnetic field at the solar surface, driving strongly stressed magnetic field configurations to a point when they become unstable and release the resulting energy in an instant. CMEs can shed large clouds of magnetized plasma into interplanetary space and can accelerate charged particles to high velocities toward the Earth. The main driver of these ejections is the magnetic field, where the energy of the eruption is stored.

Large-scale dynamos, for example the one operating in the solar convection zone, produce magnetic helicity of opposite sign at large and small scales. Here, magnetic helicity is the dot product of the magnetic field and the vector potential integrated over a certain volume. For a long time it was believed that CMEs are disconnected from the actual dynamo process, but this view has changed in the past 10 years. In the regime of large magnetic Reynolds numbers, or high electric conductivity, the magnetic helicity associated with the small-scale field, quenches the dynamo (Pouquet et al. 1976). This is a concept that is now well demonstrated using periodic box simulations of helically forced turbulence (Brandenburg 2001). However, astrophysical large-scale dynamos are inhomogeneous and drive magnetic helicity fluxes, whose divergence is relevant for alleviating what is now often referred to as catastrophic quenching of the large-scale dynamo. An important fraction of these magnetic helicity fluxes is associated with motions through the solar surface and their eventual ejection into the interplanetary space (Blackman & Brandenburg 2003). Connecting the dynamo with the physics at and above the solar surface is therefore an essential piece of dynamo physics.

In this paper we review the state of such models and their ability to shed magnetic helicity and to produce ejections of the type seen in the Sun. We begin by discussing a simpler model in Cartesian geometry and turn then to models in spherical wedges. Finally, we compare with observations of magnetic helicity in the solar wind and discuss our finding in connection with earlier dynamo models. Full details of this work have been published elsewhere (Warnecke & Brandenburg 2010; Brandenburg et al. 2011; Warnecke et al. 2011), but here we focus on an aspect that is common to all these papers, namely the nature of magnetic twist associated with the ejecta away from the Sun.

2. Plasmoid ejections in Cartesian models

A straightforward extension of dynamos in Cartesian domains is to add an extra layer on top of it that mimics a nearly force-free solar corona above it. This was done by Warnecke & Brandenburg (2010) who used a dynamo that was driven by turbulence that in turn was driven by a forcing function in the momentum equation. To imitate the effects of stratification and rotation that are known to produce helicity, they used a forcing function that was itself helical. This leads to large-scale dynamos that are more efficient than naturally occurring ones that are driven, for example, by rotating convection (see, e.g., Käpylä et al. 2010, 2012; Warnecke et al. 2012). In those

This is an Open Access article distributed under the terms of creative Commons Attribution-Noncommercial License 3.0

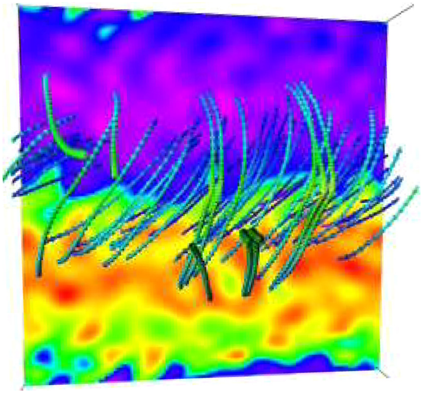

Fig. 1. Three-dimensional visualization of the magnetic field viewed from above. The vertical magnetic field component is color-coded (light/yellow pointing upward and dark/blue pointing downward). Note that the field lines form a left-handed spiral over the scale of the domain, as expected for turbulence with positive helicity at small scales. The x-axis points to the right while the y-axis points upward. Adapted from Warnecke & Brandenburg (2010).

papers, the produced kinetic helicity is much weaker. As mentioned in the beginning, such dynamos can produce magnetic fields whose small-scale contribution has magnetic helicity of the same sign as that of the forcing function and whose large-scale contribution has magnetic helicity of opposite sign.

In our Cartesian model, the two horizontal directions (x and y) are equivalent, but when the large-scale field saturates, it must finally choose one of the two possible directions. This is a matter of chance but, in the case discussed below, the field shows a large-scale variation in the y-direction. The large-scale field settles into a state with minimal horizontal wavenumber, which is here $(k_x, k_y) = (0, k_1)$, where $k_1 = 2\pi/L$ and L is the horizontal extent of the domain. Note that for fields with variation along the diagonal the wavenumber would be $\sqrt{2}$ times larger, so such a state is less preferred.

In Figure 1 we show the surface magnetic field of such a dynamo of the work of Warnecke & Brandenburg (2010). We show color-coded the vertical (line of sight) magnetic field component together with a perspective view of field lines in the volume above, which we shall refer to as the corona region. In addition to fluctuations, we can see a large-scale pattern of the field with a sinusoidal modulation in the x-direction and no systematic variation in the y-direction. The field lines in the corona region show a spiraling pattern corresponding to a left-handed spiral. This is because the helicity of the forcing function is in this model positive (right handed), so the resulting large-scale field must have helicity of the opposite sign.

The large-scale magnetic field is essentially steady in the dynamo region and does not change its overall bipolar structure; see Figure 2 for a perspective view. However, the magnetic field of the corona region shows a time-dependent oscillating structure associated with nearly regularly occurring ejection. The ejection events can be monitored in terms of the current helicity, $\boldsymbol{J} \cdot \boldsymbol{B}$, where $\boldsymbol{J} = \nabla \times \boldsymbol{B}/\mu_0$ is the current density and μ_0 is the vacuum permeability. To compensate for the radial decline of $\boldsymbol{J} \cdot \boldsymbol{B}$, we have scaled it by $\langle \boldsymbol{B}^2 \rangle_{H,t}$, which is here understood as a combined average over horizontal directions and over time. The result is shown in Figure 3.

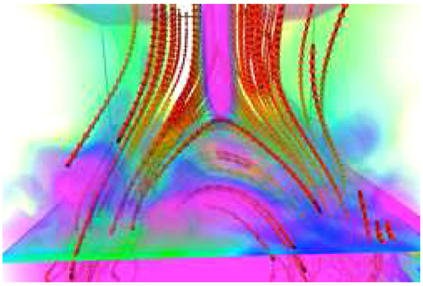

Fig. 2. Magnetic field structure in the dynamo exterior. Field lines are shown in red and the modulus of the current density is shown in pink with semitransparent opacity. Note the formation of a vertical current sheet above the arcade. Adapted from Warnecke & Brandenburg (2010).

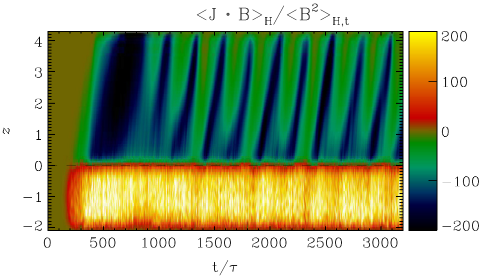

Fig. 3. Dependence of $\langle \boldsymbol{J} \cdot \boldsymbol{B} \rangle_\mathrm{H} / \langle \boldsymbol{B}^2 \rangle_\mathrm{H,t}$ on time and height. Dark/blue stands for negative and light/yellow for positive values. For this run the vertical extent of the domain is $-\frac{2}{3}\pi \le z \le \frac{4}{3}\pi$.

It is remarkable that the field does not remain steady in the outer parts. This can be seen more clearly in a sequence of field line visualizations in Figure 4. Here, the magnetic field is averaged over the x-direction and we show $\langle B_x \rangle_x$ color-coded together with magnetic field lines as contours of $\langle A_x \rangle_x$ in the yz-plane. Light/yellow shades correspond to positive values, the dark/blue to negative, similar to Figure 3. Note that a concentration in B_x emerges from the lower region to the outer one. The magnetic field lines surround the concentration and form a shape similar to plasmoid ejections, which are believed to be a two-dimensional model of producing CMEs (Ortolani & Schnack 1993). At a time of $t/\tau = 2881$ turnover times, the concentration is split into two parts, where the upper one leaves the domain through the upper boundary, while the lower one stays in the lower layer. Here, $\tau = (u_\mathrm{rms} k_\mathrm{f})^{-1}$ is the turnover time based on the forcing wavenumber k_f and u_rms is the root mean squared velocity averaged in the lower layer. At $t/\tau = 3041$, the field lines have formed an X-point in the center of the upper layer. In an X-point, field lines reconnect and release large amounts of energy through Ohmic heating. In the Sun these reconnection events are believed to trigger an eruptive flare, which can cause a CME. A similar behavior can also be seen in more realistic models in spherical geometry, as will be discussed in the next section.

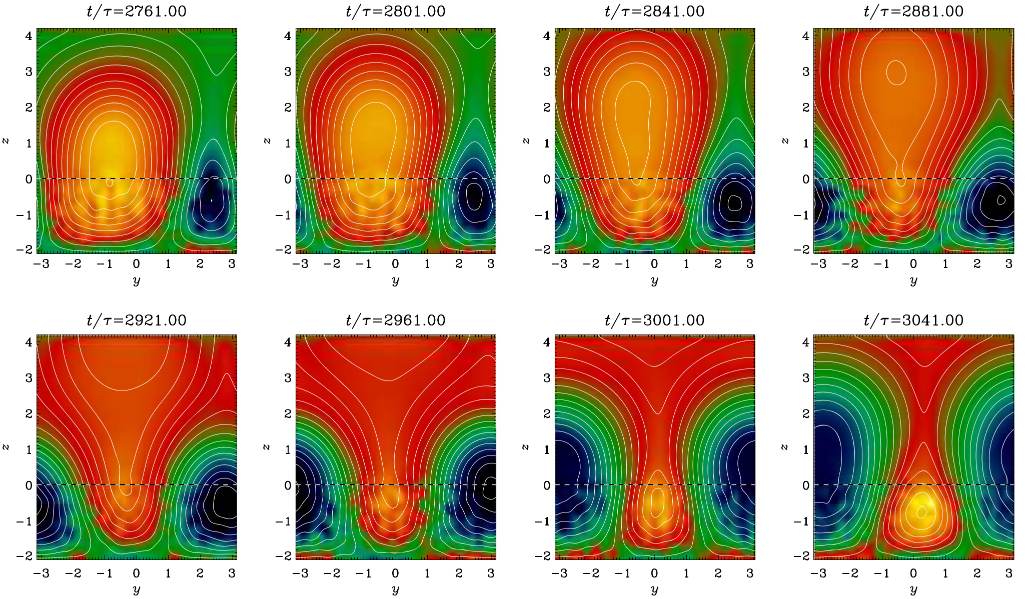

Fig. 4. Time series of the formation of a plasmoid ejection. Contours of $\langle A_x\rangle_x$ are shown together with a color-scale representation of $\langle B_x\rangle_x$; dark/blue stands for negative and light/yellow for positive values, as in Figure 3. The contours of $\langle A_x\rangle_x$ correspond to field lines of $\langle \boldsymbol{B}\rangle_x$ in the yz-plane. The dashed horizontal lines show the location of the surface at $z = 0$. For this run the vertical extent of the domain is $-\frac{2}{3}\pi \le z \le \frac{4}{3}\pi$.

3. Helicity reversals in spherical models

While similar ejection events are also seen in spherical geometry, a more surprising property is a reversal of the current helicity in the radial direction (Warnecke et al. 2011). In Figure 5 we show visualizations of $\boldsymbol{J} \cdot \boldsymbol{B}$ in meridional planes. The figure shows two examples of coronal ejections which we found to be ejected from the dynamo region into the atmosphere. At $t/\tau = 358$ we can identify a shape that is similar to that of the three-part structure of CMEs, observed on the Sun (Low 1996). It consists of an arch of one sign of current helicity in front of a bulk of opposite sign and a cavity in between. As shown in Figure 5, the ejection leaves the domain on the radial boundary and a new ejection of opposite sign occurs. We also see that in the dynamo region the current helicity is negative in the northern hemisphere and positive in the southern. This seems to be basically true also in the immediate proximity above the surface, but there is now an increasing tendency for the occurrence of magnetic helicity of opposite sign ahead of the ejecta. This seems to be associated with a redistribution of twist in the swept-up material. The current helicity is by far not always of the same sign, but both signs occur and there is only a slight preference of one sign over the other. This is seen more clearly in Figure 6, where we show a time series of $\boldsymbol{J} \cdot \boldsymbol{B}$ versus radial position r/R and time t/τ.

A time series of the normalized current helicity, $\overline{\boldsymbol{J} \cdot \boldsymbol{B}}/\langle \boldsymbol{B}^2\rangle_t$, evaluated at radius $r = 1.7\,R$ and 28° latitude, is shown in Figure 7, where we also show their running means. It is now quite clear that on average the sign of current helicity has changed relative to what it was in the dynamo region. This is seen explicitly in a time-averaged plot of current helicity in the meridional plane (Fig. 8).

This reversal is significant because similar behavior has also been seen in recent measurements of the magnetic helicity spectrum in the solar wind (Brandenburg et al. 2011), but before showing the evidence for this, let us first discuss in more detail a similar diagnostic for the simulations. In Figure 9 we show the time variations of B_θ and B_ϕ and the magnetic helicity spectrum obtained from these time series. Unlike the solar wind, where a time series can be used to mimic a scan in distance space (the so-called Taylor hypothesis), this argument fails in the present case, because no wind is produced in the present model. There is only the pattern speed associated with the CMEs. Whether this is enough to motivate the use of the Taylor hypothesis is rather unclear. Nevertheless, there is a remarkable similarity with similar helicity spectra obtained for the solar wind; see Figure 10. In both cases, magnetic helicity has been obtained under the assumption of local isotropy of the turbulence. This means that one computes the one-dimensional magnetic energy $E_{\rm M}^{\rm 1D}(k_R)$ and magnetic helicity spectra $H_{\rm M}^{\rm 1D}(k_R)$ simply as

$$E_{\rm M}^{\rm 1D}(k_R) = \left|\hat{\boldsymbol{B}}\right|^2/\mu_0, \quad H_{\rm M}^{\rm 1D}(k_R) = 4\,{\rm Im}(\hat{B}_\theta \hat{B}_\phi^*)/k_R, \qquad (1)$$

where k_R is the component of the wave vector in the radial direction. Here, a hat denotes Fourier transformation and an asterisk complex conjugation. These are the equations used by Matthaeus et al. (1982) who applied such an analysis to data from *Voyager 2*. Since *Voyager 2* flew close to the ecliptic, the magnetic helicity is dominated by fluctuations. This is why Brandenburg et al. (2011) applied this analysis to *Ulysses* data, where a net magnetic helicity was seen for the first time. An important advantage of *Ulysses* over *Voyager 1* and *2* is the high angle with the ecliptic. So, only with *Ulysses* we can measure the magnetic helicity far away from the ecliptic in both hemispheres of the heliosphere.

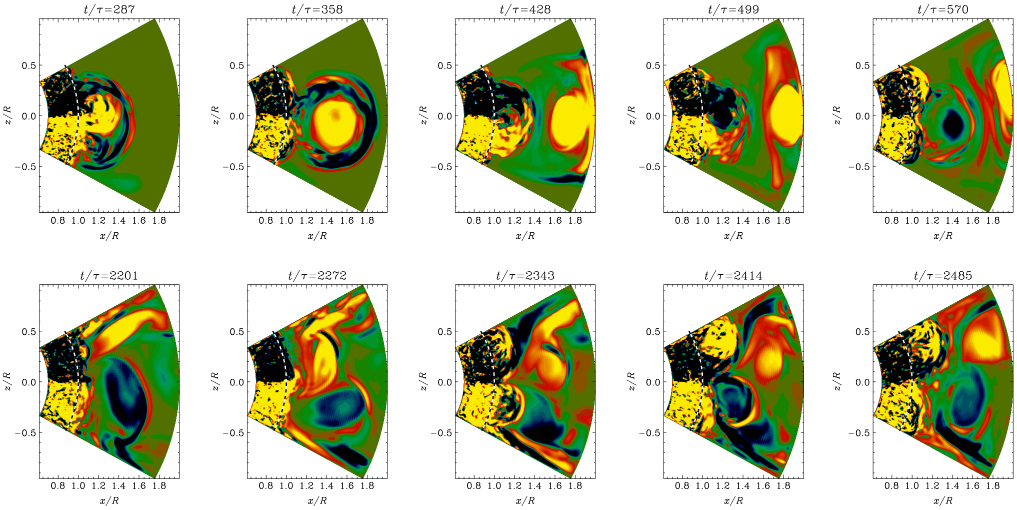

Fig. 5. Time series of coronal ejections in spherical coordinates. The normalized current helicity, $\overline{\boldsymbol{J}\cdot\boldsymbol{B}}/\langle\overline{\boldsymbol{B}^2}\rangle_t$, is shown in a color-scale representation for different times; dark/blue stands for negative and light/yellow for positive values, as in Figure 3. The dashed lines show the location of the surface at $r^2 = x^2 + z^2 = R^2$.

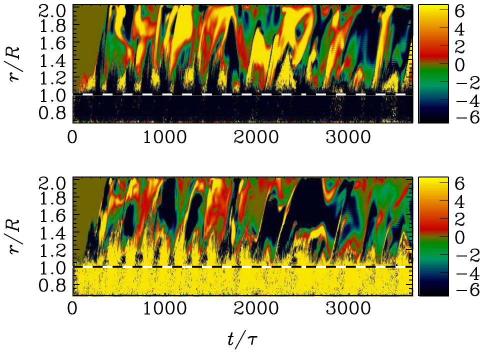

Fig. 6. Dependence of the dimensionless ratio $\overline{\boldsymbol{J}\cdot\boldsymbol{B}}/\langle\overline{\boldsymbol{B}^2}\rangle_t$ on time and radius. The top panel shows a narrow band in θ in the northern hemisphere and the bottom one a narrow band in the southern hemisphere. Dark/blue stands for negative and light/yellow for positive values. The dashed horizontal lines show the location of the surface at $r = R$.

What we see both in the simulations and in the solar wind is that there is magnetic helicity of opposite sign at large and small scales. However, it is exactly the other way around than what is found in the corona region; see Table 1. To understand the reason for this, we need to consider the equations for the production of magnetic helicity at large and small length scales. As will be argued in Section 4, the mechanism that sustains negative small-scale helicity in the north is turned off in the solar wind, and there is just the effect of turbulent magnetic diffusion which contributes with opposite sign. By contrast, inside the dynamo region, turbulent diffusion is subdominant, because otherwise no large-scale magnetic field would be generated. However, in the wind we do not expect the dynamo to be excited, so here diffusion dominates.

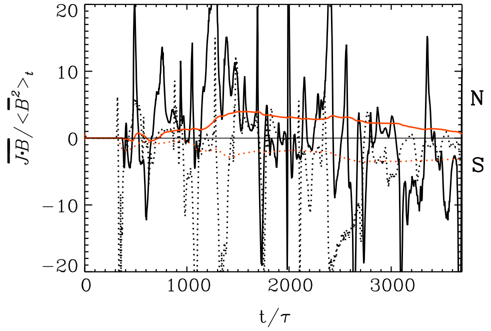

Fig. 7. Dependence of the dimensionless ratio $\overline{\boldsymbol{J}\cdot\boldsymbol{B}}/\langle\overline{\boldsymbol{B}^2}\rangle_t$ on time at radius $r = 1.7R$ and 28° latitude. The solid line stands for the northern hemisphere and the dotted for the southern hemisphere. The red lines represent the cumulative mean for each hemisphere.

4. Connection with earlier dynamo models

The purpose of this section is to make contact with dynamo theory and to understand more quantitatively why the magnetic helicity reverses sign with radius. In essence, we argue that the profile of magnetic helicity density must have a positive radial gradient to maintain a negative diffusive magnetic helicity flux and that this is the reason for the magnetic helicity to change from a negative sign to a positive one at some radius in the northern hemisphere.

We begin by discussing the magnetic helicity equation. The magnetic helicity density is $h = \boldsymbol{A}\cdot\boldsymbol{B}$, where $\boldsymbol{B} = \boldsymbol{\nabla}\times\boldsymbol{A}$ is the magnetic field expressed in terms of the magnetic vector potential $\boldsymbol{A}$ which, in the Weyl gauge, satisfies $\partial\boldsymbol{A}/\partial t = \boldsymbol{U}\times\boldsymbol{B} - \eta\mu_0\boldsymbol{J}$. The evolution equation for $\boldsymbol{A}\cdot\boldsymbol{B}$ is then

$$\frac{\partial}{\partial t}\boldsymbol{A}\cdot\boldsymbol{B} = -2\eta\mu_0\boldsymbol{J}\cdot\boldsymbol{B} - \boldsymbol{\nabla}\cdot\boldsymbol{F}, \tag{2}$$

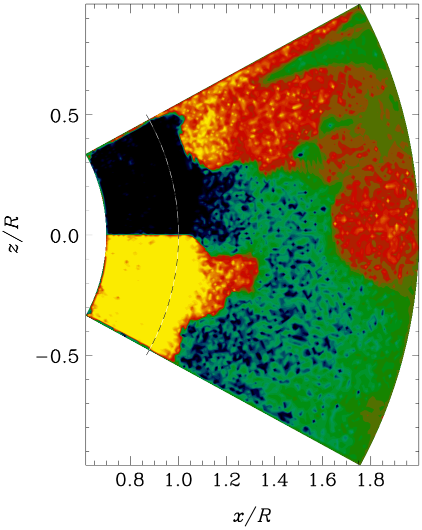

Fig. 8. Current helicity averaged over time. Dark/blue corresponds to negative values, while the light/yellow corresponds to positive value, as in Figure 6. The dashed line shows the location of the surface at $r^2 = x^2 + z^2 = R^2$.

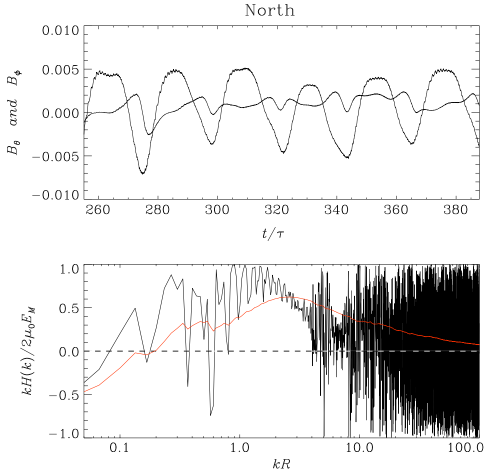

Fig. 9. Helicity in the northern outer atmosphere. The values are written out at the point, $r = 1.5\ R$, $90° - \theta = 17°$, and $\phi = 9°$. *Top panel:* phase relation between the toroidal B_ϕ and poloidal B_θ field, plotted over time t/τ. *Bottom panel:* helicity $H(k)$ is plotted over normalized wavenumber kR. The helicity is calculated with the Taylor hypothesis using the Fourier transformation of the poloidal and toroidal field. Adapted from Warnecke et al. (2011).

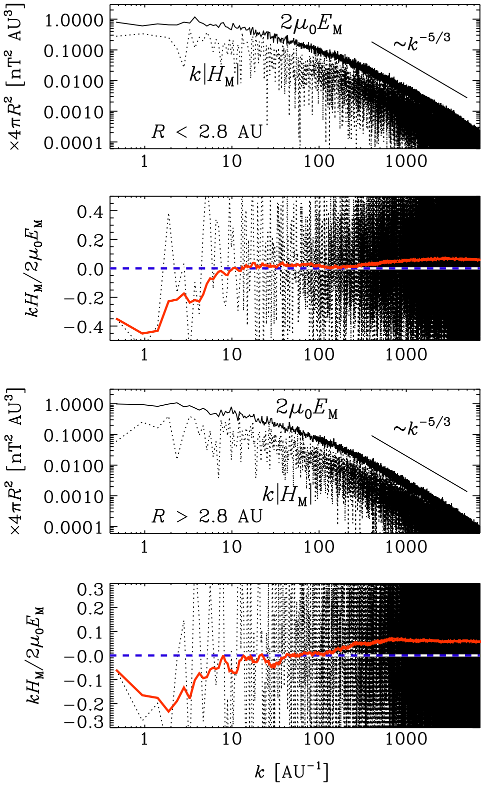

Fig. 10. Magnetic energy and helicity spectra, $2\mu_0 E_M(k)$ and $k|H_M(k)|$, respectively, for two separate distance intervals (first and third panels). Furthermore, both spectra are scaled by $4\pi R^2$ before averaging within each distance interval above and below 2.8 AU, respectively. The relative magnetic helicity, $kH_M(k)/2\mu_0 E_M(k)$, is plotted separately (second and fourth panels) together with its cumulative average starting from the low wavenumber end. The zero line is shown as dashed. Adapted from Brandenburg et al. (2011).

Table 1. Distribution of magnetic helicity at large and small scales both in the dynamo region close to or below the surface and the corona region, solar wind or the exterior of the dynamo.

Magnetic helicity	Large scales	Small scales
Dynamo region, interior	+	–
Corona region, solar wind, exterior	–	+

where $\boldsymbol{F}$ is the magnetic helicity flux. Next, we define large-scale fields as averaged quantities, denoted by an overbar, and small-scale fields as the residual, denoted by lower case characters, so the magnetic field can be split into two contributions via $\boldsymbol{B} = \overline{\boldsymbol{B}} + \boldsymbol{b}$. Likewise, $\boldsymbol{A} = \overline{\boldsymbol{A}} + \boldsymbol{a}$, $\boldsymbol{J} = \overline{\boldsymbol{J}} + \boldsymbol{j}$, and $\boldsymbol{U} = \overline{\boldsymbol{U}} + \boldsymbol{u}$. The evolution equation for the mean magnetic helicity density $\overline{h} = \overline{\boldsymbol{A}\cdot\boldsymbol{B}}$ is given by

$$\frac{\partial}{\partial t}\overline{\boldsymbol{A}\cdot\boldsymbol{B}} = -2\eta\mu_0\overline{\boldsymbol{J}\cdot\boldsymbol{B}} - \boldsymbol{\nabla}\cdot\overline{\boldsymbol{F}}. \qquad (3)$$

To determine the magnetic helicity density of the mean field, $\overline{h}_{\rm m} = \overline{\boldsymbol{A}}\cdot\overline{\boldsymbol{B}}$, we use the averaged induction equation in the Weyl gauge, $\partial\overline{\boldsymbol{A}}/\partial t = \overline{\boldsymbol{U}}\times\overline{\boldsymbol{B}} + \overline{\boldsymbol{u}\times\boldsymbol{b}} - \eta\mu_0\overline{\boldsymbol{J}}$, so that

$$\frac{\partial}{\partial t} = \overline{\boldsymbol{A}}\cdot\overline{\boldsymbol{B}} = 2\overline{\boldsymbol{u}\times\boldsymbol{b}}\cdot\overline{\boldsymbol{B}} - 2\eta\mu_0\overline{\boldsymbol{J}}\cdot\overline{\boldsymbol{B}} - \boldsymbol{\nabla}\cdot\overline{\boldsymbol{F}}_{\rm m}. \qquad (4)$$

The magnetic helicity equation for the fluctuating field, $\overline{h}_{\rm f} = \overline{h} - \overline{h}_{\rm m} = \overline{\boldsymbol{a}\cdot\boldsymbol{b}}$, takes then the form

$$\frac{\partial}{\partial t}\overline{\boldsymbol{a}\cdot\boldsymbol{b}} = -2\overline{\boldsymbol{u}\times\boldsymbol{b}}\cdot\overline{\boldsymbol{B}} - 2\eta\mu_0\overline{\boldsymbol{j}\cdot\boldsymbol{b}} - \boldsymbol{\nabla}\cdot\overline{\boldsymbol{F}}_{\rm f}, \qquad (5)$$

so that the sum of equations (4) and (5) gives equation (3). Here, the total magnetic helicity flux consists of contribution from mean and fluctuating fields, denoted by subscripts m and f, respectively, i.e., $\overline{\boldsymbol{F}}_{\rm m} + \overline{\boldsymbol{F}}_{\rm f} = \overline{\boldsymbol{F}}$. Note that, even in the limit $\eta \to 0$ and in the absence of fluxes, magnetic helicity at large and small scales is not conserved individually, but there can be an exchange of magnetic helicity between scales.

A note regarding the gauge-dependence is here in order. Obviously, equation (5) depends on the gauge choice for $\boldsymbol{a}$. However, if we are in a steady state, and if $\overline{h}_{\rm f}$ also happens to be steady (which is not automatically guaranteed), then we have

$$\nabla\cdot\overline{\boldsymbol{F}}_{\rm f} = -2\overline{\boldsymbol{u}\times\boldsymbol{b}}\cdot\overline{\boldsymbol{B}} - 2\eta\mu_0\overline{\boldsymbol{j}\cdot\boldsymbol{b}}, \qquad (6)$$

and since the right-hand side of this equation is manifestly gauge-invariant, $\nabla\cdot\overline{\boldsymbol{F}}_{\rm f}$ must also be gauge-invariant. This property was used in earlier work of Mitra et al. (2010), Hubbard & Brandenburg (2010) and Warnecke et al. (2011) to determine the scaling of $\overline{\boldsymbol{F}}_{\rm f}$ with $\nabla\overline{h}_{\rm f}$ and thus the turbulent diffusion coefficient κ_h. In addition, if there is sufficient scale separation between large and small scales, which is typically the case in the nonlinear regime at the end of the inverse cascade process (Brandenburg 2001), then $\overline{h}_{\rm f}$ can be expressed as a density of linkages, which is itself manifestly gauge-independent (Subramanian & Brandenburg 2006). This property then also applies to the flux $\overline{\boldsymbol{F}}_{\rm f}$.

The correlation $\overline{\boldsymbol{u}\times\boldsymbol{b}}$ is known to have two contributions, one proportional to $\overline{\boldsymbol{B}}$ with a pseudo-tensor in front of it (the α effect, responsible for large-scale field generation), and one proportional to $\overline{\boldsymbol{J}}$ with a coefficient $\eta_{\rm t}$ in front of it that corresponds to turbulent diffusion, i.e.,

$$\overline{\boldsymbol{u}\times\boldsymbol{b}} = \alpha\overline{\boldsymbol{B}} - \eta_{\rm t}\mu_0\overline{\boldsymbol{J}}, \qquad (7)$$

where we have again assumed isotropy. The reason why the mean magnetic helicity density of the small-scale field is negative in the north is because $\alpha > 0$ in the north (e.g., Krause & Rädler 1980), producing therefore negative magnetic helicity at a rate $-2\alpha\overline{\boldsymbol{B}}^2 < 0$ for small-scale fields and $+2\alpha\overline{\boldsymbol{B}}^2 > 0$ for large-scale fields, so that their sum vanishes. There is also turbulent magnetic diffusion which reduces this effect, because $\eta_{\rm t} > 0$ and $\overline{\boldsymbol{J}}\cdot\overline{\boldsymbol{B}} > 0$ in the north. In the solar wind no new magnetic field is generated, so turbulent magnetic diffusion could now dominate and might thus explain a reversal of magnetic helicity density (Brandenburg et al. 2011).

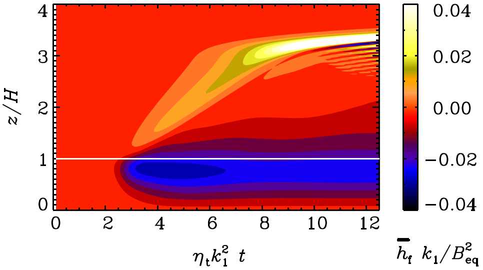

Fig. 11. *zt* diagrams of $\overline{h}_{\rm f}$ for an α^2 dynamo with a wind which stops all of a sudden at $z/H = 3$. The white horizontal line marks the location $z = H$. Light/yellow shades indicate positive values and dark/blue shades indicate negative values.

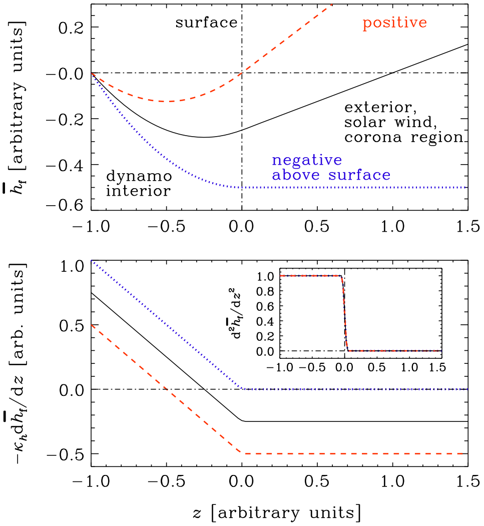

Fig. 12. Sketch showing possible solutions $\overline{h}_{\rm f}(z)$ (upper panel) to equation (8) with S = const = -1 in $z < 0$ and $S = 0$ in $z > 0$. The red (dashed) and black (solid) lines show solutions for which the magnetic helicity flux ($-\kappa_h{\rm d}\overline{h}_{\rm f}/z$, see lower panel) is negative in the exterior. This corresponds to the case observed in the Sun. The blue (dotted) line shows the case, where the magnetic helicity flux is zero above the surface and therefore does not reverse the sign of $\overline{h}_{\rm f}(z)$ in the exterior.

Support for a reversal of the sign of magnetic helicity was first seen in dynamo simulations with magnetic helicity flux in the exterior. In Figure 11 we show a representation of magnetic helicity density of small-scale fields $\overline{h}_{\rm f} = \overline{\boldsymbol{a}\cdot\boldsymbol{b}}$ versus z and t for a model similar to that of Brandenburg et al. (2009), but where the magnetic helicity flux is caused by a wind that is then running into a shock[1] where the flux is artificially suppressed at height $z = 3H$. This figure shows that there is a clear segregation of negative and positive small-scale magnetic helicities in the dynamo regime and the exterior, respectively.

In our description above we have suggested that the magnetic helicity production balances the $\partial\overline{\boldsymbol{a}\cdot\boldsymbol{b}}/{\rm d}t$ term, but this cannot be true in the steady state. Instead, it must be the divergence of the magnetic helicity flux, $\boldsymbol{\nabla}\cdot\overline{\boldsymbol{F}}_{\rm f}$. Let us assume that $\overline{\boldsymbol{F}}_{\rm f}$ can be approximated by a Fickian diffusion law, i.e., $\overline{\boldsymbol{F}}_{\rm f} = -\kappa_h\boldsymbol{\nabla}\overline{h}_{\rm f}$. Simulations have suggested that $\kappa_h/\eta_{\rm t}$ is around 0.3 (Hubbard & Brandenburg 2010; Mitra et al. 2010; Warnecke et al. 2011). Thus, balancing now the source $S(z) \equiv -2\alpha\overline{\boldsymbol{B}}^2 + 2\eta_{\rm t}\mu_0\overline{\boldsymbol{J}\cdot\boldsymbol{B}}$ against the divergence of the flux of magnetic helicity at small scales, we have, in a one-dimensional model (neglecting the molecular diffusion term, $2\eta\mu_0\overline{\boldsymbol{j}\cdot\boldsymbol{b}}$):

---

[1] Note that the shock at $z/H = 3$ becomes eventually underresolved and the simulation has to be terminated. This is what causes the wiggles in the proximity of the shock.

$$S(z) = -\kappa_h \frac{\mathrm{d}^2\overline{h}_\mathrm{f}}{\mathrm{d}z^2}. \tag{8}$$

Taking as an example a source where $S(z)/\kappa_h = -1$ in the dynamo interior ($z < 0$), and $S(z) = 0$ in $z > 0$, we have a family of solutions of equation (8) that only differ in an undetermined integration constant corresponding to a constant offset in the flux; see the second panel of Figure 12. The solutions for which the magnetic helicity flux, $-\kappa_h \mathrm{d}\overline{h}_\mathrm{f}/\mathrm{d}z$, is negative in the exterior are those for which $\overline{h}_\mathrm{f}$ reaches an extremum below the surface. This seems to be what happens both in simulations and in the solar wind. We can thus conclude that the reason for a sign change is not a dominance of turbulent diffusion in the solar wind, but just the possibility of the magnetic helicity density reaching an extremum *below* the surface (dashed red and solid black lines in Figure 12), not at the surface (dotted blue lines).

5. Conclusions

As we have seen in the present paper, magnetic twist (or helicity) plays an important role for the solar dynamo (Brandenburg 2001; Blackman & Brandenburg 2002) and for producing eruptions of the form of CMEs (Low 1996, 2001). The recent work of Warnecke & Brandenburg (2010) and Warnecke et al. (2011) tries to combine both aspects into one. Although the models are still rather unrealistic in many respects, they have already now led to useful insights into the interplay between dynamo models and solar wind turbulence. In particular, they have allowed us to understand the properties of magnetic helicity fluxes. We have confirmed that the hemispheric sign rule of magnetic helicity does not extend unchanged into the interplanetary space, but we have now shown that it must flip sign somewhere above the solar surface. On the other hand, Bothmer & Schwenn (1998) found that the magnetic clouds follow Hale's polarity and that the sign of the magnetic helicity is the same as in the interior. However, this result is not based on rigorous statistics.

Future work in this direction should include more realistic modeling of the solar convection zone. Preliminary work in this direction is already underway (Warnecke et al. 2012). Furthermore, it will be necessary to allow for the development of a proper solar wind from the dynamo region. One of the difficulties here is that, if the critical point is assumed to be too close to the solar surface, which would be computationally convenient because it would allow us to use a smaller domain, the mass loss rate would be rather high and could destroy the dynamo. In future work we will be trying to strike an appropriate compromise that will allow us to study the qualitatively new effects emerging from this.

Acknowledgements. We acknowledge the allocation of computing resources provided by the Swedish National Allocations Committee at the Center for Parallel Computers at the Royal Institute of Technology in Stockholm, the National Supercomputer Centers in Linköping and the High Performance Computing Center North in Umeå. This work was supported in part by the European Research Council under the AstroDyn Research Project No. 227952 and the Swedish Research Council Grant No. 621-2007-4064, and the National Science Foundation under Grant No. NSF PHY05-51164.

References

Blackman, E.G., and A. Brandenburg, Dynamic nonlinearity in large scale dynamos with shear, *Astrophys. J.*, **579**, 359–373, 2002.

Blackman, E.G., and A. Brandenburg, Doubly helical coronal ejections from dynamos and their role in sustaining the solar cycle, *Astrophys. J.*, **584**, L99–L102, 2003.

Bothmer, V., and R. Schwenn, The structure and origin of magnetic clouds in the solar wind, *Ann Geophysicae*, **16**, 1–24, 1998.

Brandenburg, A., The inverse cascade and nonlinear alpha-effect in simulations of isotropic helical hydromagnetic turbulence, *Astrophys. J.*, **550**, 824–840, 2001.

Brandenburg, A., S. Candelaresi, and P. Chatterjee, Small-scale magnetic helicity losses from a mean-field dynamo, *MNRAS*, **398**, 1414–1422, 2009.

Brandenburg, A., K. Subramanian, A. Balogh, and M.L. Goldstein, Scale-dependence of magnetic helicity in the solar wind, *Astrophys. J.*, **734**, 9, 2011.

Hubbard, A., and A. Brandenburg, Magnetic helicity fluxes in an α^2 dynamo embedded in a halo, *Geophys. Astrophys. Fluid Dyn.*, **104**, 577–590, 2010.

Käpylä, P.J., M.J. Korpi, A. Brandenburg, D. Mitra, and R. Tavakol, Convective dynamos in spherical wedge geometry, *Astron. Nachr.*, **331**, 73–81, 2010.

Käpylä, P.J., M.J. Mantere, and A. Brandenburg, Cyclic magnetic activity due to turbulent convection in spherical wedge geometry, *Astrophys. J. Lett.*, **755**, L22, 2012.

Krause, F., and K.-H. Rädler, *Mean-Field Magnetohydrodynamics and Dynamo Theory*, Pergamon Press, Oxford, 1980.

Low, B.C., Solar Activity and the Corona, *Sol. Phys.*, **167**, 217–265, 1996.

Low, B.C., Coronal mass ejections, magnetic flux ropes, and solar magnetism, *J. Geophys. Res.*, **106**, 25141–25163, 2001.

Matthaeus, W.H., M.L. Goldstein, and C. Smith, Evaluation of magnetic helicity in homogeneous turbulence, *Phys. Rev. Lett.*, **48**, 1256–1259, 1982.

Mitra, D., S. Candelaresi, P. Chatterjee, R. Tavakol, and A. Brandenburg, Equatorial magnetic helicity flux in simulations with different gauges, *Astron Nachr.*, **331**, 130–135, 2010.

Ortolani, S., and D.D. Schnack, *Magnetohydrodynamics of Plasma Relaxation*, World Scientific, Singapore, 1993.

Pouquet, A., U. Frisch, and J. Léorat, Strong MHD helical turbulence and the nonlinear dynamo effect, *J. Fluid Mech.*, **77**, 321–354, 1976.

Subramanian, K., and A. Brandenburg, Magnetic helicity density and its flux in weakly inhomogeneous turbulence, *Astrophys. J.*, **648**, L71–L74, 2006.

Warnecke, J., and A. Brandenburg, Surface appearance of dynamo-generated large-scale fields, *A&A*, **523**, A19, 2010.

Warnecke, J., A. Brandenburg, and D. Mitra, Dynamo-driven plasmoid ejections above a spherical surface, *A&A*, **534**, A11, 2011.

Warnecke, J., P.J. Käpylä, M.J. Mantere, and A. Brandenburg, *Sol. Phys.*, 2012, in press, arXiv:1112.0505.

IV

Solar Phys
DOI 10.1007/s11207-012-0108-4

ADVANCES IN EUROPEAN SOLAR PHYSICS

Ejections of Magnetic Structures Above a Spherical Wedge Driven by a Convective Dynamo with Differential Rotation

**Jörn Warnecke · Petri J. Käpylä · Maarit J. Mantere ·
Axel Brandenburg**

Received: 2 December 2011 / Accepted: 14 August 2012
© Springer Science+Business Media B.V. 2012

Abstract We combine a convectively driven dynamo in a spherical shell with a nearly isothermal density-stratified cooling layer that mimics some aspects of a stellar corona to study the emergence and ejections of magnetic field structures. This approach is an extension of earlier models, where forced turbulence simulations were employed to generate magnetic fields. A spherical wedge is used which consists of a convection zone and an extended coronal region to ≈ 1.5 times the radius of the sphere. The wedge contains a quarter of the azimuthal extent of the sphere and 150° in latitude. The magnetic field is self-consistently generated by the turbulent motions due to convection beneath the surface. Magnetic fields are found to emerge at the surface and are ejected to the coronal part of the domain. These ejections occur at irregular intervals and are weaker than in earlier work. We tentatively associate these events with coronal mass ejections on the Sun, even though our model of the solar atmosphere is rather simplistic.

Keywords Magnetic fields, corona · Coronal mass ejections, theory · Interior, convective zone · Turbulence · Helicity, current

---

Advances in European Solar Physics
Guest Editors: Valery M. Nakariakov, Manolis K. Georgoulis, and Stefaan Poedts

---

J. Warnecke (✉) · P.J. Käpylä · A. Brandenburg
Nordita, KTH Royal Institute of Technology and Stockholm University, Roslagstullsbacken 23,
10691 Stockholm, Sweden
e-mail: joern@nordita.org

J. Warnecke · A. Brandenburg
Department of Astronomy, Stockholm University, 10691 Stockholm, Sweden

P.J. Käpylä · M.J. Mantere
Department of Physics, Gustaf Hällströmin katu 2a, P.O. BOX 64, 00014 Helsinki University, Finland

Published online: 27 September 2012

1. Introduction

Recent observations of the *Solar Dynamic Observatory* (SDO: Pesnell, Thompson, and Chamberlin, 2012) have provided us with a record of impressive solar eruptions. These eruptions are mostly associated with coronal mass ejections (CMEs). These are events through which the Sun sheds hot plasma and magnetic fields from the corona into the interplanetary space. The energy causing such huge eruptions is stored in the magnetic field and can be released *via* reconnection of field lines (Sturrock, 1980; Antiochos, De Vore, and Klimchuk, 1999). Some of the CMEs are directed towards the Earth, hitting its magnetosphere and causing phenomena like aurorae. Furthermore, encounters with CMEs can cause sudden outages of GPS signals due to ionospheric scintillation. The resulting radiation dose from such events poses risks to astronauts. This is now also of concern to airlines, because the radiation load during polar flights can reach annual limits, especially for pregnant women. This leads to great interest of scientists in many fields of physics. However, there is an additional motivation which comes along with space weather effects. The solar dynamo, which is broadly believed to be responsible for the generation of the solar magnetic field, needs to be sustained by shedding magnetic helicity from the Sun's interior (Blackman and Brandenburg, 2003). Mean-field and direct numerical simulations have shown that the magnetic field generation is catastrophically quenched at high magnetic Reynolds numbers in closed systems (Vainshtein and Cattaneo, 1992) that do not allow magnetic helicity fluxes out of the domain (Blackman and Field, 2000a, 2000b; Brandenburg and Sandin, 2004), or between different parts of it (Brandenburg, Candelaresi, and Chatterjee, 2009; Mitra *et al.*, 2010; Hubbard and Brandenburg, 2010). The magnetic Reynolds number, which quantifies the relative importance of advective to diffusive terms in the induction equation, is known to be very large in the Sun, therefore implying the possibility of catastrophic quenching in models of the solar dynamo, unless efficient magnetic helicity fluxes occur, for example through CMEs (Blackman and Brandenburg, 2003). Indeed, CMEs are well known to be closely associated with magnetic helicity (Low, 2001). In particular observations (Plunkett *et al.*, 2000; Régnier, Amari, and Kersalé, 2002) and a recent study by Thompson, Kliem, and Török (2011), where the observations are compared with numerical models, suggest that CMEs have a twisted magnetic structure, implying that CMEs transport helicity outwards.

There has been significant progress in the study of CMEs in recent years. In addition to improved observations from spacecraft, *e.g.* SDO or the *Solar TErestical RElation Observatory* (STEREO: Kaiser *et al.*, 2008), there have also been major advances in the field of numerical modeling of CME events (Roussev *et al.*, 2002; Archontis *et al.*, 2009). However, the formation and the origin of eruptive events like CMEs is not yet completely understood. Simulating CMEs and their formation is challenging. Leaving the difficulties of modeling the interplanetary space aside, a CME, after being ejected into the chromosphere or the lower corona, travels over an extended radial distance to the upper corona. In this environment, density and temperature vary by several orders of magnitude, which is not easy to handle in numerical models. Additionally, the origin of the CMEs is assumed to relate to the magnetic fields and the velocity pattern at the surface. However, the surface magnetic and velocity fields are rooted in the solar convection zone, where convective motions, in interplay with differential rotation, generate the magnetic field and the velocity patterns that are observed at the surface. The majority of researchers modeling CMEs do not include the convection zone in their setup, and thereby neglect the effect of the magnetic and velocity fields being rooted to this layer. Often the initial conditions for the magnetic and velocity fields are prescribed or taken from 2D observations; see for example Antiochos, De Vore, and Klimchuk (1999) and Amari *et al.* (1999) as well as Török and Kliem (2003).

Another approach is to study the emergence of flux ropes from the lower convection zone into the corona. In the presence of strong shear, convection simulations have been showing the formation of flux tubes (Guerrero and Käpylä, 2011; Nelson *et al.*, 2011), but such structures are similar to vortex tubes whose diameter is known to relate with the visco-resistive scale (Brandenburg, Procaccia, and Segel, 1995). In other approaches flux ropes are inserted in a self-consistent model, but their origin is left unexplained. In several recent papers (Martínez-Sykora, Hansteen, and Carlsson, 2008; Jouve and Brun, 2009; Fang *et al.*, 2010), the focus lies on the emergence of magnetic flux and the resulting features in the solar atmosphere. However, eruptive events have not been investigated with this setup. In earlier work (Warnecke and Brandenburg, 2010, hereafter WB) a different approach was developed. The solar convection zone was combined with a simple model of the solar corona. The magnetic field, which was here generated by dynamo action beneath the solar surface, emerged through the surface and was ejected out of the domain. The focus was on the connection of the dynamo-generated field and eruptive events like CMEs through the dynamo-generated twist. WB used a simplified coronal model and drove the dynamo with forced turbulence. These simplifications allowed them to study the emergence and a new mechanism to drive ejections in great detail. In subsequent work (Warnecke, Brandenburg, and Mitra, 2011, hereafter WBM), the setup of WB was improved by using a spherical coordinate system and helical forcing with opposite signs in each hemisphere to mimic the effects of rotation on inhomogeneous turbulence. In addition, WBM included the stratification resulting from radial gravity for an isothermal fluid. To improve this model, we now employ convection to generate the velocity field. In a related approach, Pinto and Brun (2011) considered convective overshoot into the chromosphere and the excitation of gravity waves therein, but dynamo-generated twist seemed to be unimportant in their work. The turbulent motions driving the generation of magnetic field are now self-consistently generated by convective cells operating beneath the surface. The setup of the convection zone follows ideas of Käpylä, Korpi, and Brandenburg (2008), Käpylä *et al.* (2010, 2011) and Käpylä, Mantere, and Brandenburg (2011, 2012). There are other approaches simulating convection in hot massive stars, which have thin subsurface convection zones (Cantiello *et al.*, 2011). But we now use an extended cooling layer to describe some properties of a solar corona. The results of this work complement those of earlier work and can be compared with observations. The model of the solar atmosphere is still a very simplified one, but can be regarded as a preliminary step, which will provide a reference point for improved work in that direction.

2. The Model

As in WB and WBM, a two-layer model is used, which represents the convection zone and an extended corona-like layer in one and the same model. Our convection zone is similar to those of Käpylä *et al.* (2010, 2011). The domain is a segment of the Sun and is described in spherical polar coordinates (r,θ,ϕ). We model the convection zone starting at radius $r = 0.7\,R$ and the solar corona until $r = R_{\mathrm{c}}$, where $R_{\mathrm{c}} = 1.5\,R$ in the present models, where R corresponds to the solar radius. In the latitudinal direction, our domain extends in colatitude from $\theta = 15^\circ$ to 165° and in the azimuthal direction from $\phi = 0^\circ$ to 90°. We solve the following equations of compressible magnetohydrodynamics:

$$\frac{\partial \boldsymbol{A}}{\partial t} = \boldsymbol{U} \times \boldsymbol{B} + \eta \nabla^2 \boldsymbol{A}, \tag{1}$$

$$\frac{\mathrm{D} \ln \rho}{\mathrm{D} t} = -\boldsymbol{\nabla} \cdot \boldsymbol{U}, \tag{2}$$

$$\frac{\mathrm{D}\boldsymbol{U}}{\mathrm{D}t} = \boldsymbol{g} - 2\boldsymbol{\Omega}_0 \times \boldsymbol{U} + \frac{1}{\rho}(\boldsymbol{J} \times \boldsymbol{B} - \nabla p + \nabla \cdot 2\nu\rho\mathsf{S}) - \boldsymbol{D}(r,\theta,t), \tag{3}$$

$$T\frac{\mathrm{D}s}{\mathrm{D}t} = \frac{1}{\rho}\nabla \cdot K\nabla T + 2\nu\mathsf{S}^2 + \frac{\mu_0\eta}{\rho}\boldsymbol{J}^2 - \Gamma_{\mathrm{cool}}, \tag{4}$$

where the magnetic field is given by $\boldsymbol{B} = \nabla \times \boldsymbol{A}$ and thus obeys $\nabla \cdot \boldsymbol{B} = 0$ at all times, μ_0 is the vacuum permeability, η and ν are the magnetic diffusivity and kinematic viscosity, respectively, $\mathrm{D}/\mathrm{D}t = \partial/\partial t + \boldsymbol{U} \cdot \nabla$ is the advective time derivative, ρ is the density, and $\boldsymbol{U}$ is the velocity. The traceless rate-of-strain tensor is given by

$$\mathsf{S}_{ij} = \frac{1}{2}(U_{i;j} + U_{j;i}) - \frac{1}{3}\delta_{ij}\nabla \cdot \boldsymbol{U}, \tag{5}$$

where semicolons denote covariant differentiation; see Mitra *et al.* (2009) for details. $\boldsymbol{\Omega}_0 = \Omega_0(\cos\theta, -\sin\theta, 0)$ is the rotation vector, p is the pressure, K is the radiative heat conductivity, and $\boldsymbol{D}(r,\theta,t)$ describes damping in the coronal region; see Section 2.2 for details. The gravitational acceleration is given by

$$\boldsymbol{g} = -GM\boldsymbol{r}/r^3, \tag{6}$$

where G is Newton's gravitational constant, and M is the mass of the star. The fluid obeys the ideal gas law, $p = (\gamma - 1)\rho e$, where $\gamma = c_p/c_v = 5/3$ is the ratio of specific heats at constant pressure and constant volume, respectively, and $e = c_v T$ is the internal energy density, which defines the temperature T. The cooling term Γ_{cool} will be explained in Equation (10) below in more detail.

2.1. Initial Setup and Boundary Conditions

For the thermal stratification in the convection zone, we consider a simple analytical setup instead of profiles from solar structure models as in, *e.g.*, Brun, Miesch, and Toomre (2004). The hydrodynamic temperature gradient is given by

$$\frac{\partial T}{\partial r} = \frac{-|\boldsymbol{g}|}{c_v(\gamma - 1)(m + 1)}, \tag{7}$$

where $m = m(r)$ is the radially varying polytropic index, for which we assume a stepwise constant profile. We also use Equation (7) as the lower boundary condition for the temperature. This gives the logarithmic temperature gradient ∇ (familiar to those working in stellar physics, but not to be confused with the operator $\boldsymbol{\nabla}$) as

$$\nabla = \frac{\partial \ln T}{\partial \ln p} = \frac{1}{m + 1}. \tag{8}$$

The stratification is convectively unstable if $\nabla - \nabla_{\mathrm{ad}} > 0$, where $\nabla_{\mathrm{ad}} = 1 - 1/\gamma$ is the adiabatic temperature gradient, corresponding to $m < 1.5$ for unstable stratification. We choose $m = 1$ in the convectively unstable layer beneath the surface, $r < R$. The region above $r = R$ is stably stratified and isothermal due to a cooling term Γ_{cool} with respect to a constant reference temperature in the entropy equation. The density stratification is obtained by requiring the hydrostatic equilibrium condition to be satisfied.

The thermal conductivity follows from the constancy of the radial luminosity profile $L(r) = L_0 = \mathrm{const}$ throughout the domain and is given by

$$K = \frac{L_0}{4\pi r^2 \partial T/\partial r}. \tag{9}$$

Figure 1 Initial stratification of temperature (dashed line), density (solid), pressure (dot-dashed) and the Brunt–Väisälä frequency $N^2 = -(|\boldsymbol{g}|/H_p)(\nabla - \nabla_{\rm ad})$ (dash-triple-dotted) for Run A5. The subscripts b refers to the values at $r = 0.7\,R$. The dotted horizontal (vertical) line denotes the value of zero ($r = R$)

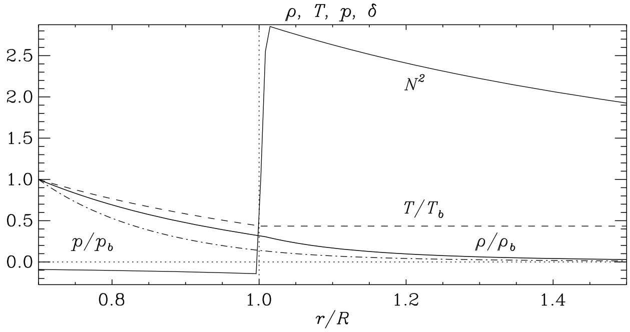

To speed up the thermal relaxation processes, we apply shallower profiles, corresponding to $\rho \propto T^{1.4}$, for the thermal variables within the convectively unstable layer. The value $m = 1$ is just used in the convection zone to determine the thermal conductivity. In Figure 1 we show the initial non-convecting stratification. The radial temperature gradient at the bottom of the domain is set to a constant value, which leads to a constant heat flux into the domain. In the coronal part the gradient goes smoothly to 0 by using the r dependent cooling function $\varGamma_{\rm cool}$, which is included in the entropy evolution (4). The cooling term is given by

$$\varGamma_{\rm cool} = \varGamma_0 f(r)\left(\frac{c_{\rm s}^2 - c_{\rm s0}^2}{c_{\rm s0}^2}\right), \tag{10}$$

where $f(r)$ is a profile function equal to unity in $r > R$ and smoothly connecting to zero in $r \le R$, and $\varGamma_0$ is a cooling luminosity chosen so that the sound speed in the coronal part relaxes towards $c_{\rm s0}^2 \equiv c_{\rm s}^2(r = R_{\rm c})$. Whether the stratification is convectively stable or not depends on the Brunt–Väisälä frequency N, defined through

$$N^2 = |\boldsymbol{g}|\left(\frac{1}{\gamma}\frac{\partial \ln p}{\partial r} - \frac{\partial \ln \rho}{\partial r}\right) = -\frac{|\boldsymbol{g}|}{H_p}(\nabla - \nabla_{\rm ad}), \tag{11}$$

where $H_p = -\partial r/\partial \ln p$ is the pressure scale height. If N^2 is negative, the stratification is unstable.

We initialize the magnetic field as a weak, random, Gaussian-distributed seed field in the whole domain. In the coronal part the magnetic field diffuses after a short time. We do not use a background coronal field, so the field is self-consistently generated by the dynamo in the convective layer. We apply periodic boundary conditions in the azimuthal direction over a 90° fraction of the full circumference. For the velocity we take stress-free boundary conditions on all other boundaries. As in WBM, the stress-free boundary conditions prevent mass flux, so no stellar wind is possible. Because no mass can escape, material will eventually fall back from the boundary. Thermodynamic variables have zero gradients at the latitudinal boundaries. We employ perfect conductor boundaries for the magnetic field at the latitudinal and at the lower radial boundaries, and radial field conditions at the outer radial boundary. The latter is motivated by the fact that in the Sun, the solar wind pushes the magnetic field to open field lines and at a radius of $r = 2.0\ldots2.5$ solar radii. The field lines are mostly radial (Levine, Schulz, and Frazier, 1982; Hoeksema, Wilcox, and Scherrer, 1982). This choice has been substantiated by subsequent work of Wang and Sheeley (1992) as well as Schrijver and De Rosa (2003). While this choice might still be too restrictive for coronal holes and coronal streamers, and given also that our radial extent in most of the simulations is smaller than $r = 2R$, we nevertheless choose the vertical field boundary condition, because it satisfies our primary objective of letting magnetic helicity leave the domain, which is believed to be crucial for the dynamo to operate at large values of Re_M (Blackman and Field, 2000a, 2000b; Brandenburg and Sandin, 2004). However, we must be aware of the fact that with this choice our description of the field in the exterior layer is not a realistic one.

To describe the corona as an isothermal extended cooling layer is a serious simplification, in that the temperature inside the coronal layer is not higher than in the convection zone as in a real stellar corona, but it stays fixed at the surface value; see Figure 1. Besides the fact that a simple cooling layer is easy to handle numerically, we emphasize the importance of facilitating comparison with previous models of WBM. It can also be seen as a step towards studying effects that are not solely due to a low plasma β corona, for which the magnetic pressure, *i.e.* the magnetic field, is strong compared with the gas pressure ($\beta = 2\mu_0 p/\boldsymbol{B}^2$). Indeed, given that our initial field is weak, the plasma β is necessarily large in the outer parts. We note that it is not even clear whether a hot corona promotes or hinders coronal ejections. To understand the formation and evolution of magnetic ejections, studies that isolate these effects, such as the present one, may be important.

We use the PENCIL CODE[1] with sixth-order centered finite differences in space and a third-order accurate Runge–Kutta scheme in time; see Mitra *et al.* (2009) for the extension of the PENCIL CODE to spherical coordinates. We use a grid size of 128 × 128 × 64 mesh points (Runs A5 and Ar1), and 256 × 256 × 128 (Run A5a).

2.2. Velocity Damping in the Corona

Whether the solar corona rotates like a solid body or differentially coupled with the photosphere is unclear. In recent work by Wöhl *et al.* (2010), where SOHO-EIT data of the bright points in the solar corona were used to estimate the rotation speeds, it was found that the corona rotates similarly as the small magnetic features in the photosphere. Similar results have been obtained by Badalyan (2010), where the coronal rotation has been measured by analyzing the green Fe XIV 530.3 nm line. This author finds also a variation pattern with the activity cycle. However, the observations of the "boot" coronal hole by SKYLAB suggested rigid rotation (Timothy, Krieger, and Vaiana, 1975). Recent work on coronal holes by Lionello *et al.* (2005) claims that the rigid rotation is only an apparent one. The magnetic field is sheared by the differential rotation, but the boundary of the hole remains relatively unchanged, due to reconnection. Owing to the low plasma β in the solar corona, the fluid motions are dominated by the magnetic fields whose footpoints are anchored in the photosphere or even further down. So the magnetic field might then be rigid enough to prevent differential rotation of the solar corona. However, the observed bright points and other features in the corona are strongly correlated with the magnetic field so they can give a misleading picture about the global rotation of the corona.

In our simulations, the Coriolis force is included in the momentum equation as a consequence of the rotation. In the solar corona the density is more than 14 orders of magnitude smaller than in the lower convection zone. Because of the weak density stratification in our simulation, the Coriolis force in our coronal part is too strong and can cause possible artifacts such as the magnetorotational instability. To avoid this – at least for runs with rapid rotation – we apply a damping function $\boldsymbol{D}(r,\theta)$ in the momentum equation, which is given by

$$\boldsymbol{D}(r,\theta,t) = \frac{1}{\tau_{\mathrm{D}}}\Theta(r-R)\overline{\boldsymbol{U}}(r,\theta,t), \tag{12}$$

---

[1] http://pencil-code.googlecode.com.

where

$$\Theta(r-R)=\frac{1}{2}\left[1+\tanh\left(\frac{r-R}{w}\right)\right], \tag{13}$$

with τ_D being the damping time and w the width of the transition layer from convection zone to the coronal part. Here and elsewhere, the overbar denotes averaging over ϕ, defined as $\overline{F}(r,\theta,t)=\int F(r,\theta,\phi,t)\,\mathrm{d}\phi/2\pi$. Occasionally, we also use time averages denoted by $\langle.\rangle_t$.

2.3. Units, Nondimensional Quantities, and Parameters

Dimensionless quantities are obtained by setting

$$R=GM=\rho_\mathrm{b}=c_p=\mu_0=1, \tag{14}$$

where ρ_b is the density at $r=0.7\,R$. Below, we will describe the properties of the runs by the following dimensionless parameters: fluid Reynolds number $\mathrm{Re}=u_\mathrm{rms}/\nu k_\mathrm{f}$, magnetic Reynolds number $\mathrm{Re}_M=u_\mathrm{rms}/\eta k_\mathrm{f}$, where $k_\mathrm{f}=2\pi/0.3R$ is an estimate for the typical wavenumber of the energy-carrying eddies and $u_\mathrm{rms}=\sqrt{3/2\langle U_r^2+U_\theta^2\rangle}$ is the volume-averaged rms velocity in the convection zone ($r\le R$). In our definition of u_rms we omit the contribution from the ϕ-component of the velocity, because it is dominated by contributions from the large-scale differential rotation that develops when rotation is included and would give an atypical estimate of the convective turnover time. To compensate for this, and to have an estimate of u_rms comparable with earlier work, we apply the 3/2 correction factor. We also define the magnetic Prandtl number $\mathrm{Pr}_M=\nu/\eta=\mathrm{Re}_M/\mathrm{Re}$ and the Coriolis number $\mathrm{Co}=2\Omega_0/u_\mathrm{rms}k_\mathrm{f}$. Time is expressed in units of $\tau=(u_\mathrm{rms}k_\mathrm{f})^{-1}$, which is the eddy turnover time in the convection zone. We measure the magnetic field strength as the rms value averaged over the convection zone B_rms, where we often normalize this value with the equipartition value of the magnetic field defined by $B_\mathrm{eq}^2=\mu_0\langle\overline{\rho}u_\mathrm{rms}^2\rangle_{r\le R}$. The relative kinetic helicity is $h_\mathrm{rel}(r,t)=\overline{\boldsymbol{\omega}\cdot\boldsymbol{u}}/\omega_\mathrm{rms}u_\mathrm{rms}$, where $\boldsymbol{\omega}=\nabla\times\boldsymbol{u}$ is the vorticity and ω_rms is its rms value inside the convection zone.

3. Results

3.1. Hydrodynamic Phase of the Simulations

After around 100 turnover times, convection has reached saturation and we find convection cells as typical patterns in the radial velocity just below the surface. In our model, the dominant energy transport mechanisms are radiative and convective fluxes in the bulk of the convection zone and an (optically thin) cooling flux in the outer (coronal) parts. The radiative and convective fluxes are defined as

$$F_\mathrm{rad}=-K\frac{\partial\overline{T}}{\partial r},\qquad F_\mathrm{conv}=c_P\overline{\rho}\,\overline{u_r'T'}, \tag{15}$$

where the averages are taken over θ and ϕ and the prime indicates fluctuations about the respective mean quantity. In our present setup, however, the convective flux reaches barely about 5 % in the convection zone; see Figure 2, where we plot the relevant contributions to the luminosity for Run A5. Above the surface the cooling takes over to maintain an approximately isothermal atmosphere. The total flux is constant, except for small departures near the surface. The kinetic energy and viscous fluxes are negligible in the present runs.

Figure 2 Flux balance from Run A5. The different contributions to the total luminosity (solid blue line) are due to radiative diffusion (dashed red line), resolved convection (dotted black line) and cooling (dash-triple-dotted black line). The black thin line denotes the zero level and the surface ($r = R$), respectively.

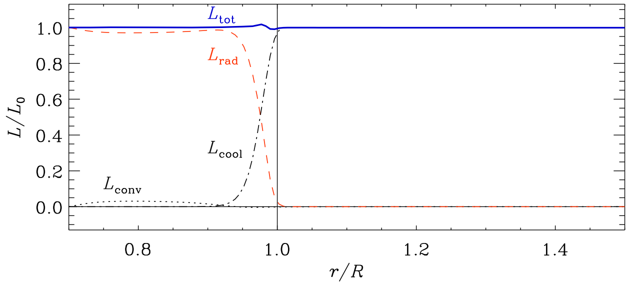

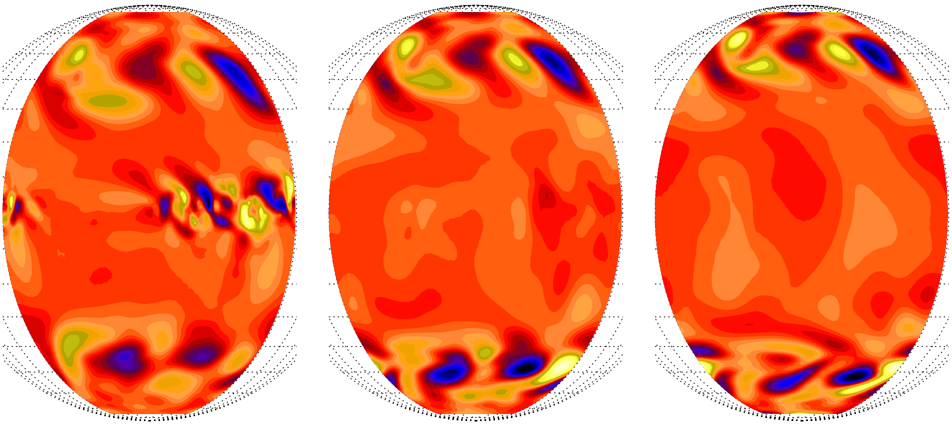

Figure 3 Radial velocity (U_r) above the surface for $r = 1.15$, 1.25, 1.35 R from left to right, for Run A5. Dark blue shades represent negative and light yellow positive values.

Figure 4 Root-mean-square values of U_r (dotted), U_θ (dashed), and U_ϕ (dash-dotted) as a function of radius for Run A5. The solid line shows the radial profile of our nominal rms velocity, $u_{\rm rms} = \sqrt{3/2(U_r^2 + U_\theta^2)}$. The (red) vertical line indicated the surface at ($r = R$). The values are normalized by $\sqrt{GM/R}$.

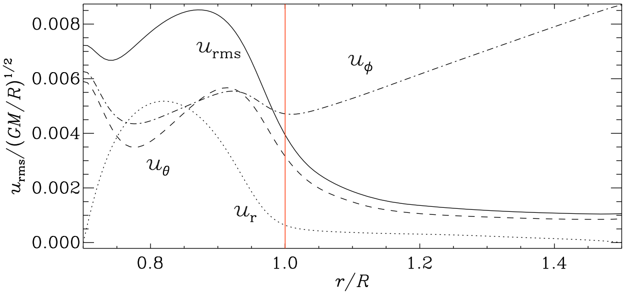

To determine the degree of overshooting and penetration into the stably stratified layers above the convection zone, we show in Figure 3 the radial velocity above the surface at $r = 1.15$, 1.25, and 1.35 R for Run A5. At low latitudes, there is very little radial penetration (velocity features are only seen until $r = 1.15\,R$), while at higher latitudes the radial velocity pattern is transmitted all the way to 1.35 R. This is not surprising in view of the Taylor–Proudman theorem, which states that for rapid rotation (large values of Co) the local angular velocity of the gas is constant along cylindrical surfaces.

Next, we plot in Figure 4 the rms values of all three velocity components for Run A5. The amplitude of the radial velocity component falls off the fastest. The latitudinal component also falls off with radius, but remains about three times larger than the radial component. The

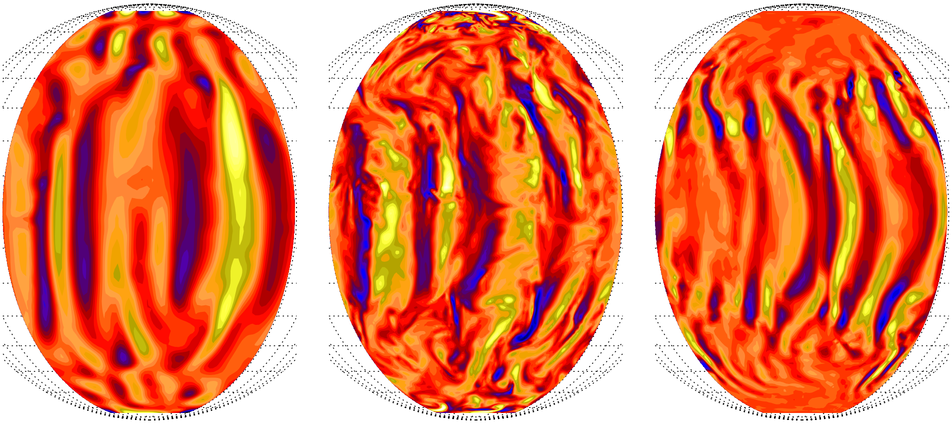

Figure 5 Radial velocity (U_r) beneath the surface ($r = 0.89\,R$) for Runs A5, A5a, and Ar1 from left to right. Dark blue shades represent negative and light yellow positive values.

Table 1 Summary of the runs. Re is the fluid Reynolds number, $u_{\rm rms} = \sqrt{3/2(U_r^2 + U_\theta^2)}$ is the volume-averaged rms velocity in the convection zone normalized by $\sqrt{GM/R}$, Pr_M is the magnetic Prandtl number, Co is the Coriolis number, and $h_{\rm rel}$ is the maximum value of the relative kinetic helicity using azimuthal averages as defined in Section 2.3. $\frac{\rho_{\rm b}}{\rho_{\rm s}}$ and $\frac{\rho_{\rm b}}{\rho_{\rm t}}$ give the density ratios of the bottom of the convection zone to those at the surface and the top of the domain, respectively. In the right-most column we note if damping for velocity in the coronal part is used (Y) or not (N); see Section 2.2.

Run	Resolution	$\frac{u_{\rm rms}}{\sqrt{GM/R}}$	Re	Pr_M	$\frac{B_{\rm rms}^2}{B_{\rm eq}^2}$	$\frac{\rho_{\rm b}}{\rho_{\rm s}}$	$\frac{\rho_{\rm b}}{\rho_{\rm t}}$	Co	$h_{\rm rel}$	D
A5	$128^2 \times 64$	0.0072	3.3	10	$0.1-0.4$	3.6	39	7	0.5	N
A5a	$256^2 \times 128$	0.0105	100	1	0.2	3.6	39	4.5	0.3	N
Ar1	$128^2 \times 64$	0.0040	38	1	$1.5-5.5$	3.6	39	50	0.3	Y

longitudinal component, on the other hand, increases with radius in a way that is compatible with rigid rotation with an angular velocity that is somewhat larger than the rotation rate of the frame of reference.

The size of the convection cells depends strongly on the strength of rotation and the degree of density stratification; see also Käpylä, Mantere, and Brandenburg (2011). We plot the radial velocity U_r at $r = 0.89\,R$ for Runs A5, A5a, and Ar1 in Figure 5. The Run A5 has a low fluid Reynolds number and therefore the convection cells are large; see Table 1. The flow pattern shows clear 'banana cells' as in previous work with comparable Coriolis parameter, *cf.* Käpylä *et al.* (2011). A higher fluid Reynolds number and higher resolution, as in Run A5a, allow the velocity field to form more complex structures. However, the banana cells are still visible. If one now looks at a simulation with more rapid rotation (Run Ar1, plotted in the right-most panel of Figure 5) with a Coriolis number of Co = 50, the number of banana cells increases and they are more clearly visible than in Run A5a. Note also that the radial velocity is now significantly reduced at high latitudes inside the inner tangent cylinder.

In the Sun, differential rotation is an important element to produce the magnetic field structures observed at large scales, exhibiting a cyclic behavior over time, as manifested by the sunspot cycle. To illustrate the differential rotation profiles generated in the simulations,

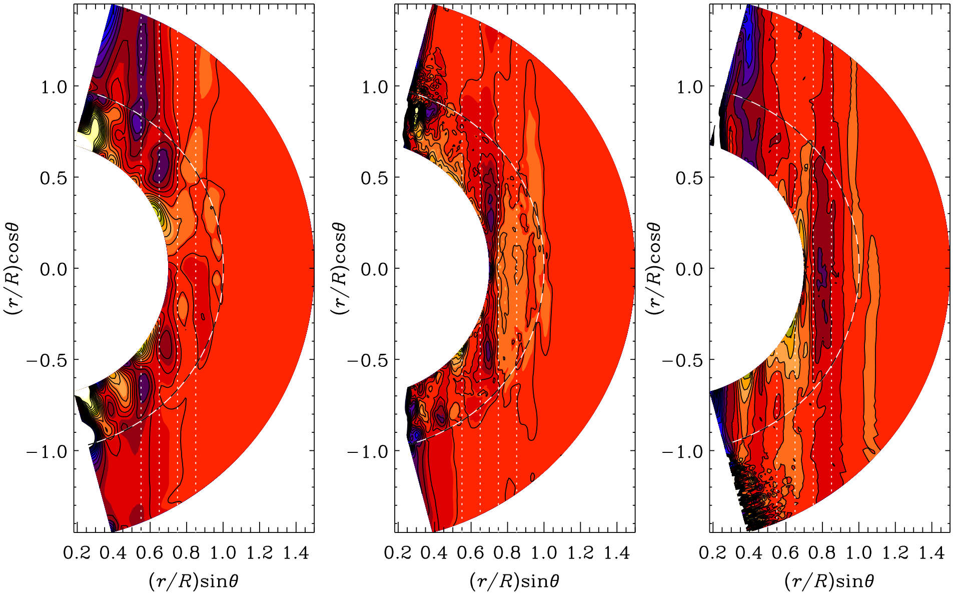

Figure 6 Differential rotation profiles $\overline{\Omega}(r,\theta)=\overline{U}_\phi/(r\sin\theta)+\Omega_0$ for Runs A5, A5a, and Ar1 from left to right. Dark blue shades represent low and light yellow high values, overplotted by the isocontours with solid black lines. The dotted white lines parallel to the rotation axis are given for orientation and the dashed line indicates the surface ($r=R$).

we plot the azimuthally averaged angular velocity, $\overline{\Omega}(r,\theta)=\overline{U}_\phi/(r\sin\theta)+\Omega_0$, for Runs A5, A5a, and Ar1 in the saturated state of the simulation; see Figure 6. In the plot, we show isocontours of angular velocity with solid black lines. In the convection zone the contours of local angular velocity tend to be cylindrical, which is likely a consequence of the absence of a strong latitudinal modulations of specific entropy (Brandenburg, Moss, and Tuominen, 1992; Kitchatinov and Rüdiger, 1995; Miesch, Brun, and Toomre, 2006). The coronal part seems to rotate as a solid body outside the outer tangent cylinder (*i.e.*, for $r\sin\theta > R$), while inside it some differential rotation occurs also in the coronal part. In the convection zone between the inner and outer tangent cylinders, the angular velocity is enhanced relative to that inside the inner tangent cylinder (see the first and second panels of Figure 6), while in the case of extremely rapid rotation this may actually be reversed.

In the three runs shown in Figure 6 the stratification in the whole domain is just $\rho_\mathrm{b}/\rho_\mathrm{t}=40$, which is rather small compared to the stratification of the Sun ($\rho_\mathrm{b}/\rho_\mathrm{t}\sim 10^{14}$). It seems, therefore, that the Coriolis force is acting much more strongly in the coronal part of our simulation than in reality. In the Sun the Lorentz force plays a more important role in the corona than in our model. In the convection zone, we find quenching of convection due to rapid rotation. In Run A5, where $\mathrm{Co}=7$, the lines of constant rotation rate are more radial than vertical and show super-rotation, *i.e.*, the equator rotates faster than the poles. As expected, this tends to coincide with locations where the Reynolds stress in the radial direction is negative (see, *e.g.*, Rüdiger, 1980). However, the convection cells are rather big and have a strong local influence on U_ϕ and could in principle lead to subrotation; see the corresponding discussion in Dobler, Stix, and Brandenburg (2001). Note that the rms velocity in Run A5 is two times smaller than in Run A5a, which has higher resolution and higher fluid and magnetic Reynolds numbers ($\mathrm{Re}=\mathrm{Re}_M=100$). Due to this, we find clear super-rotation, even though the Coriolis number is slightly lower ($\mathrm{Co}=4.5$) than what

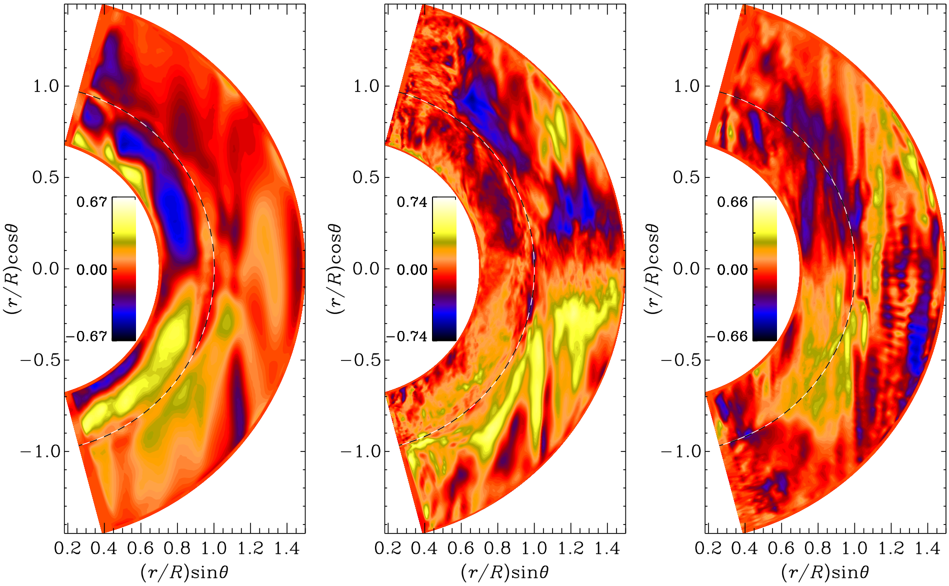

Figure 7 Relative helicity $h_{\mathrm{rel}}(r,t) = \overline{\boldsymbol{\omega}\cdot\boldsymbol{u}}/\omega_{\mathrm{rms}}u_{\mathrm{rms}}$ plotted for Runs A5, A5a, and Ar1 from left to right. Dark blue shades represent negative and light yellow positive values. The dashed line indicates the surface ($r = R$).

is realized in Run A5. In the third case, Run Ar1, where the rotation is extremely rapid ($\mathrm{Co} = 50$), we also find super-rotation, where the lines of constant rotation rate are almost all vertical. In comparable work (Käpylä *et al.*, 2011; Käpylä, Mantere, and Brandenburg, 2011), super-rotation has been found, when the Coriolis number was larger than 4. This is similar to our results including a coronal part. In addition, there is a minimum of the rotation rate at mid-latitudes and a polar vortex at high latitudes. Rotation profiles, which show a comparable behavior, have been found by several groups (Miesch *et al.*, 2000; Elliot, Miesch, and Toomre, 2000; Käpylä *et al.*, 2011; Käpylä, Mantere, and Brandenburg, 2011). The region with the higher rotation rate near the equator is limited to the upper convection zone and can even penetrate into the coronal part. In Run Ar1 the velocity damping described in Section 2.2 is used. By comparing the right-most panel of Figure 6, with damping, to the left-most panels, without it, we conclude that the damping does not make much of a difference to the coronal velocity structures.

Simulations with randomly forced turbulence (WB, WBM) have shown that the relative kinetic helicity h_{rel} has a strong influence both on the generation of large-scale magnetic fields and the ejection events. In WB and WBM, values of h_{rel} of order unity were achieved by using a forcing function with purely helical plane waves. In the convection runs presented here, however, values of large relative helicity, $h_{\mathrm{rel}} = 0.5$, are obtained (for Run A5), at least at certain radii. In Figure 7, we present contour plots of azimuthally averaged relative helicity in the meridional plane for Runs A5, A5a, and Ar1. All three show the typical sign rule of kinetic helicity under the influence of rotation, *i.e.* the northern hemisphere has predominantly a negative sign and the southern a positive one. Close to the bottom of the convection zone, the sign changes, which has earlier been reported by several authors both in Cartesian (*e.g.*, Brandenburg *et al.*, 1990; Ossendrijver, Stix, and Brandenburg, 2001) and spherical geometries (*e.g.* Miesch *et al.*, 2000; Käpylä *et al.*, 2010). Only in Run Ar1 with rapid rotation, the behavior is not that clear. The relative helicity is no longer confined to the

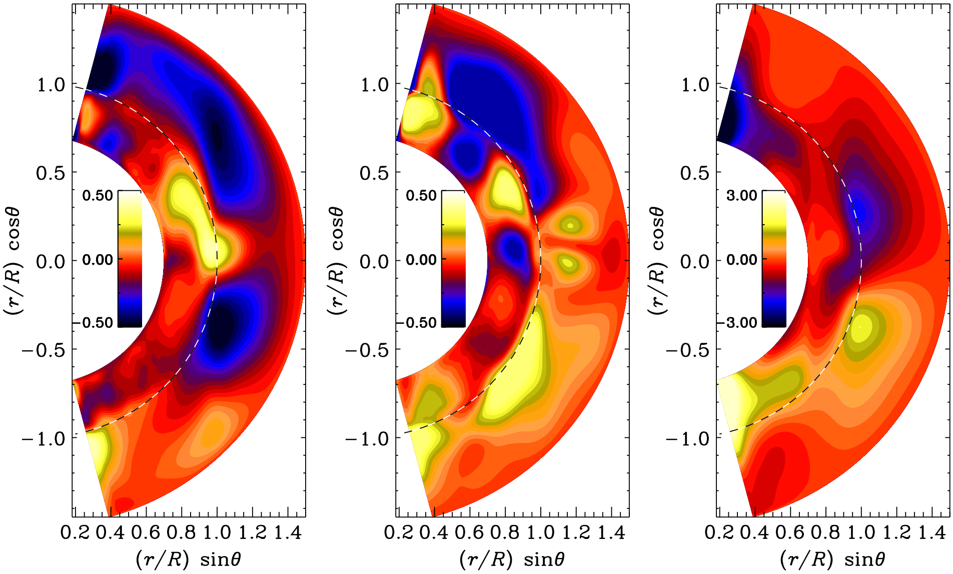

Figure 8 Time-averaged $\overline{B}_\phi$ for Run A5, A5a, and Ar1 from left to right. Dark blue shades represent negative and light yellow positive values. The magnetic field is normalized by the equipartition value. The dashed line indicates the surface ($r = R$).

convection zone, but significant values occur also in the coronal region. The sign rule still holds within the convection zone, while a more complicated sign behavior is visible in the coronal part. The maximal values of the azimuthally averaged helicity are around $h_{\mathrm{rel}} = 0.3$, occurring close to the surface. In Run A5a, the maximum value is slightly higher and is located in the middle of the convection zone, although relatively high values are present in the coronal part as well. It is not yet completely clear how high values of relative kinetic helicity can be achieved; strong rotation tends to suppress it, whereas strong stratification increases it. Its exact role in generating coronal ejections is yet unclear.

3.2. Convective Dynamo

The convective motions generate a large-scale magnetic field due to dynamo action. The magnetic field grows first exponentially and begins then to affect the velocity field. The effects of this backreaction can be subtle in that we found a 6 % enhancement of the rms velocity after saturation. The growth of the magnetic field saturates after around 200 to 1000 turnover times, depending on the Coriolis and Reynolds numbers. In the runs in Table 1, we obtain different dynamo solutions for the saturated field.

In Figure 8 we show the time-averaged azimuthal magnetic field $\overline{B}_\phi$ for Run A5, A5a, and Ar1. Note that the ϕ component of the magnetic field is also strong in the coronal part and roughly antisymmetric about the equator. Furthermore we find an oscillation of the volume-averaged rms magnetic field in the convection zone; see the left-hand panel of Figure 9 for Run A5. The growth tends to be steeper than the decline, the period being around $t/\tau = 220$. The field reaches a maximum of 60 % of the equipartition field strength, B_{eq}, which is comparable to the values obtained in the forced turbulence counterparts both in Cartesian and spherical coordinates (WB, WBM). Comparing this with the change of the kinetic energy, plotted as fluctuations of the rms velocity squared, we find an anti-correlation

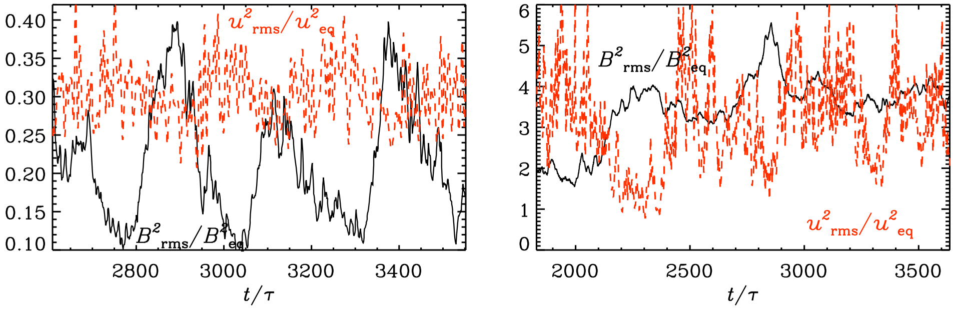

Figure 9 Phase relation of the magnetic field ($B^2_{\rm rms}/B^2_{\rm eq}$, solid black lines) and the velocity field ($u_{\rm rms}(t)^2/\langle u^2_{\rm rms}\rangle_t$, dashed red lines) in the convection zone for Runs A5 (left panel) and Ar1 (right). The velocity has been multiplied by a factor of 0.3 (left panel) and 3 (right), respectively, and smoothed over five neighboring data points.

Figure 10 Variation of $\overline{B}_\phi$ and $\overline{B}_r$ in the convection zone at $r = 0.9R$ for Run A5. Dark blue shades represent negative and light yellow positive values. The dashed horizontal lines show the location of the equator at $\theta = \pi/2$. The magnetic field is normalized by the equipartition value.

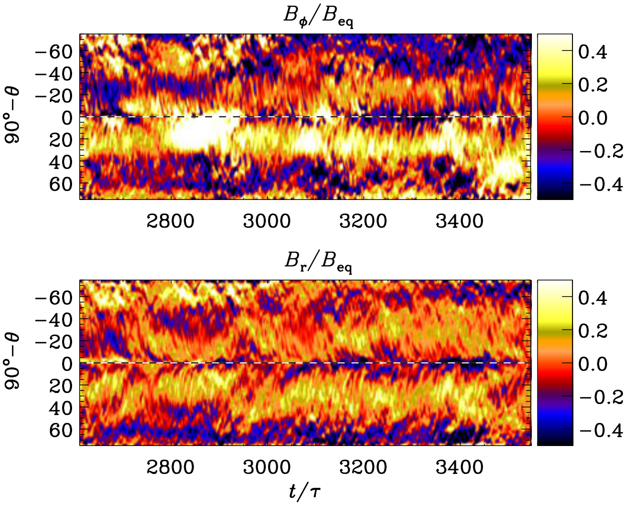

with respect to the magnetic field oscillation. The magnetic field is high (low), when the velocity is low (high). In the work by Brun, Browning, and Toomre (2005), the authors interpret this behavior as the interplay of the magnetic backreaction and the dynamo effect of the differential rotation. Due to the Lorentz force a higher magnetic field strength leads to quenching of the differential rotation. An increased magnetic field quenches the Reynolds stress and thus lowers the differential rotation, which limits the magnetic field. A weak magnetic field leads to stronger differential rotation. Similar behavior has been observed also in previous forcing simulations (WBM). This behavior is not seen as clearly in the large-scale magnetic field which shows variations in strength, but not in sign. As shown in Figure 10 for Run A5, the $\overline{B}_\phi$ and $\overline{B}_r$ have local maxima in time and in latitude, but the overall structure is nearly constant in time. Even though the large-scale field structure is stationary, the small-scale structures show an equatorward migration near the equator. The reason for this is unclear, but meridional circulation does not seem to play a role here.

In Run Ar1, the magnetic field reaches up to 5.5 times the equipartition value, but does not show a periodic oscillation; see the right hand panel of Figure 9. In comparable work (Käpylä *et al.*, 2010), similar values for the field strength were found. However, the rms

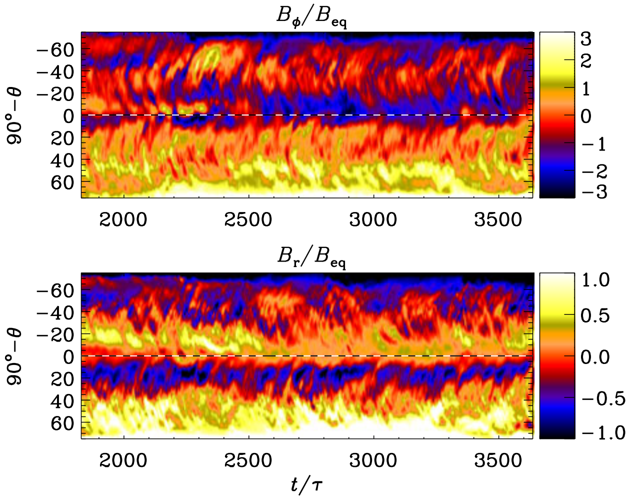

Figure 11 Variation of $\overline{B}_\phi$ and $\overline{B}_r$ in the convection zone at $r = 0.9R$ for Run Ar1. Dark blue shades represent negative and light yellow positive values. The dashed horizontal lines show the location of the equator at $\theta = \pi/2$. The magnetic field is normalized by the equipartition value.

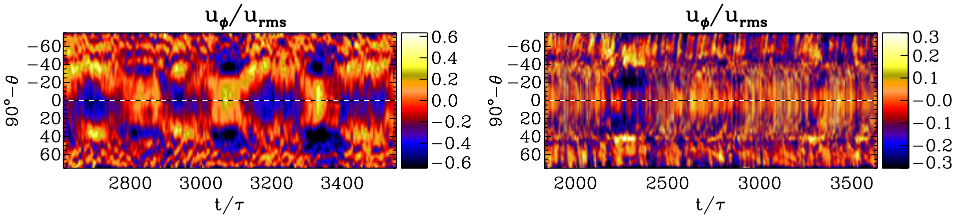

Figure 12 Variation of $\overline{U}_\phi$ in the convection zone at $r = 0.9R$ for Run A5 (left panel) and Run Ar1 (right panel). Dark blue shades represent negative and light yellow positive values. The dashed horizontal lines show the location of the equator at $\theta = \pi/2$. The velocity is normalized by the mean rms velocity in the convection zone.

velocity is also quenched, when the magnetic field is high. Looking at $\overline{B}_\phi$ and $\overline{B}_r$, plotted over time and latitude in Figure 11, the large-scale magnetic field is similar to Run A5, which is constant in time without any oscillation. In the recent work by Käpylä, Mantere, and Brandenburg (2012), the authors found an oscillatory behavior of $\overline{B}_\phi$ and $\overline{B}_r$ including equatorward migration for latitudes below 60°, which is the first time that such a result is obtained from direct numerical convection simulation of rotating convection.

The azimuthal velocity $\overline{U}_\phi$ versus time and latitude (Figure 12) shows minima at the same times as the maxima of the magnetic field occur. In Run A5a, the occurrence of strong magnetic fields suppresses the differential rotation. The pattern of the azimuthal velocity is symmetric about the equator and shows an oscillatory behavior, which is not that clear in the large-scale magnetic field. In the $\overline{U}_\phi$ plot in Figure 12 of Run Ar1, we find just one localized minimum, which coincides with the low values of $u_{\rm rms}(t)^2/\langle u_{\rm rms}^2\rangle_t$ between $t/\tau = 2100$ and 2400.

3.3. Coronal Ejections

In the runs that we have been performed so far, and of which only three have been discussed in this paper, only a small fraction of events can be identified with actual coronal ejections similar to the ones seen in WB and WBM. Especially the Runs A5 and Ar1 show some clear ejection events. There the magnetic field emerges out of the convection zone and is

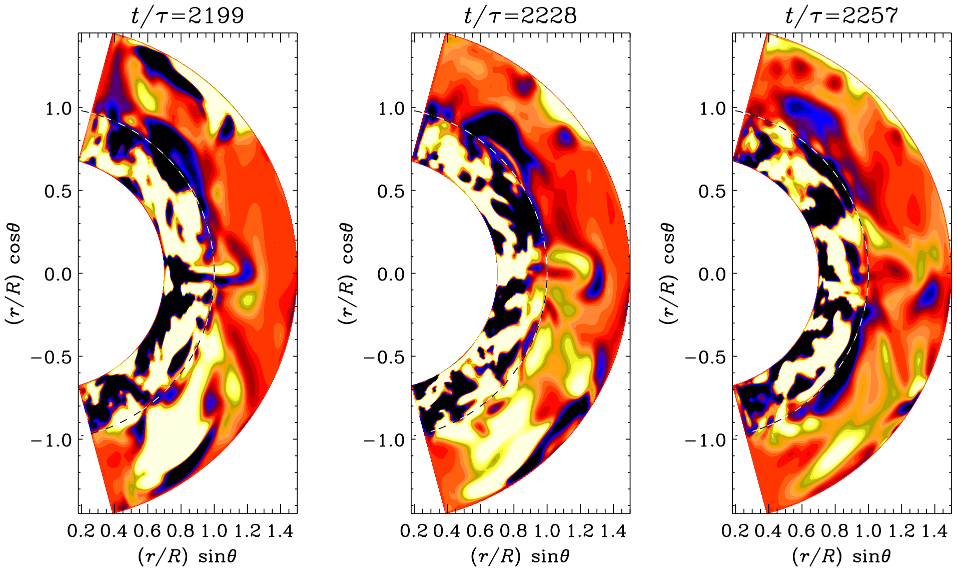

Figure 13 Time series of a coronal ejection near the equator ($\theta = \pi/2$), taken from Run A5. The normalized current helicity, $\mu_0 R\overline{\boldsymbol{J} \cdot \boldsymbol{B}}/\langle\overline{\boldsymbol{B}^2}\rangle_t$, is shown in a color-scale representation from different times; dark blue represents negative and light yellow positive values. The dashed horizontal lines show the location of the surface at $r = R$.

ejected as an isolated structure. In Figure 13 we have plotted the normalized current helicity, $\mu_0 R\overline{\boldsymbol{J} \cdot \boldsymbol{B}}/\langle\overline{\boldsymbol{B}^2}\rangle_t$, as a time series for Run A5. At small scales, the current helicity density, $\boldsymbol{J} \cdot \boldsymbol{B}$, is a good proxy for magnetic helicity density, $\boldsymbol{A} \cdot \boldsymbol{B}$, and is, as opposed to the latter, gauge invariant. In addition, the current helicity can be an indicator of helical magnetic structures, which are believed to be present in coronal mass ejections (Low, 1994, 2001; Plunkett *et al.*, 2000; Régnier, Amari, and Kersalé, 2002; Thompson, Kliem, and Török, 2011). Close to the equator a bipolar structure emerges through the surface. The inner bulk has a positive current helicity, in Figure 13 represented by a yellow color, and it pushes an arc with negative current helicity ahead of it; see Figure 14. Such bipolar ejections have been identified in earlier work (WBM) and compared with the 'three-part structure' of coronal mass ejection, which is described in Low (1996). The three parts consist of a prominence, which is similar to the bulk seen in our simulations, a front with an arc shaped structure corresponding to our arc, and a cavity between these two features. A bipolarity of twisted magnetic field has also been seen in observed magnetic clouds by Li *et al.* (2011). Even though the domain of the simulation is larger in the θ direction than in WBM, the ejections are much smaller, which is actually closer to the CMEs observed on the Sun. In the work of WBM the ejections have a size that corresponds to about 500 Mm, whereas in this work they seems to have a size corresponding to around 100 Mm if scaled to the solar radius. The ejections seem to expand slightly, but no significant expansion rate can be measured using this resolution. Comparing with the forced turbulence runs, the difference in size is mostly due to the more complex and fluctuating magnetic field in convection runs. In the sequence of images of Figure 14, an ejection near the equator reaches the outer boundary and leaves the domain. To investigate the mechanism driving the ejection, we look at the dynamics of the magnetic field in Figure 14, where field lines of the azimuthally averaged mean field are shown as contours of $r \sin\theta \overline{A}_\phi$, and colors represent $\overline{B}_\phi$ together with the density fluctuations and

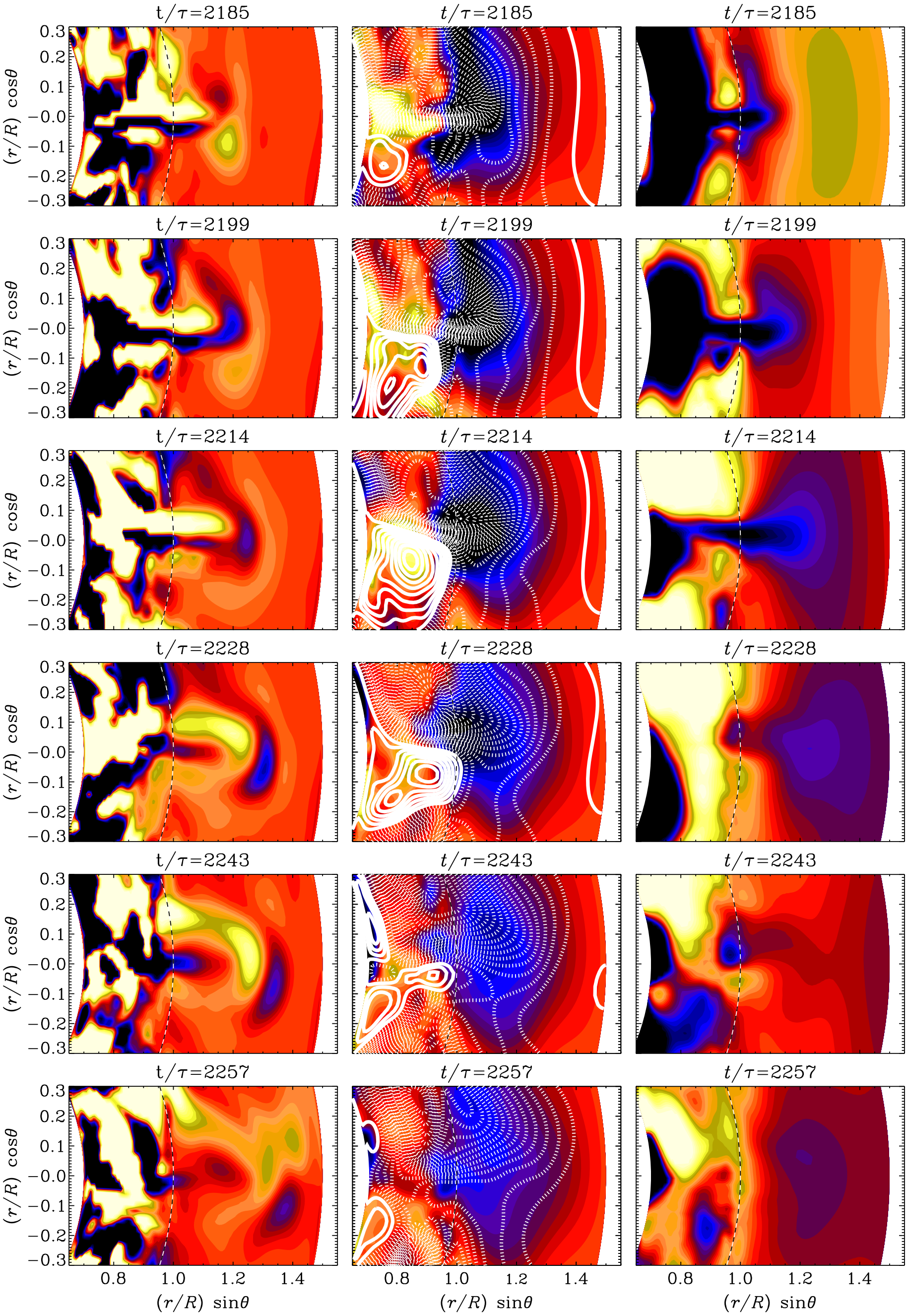

Figure 14 Time series of a coronal ejection zoomed into the region of the ejection near the equator ($\theta = \pi/2$), taken from Run A5. The dashed horizontal lines show the location of the surface at $r = R$. Left column: normalized current helicity, $\mu_0 R\overline{\boldsymbol{J}\cdot\boldsymbol{B}}/\langle\overline{\boldsymbol{B}^2}\rangle_t$. Middle column: magnetic field, contours of $r\sin\theta\overline{A}_\phi$ are shown together with a color-scale representation of $\overline{B}_\phi$. The contours of $r\sin\theta\overline{A}_\phi$ correspond to field lines of $\overline{\boldsymbol{B}}$ in the r,θ plane, where solid lines represent clockwise magnetic field lines and the dashed ones counter–clockwise. Right column: density fluctuations $\Delta\overline{\rho(t)} = \overline{\rho(t)} - \langle\overline{\rho}\rangle_t$. For all plots, the color-scale represents negative as dark blue and positive as light yellow.

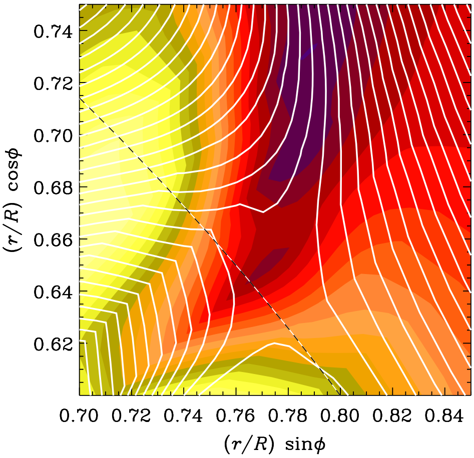

Figure 15 X-point-like structure in the r, ϕ plane at the equator ($\theta = \pi/2$) at $t/\tau = 2204$ zoomed into the ejection region, taken from Run A5. Contours of rA_θ are shown together with a color-scale representation of B_θ; dark blue stands for negative and light yellow for positive values. The contours of rA_θ correspond to field lines of $\boldsymbol{B}$ in the r, ϕ plane. The dashed horizontal lines show the location of the surface at $r = R$.

current helicity. During the ejection, one may notice a strong concentration of magnetic field lines that are directed radially outwards. This concentration appears first beneath the surface and then emerges below the current helicity structure and follows it up into the coronal part. Investigating the direction of field lines of the mean field in the time series in Figure 14, an X-point can be found. In the first panel, at $r = 1.07\,R$ and $\theta = \pi/2 + 0.1$, the magnetic field lines form a junction-like shape. The dotted line represents a counter-clockwise oriented field loop, so at the two corners of the junction there are field lines with opposite signs. After around 14 turnover times this "junction" has reconnected at the same position as where the ejection is detected. It appears that these two events are related to each other. Looking at the magnetic field line in the r, ϕ plane, which here *is not* averaged over the perpendicular direction (Figure 15), we identify a structure which has a shape similar to an X-point.

The ejection causes also a strong variation in the density. If the time-averaged density profile is subtracted from instantaneous ones, the density fluctuations are obtained. After removing the density stratification one obtains $\Delta\overline{\rho(t)} = \overline{\rho(t)} - \langle\overline{\rho}\rangle_t$. We plot these density fluctuations, $\Delta\overline{\rho(t)}$, in the right column of Figure 14 to visualize the effect of the ejection on the density. The density in the ejection is much lower than in the rest of the coronal part. However, the density variations are also associated with fluctuations in the specific entropy ($\Delta s/c_p \approx 0.01$), which suggests that thermal buoyancy also plays a role. One interpretation could be that the strong magnetic field reduces the density to achieve total pressure equilibrium and the ejection rises partly because of magnetic buoyancy. Such an effect is also seen by inspecting other ejections.

To characterize the emergence we plot different properties of the ejection in the θ, ϕ plane; see Figure 16. The magnetic field shows a strong concentration in its radial and azimuthal components. The concentration is associated with a downflow in spite of it being a low-density region. It is interesting to note that in this case the gas velocity does not reflect the actual pattern speed. From the time evolution of the low-density region shown in Figure 14, we know that this region is moving radially upwards in a way that is consistent with a motion expected from buoyancy forces. In particular, the specific entropy has a high value in this region. In visualizations of the current density, we see the formation of two current sheets. This leads to two current helicity regions of opposite sign.

When discussing coronal ejections, one is usually interested in the plasma β parameter to characterize the corona. In our simplified coronal part, the plasma β does not decrease with

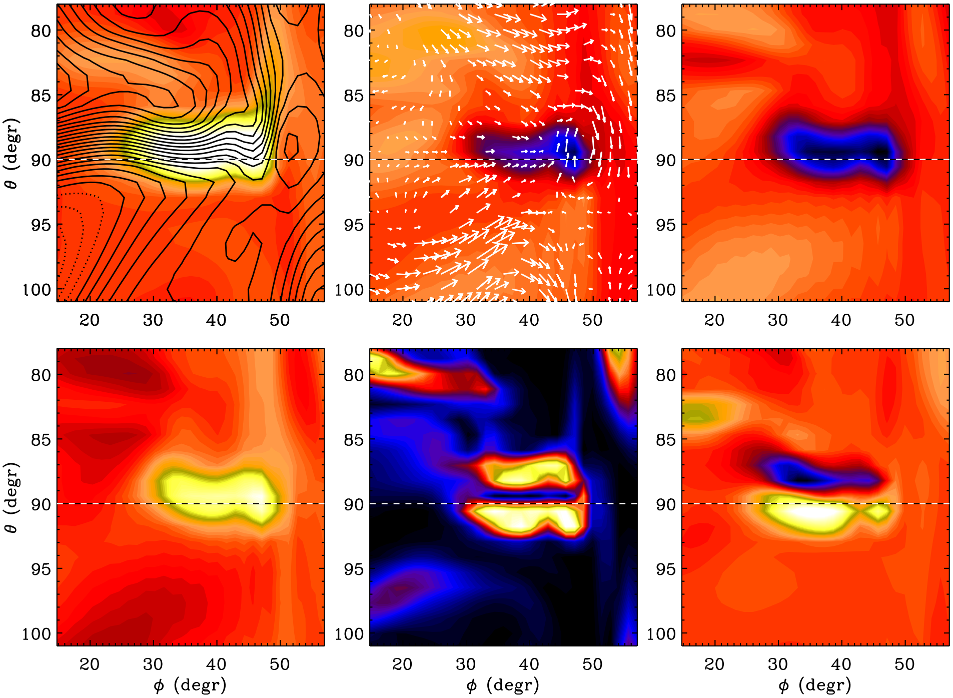

Figure 16 Different properties of the ejection in the θ, ϕ plane at the surface ($r = R$) at $t/\tau = 2204$, taken from Run A5. Upper row, left panel: Contours of A_r are shown together with a color-scale representation of B_r; dark blue stands for negative and light yellow for positive values. The contours of A_r correspond to field lines of that part of $\boldsymbol{B}$ that is solenoidal in the θ, ϕ plane. Solid lines represent clockwise-oriented magnetic field lines and dotted lines counter-clockwise ones. Middle panel: The arrows show (U_θ, U_ϕ) and colors show U_r (blue corresponds to downflows). Right panel: Color-scale representation of the density ρ; dark blue stands for low and light yellow for high values. Lower row, left panel: Color-scale representation of specific entropy s; dark blue stands for low and light yellow for high values. Middle panel: Color-scale representation of the current density squared $\boldsymbol{J}^2$; dark blue stands for low and light yellow for high values. Right panel: Current helicity $\boldsymbol{J} \cdot \boldsymbol{B}$, color-scale as in Figure 13. The dashed line indicates the equator at $\theta = \pi/2 = 90°$.

radius, but it stays rather high, which is due to the low magnetic field strength, especially in the coronal part, even though $B^2_{\mathrm{rms}}/B^2_{\mathrm{eq}} = 0.1-0.4$ in the convection zone. The time-averaged value is always above 5×10^4, and is therefore not comparable with the values in the solar corona, where the plasma β is very low because of the low density. There the magnetic field can drag dense plasma from the lower corona to its upper part. In our simulations the density stratification of the convection zone is much lower than in the Sun. Therefore, the density in the corona in our model is much higher and is closer to the density of the photosphere or the chromosphere. A rising magnetic flux tube has formed a low-density region in its interior due to a higher magnetic pressure. As the tube rises further into the coronal part, the density inside the tube is still lower than that outside because the coronal density is rather high in our model.

The simplification of a high plasma β corona might not be suitable to describe properly the mass flux of the plasma dragged by the magnetic field of the CME in the corona. However, the early work of Mikić, Barnes, and Schnack (1988), Ortolani and Schnack (1993), and Wiegelmann (2008) has shown that an isothermal force-free approach (not to be con-

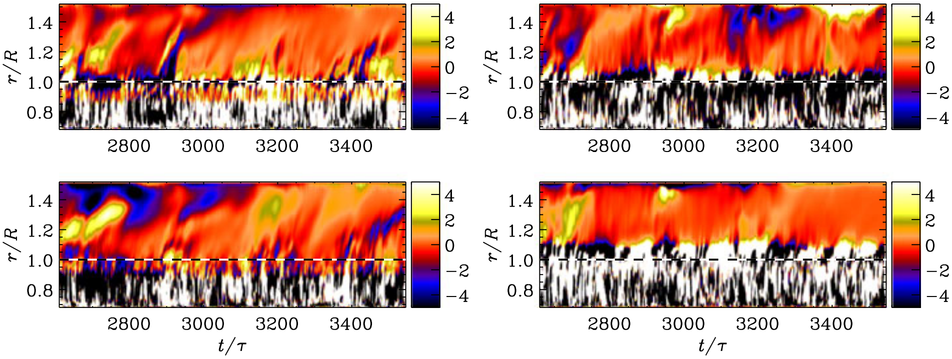

Figure 17 Recurrence of ejections shown by plotting the dependence of the dimensionless ratio $\mu_0 R\overline{\boldsymbol{J}\cdot\boldsymbol{B}}/\langle\overline{\boldsymbol{B}^2}\rangle_t$ on time t/τ and radius r in terms of the solar radius, taken from Run A5. The top panels show a narrow band in θ in the northern hemisphere and the bottom ones in the southern hemisphere. We have also averaged in latitude from 4.1° to 19.5° (left panel) and 32.5° to 45.5° (right). Dark blue shades represent negative and light yellow positive values. The dashed horizontal lines show the location of the surface at $r = R$.

fused with force-free magnetic equilibria) can describe the coronal magnetic field and even plasmoid ejections rather well. Note that in those papers the pressure gradient term was omitted, just like in the coronal part of WB. How important this really is remains unclear, because the pressure gradient term was not omitted in the work of WBM, which still showed ejections similar to those of WB. It would therefore be useful to compare our present model with one where the pressure gradient term is ignored in the coronal part, just like in WB.

The ejection seen in Figures 13 – 16 is not a single event – others follow in a recurrent fashion. However, the periodicity is not as clear as in previous work (WB, WBM). For Run A5, for example, we observe around five ejections during a time interval of about 1000 turnover times. A clearer indication for the recurrence of the ejections can be seen in Figure 17, where the normalized current density is averaged over two narrow latitude bands in each hemisphere. The slope of structures in the outer parts in these rt diagrams gives an indication about the ejection speed $V_{\rm ej}$ which turns out to be around one solar radius in 200 – 250 turnover times. This translates to $V_{\rm ej}/u_{\rm rms} \approx 0.1$, which is somewhat less than the values 0.2 – 0.5 found for the simulations of WBM. However, the mechanism which sets the time scale of ejections is at present still unclear.

Given that gravity decreases with radius, there is in principle the possibility of a radial wind with a critical point at $r_* = GM/2c_{\rm s}^2$ (Choudhuri, 1998), which would be at $r_* = 9.3\,R$, *i.e.* well outside our coronal part. Because of this and the fact that we use closed boundary conditions with no mass flux out of the domain, no such wind can occur in our simulations. Using a boundary condition that would allow a mass flux in the radial direction could change the speed and the ejection properties significantly. Including a solar-like wind in a model can have two major effects, which require a much higher amount of computational resources. The radial variation of gravity applied in these simulations implies the presence of a critical point rather close to the surface of the convection zone. Therefore, if a wind were to develop, the resulting velocity in the convection zone would be too high for a dynamo to develop; the magnetic field would be blown out too quickly. Using instead a more realistic profile for the solar wind with a position of the critical point around $r_* = 10R$, the corresponding density stratification would be too strong to be stably resolved.

4. Conclusions

In the present paper we have presented an extension of the two-layer approach of WB and WBM by including a self-consistent rotating convection zone into the model. We find a large-scale magnetic field generated by the convective turbulent motion in the convection zone. At moderate rotation rates, for a Coriolis number larger than three, we obtain a differential rotation pattern showing super-rotation, *i.e.*, an equator rotating faster than the poles. The dynamo solutions we find are different and some of them have a periodic oscillatory behavior, where the large-scale magnetic field does not change sign; only the strength is varying. At the maxima, the velocity is suppressed due to the backreaction via the Lorentz force. Small-scale magnetic structures seem to show an equatorward migration near the equator and a poleward one near the poles.

Using a convectively driven dynamo complicates the generation of ejections into a coronal part due to lower relative kinetic helicity. However, it was possible to produce ejections in two of the runs. The shape and the bipolar helicity structure are comparable with those of WBM. Due to the relatively high plasma β in the outer parts of our model (compared with the solar corona), the ejections produce local minima of density which are carried along and ejected out to the top of the domain. The ejections occur recurrently, but not clearly periodically, which is similar to the Sun.

Note that our results have to be interpreted cautiously, given the use of a simplistic solar atmosphere. We neglect the effects of high temperature and low plasma β. However, we feel that the mechanism of emergence of magnetic structures driven by dynamo action from self-consistent convection may not strongly depend on these two conditions. This suggestion has to be proven in more detail in forthcoming work.

An extension of the present work would require a detailed parameter study of cause and properties of the ejections. This also includes an advanced model for the solar corona with a lower plasma β and more efficient convection, which has a stronger stratification and is cooled by radiation. Another important aspect would be the generation of a self-consistent solar wind which supports and interacts with the ejections.

Acknowledgements The authors thank Hardi Peter for discussion of the dynamics and rotation behavior of the solar corona. We also thank the anonymous referee for many useful suggestions. We acknowledge the allocation of computing resources provided by the Swedish National Allocations Committee at the Center for Parallel Computers at the Royal Institute of Technology in Stockholm, the National Supercomputer Centers in Linköping and the High Performance Computing Center North in Umeå. Part of the computations have been carried out in the facilities hosted by the CSC – IT Center for Science in Espoo, Finland, which are financed by the Finnish ministry of education. This work was supported in part by the European Research Council under the AstroDyn Research Project No. 227952, the Swedish Research Council Grant No. 621-2007-4064, and the Academy of Finland grants 136189, 140970 (PJK) and 218159, 141017 (MJM) as well as the HPC-Europa2 project, funded by the European Commission – DG Research in the Seventh Framework Programme under grant agreement No. 228398.

References

Amari, T., Luciani, J.F., Mikic, Z., Linker, J.: 1999, *Astrophys. J.* **529**, L49.
Antiochos, S.K., De Vore, C.R., Klimchuk, J.A.: 1999, *Astrophys. J.* **510**, 485.
Archontis, V., Hood, A.W., Savcheva, A., Golub, L., DeLuca, E.: 2009, *Astrophys. J.* **691**, 1276.
Badalyan, O.G.: 2010, *New Astron.* **135**, 143.
Blackman, E.G., Brandenburg, A.: 2003, *Astrophys. J.* **584**, L99.
Blackman, E.G., Field, G.B.: 2000a, *Astrophys. J.* **534**, 984.
Blackman, E.G., Field, G.B.: 2000b, *Mon. Not. Roy. Astron. Soc.* **318**, 724.
Brandenburg, A., Candelaresi, S., Chatterjee, P.: 2009, *Mon. Not. Roy. Astron. Soc.* **398**, 1414.

Brandenburg, A., Moss, D., Tuominen, I.: 1992, *Astron. Astrophys.* **265**, 328.

Brandenburg, A., Procaccia, I., Segel, D.: 1995, *Phys. Plasmas* **2**, 1148.

Brandenburg, A., Sandin, C.: 2004, *Astron. Astrophys.* **427**, 13.

Brandenburg, A., Nordlund, Å., Pulkkinen, P., Stein, R.F., Tuominen, I.: 1990, *Astron. Astrophys.* **232**, 277.

Brun, A.S., Browning, M.K., Toomre, J.: 2005, *Astrophys. J.* **629**, 461.

Brun, A.S., Miesch, M.S., Toomre, J.: 2004, *Astrophys. J.* **614**, 1073.

Cantiello, M., Braithwaite, J., Brandenburg, A., Del Sordo, F., Käpylä, P.J., Langer, N.: 2011, In: *IAU Symp.* **272**, 32.

Choudhuri, A.R.: 1998, *The Physics of Fluids and Plasmas*, Cambridge University Press, Cambridge

Dobler, M., Stix, M., Brandenburg, A.: 2001, *Astrophys. J.* **638**, 336.

Elliot, J.R., Miesch, M.S., Toomre, J.: 2000, *Astrophys. J.* **533**, 546.

Fang, F., Manchester, W., Abbett, W.P., van der Holst, B.: 2010, *Astrophys. J.* **714**, 1649.

Guerrero, G., Käpylä, P.J.: 2011, *Astron. Astrophys.* **533**, A40.

Hoeksema, J.T., Wilcox, J.M., Scherrer, P.H.: 1982, *J. Geophys. Res.* **87**, A12.

Hubbard, A., Brandenburg, A.: 2010, *Geophys. Astrophys. Fluid Dyn.* **104**, 577.

Jouve, L., Brun, A.S.: 2009, *Astrophys. J.* **701**, 1300.

Kaiser, M.L., Kucera, T.A., Davila, J.M., St. Cyr, O.C., Guhathakurta, M., Christian, E.: 2008, *Space Sci. Rev.* **136**, 5.

Käpylä, P.J., Korpi, M.J., Brandenburg, A.: 2008, *Astron. Astrophys.* **491**, 353.

Käpylä, P.J., Mantere, M.J., Brandenburg, A.: 2011, *Astron. Nachr.* **332**, 883.

Käpylä, P.J., Mantere, M.J., Brandenburg, A.: 2012, *Astrophys. J. Lett.* **755**, L22.

Käpylä, P.J., Korpi, M.J., Brandenburg, A., Mitra, D., Tavakol, R.: 2010, *Astron. Nachr.* **331**, 73.

Käpylä, P.J., Korpi, M.J., Guerrero, G., Brandenburg, A., Chatterjee, P.: 2011, *Astron. Astrophys.* **531**, A162.

Kitchatinov, L.L., Rüdiger, G.: 1995, *Astron. Astrophys.* **299**, 446.

Levine, R.H., Schulz, M., Frazier, E.N.: 1982, *Solar Phys.* **77**, 363.

Li, Y., Luhmann, J.G., Lynch, B.J., Kilpua, E.K.J.: 2011, *Solar Phys.* **270**, 331.

Lionello, R., Riley, P., Linker, J.A., Mikić, Z.: 2005, *Astrophys. J.* **625**, 463.

Low, B.C.: 1994, *Phys. Plasmas* **1**, 1684.

Low, B.C.: 1996, *Solar Phys.* **167**, 217.

Low, B.C.: 2001, *J. Geophys. Res.* **106**, 25141.

Martínez-Sykora, J., Hansteen, V., Carlsson, M.: 2008, *Astrophys. J.* **679**, 871.

Miesch, M.S., Brun, A.S., Toomre, J.: 2006, *Astrophys. J.* **641**, 618.

Miesch, M.S., Elliot, J.R., Toomre, J., Clune, T.L., Glatzmaier, G.A., Gilman, P.A.: 2000, *Astrophys. J.* **532**, 59.

Mikić, Z., Barnes, D.C., Schnack, D.D.: 1988, *Astrophys. J.* **328**, 830.

Mitra, D., Tavakol, R., Brandenburg, A., Moss, D.: 2009, *Astrophys. J.* **697**, 923.

Mitra, D., Candelaresi, S., Chatterjee, P., Tavakol, R., Brandenburg, A.: 2010, *Astron. Nachr.* **331**, 130.

Nelson, N.J., Brown, B.P., Brun, A.S., Miesch, M.S., Toomre, J.: 2011, *Astrophys. J. Lett.* **739**, L38.

Ortolani, S., Schnack, D.D.: 1993, *Magnetohydrodynamics of Plasma Relaxation*, World Scientific, Singapore.

Ossendrijver, M., Stix, M., Brandenburg, A.: 2001, *Astron. Astrophys.* **376**, 713.

Pesnell, W.D., Thompson, B.J., Chamberlin, P.C.: 2012, The Solar Dynamics Observatory (SDO). *Solar Phys.* **275**, 3 – 15. doi:10.1007/s11207-011-9841-3.

Pinto, R., Brun, S.: 2011, In: *IAU Symp.* **271**, 393.

Plunkett, S.P., Vourlidas, A., Šimberová, S., Karlický, M., Kotrč, P., Heinzel, P., Kupryakov, Y.A., Guo, W.P., Wu, S.T.: 2000, *Solar Phys.* **194**, 371.

Régnier, S., Amari, T., Kersalé, E.: 2002, *Astron. Astrophys.* **392**, 1119.

Roussev, I.I., Forbes, T.G., Gombosi, T.I., Sokolov, I.V., DeZeeuw, D.L., Birn, J.: 2002, *Astrophys. J.* **588**, L45.

Rüdiger, G.: 1980, *Geophys. Astrophys. Fluid Dyn.* **16**, 239.

Schrijver, C.J., De Rosa, M.L.: 2003, *Solar Phys.* **212**, 165.

Sturrock, P.A.: 1980, *Solar Flares*, Colorado Associated University Press, Boulder.

Thompson, W.T., Kliem, B., Török, T.: 2011, *Solar Phys.* **276**, 241.

Timothy, A.F., Krieger, A.S., Vaiana, G.S.: 1975, *Solar Phys.* **42**, 135.

Török, T., Kliem, B.: 2003, *Astron. Astrophys.* **406**, 1043.

Vainshtein, S.I., Cattaneo, F.: 1992, *Astrophys. J.* **393**, 165.

Wang, Y.-M., Sheeley, N.R. Jr.: 1992, *Astrophys. J.* **392**, 310.

Warnecke, J., Brandenburg, A.: 2010, *Astron. Astrophys.* **523**, A19 (WB).

Warnecke, J., Brandenburg, A., Mitra, D.: 2011, *Astron. Astrophys.* **534**, A11 (WBM).

Wiegelmann, T.: 2008, *J. Geophys. Res.* **113**, A3.

Wöhl, H., Brajša, R., Hanslmeier, A., Gissot, S.F.: 2010, *Astron. Astrophys.* **520**, A29.

V

DRAFT VERSION APRIL 22, 2013
Preprint typeset using LaTeX style emulateapj v. 08/22/09

SOLAR-LIKE DIFFERENTIAL ROTATION IN A CONVECTIVE DYNAMO WITH A CORONAL ENVELOPE

JÖRN WARNECKE[1,2], PETRI J. KÄPYLÄ[1,3], MAARIT J. MANTERE[3,4] AND AXEL BRANDENBURG[1,2]
[1]NORDITA, KTH Royal Institute of Technology and Stockholm University, Roslagstullsbacken 23, SE-10691 Stockholm, Sweden
[2]Department of Astronomy, AlbaNova University Center, Stockholm University, SE-10691 Stockholm, Sweden
[3]Physics Department, Gustaf Hällströmin katu 2a, PO Box 64, FI-00014 University of Helsinki, Finland
[4]Aalto University, Department of Information and Computer Science, PO Box 15400, FI-00076 Aalto, Finland

Draft version April 22, 2013

ABSTRACT

We report on the results of four convective dynamo simulations with an outer coronal layer. The magnetic field is self-consistently generated by the convective motions beneath the surface. Above the convection zone we include a polytropic layer that extends to 1.6 solar radii. The temperature increases in this region to ≈ 8 times the value at the surface, corresponding to ≈ 1.2 times the value at the bottom of the spherical shell. We associate this region with the solar corona. We find solar-like differential rotation with radial contours of constant rotation rate, together with a near-surface shear layer. This non-cylindrical rotation profile is caused by a non-zero latitudinal entropy gradient which offsets the Taylor-Proudman balance through the baroclinic term. The meridional circulation is multicellular with a solar-like poleward flow near the surface at low latitudes. In most of the cases the mean magnetic field is oscillatory with equatorward migration in two cases. In other cases the equatorward migration is overlaid by stationary or even poleward migrating mean fields.

Subject headings: Magnetohydrodynamics – convection – turbulence – Sun: dynamo – Sun: rotation – Sun: activity

1. INTRODUCTION

The Sun has an activity cycle of eleven years, which is manifested by sunspots occurring at the solar surface. The sunspot number changes from a few during minimum to over 200 during maximum. The sunspot locations display a latitudinal dependence during the cycle. At solar minimum, sunspots emerge preferably at higher latitudes and during maximum at lower latitudes. By plotting these for several cycles, one obtains the 'butterfly diagram'. Every eleven years the polarity of sunspot pairs changes sign, which is characteristic of the 22-year magnetic cycle. To understand this cyclic behavior, one has to connect the fluid motions in the Sun with magnetic field generation to construct dynamo models. These dynamo models should be able to reproduce the 22-year magnetic activity cycle as well as the large-scale magnetic field evolution at the surface of the Sun. It is widely believed that the sunspots are correlated with the large–scale magnetic field distribution. Therefore, a successful solar dynamo model should reproduce the equatorward migration of the large-scale field as we observe it indirectly from sunspots and more directly from synoptic magnetograms.

Until recently, only kinematic mean-field models, where turbulent effects are parameterized through transport coefficients (e.g. Krause & Rädler 1980), have been able to show equatorward migration (e.g. Dikpati & Charbonneau 1999; Käpylä et al. 2006; Kitchatinov & Olemskoy 2012). Such models have been used to reproduce certain features of the solar cycle, such as the Maunder minimum (e.g., Karak 2010). However, those models are only valid in the kinematic regime in which the fluid motions are assumed given, so they are not self-consistently generated. The backreaction from the magnetic field is either ignored or taken into account in a rudimentary way involving ad hoc quenching for the turbulent transport coefficients. Direct numerical simulations (DNS) of the solar dynamo have been unsuccessful in producing equatorward migration using convective motions to drive a dynamo (e.g. Gilman 1983; Brun et al. 2004; Käpylä et al. 2010; Ghizaru et al. 2010; Brown et al. 2011; Nelson et al. 2013) so far. This was presumably due to the low fluid and magnetic Reynolds numbers of the simulations. Equatorward migration of the mean magnetic field was, for the first time, found in DNS by Käpylä et al. (2012). The exact cause is not yet fully understood, but the amount of density stratification seems to play an important role (Käpylä et al. 2013).

An important ingredient of the solar dynamo is differential rotation. It is believed that strong shear at the bottom of the convection zone (Spiegel & Weiss 1980) or near the surface (Brandenburg 2005), plays an important role in amplifying the magnetic field. However, even today it is not straightforward to reproduce a solar-like differential rotation profile. Mean-field simulations (Brandenburg et al. 1992; Kitchatinov & Rüdiger 1995) have been able to reproduce a solar-like rotation profile by modeling small-scale effects by mean-field coefficients through the Λ effect and anisotropic heat transport (see e.g. Rüdiger 1980, 1989). These models reproduce the positive (negative) latitudinal gradient of angular velocity in the northern (southern) hemisphere – i.e., the equator rotates faster than the poles – together with 'spoke-like' contours in the meridional plane. DNS of convective dynamos are able to reproduce a rapidly rotating equator at sufficiently large Coriolis numbers (Brun et al. 2004; Käpylä et al. 2011b). In purely hydrodynamical large-eddy simulations (LES), spoke-like differential rotation has only been found by imposing a latitudinal entropy gradient (Miesch et al. 2006) or, recently, by adding a stably stratified layer (Brun et al. 2011) at the bottom of the convection zone. A self-consistently generated spoke-like profile in DNS of magnetohydrodynamics has not yet been found.

An important issue with solar dynamo models is the effect of catastrophic quenching of the dynamo at high magnetic

Electronic address: joern@nordita.org (Revision: 1.256)

Reynolds numbers; see Brandenburg & Subramanian (2005). This is caused by the accumulation of magnetic helicity in the dynamo region. DNS provide evidence that magnetic helicity fluxes both within and through the boundaries of the dynamo domain can prevent the dynamo from being catastrophically quenched (e.g. Brandenburg & Sandin 2004; Hubbard & Brandenburg 2012). In the case of the Sun, magnetic helicity flux can emerge through the solar surface and can be transported away from the Sun by coronal mass ejections or by the solar wind (Blackman & Brandenburg 2003). In earlier work we mimic the case of the Sun by using an upper layer on the top of a dynamo region to allow for magnetic helicity fluxes leaving the domain (Warnecke & Brandenburg 2010; Warnecke et al. 2011, 2012a,b). This two-layer model was successful in showing that the dynamo is not only enhanced, but it can actually trigger the emergence of coronal ejections. These ejections have a similar shape as coronal mass ejections and carry a significant amount of magnetic helicity out of the dynamo region. In these models, the temperature in the coronal layer was the same as at the surface of the convection zone, which did not allow for a large density jump to develop. Furthermore, in the polytropic convection zone of Warnecke et al. (2012b), the convective flux was smaller than the radiative flux.

In this work we use the two-layer approach to investigate the influence of the coronal layer as an upper boundary condition for a convective dynamo. We focus on the physical properties and dynamics in the convection zone. The effects of varying the strength of stratification on a convective dynamo without corona is studied in a companion paper (Käpylä et al. 2013).

2. MODEL AND SETUP

We use a two-layer model in spherical polar coordinates (r, θ, ϕ), where the lower layer ($r \leq R$) represents the convection zone and the upper one the corona. The simulations are performed in a spherical wedge with radial extent $r_0 \leq r \leq R_\mathrm{c} = 1.6\,R$, where $r_0 = 0.7\,R$ corresponds to the bottom of the convection zone and R to the solar radius, for colatitudes $15^\circ \leq \theta \leq 165^\circ$ and an azimuthal extent $0 \leq \phi \leq 45^\circ$. We solve the following equations of compressible magnetohydrodynamics,

$$\frac{\partial \boldsymbol{A}}{\partial t} = \boldsymbol{u} \times \boldsymbol{B} + \eta \boldsymbol{\nabla}^2 \boldsymbol{A}, \tag{1}$$

$$\frac{\mathrm{D} \ln \rho}{\mathrm{D}t} = -\boldsymbol{\nabla} \cdot \boldsymbol{u}, \tag{2}$$

$$\frac{\mathrm{D}\boldsymbol{u}}{\mathrm{D}t} = \boldsymbol{g} - 2\boldsymbol{\Omega}_0 \times \boldsymbol{u} + \frac{1}{\rho}\left(\boldsymbol{J} \times \boldsymbol{B} - \boldsymbol{\nabla} p + \boldsymbol{\nabla} \cdot 2\nu\rho\mathsf{S}\right), \tag{3}$$

$$T\frac{\mathrm{D}s}{\mathrm{D}t} = -\frac{1}{\rho}\boldsymbol{\nabla}\cdot\left(\boldsymbol{F}^{\mathrm{rad}} + \boldsymbol{F}^{\mathrm{SGS}}\right) + 2\nu\mathsf{S}^2 + \frac{\mu_0\eta}{\rho}\boldsymbol{J}^2 - \Gamma_{\mathrm{cool}}(r), \tag{4}$$

where the magnetic field is given by $\boldsymbol{B} = \boldsymbol{\nabla} \times \boldsymbol{A}$ and thus obeys $\boldsymbol{\nabla} \cdot \boldsymbol{B} = 0$ at all times, $\boldsymbol{J} = \mu_0^{-1}\boldsymbol{\nabla} \times \boldsymbol{B}$ is the current density, μ_0 is the vacuum permeability, η and ν are the magnetic diffusivity and kinematic viscosity, respectively, $\mathrm{D}/\mathrm{D}t = \partial/\partial t + \boldsymbol{u} \cdot \boldsymbol{\nabla}$ is the advective time derivative, ρ is the density, and $\boldsymbol{u}$ is the velocity. The traceless rate-of-strain tensor is given by

$$\mathsf{S}_{ij} = \tfrac{1}{2}(u_{i;j} + u_{j;i}) - \tfrac{1}{3}\delta_{ij}\boldsymbol{\nabla} \cdot \boldsymbol{u}, \tag{5}$$

where semicolons denote covariant differentiation; see Mitra et al. (2009) for details. Furthermore, $\boldsymbol{\Omega}_0 = \Omega_0(\cos\theta, -\sin\theta, 0)$ is the rotation vector and p is the pressure. The gravitational acceleration is given by

$$\boldsymbol{g} = -GM\boldsymbol{r}/r^3, \tag{6}$$

where G is Newton's gravitational constant and M is the mass of the star. The radiative and sub-grid scale (SGS) heat fluxes are defined as

$$\boldsymbol{F}^{\mathrm{rad}} = -K\boldsymbol{\nabla}T, \quad \boldsymbol{F}^{\mathrm{SGS}} = -\chi_{\mathrm{SGS}}\rho T\boldsymbol{\nabla}s, \tag{7}$$

where K is the radiative heat conductivity and χ_{SGS} turbulent heat diffusivity, which represents the unresolved convective transport of heat. The fluid obeys the ideal gas law, $p = (\gamma - 1)\rho e$, where $\gamma = c_\mathrm{P}/c_\mathrm{V} = 5/3$ is the ratio of specific heats at constant pressure and constant volume, respectively, and $e = c_\mathrm{V}T$ is the internal energy density, defining the temperature T. Finally, $\Gamma_{\mathrm{cool}}(r)$ is the radial cooling profile which is specified in Equation (10).

The two-layer model is similar to that used in the previous work (Warnecke & Brandenburg 2010; Warnecke et al. 2011, 2012a,b), except that here we improve the model of Warnecke et al. (2012b) in two important ways. First, we use a more realistic model for the convection zone as in Käpylä et al. (2011a, 2012). Instead of using a polytropic setup with $m = 1$, we lower the radiative flux by using a profile for m (defined below) and introducing a turbulent heat conductivity χ_{SGS} (referred to as χ_t in Käpylä et al. 2012). We apply a piecewise constant profile for χ_{SGS} such that in the interval of $0.75\,R \leq r \leq 0.97\,R$ it is equal to a quantity $\overline{\chi}_{\mathrm{SGS}}$ (whose value is similar to that of the micro-physical viscosity ν), and it goes smoothly to zero above and below the boundaries of the interval. Additionally, we change the temperature profile compared to our earlier isothermal cold corona to a temperature-stratified corona, which is ≈ 8 times hotter than the surface and ≈ 1.2 hotter times than the bottom of the convection zone. In Figure 1, the profiles of averaged temperature, density, pressure, and entropy are shown for a typical run.

We initialize the simulations with precalculated radial profiles of temperature, density, and pressure. In the convection zone ($r \leq R$) we have an isentropic and hydrostatic initial state for the temperature, whose gradient is given by

$$\frac{\partial T}{\partial r} = \frac{-|\boldsymbol{g}(r)|}{c_\mathrm{V}(\gamma - 1)(m_{\mathrm{ad}} + 1)}, \tag{8}$$

where $m_{\mathrm{ad}} = 1.5$ is the polytropic index for an adiabatic stratification. This leads to a temperature minimum T_{min} above the surface of the convective layer at $r = R$. In the corona ($R \leq r \leq R_\mathrm{c}$), we prescribe the temperature as

$$T(r) = T_{\mathrm{min}} + \tfrac{1}{2}\left(T_{\mathrm{cor}} - T_{\mathrm{min}}\right)\left[1 + \tanh\left(\frac{r - r_{\mathrm{tra}}}{w}\right)\right], \tag{9}$$

where T_{cor} is temperature in the corona, and r_{tra} and the width $w = 0.02\,R$ are chosen to produce a smooth temperature profile as shown in Figure 1. The radial cooling profile $\Gamma_{\mathrm{cool}}(r)$ in Equation (4) maintains the temperature profile,

$$\Gamma_{\mathrm{cool}} = \Gamma_0 f(r)(c_\mathrm{s}^2 - c_{s0}^2)/c_{s0}^2, \tag{10}$$

where $f(r)$ is a profile function equal to unity in $r > R$ and going smoothly to zero in $r \leq R$, and Γ_0 is a cooling luminosity chosen such that the sound speed in the corona relaxes to-

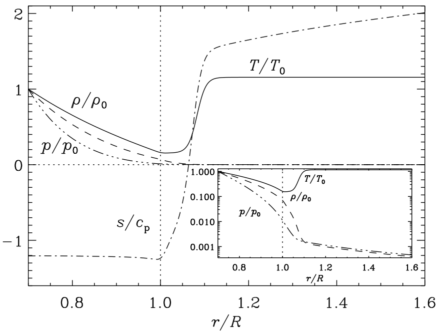

FIG. 1.— Radial profiles of stratification for Run A. The normalized density ρ/ρ_0 (dashed lines), pressure p/p_0 (dash-triple-dotted), temperature T/T_0 (solid) are plotted together with the specific entropy $s/c_{\rm P}$ (dash-dotted) over the radius. The inset shows various profiles in logarithmic representation to emphasize the steep decrease of the pressure and density in the coronal layer. The index 0 represents the value at the bottom of the convection zone.

wards the temperature profile given in Equation (9). As stated in Equation (10), the cooling function is sensitive to the local sound speed and hence to the total temperature consisting of a mean and a fluctuating part. Nevertheless, temperature fluctuations can still develop. The stratification of density follows from hydrostatic equilibrium. The density contrast within the convection zone is $\rho_0/\rho_{\rm s} \approx 15$ (see the sixth column in Table 1), while in the whole domain $\rho_0/\rho_{\rm t} \approx 2000$, where $\rho_{\rm s}$ is the density at the surface ($r = R$) and $\rho_{\rm t}$ the density at the top of the corona ($r = 1.6\,R$). The location of the surface, $r = R$, is determined by the position where the radial entropy gradient changes sign; see Figure 1. This implies that, similar to the Sun, convection ceases just below the surface. The radial heat conductivity profile is chosen such that the energy in the convection zone is transported mostly by convective motions. We apply a profile for the viscosity ν which is constant in the convection zone ($r \le R$) and increases smoothly above the surface to a value that is 20 times higher in the corona. This helps to suppress high velocities and sharp flow structures aligned with the rotation vector in the corona especially in the beginning of the simulation, when the magnetic field is weak. Compared with the use of a velocity damping in Warnecke et al. (2012b), this approach is Galilean invariant and allows the flow to develop more freely. The magnetic diffusivity η is constant throughout the convection zone, but decreases by 20% in the corona. In the convection zone, the radiative heat conductivity K is defined via a polytropic index m given by

$$m = 2.5\,(r/r_0)^{-15} - 1, \qquad (11)$$

which has a value of 1.5 at the bottom of the convection zone. The conductivity is proportional to $m+1$ and decreases toward the surface like r^{-15}. In the corona, K is chosen such that $\chi = K/\rho = \mathrm{const}$. The radiative diffusivity χ varies from $0.5\overline{\chi}_{\rm SGS}$ at the bottom of the convection zone to $0.04\overline{\chi}_{\rm SGS}$ near the surface and $0.3\overline{\chi}_{\rm SGS}$ in the corona. We initialize the magnetic field with weak Gaussian-distributed perturbations inside the convection zone.

We use periodic boundary conditions in the azimuthal direction. For the velocity field we apply stress-free boundary conditions at the radial and latitudinal boundaries. The magnetic field follows a perfect conductor condition at the lower radial and the two latitudinal boundaries. On the outer radial boundary, we force the field to be radial; for a discussion on the applicability of this boundary condition for the Sun see Warnecke et al. (2012b). We fix the gradient of the temperature at the lower radial boundary such that it corresponds to a given radiative flux, and at the radial outer boundary we set the temperature to a constant value. At the latitudinal boundaries, we impose a vanishing θ-derivative of entropy to have zero heat flux through the boundary.

Our runs are characterized by the values of the fluid and magnetic Reynolds numbers, $\mathrm{Re} = u_{\rm rms}/\nu k_{\rm f}$ and $\mathrm{Rm} = u_{\rm rms}/\eta k_{\rm f}$, respectively, where $u_{\rm rms}$ is the volume averaged rms velocity in the convection zone, and $k_{\rm f} = 2\pi/(R - r_0) \approx 21/R$ is used as a reference wavenumber. To represent the turbulent velocities in a proper way, we define $u_{\rm rms} = \sqrt{3/2\langle u_r^2 + u_\theta^2\rangle_{\theta\phi r\le R}}$, which corrects for the removal of the differential rotation-dominated ϕ-component of velocity. In our case, $\overline{\chi}_{\rm SGS} \approx 0.02\chi_{t0}$, where $\chi_{t0} = u_{\rm rms}/3k_{\rm f}$ is an estimate for the macro-physical turbulent diffusivity. We also define the fluid and magnetic Prandtl numbers $\mathrm{Pr} = \nu/\overline{\chi}_{\rm SGS}$ and $\mathrm{Pm} = \nu/\eta = \mathrm{Rm}/\mathrm{Re}$, the Coriolis number $\mathrm{Co} = 2\Omega_0/u_{\rm rms}k_{\rm f}$ and Taylor number $\mathrm{Ta} = (2\Omega_0 R^2/\nu)^2$. Time is given in turnover times, $\tau = (u_{\rm rms}k_{\rm f})^{-1}$. We measure the magnetic field strength as the rms value over the convection zone $B_{\rm rms}$, and we normalize this value with the equipartition value of the magnetic field defined by $B_{\rm eq}^2 = \mu_0\langle\rho\boldsymbol{u}^2\rangle_{r\le R}$. The typical diffusion time of the system is characterized by the fluid and magnetic Reynolds numbers times the turnover time. We use the (semi-) turbulent Rayleigh number $\mathrm{Ra_t}$ from the thermally relaxed state of the run,

$$\mathrm{Ra_t} = \frac{GM(R-r_0)^4}{\nu\overline{\chi}_{\rm SGS}R^2}\left(-\frac{1}{c_{\rm P}}\frac{{\rm d}\langle s\rangle_{\theta\phi t}}{{\rm d}r}\right)_{r=0.85\,R}. \qquad (12)$$

To monitor the solutions in the convection zone, we use two different heights, one near the surface at $r_1 = 0.97\,R$, and one in the middle of the convection zone at $r_2 = 0.84\,R$. We use the PENCIL CODE[1] with sixth-order centered finite differences in space and a third-order Runge-Kutta scheme in time; see Mitra et al. (2009) for the extension of the PENCIL CODE to spherical coordinates.

3. RESULTS

In this work we focus on four simulations that are summarized in Table 1. The main differences between these runs is their rotation rate and the magnetic Reynolds number. Runs Ab and Ac are a continuation of Run A after $t/\tau = 1350$ and $t/\tau = 1150$, respectively, but with smaller and higher diffusivities η in the convection zone. The Runs A, Ab, and Ac have a higher Coriolis number Co and lower values of Re than Run B. The Coriolis number of Run A is more than twice that of Run B. However, the nominal rotation rate determined by Ω_0 is only 1.8 times larger. We show the time evolution of the total rms velocity and magnetic field, averaged over the whole domain, $u_{\rm rms}^{\rm tot} = \langle u_r^2 + u_\theta^2 + u_\phi^2\rangle_{r\theta\phi}^{1/2}$ and $B_{\rm rms}^{\rm tot} = \langle B_r^2 + B_\theta^2 + B_\phi^2\rangle_{r\theta\phi}^{1/2}$, in all the four runs in Figure 2. Here, the subscripts on angle brackets denote averaging over r, θ, ϕ. Convection is sufficiently super-critical to develop during the first few tens of turnover times. After 50–200 turnover times, the dynamo starts to operate and a

[1] `http://pencil-code.googlecode.com`

TABLE 1
SUMMARY OF THE RUNS.

Run	grid	Pr	Pm	Ta	ρ_0/ρ_s	Ma	$\mathrm{Ra_t}$	Re	Rm	Co	$B^2_{\rm rms}/B^2_{\rm eq}$	Δ_Ω	ΔT
A	$400 \times 256 \times 192$	5	1	$1.4 \cdot 10^{10}$	14	0.08	$1.8 \cdot 10^{6}$	25	25	11	0.25	-0.011	0.08
Ab	$400 \times 256 \times 192$	5	0.71	$1.4 \cdot 10^{10}$	14	0.08	$1.8 \cdot 10^{6}$	25	18	11	0.22	-0.014	0.08
Ac	$400 \times 256 \times 192$	5	1.67	$1.4 \cdot 10^{10}$	14	0.08	$2.1 \cdot 10^{6}$	25	41	11	0.27	0.009	0.08
B	$400 \times 256 \times 192$	4	1	$7.2 \cdot 10^{9}$	14	0.09	$1.2 \cdot 10^{6}$	37	37	5.2	0.36	-0.06	0.12

NOTE. — The second to sixth columns show quantities that are input parameters to the models, whereas the quantities in the last eight columns are results of the simulations computed from the saturated state. All quantities are volume averaged over the convection zone $r \leq R$, unless explicitly stated otherwise. The Mach number is defined as $\mathrm{Ma} = u_{\rm rms}/c_{\rm s}|_{r=0.97\,R}$ and latitudinal differential rotation is quantified through $\Delta_\Omega = \partial\overline{\Omega}/\partial\cos^2\theta|_{r\leq R}/\Omega_0$. $\Delta T = (T_{\rm pol} - T_{\rm eq})/T_{\rm eq}$ is the normalized temperature difference between pole $T_{\rm pol} = \left(T(\theta = 15^\circ) + T(\theta = 165^\circ)\right)/2$ and equator $T_{\rm eq} = T(\theta = 90^\circ)$, measured at the surface ($r = R$).

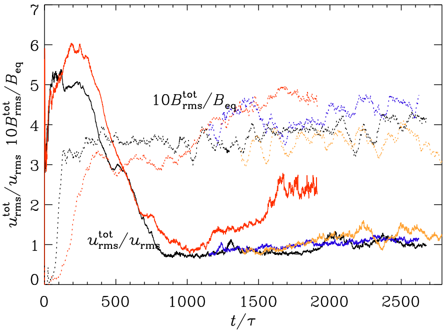

FIG. 2.— Time evolution of the total rms velocity and magnetic field. The rms velocity of the whole domain $u^{\rm tot}_{\rm rms}$ is normalized by $u_{\rm rms}$ (solid lines) and is plotted together with the rms magnetic field of the whole domain $B^{\rm tot}_{\rm rms}$ normalized by the equipartition field in the convection zone, $B_{\rm eq}$, (dotted lines) and multiplied by ten for visualization purposes for Runs A (black line), Run Ab (yellow), Run Ac (blue), and Run B (red).

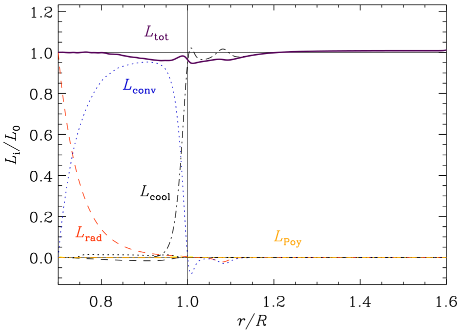

FIG. 3.— The different contributions to the total luminosity (solid purple line) are due to radiative diffusion (dashed red line), resolved convection (blue dotted), unresolved turbulent convection (black dotted), viscosity (yellow dashed), cooling flux (dash-dotted), and the Poynting flux (orange dash-dotted) for Run A. The thin solid black lines denote the zero level and the total luminosity through the lower boundary, respectively.

magnetic field grows at a rate that is higher for faster rotation (compare Runs A and B). Due to the high rotation rate and the lower density in the corona, the velocities there grow to higher values than in the convection zone. As described in Section 2, we use a higher viscosity to suppress these velocities and associated numerical difficulties. After the magnetic field in the convection zone has reached sufficient strength and expanded throughout the whole domain, it quenches the high velocities in the corona significantly, as is evident from Figure 2. When the magnetic field reaches $B^{\rm tot}_{\rm rms} \approx 0.3B_{\rm eq}$, the rms velocity decreases from $u^{\rm tot}_{\rm rms} \approx 6$ to ≈ 1, i.e., the contribution from the corona is now sub-dominant. This is caused by the Lorentz force, which becomes much stronger and comparable to the Coriolis force in the corona when the magnetic field has expanded into the whole domain. In the saturated state we have $u^{\rm tot}_{\rm rms} \approx u_{\rm rms}$, which is reached after around $t/\tau = 1000$ turnover times for Run A. Runs Ab and Ac are restarted from Run A after this saturation point either by increasing (Ab) or decreasing (Ac) the magnetic diffusivity η.

For Run B, at first it seems that the saturated state has been reached at $t/\tau = 1000$, but it turns out that both $u^{\rm tot}_{\rm rms}$ and the magnetic field start to grow again to reach another saturation level at $t/\tau \approx 1700$. While the differential rotation profile remains roughly unchanged despite of the growth of the energies (see Section 3), the magnetic field seems to undergo a mode change from an oscillatory to a stationary solution or an oscillatory solution with a much longer period in Run B (see Section 3.4). We note that an increase of $B^{\rm tot}_{\rm rms}$ in Figure 2, where we show the rms values of the magnetic field computed over the whole domain, does not necessarily imply an increase of the magnetic field inside the convection zone. The increase of the rms magnetic field can also be attributed to the development of magnetic structures ejected from the convection zone into the coronal region.

In Figure 3 we show the balance of various energy fluxes, contributing to the total luminosity for Run A. The radial components of radiative, convective, kinetic, viscous, and Poynting fluxes, as well as the flux due to the turbulent heat conductivity, are defined as

$$\overline{F}_{\rm rad} = \left\langle F^{\rm rad}_r \right\rangle, \tag{13}$$

$$\overline{F}_{\rm conv} = c_{\rm P} \left\langle (\rho u_r)' T' \right\rangle, \tag{14}$$

$$\overline{F}_{\rm kin} = \tfrac{1}{2} \left\langle (\rho u_r)' \boldsymbol{u}'^2 \right\rangle, \tag{15}$$

$$\overline{F}_{\rm visc} = -2\nu \left\langle (\rho u_i)' \mathsf{S}_{ir} \right\rangle, \tag{16}$$

$$\overline{F}_{\rm SGS} = \left\langle F^{\rm SGS}_r \right\rangle, \tag{17}$$

$$\overline{F}_{\rm Poy} = \langle E_\theta B_\phi - E_\phi B_\theta \rangle / \mu_0, \tag{18}$$

where $\boldsymbol{E} = \eta\mu_0 \boldsymbol{J} - \boldsymbol{u} \times \boldsymbol{B}$ is the electric field, the primes denote fluctuations, and angle brackets averaging over θ, ϕ, and a time interval over which the turbulence is statistically stationary. The resolved convective flux dominates inside the convection zone and reaches here much higher values than in our earlier model (Warnecke et al. 2012b). In the corona

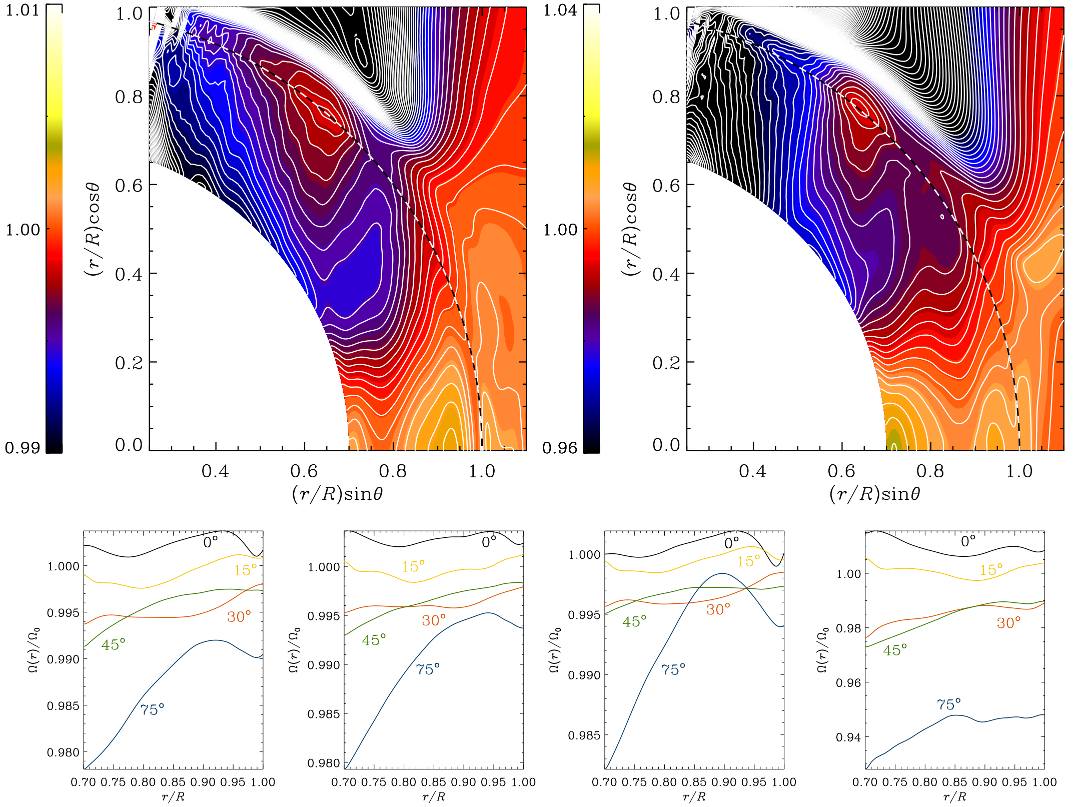

FIG. 4.— Zoomed-in differential rotation profiles the northern hemisphere in the convection zone. *Top row*: mean rotation profiles $\overline{\Omega}(r,\theta)/\Omega_0$ for Runs A and B. The black dashed lines indicate the surface ($r = R$). *Bottom row*: mean rotation profiles at four different latitudes for the four Runs A, Ab, Ac, and B: $90° - \theta = 0°$ (solid black), $90° - \theta = 15°$ (yellow), $90° - \theta = 30°$ (red), $90° - \theta_3 = 45°$ (green), and $90° - \theta_3 = 75°$ (blue).

the cooling keeps the total flux constant. Note the convective overshoot into the exterior and the negative radiative flux just above the surface ($r = R$), caused by the higher temperature in the corona. The kinetic energy flux has small negative values in the convection zone. The luminosity due to viscosity and Poynting flux are too small to be visible.

3.1. *Differential rotation*

In Figure 4, we show the mean rotation profiles $\overline{\Omega}(r,\theta) = \Omega_0 + \overline{u}_\phi/r\sin\theta$ for Runs A and B in the meridional plane and for Runs A, Ab, Ac, and B at four different latitudes. The contours of constant rotation are clearly not cylindrical for any of the four runs. They show a 'spoke-like' structure, i.e. the contours are more radial than cylindrical, which is similar to the solar rotation profile obtained by helioseismology. The equator is rotating faster than the poles, which has been seen in in many earlier simulations (Gilman 1983; Brun et al. 2004; Miesch et al. 2006; Käpylä et al. 2010, 2011b) and resembles the observed rotation of the Sun for our slower rotation case (Run B).

The source of differential rotation is the anisotropy of convection and is described by the $r\phi$ and $\theta\phi$ components of the Reynolds stress. Using a suitable parameterization of the Reynolds stress in terms of the Λ effect, one obtains differential rotation where the equator rotates faster than the poles. However, nonlinear mean-field hydrodynamic simulations have shown that for rotation rates comparable to those of the Sun, the contours of constant angular velocity become cylindrical (Brandenburg et al. 1992; Kitchatinov & Rüdiger 1995). To produce spoke-like rotation contours, the Taylor–Proudman balance has to be overcome by an important contribution in the evolution equation for the mean azimuthal vorticity $\overline{\omega_\phi}$, which is given by:

$$\frac{\partial\overline{\omega_\phi}}{\partial t} = r\sin\theta\frac{\partial\overline{\Omega}^2}{\partial z} + \left(\overline{\boldsymbol{\nabla}T\times\boldsymbol{\nabla}s}\right)_\phi + ... \qquad (19)$$

where $\partial/\partial z = \cos\theta\,\partial/\partial r - r^{-1}\sin\theta\,\partial/\partial\theta$ is the derivative along the rotation axis. The first term in Equation (19) is related to the curl of the Coriolis force and vanishes for cylindrical $\overline{\Omega}$ contours. The second term is the mean baroclinic term, which is caused mainly by latitudinal entropy variations. We ignore here additional contributions such as merid-

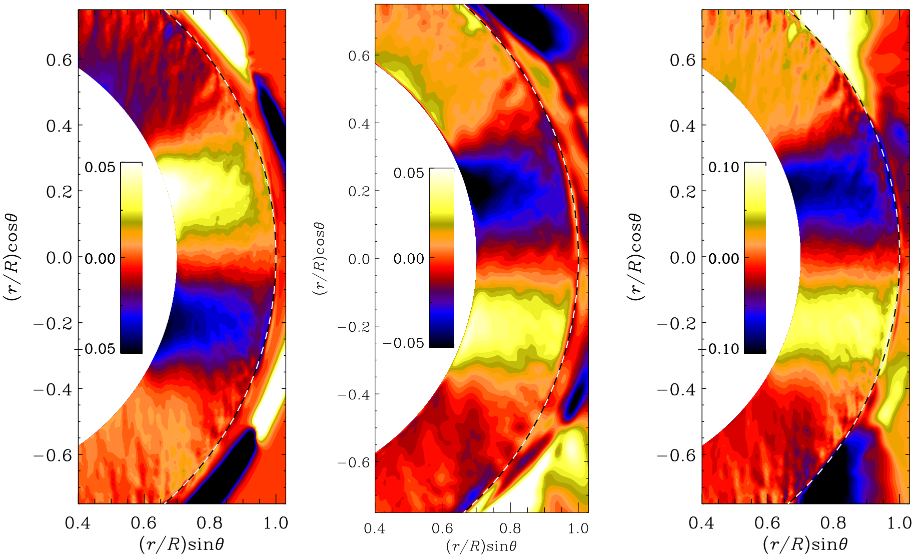

FIG. 5.— Representation of the two dominant terms in the evolution equation of mean azimuthal vorticity for Run A: $(\overline{\boldsymbol{\nabla} T \times \boldsymbol{\nabla} s})_\phi$ (left panel), and $r\sin\theta\,\partial\overline{\Omega}^2/\partial z$ (middle), both normalized by Ω_0^2. The rightmost panel shows the mean latitudinal entropy gradient $R\nabla_\theta\overline{s}/c_\mathrm{P}$. The dashed lines indicate the surface ($r = R$).

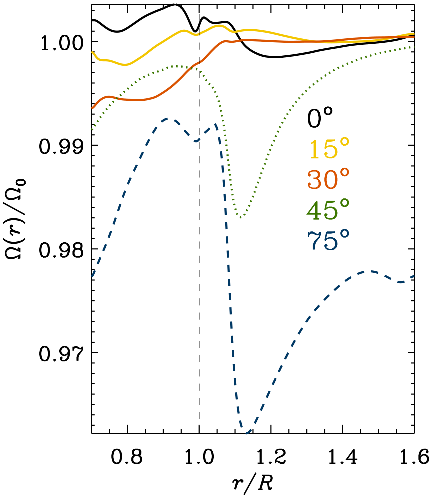

FIG. 6.— Differential rotation in the northern hemisphere including the coronal layer. Mean rotation profiles, $\overline{\Omega}(r,\theta)/\Omega_0$, at five different latitudes for Run A, $90° - \theta = 0°$ (solid black), $90° - \theta = 15°$ (yellow), $90° - \theta = 30°$ (red), $90° - \theta_3 = 45°$ (dotted green), and $90° - \theta_3 = 75°$ (dashed blue). The black dashed lines indicate the zero line, the surface ($r = R$).

ional Reynolds and Maxwell stresses which turn out to be small. In Figure 5, we plot the first and second terms of Equation (19) for Run A. These two contributions balance each other nearly perfectly. This leads us to conclude that these two terms give the dominant contribution to the production of mean azimuthal vorticity, and that the Taylor–Proudman balance is broken by the baroclinic term. It is remarkable that there is such a large and spatially coherent latitudinal entropy gradient, which is crucial to having a significant azimuthal baroclinic term and is self-consistently produced in the simulations.

Similar results have been obtained in mean-field simulations by including an anisotropic convective heat conductivity (Brandenburg et al. 1992; Kitchatinov & Rüdiger 1995) or by including a subadiabatic part of the tachocline (Rempel 2005), and in convection simulations by prescribing a latitudinal entropy gradient at the lower radial boundary of the convection zone (Miesch et al. 2006). More recently, Brun et al. (2011) showed that spoke-like contours can also be obtained by including a lower stably stratified overshoot layer in a purely hydrodynamical simulation.

The last column of Figure 5 shows the mean latitudinal entropy gradient $\nabla_\theta\overline{s}$ for Run A. The spatial distribution of the gradient agrees with the baroclinic term as well, because $\nabla_r\overline{T} \approx \mathrm{const}$, so we can conclude that the dominant contribution in the baroclinic term is due to the product of the latitudinal entropy gradient and the radial temperature gradient, which is more important than the radial entropy gradient multiplying the latitudinal temperature gradient. Compared with Run A, the other three runs, not shown here, have similar (Run B) or even identical (Runs Ab and Ac) distributions of the two terms of Equation (19) as well as the latitudinal entropy gradient.

We also note that, owing to the coronal envelope, differential rotation is able to develop a near-surface-shear layer. This is manifested by the concentration of contours of $\overline{\Omega}$ near the surface at lower latitudes for Runs A and B, and is also visible in the other runs as a negative gradient of $\overline{\Omega}$ in the same locations; see Figure 4. In Run B, there exists also a concentration around $r = 1.1\,R$. In all the simulations, the shear layer is radially more extended than in the Sun and penetrates deeper into the convection zone. Further studies using higher stratification should prove if this is just an artifact of weak stratification. However, the spoke-like rotation profile with strong shear near the surface occurs mostly at lower latitudes ($\theta - 90^\circ \leq 15^\circ$), i.e. close to the equator. At latitudes above $\pm 30^\circ$ the contours of constant rotation are more complex, but show some indication of strong shear close to the surface and only in Run B the contours become cylindrical beyond $\pm 60^\circ$ latitude. At higher latitudes ($\theta - 90^\circ \leq 75^\circ$) the near-surface shear layer is again visible. The location of the spoke-like differential rotation profile coincides with a similarly shaped mean latitudinal entropy gradient. The entropy gradient in the northern (southern) hemisphere is negative (positive) below $\pm 30^\circ$ latitude. In Run B, this region reaches to higher latitudes than in Runs A, Ab and, Ac, which leads to radial contours of angular velocity at higher latitudes.

We were not able to see spoke-like rotation profiles in our previous work (Warnecke et al. 2012b). Therefore the applied changes might play an important role in the formation of spoke-like profiles. There are three main differences between the two setups. First, the fractional convective flux in Warnecke et al. (2012b) is much lower than in the present setup; compare Fig. 2 of Warnecke et al. (2012b) with Fig. 3. A stronger convective flux can give rise to more vigorous heat fluxes and thus a more efficient thermal redistribution, causing a more pronounced latitudinal entropy gradient. Secondly, the temperature in the current setup increases sharply above the surface, generating a hot corona instead of being constant as in Warnecke et al. (2012b). It is possible that the resulting steep temperature gradient is important in providing enough thermal insulation between the convection zone and the corona. Thirdly, the hot corona leads to higher density stratification both in the convection zone and in the corona.

As seen in Figure 6, the corona rotates nearly uniformly with $\overline{\Omega}(r,\theta)/\Omega_0 = 1$ at lower latitudes ($90^\circ - \theta \leq 30^\circ$). We suggest that the magnetic field, which connects the surface with the corona, is responsible for this. Near the poles ($90^\circ - \theta \geq 45^\circ$), the rotation rate drops sharply above the surface ($r \approx 1.1\,R$). This drop coincides with the steep temperature and density gradients above the surface, but also with the increase in the applied viscosity profile. Further outside and away from this drop, the rotation profile is cylindrical at high latitudes. This behavior is similar in all four runs.

3.2. *Connection with anisotropic turbulent diffusivity tensor*

As mentioned above, we expect the latitudinal entropy gradient to be a consequence of an anisotropic convective (turbulent) diffusivity tensor. Such anisotropies are caused by the rotational influence on the turbulence (see, e.g., Weiss 1965; Rüdiger 1989). In particular, there is a term proportional to $\Omega_{0i}\Omega_{0j}$; here, Ω_{0i} is the ith component of $\boldsymbol{\Omega}_0 = (\cos\theta, -\sin\theta, 0)\Omega_0$, which gives a symmetric contribution $\chi_{r\theta} = \chi_{\theta r}$ proportional to $\cos\theta\sin\theta$, so it vanishes at the poles and at the equator. In the presence of a latitudinal entropy gradient, it leads to an additional contribution to the radial convective flux,

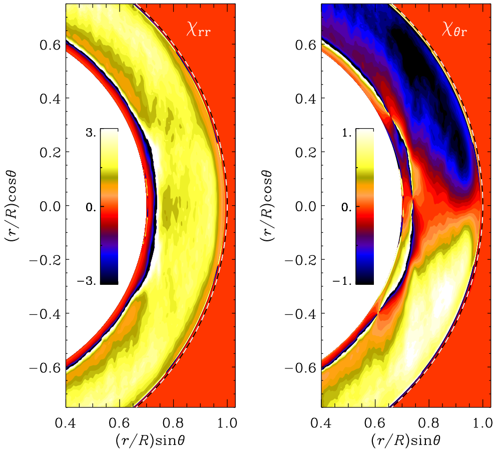

FIG. 7.— Radial component χ_{rr} (left panel) and off-diagonal component $\chi_{\theta r}$ (right) of the turbulent heat conductivity tensor normalized by $\chi_{t0} = u_{\rm rms}/3k_{\rm f}$ and calculated from Equations (23) and (24) for Run A. Note the high values at the bottom of the convection zone, which are due to the vanishing radial entropy gradient.

$$\overline{F}_r = -\chi_{rr}\overline{\rho}\,\overline{T}\boldsymbol{\nabla}_r\overline{s} - \chi_{r\theta}\overline{\rho}\,\overline{T}\boldsymbol{\nabla}_\theta\overline{s}. \qquad (20)$$

Since $\chi_{r\theta} = \chi_{\theta r}$, and since there is a radial entropy gradient, it also leads to a contribution in the latitudinal flux,

$$\overline{F}_\theta = -\chi_{\theta r}\overline{\rho}\,\overline{T}\boldsymbol{\nabla}_r\overline{s} - \chi_{\theta\theta}\overline{\rho}\,\overline{T}\boldsymbol{\nabla}_\theta\overline{s}. \qquad (21)$$

If we ignore the second term proportional to $\boldsymbol{\nabla}_\theta\overline{s}$, we can estimate $\chi_{\theta r}$ by measuring

$$\overline{F}_\theta = c_{\rm P}\overline{\rho}\,\overline{u'_\theta T'}, \qquad (22)$$

so

$$\chi_{\theta r} \approx -c_{\rm P}\overline{u'_\theta T'}\Big/\overline{T}\boldsymbol{\nabla}_r\overline{s}. \qquad (23)$$

The result is shown in Figure 7, where we also plot a similar estimate of the radial component,

$$\chi_{rr} \approx -c_{\rm P}\overline{u'_r T'}\Big/\overline{T}\boldsymbol{\nabla}_r\overline{s}. \qquad (24)$$

We normalize χ_{ij} by $\chi_{t0} = u_{\rm rms}/3k_{\rm f}$ and find $\chi_{\theta r}/\chi_{t0} \approx 1$ and $\chi_{rr}/\chi_{t0} \approx 2$, corresponding to $\chi_{\theta r}/\overline{\chi}_{\rm SGS} \approx 0.02$ and $\chi_{rr}/\overline{\chi}_{\rm SGS} \approx 0.04$.

In reality, and as a consequence, we cannot neglect the second term proportional to $\boldsymbol{\nabla}_\theta\overline{s}$, even though it is about 10 times smaller than $|\boldsymbol{\nabla}_r\overline{s}|$ in our simulations. To test the accuracy of Equations 23 and 24, we compute two-dimensional histograms of latitudinal and radial heat fluxes vs. latitudinal and radial entropy gradients; see Figure 8. The determined values of the turbulent heat diffusivities of Figure 7 are consistent with those results. However, a clear linear trend is not visible, except for a narrow range in the case of χ_{rr}. In the first panel, the line with $\chi_{rr} = 1.85\chi_{t0}$ fits well with maximum of correlation. Indeed, looking at the left panel of Figure 7, $\chi_{rr} = 2\chi_{t0}$ is compatible with this. A similar behavior can be seen in the top right panel of Figure 8. We see that the lines of $\chi_{\theta r} = \pm 0.7\chi_{t0}$ fit well through the maxima of the

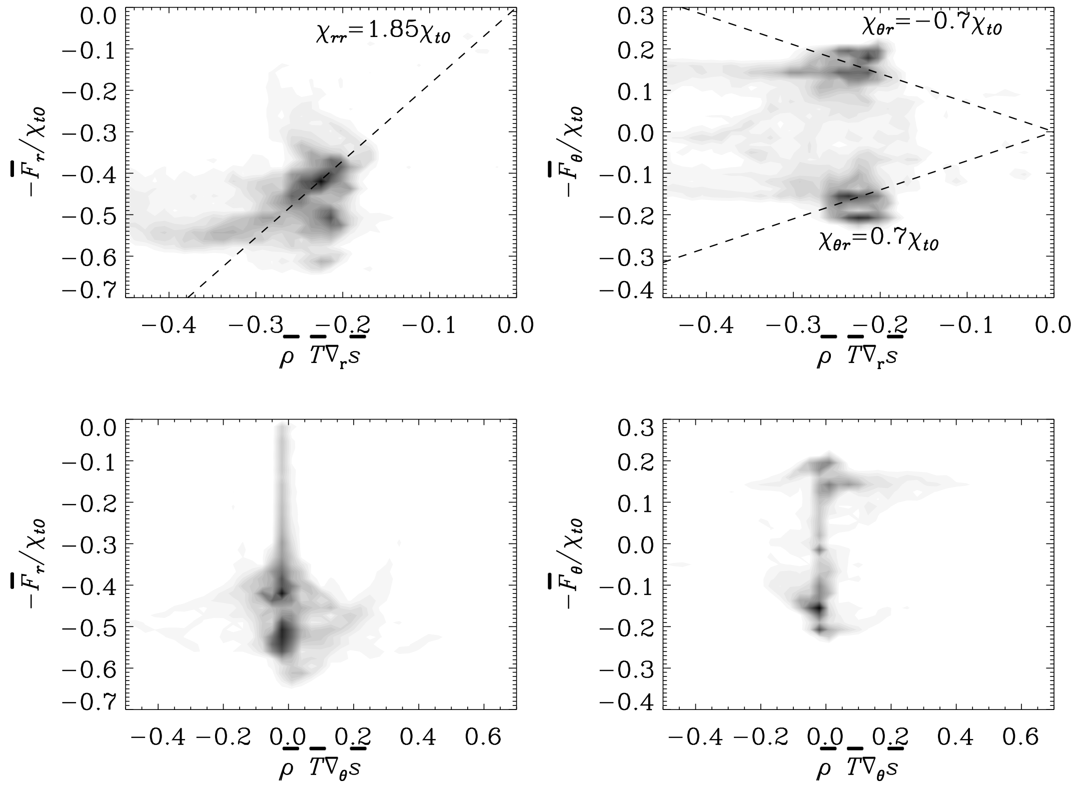

FIG. 8.— Two-dimensional histograms of the radial and latitudinal heat flux versus the radial and latitudinal entropy gradient for Run A. The four panels show from top left to bottom right, $\overline{F}_r$ vs. $\overline{\rho}\overline{T}\boldsymbol{\nabla}_r\overline{s}$, $\overline{F}_\theta$ vs. $\overline{\rho}\overline{T}\boldsymbol{\nabla}_r\overline{s}$, $\overline{F}_r$ vs. $\overline{\rho}\overline{T}\boldsymbol{\nabla}_\theta\overline{s}$, and $\overline{F}_\theta$ vs. $\overline{\rho}\overline{T}\boldsymbol{\nabla}_\theta\overline{s}$. In the first two panels, we overplot the corresponding values for the turbulent heat diffusivities, determined from Figure 7 (dashed black lines) and slightly smaller values (red lines).

data, but we cannot find any indication of a linear correlation as suggested by Equations 23 and 24. The last two panels support our assumption that the latitudinal entropy gradient can be neglected when calculating the turbulent heat diffusivity. The main conclusion of the two-dimensional histogram is that the correlation suggested by Equation 23 and 24 is at best only true for the radial gradient of $\overline{s}$, but not for the latitudinal one. The ratio of the convective flux and the entropy gradient is dominated by the ratio of two points rather than a correlation. Although the latitudinal entropy gradient is only ten times smaller than the radial one, we cannot find a linear correlation. This is surprising, given that these mean field relations have been used successfully to model the differential rotation profile as well as the turbulent heat transport of Sun in good agreement with observation (see e.g. Kitchatinov & Rüdiger 1995). In fact, as shown in the mean field calculations of Brandenburg et al. (1992), it tends to balance the first term so as to reduce the latitudinal heat flux and thus to produce a latitudinal entropy gradient and thus a baroclinic term as we see it.

To investigate the baroclinic term and the turbulent heat diffusivities as well as their influence on the differential rotation in more detail, we compare the present runs, where we include a coronal envelope, with runs without a coronal envelope. The runs without a coronal envelope are taken from Käpylä et al. (2012) and Käpylä et al. (2013). Thus, we compare Figures 5 and 7 for Run A with the corresponding ones for Run C1 of Käpylä et al. (2013), which is the same as Run B4m of Käpylä et al. (2012); see Figures 9 and 10. As in Run A above, the baroclinic term of Run C1 balances the advection term. However, the values are 4 times larger and the shape shows a clear radial variation. The baroclinic term is largest near the surface, whereas in Figure 5 of Run A, the term is stronger near the bottom of the convection zone. In Run C1, on the other hand, the terms are small near the bottom and close to the equator. The component of the turbulent heat diffusivity tensor (Figure 10) looks quite different from Run A; compare with Figure 7. The radial heat conductivity is about 2 times smaller than in the runs with a corona. The mean radial entropy gradient has a positive sign at ±15° latitude, and extends from the bottom to the middle of the convection zone. How these two behaviors can change the solar-like rotation to a more cylindrical rotation is unclear. Stratification may be important, because in Run C1 without corona the density con-

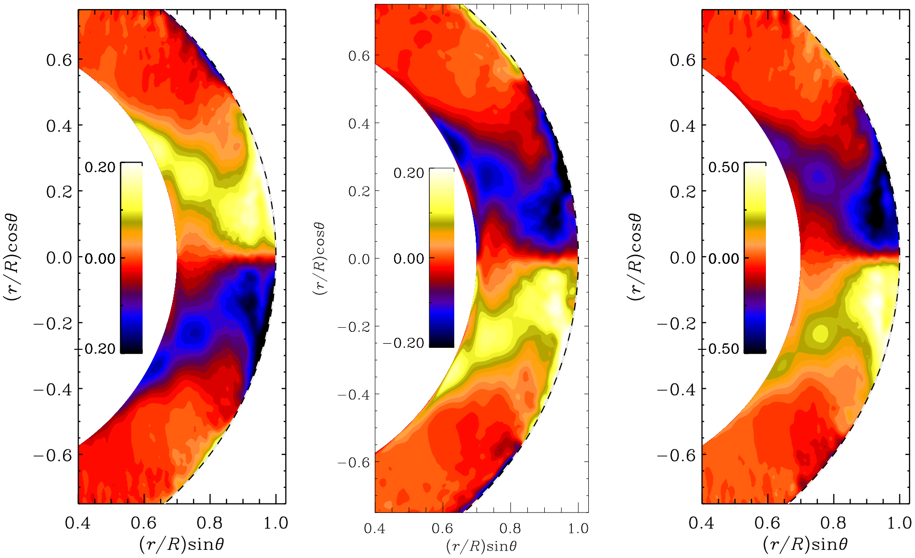

FIG. 9.— The same Figure as 5, but for Run C1 of Käpylä et al. (2013), which is the same as Run B4m of Käpylä et al. (2012).

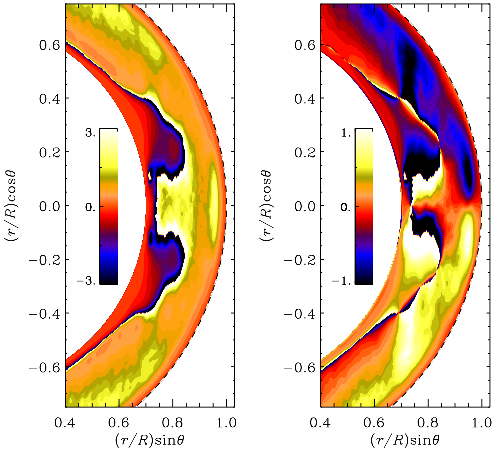

FIG. 10.— The same Figure as 7, but for Run C1 of Käpylä et al. (2013), which is the same as Run B4m of Käpylä et al. (2012). This Run is similar to those of the present work without a coronal envelope.

trast is $\rho_0/\rho_s = 22$, which is slightly higher than in the four runs of this work.

3.3. *Meridional circulation*

Another important result is the solar-like meridional circulation in the convection zone. In Figure 11 we plot the meridional circulation in terms of the mass flux as vectors of $\overline{\rho}(\overline{u}_r, \overline{u}_\theta, 0)$ and as radial cuts of $\overline{\rho u_\theta}$ through colatitudes $\theta_1 = 60°$, $\theta_2 = 75°$, and $\theta_3 = 83°$, corresponding to latitudes $30°$, $15°$, and $7°$. Note here that in the northern (southern) hemisphere a negative $\overline{\rho u_\theta}$ means poleward (equatorward) flow, and a positive one equatorward (poleward) flow. Runs A, Ab, and Ac show significant solar-like surface profiles of meridional circulation, while Run B shows a different pattern. Looking at Run A, in the northern hemisphere at lower latitudes ($\leq 20°$) just below the surface ($r_1 = 0.97\,R$), the meridional circulation is poleward with $\overline{\rho}\,\overline{u}_\theta = -0.007\rho_0 u_{\rm rms}$. Above the surface there is a return flow in the equatorward direction. This return flow peaks above the surface with a similar flux. The turning point $\overline{\rho}\,\overline{u}_\theta = 0$ is just below the surface, at around $r = 0.985\,R$. The location of this turning point is consistent with the location where the entropy gradient changes from negative to positive, i.e., from convectively unstable to convectively stable; see Figure 1. If we were to redefine the surface of the simulated star to this radius, we would obtain a solar-like meridional circulation, where the circulation is poleward at the surface. The velocity near the surface is $u_\theta \approx 0.07 u_{\rm rms}$. To compare this with the meridional circulation at the surface of the Sun, which is $10 - 30\,{\rm m\,s^{-1}}$ (Zhao & Kosovichev 2004), we calculate the corresponding value of $u_{\rm rms}$ from the convective flux, $\overline{F}_{\rm conv} \approx \rho u_{\rm rms}^3$, with a typical density of $\rho_{\rm conv} = 2.5\,{\rm kg\,m^{-3}}$ near the surface of the convection zone at $r = 0.996\,R$ (Stix 2002). Our estimate of corresponding meridional circulation gives $u_{\rm m} = 0.07(\overline{F}_{\rm conv}/\rho_{\rm conv})^{1/3} \approx 20\,{\rm m\,s^{-1}}$, which is consistent with the solar value. Similar estimates apply to the southern hemisphere, but the meridional circulation is here a bit weaker. This behavior can also be found in Runs Ab and Ac, where the flows are weaker and the turning points lie slightly deeper. Note that the larger return flow is a cause of our particular setup, which has much weaker stratification than the Sun; see Figure 1. Higher stratification should lead to a much weaker return flow above the surface. In

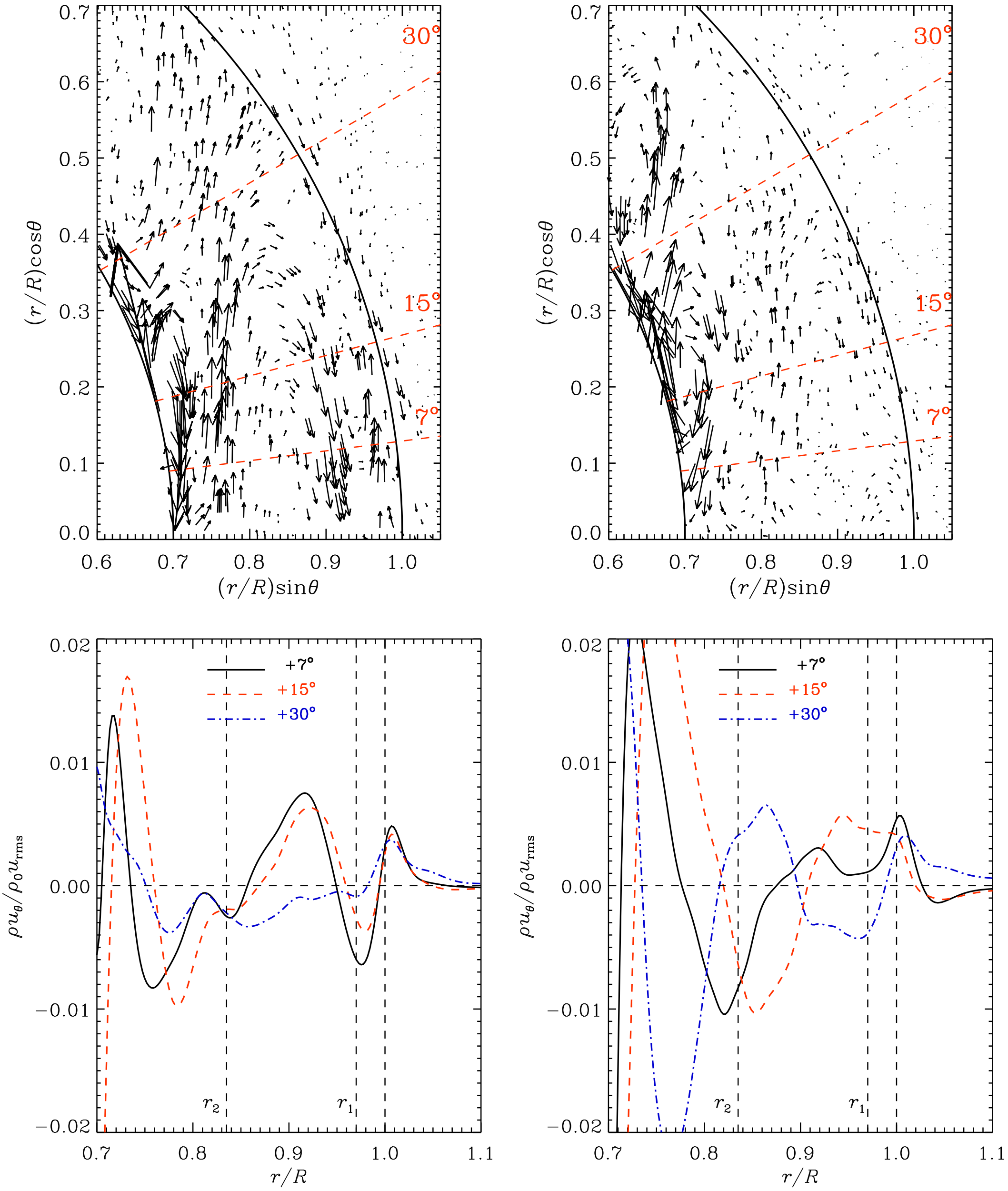

FIG. 11.— Meridional circulation in the northern hemisphere in the convection zone. *Top row*: meridional circulation as vectors in terms of the mass flux $\overline{\rho}(\overline{u}_r, \overline{u}_\theta, 0)$ for Runs A (left) and B (right), where for Run B the arrows are reduced in size by a factor of 3. The three red dashed lines represent the latitudes $90^\circ - \theta_1 = 30^\circ$, $90^\circ - \theta_2 = 15^\circ$, and $90^\circ - \theta_3 = 7^\circ$, which are used in the bottom row and in Figures 12 and 13. The black solid lines indicate the surface ($r = R$) and the bottom of the convection zone ($r = 0.7\,R$). *Bottom row*: latitudinal mass flux $\overline{\rho u_\theta}/\rho_0 u_{\rm rms}$ plotted over radius r/R for three different latitudes θ_1 (blue dotted-dashed line), θ_2 (red dashed line) and θ_3 (black solid line) in the northern hemisphere for Runs A (left) and B (right). ρ_0 is the density at the bottom of the convection zone. The black dashed lines indicate the surface ($r = R$) and the radii $r_1 = 0.97\,R$ and $r_2 = 0.84\,R$.

Run B, a poleward flow develops in the northern hemisphere only close to poles ($\theta = \theta_1$). The meridional circulation has a latitudinal dependence. In Run A the return flow reaches higher velocities at lower latitudes ($\leq \pm 20°$). The same is true for the poleward circulation below the solar surface. In Run B, we find the opposite and the return flow increases with latitude, and so does the meridional circulation.

From the bottom row of Figure 11, we can estimate the number of meridional circulation cells at low latitudes. We find that there are at least two cells in the convection zone. In Run A, there is one cell with poleward flow maxima around $r = r_1$ and minima around $r = 0.91\,R$, where the mass flux closer to the surface is as large as that in the return flow deeper in the convection zone. A second cell is deeper down in the convection zone and has similar extent and flux. In Runs Ab and Ac, the pattern is different and the flux weaker, but there are indications of a third cell. Note that the stratification leads to stronger mass fluxes over a smaller cross-sectional area deeper in the convection zone than near the surface, while the velocity is similar. In Run B, there are two strong cells of meridional circulation. The cells seem to be more cylindrical than latitudinal, which can also be seen in the phase shift of the pattern for different latitudes. Even deeper down in the convection zone, the meridional flow is much stronger than in Runs A, Ab, and Ac. This is consistent with results from models with anisotropic viscosity (or lowest order Λ effect), which show a maximum of meridional circulation for Taylor numbers around 10^7 (Köhler 1970). Our Taylor number is above this value, so the circulation decreases with faster rotation, which is also in agreement with numerical simulations (Ballot et al. 2007; Brown et al. 2008; Augustson et al. 2012). We emphasize that this does not apply to the non-dimensional meridional circulation, normalized with viscosity, which does not show a maximum.

3.4. *Mean magnetic field evolution*

The turbulent helical motions generated by convective heat transport together with differential rotation produce a large-scale magnetic field inside the convection zone. It grows exponentially and shows an initial saturation after around $t/\tau = 100$ for Run A; see Figure 2. Run B shows a more peculiar behavior: the field seems to have saturated at around $t/\tau = 300$, but it starts growing again at around $t/\tau = 700$ and appears to saturate at $t/\tau = 1700$. The latter growth is possibly related to a change of the oscillatory mode into stationary one; see Figures 12 and the discussion below. The magnetic and fluid Reynolds numbers of Run B are higher than for the other cases, which should lead to a higher growth rate. However, the rotation rate measured by Co is around half that of Run A, which leads to a slower amplification of the field. At a later time, around $t/\tau = 1000$, the field of Run B becomes comparable to or even stronger than that of Run A. The value of B_{rms} reaches around 0.5 of the equipartition field strength in Runs A, Ab, and Ac, and 0.6 in Run B; see Table 1. By comparison, $B_{\mathrm{rms}}^{\mathrm{tot}}$ is around 20% lower because the field is mainly concentrated in the convection zone. The equatorward migration pattern is visible in three of the four runs at high latitudes. In Run A, the pattern seems to transform into slow poleward migration at lower latitudes, but the equatorward migration pattern re-appears at $t/\tau = 2300$. We suggest that the equatorward migrating dynamo mode is dominant after $t/\tau = 500$, while being overcome by other modes between $t/\tau = 1500$ and $t/\tau = 2300$. Comparing these results with those of Käpylä et al. (2012) without a corona but an otherwise comparable setup, the magnetic field in the current simulations is slightly weaker. In Figure 2 of the work by Käpylä et al. (2012), the mean toroidal magnetic field strength is close to super-equipartition ($\overline{B}_\phi \approx B_{\mathrm{eq}}$), whereas in Figure 12 the mean magnetic field strength is roughly $\overline{B}_\phi = 0.5 B_{\mathrm{eq}}$. Additionally, the growth rate of the dynamo is greater than in the models without corona, where it takes up to five time longer to reach dynamically important field strengths. This is not surprising because the dynamo in the two-layer model is less restricted and has more freedom for different dynamo modes to be excited. There is no restriction due to the magnetic boundary at the surface, which is open in our simulations and restricted to vertical field in the convection zone simulations of Käpylä et al. (2012). This could explain the fast growth in the beginning, but not the decreased saturation level. On the other hand, the runs in this work and the runs of Käpylä et al. (2012, 2013) have also differences in other parameters, such as stratification, rotation rate, and the Reynolds numbers Re, Rm, so direct comparison might not be possible.

Recently, also other authors have reported magnetic cycles. In the work by Brown et al. (2011) and Nelson et al. (2013), using anelastic LES, the authors were able to produce an oscillatory field, but without a clear pattern and no equatorward migration. In the simulations by Ghizaru et al. (2010) and Racine et al. (2011), who used an implicit method, the mean magnetic field shows a clear oscillatory behavior, but no clear signs of equatorward migration; see Figure 4 of Ghizaru et al. (2010) and Figure 8 of Racine et al. (2011). At the moment, only the work by Käpylä et al. (2012, 2013) and the present work show clear evidence of equatorward migration.

Looking just at B_{rms} in the convection zone or at $B_{\mathrm{rms}}^{\mathrm{tot}}$ in the whole domain in Figure 2, we find evidence of cyclic behavior of the field for Runs A, Ab, and Ac. The cycle period is $t/\tau \approx 100$. In Run B, there is no clear evidence of cyclic behavior. Investigating the different components of the mean magnetic field we also find signs of oscillatory behavior. In Figure 12, we plot the azimuthal mean magnetic field $\overline{B}_\phi$ over time and latitude at r_1 for Runs A, Ab, Ac, and B, while in Figure 13 we show $\overline{B}_\phi$ at r_2 and the radial mean field $\overline{B}_r$ at r_1 and r_2 for Run A. The structure of the magnetic field changes as the dynamo evolves from the kinematic regime, where the magnetic field is weak and does not significantly influence the flow. In Run A, the azimuthal and radial mean fields migrate poleward close to the equator in the kinematic regime. The cycle period is short, just around $t/\tau = 20$. In Run B, we found a similar behavior. The fast poleward migration happens at lower latitudes ($\pm 40°$) for both runs. We recall that in Run A, after a short time ($t/\tau \sim 100$) the field is strong enough to backreact on the flow. Now two things happen simultaneously: an oscillating mean magnetic field is starting to migrate equatorward at higher latitudes and the fast poleward migration becomes slower. The period of the equatorward oscillation is longer and is between $t/\tau = 100$ and 150 for the rest of the run. This period is consistent with those obtain from the $B_{\mathrm{rms}}^{\mathrm{tot}}$ time series. The poleward migration near the equator slows down until it finally turns into an equatorward migration aligned with the migration at the higher latitudes ($t/\tau = 500$). Thus we have equatorward migration of the mean radial and azimuthal fields at all latitudes until around $t/\tau = 1500$ and again after $t/\tau = 2300$; see Figure 13. During this interval, the dynamo mode changes and, consequently, its latitudinal migration pattern changes. The equatorward migrating and oscillating field near the poles show a stable pattern during the

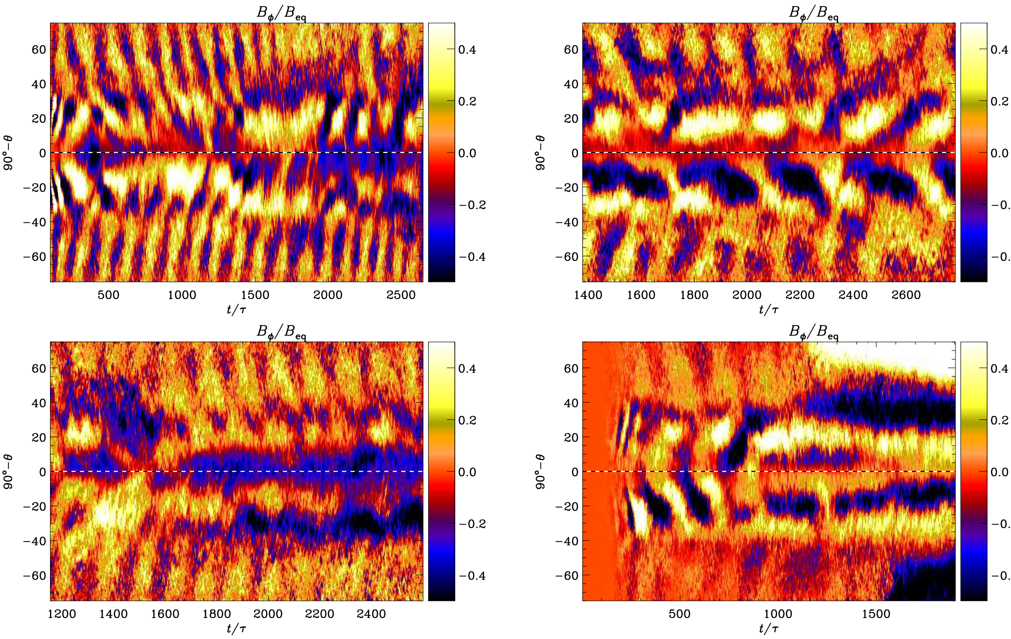

FIG. 12.— Time evolution of the mean magnetic field in the convection zone. From top left to bottom right we show $\overline{B}_\phi$ for Runs A, Ab, Ac, and B at $r_1 = 0.97R$. Dark blue shades represent negative and light yellow positive values. The dashed horizontal lines show the location of the equator at $\theta = \pi/2$. The magnetic field is normalized by its equipartition value, $B_{\rm eq}$.

whole simulation, but near the equator the field changes with time. In the northern hemisphere there is a transient poleward migration, which is in phase with the equatorward migration near the poles. In the southern hemisphere the equatorward migration is still dominant, but a stationary mode is superposed near the equator. After $t/\tau = 2300$, the equatorward migration returns and penetrates again to lower latitudes. The migration patterns are not just features appearing close to the surface, but they penetrate the whole convection zone until the bottom, as seen in Figure 13. Therefore, we can rule out that the meridional circulation is the main driver of this migration. As discussed in Section 3, the meridional circulation shows strong variability in radius and has at least two cells.

Runs Ab and Ac have been restarted from a snapshot of Run A after $t/\tau \approx 1350$ and 1150, respectively. In Run Ab we decrease the magnetic Prandtl number, while in Run Ac we increase it; see Table 1. This was done to investigate the influence of the magnetic Reynolds number on the equatorward migration. As seen from Figure 12 the pattern of the mean magnetic field is not strongly effected by this change. There is clear equatorward migration near the poles and some indication of poleward migration at low latitudes. It seems that Run Ac, with a higher magnetic Reynolds number, shows a clearer equatorward migration pattern. However, there the field is superimposed by some stationary fields near the equator. In Run Ab, the field tends to migrate poleward near the equator and equatorward near the poles. In any case a higher magnetic Reynolds number, while leaving the other parameter the same, seems to support equatorward migration. This is promising because it leads in the right direction towards the Sun, although the difference in Reynolds number is not that large to draw strong conclusions.

In Run B, where the fluid and magnetic Reynolds numbers are higher and the rotation slower than in Run A, the structure of the mean field evolution shows some differences. In the kinematic regime, the field is similar to that of Run A in which it migrates poleward at lower latitudes. Also, as the field gets stronger it begins to migrate from higher latitudes toward the equator and the fast poleward branch becomes slower. The main difference to Run A is that the poleward migration does not turn into equatorward migration near the equator. In Runs A, Ab, and Ac, the field strength has no clear latitudinal dependence. By contrast in Run B the field strength near the poles is around half the strength near the equator. Only during late times the polar branch increases in strength. In Runs A and Ac, the radial and azimuthal components have approximately the same strength, whereas in Run B, the radial mean magnetic field seems to be weaker by a factor of two. Also, Run B shows no clear radial dependence in the structure of the mean field. The period of the equatorward migrating field is $t/\tau \approx 200$, which is a bit longer than for Run A. The poleward migration near the equator has an irregular oscillation and is usually not in phase with the equatorward migration near the poles. At $t/\tau \approx 1000$ the dynamo mode changes significantly. Not only does the magnetic field start to grow (see Figure 2), but also the magnetic field changes from an oscillatory pattern to a stationary one, or at least an oscillatory one with a much longer period; see Figure 12. In particular in the northern hemisphere the mean azimuthal field shows a strong increase in strength. The field pattern now consists of

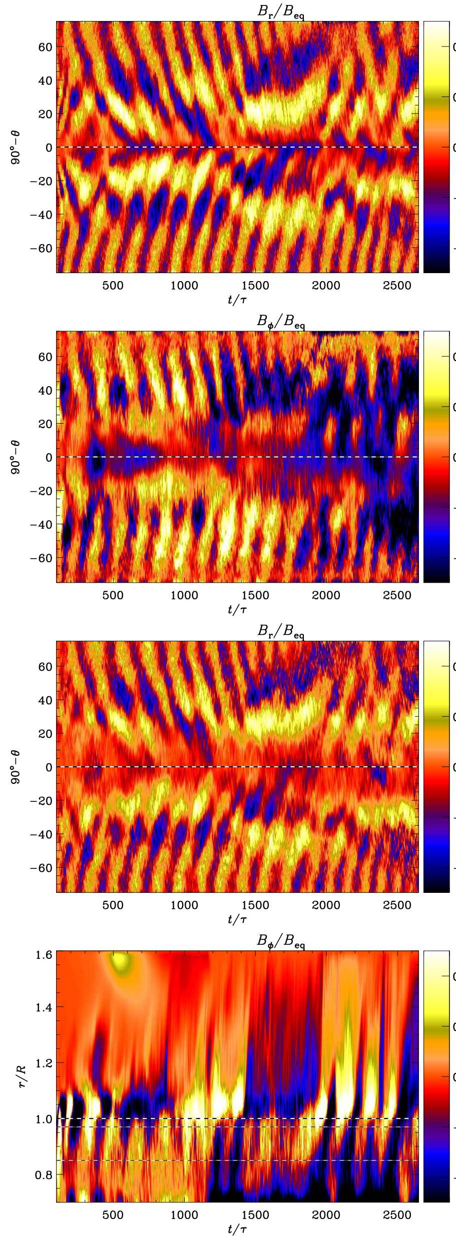

FIG. 13.— Time evolution of the mean magnetic field in the convection zone for Run A. From top to bottom: Mean radial field $\overline{B}_r$ at $r_1 = 0.97R$, mean azimuthal field $\overline{B}_\phi$ at $r_2 = 0.84R$, mean radial field $\overline{B}_r$ at $r_2 = 0.84R$ and mean azimuthal field $\overline{B}_\phi$ at $25°$ latitude for the whole radial extent. Otherwise the same as in Figure 12. In the last panel the dashed lines indicate the surface ($r = R$) and the radii $r_1 = 0.97R$ and $r_2 = 0.84R$.

a strong time-independent component with latitudinal dependence. Near the surface (at r_1; see Section 2) the field seems to migrate slowly toward the equator, but it is not possible to identify a migrating pattern in the present run.

If one translates the cycle period of the equatorward migration to solar values using a turnover time τ of 1 month, we obtain a cycle period of 12 and 16 years for Runs A and B, respectively. This would be a typical value in the middle of the convection zone. However, if one computes the turbulent turnover time from the rotation period of the Sun, $\tau = P_{\rm sun}{\rm Co}/4\pi$ is 0.7 month, which would lead to 9 years and 12 years for Runs A and B, respectively. The regular magnetic cycles in the work of Ghizaru et al. (2010) and Racine et al. (2011) have a somewhat longer period of 60 years. Nelson et al. (2013) and Brown et al. (2011) were only able to generate highly irregular cycles, with no clear reversal on both hemispheres. They found therefore a large range of cycle periods, which span from one year to around 60 years.

To investigate the equatorward migration in the first half of the simulations, we plot the mean azimuthal magnetic field $\overline{B}_\phi$ for eight different times for Run A, resolving one cycle; see Figure 14. The field penetrates the whole convection zone and has up to four regions with different polarities in one hemisphere. These polarities are migrating toward the equator. In the northern hemisphere at around $45°$ latitude, there is a magnetic field concentration with positive polarity. After $\Delta t/\tau = 827 - 740 = 87$ (panel 5), at the same location we find a negative magnetic field concentration, and again after $\Delta t/\tau = 65$ (panel 8) the same polarity as in the beginning of the cycle appears. One can see a clear cyclic equatorward migration of the field, but it is irregular. The two hemispheres do not show the same magnetic field strength and it seems that, from time to time, there is only one dominant polarity in one hemisphere, while in the other there are three. Note also the strong negative magnetic fields near and above the surface, which seem to show also a cycle dependency.

It is still unclear why the equatorward migration takes place, so we can only speculate about it. At the moment there are two main candidates. One is the meridional circulation, which shows a solar-like pattern in Runs A, Ab, and Ac. But, as shown in Figure 13, the equatorward migration is present throughout the entire convective zone, while the meridional circulation becomes more incoherent with depths. The incoherence is a manifestation of the multi-cellar structure of the meridional circulations. The shape and number of cells are similar to those obtained in recent simulations by Käpylä et al. (2012) and Nelson et al. (2013) and observations by Zhao et al. (2012). This is quite different the single cell circulation postulated in flux transport dynamo models to drive equatorward migration (e.g. Choudhuri et al. 1995; Dikpati & Charbonneau 1999; Käpylä et al. 2006; Kitchatinov & Olemskoy 2012). We can therefore conclude that we find no evidence for magnetic field generation similar to the mechanism proposed by the flux transport dynamo models. A second candidate is the contribution of current helicity of small-scales in the magnetic α tensor. However, preliminary studies suggest that the isotropic part seems not to play an important role here (Warnecke et al. 2012c). This point is not fully conclusive, because we have not yet determined the full anisotropic contributions to the magnetic quenching term (see Brandenburg & Subramanian 2007, for a detailed description and discussion).

The radial dependence of the mean azimuthal magnetic

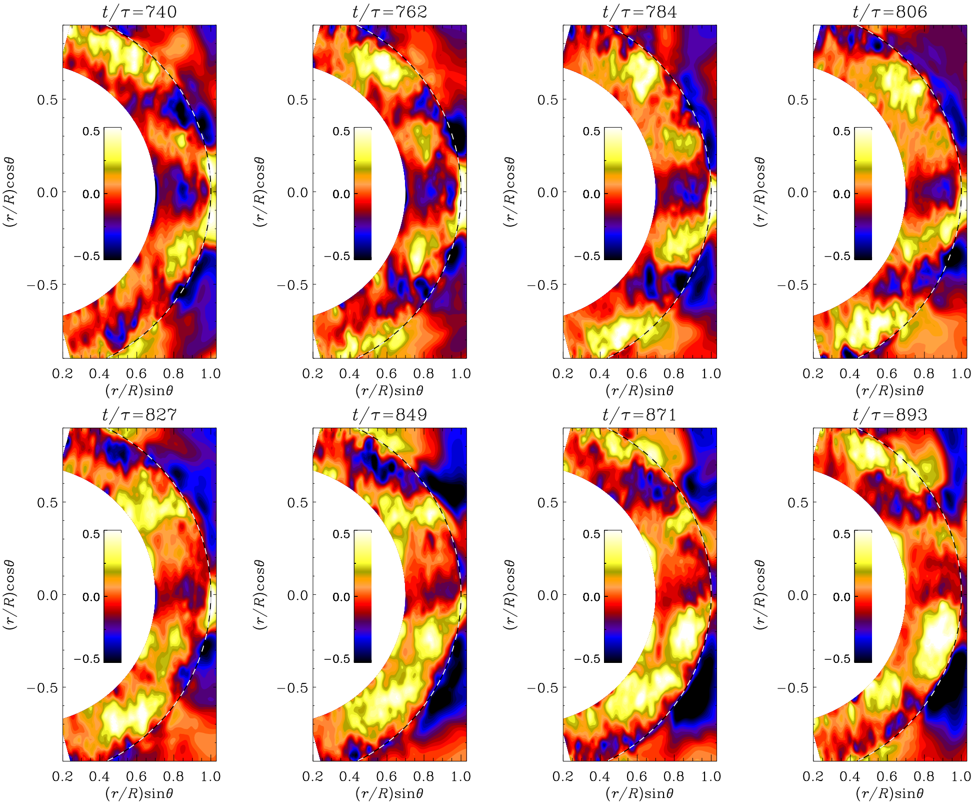

FIG. 14.— Time series of eight snapshots of the mean azimuthal magnetic field $\overline{B}_\phi$ separated by 22 turnover times and covering one full magnetic cycle. Dark blue shades represent negative and light yellow positive values. The dashed line indicates the surface ($r = R$). The field is normalized by the equipartition field strength $B_{\rm eq}$.

field (see the last panel of Figure 13) suggests that most of the contribution to cyclic behavior comes from the surface layers. First of all, the field is strong near and above the surface where the density stratification is large, but also at the bottom of the convection zone, at least after saturation. The oscillation pattern seems to be predominantly a surface phenomenon rather than one rooted deep in the convection zone. The field at the bottom of the convection zone has constant polarity, while in the bulk and at the surface of the convection the oscillation is quite pronounced. Nevertheless, the negative field rises from the bottom and gets concentrated near the surface, for example at $t/\tau \approx 2000$. At the same time, positive field seems to be formed close to the surface and emerges above the surface where it gets concentrated. This suggest that the strong density stratification, which is present only very close to the surface of the Sun, might be responsible for the oscillation and the equatorward migration of the solar magnetic field.

Further investigations, measuring the turbulent transport coefficients in their full tensorial form is necessary to determine the reason for the equatorward migration. Measuring the components of α by neglecting the contributions of the turbulent magnetic diffusivity $\eta_{\rm t}$ as by Racine et al. (2011) can be misleading and gives wrong results. A more sophisticated approach is to use the so-called test-field method (Schrinner et al. 2007; Brandenburg et al. 2010) adapted for spherical coordinates.

4. CONCLUSIONS

We have used a model that combines the turbulent convective dynamo with a coronal layer to reproduce properties of the Sun. We found a solar-like differential rotation with roughly radial contours of angular velocity at low latitudes. This is accompanied by poleward meridional circulation just below the surface and a return flow above the surface. Additionally the differential rotation profiles show a near-surface shear layer in all of the four simulations we perform. In one of the four simulations there exist also a similar layer above the surface. We identify as the main cause of spoke-like differential rotation the non-zero latitudinal entropy gradient, which is self-consistently generated.

The mean magnetic field shows a pattern of equatorward migration similar to Käpylä et al. (2012, 2013). This pattern is mostly visible at higher latitudes and only in two of the simulation at lower latitudes. However, at intermediate times of the simulation, the equatorward migration is only visible at high latitudes, while at lower latitudes poleward migration or stationary modes occur. In one of the simulations the dynamo mode changed to a stationary one on all latitudes at later stages. The dynamo has a shorter excitation time than in the earlier work of Käpylä et al. (2012).

This work leads to the conclusion that the inclusion of a coronal layer to a convective dynamo simulation has an influence on the fluid and magnetic properties of the interior. In recent simulations, we were able to produce recurrent coronal ejections from the solar surface (Warnecke et al. 2012b) using a two layer approach. In earlier models of forced turbulence with a coronal layer (Warnecke & Brandenburg 2010; Warnecke et al. 2011, 2012a), we also found the ejection of magnetic helicity out of the dynamo region. These ejections can support and amplify the magnetic field due to enhanced helicity fluxes.

Here, we present evidence that even the fluid properties in the bulk of the convection zone might be influenced by the coronal layer. Solar-like rotation profiles could not be reproduced by earlier direct numerical simulations of convective dynamo (Käpylä et al. 2012) without prescribing a latitudinal entropy gradient at the bottom of the convection zone (Miesch et al. 2006) or adding a stably stratified layer below the convection zone (Brun et al. 2011) in purely hydrodynamical large-eddy simulations. However, to have more convincing evidence in support of this, we need to perform a detailed parameter study using different coronal sizes and compare them with simulations without a corona.

Another extension of our work is the measurement of magnetic helicity fluxes through the surface and their dependence on the size of the corona. To investigate the mechanism of the equatorward migration, which is crucial for understanding the solar dynamo, one should measure the turbulent transport coefficients through approaches like the test-field method (Schrinner et al. 2007).

In further work we will investigate the possibility of producing coronal ejections using the setup of these runs. In comparison with Warnecke et al. (2012b), we use here a corona with a much higher temperature, and a lower plasma beta. It will be interesting to see how the coronal ejections are influenced by this.

We thank the anonymous referee for many useful suggestions. We acknowledge the allocation of computing resources provided by the Swedish National Allocations Committee at the Center for Parallel Computers at the Royal Institute of Technology in Stockholm, the National Supercomputer Centers in Linköping and the High Performance Computing Center North in Umeå. Part of the computations have been carried out in the facilities hosted by the CSC – IT Center for Science in Espoo, Finland, which are financed by the Finnish ministry of education. This work was supported in part by the European Research Council under the AstroDyn Research Project No. 227952, the Swedish Research Council Grant No. 621-2007-4064, and the Academy of Finland grants 136189, 140970 (PJK) and 218159, 141017 (MJM), University of Helsinki ‘Active Suns’ research project, as well as the HPC-Europa2 project, funded by the European Commission - DG Research in the Seventh Framework Programme under grant agreement No. 228398. The authors thank NORDITA for hospitality during their visits.

REFERENCES

Augustson, K. C., Brown, B. P., Brun, A. S., Miesch, M. S., & Toomre, J. 2012, ApJ, 756, 169

Ballot, J., Brun, A. S., & Turck-Chièze, S. 2007, ApJ, 669, 1190

Blackman, E. G., & Brandenburg, A. 2003, ApJ, 584, L99

Brandenburg, A. 2005, ApJ, 625, 539

Brandenburg, A., Chatterjee, P., Del Sordo, F., Hubbard, A., Käpylä, P. J., & Rheinhardt, M. 2010, Physica Scripta Volume T, 142, 014028

Brandenburg, A., Moss, D., & Tuominen, I. 1992, A&A, 265, 328

Brandenburg, A., & Sandin, C. 2004, A&A, 427, 13

Brandenburg, A., & Subramanian, K. 2005, Phys. Rep., 417, 1

—. 2007, Astron. Nachr., 328, 507

Brown, B. P., Browning, M. K., Brun, A. S., Miesch, M. S., & Toomre, J. 2008, ApJ, 689, 1354

Brown, B. P., Miesch, M. S., Browning, M. K., Brun, A. S., & Toomre, J. 2011, ApJ, 731, 69

Brun, A. S., Miesch, M. S., & Toomre, J. 2004, ApJ, 614, 1073

—. 2011, ApJ, 742, 79

Choudhuri, A. R., Schussler, M., & Dikpati, M. 1995, A&A, 303, L29

Dikpati, M., & Charbonneau, P. 1999, ApJ, 518, 508

Ghizaru, M., Charbonneau, P., & Smolarkiewicz, P. K. 2010, ApJ, 715, L133

Gilman, P. A. 1983, ApJS, 53, 243

Hubbard, A., & Brandenburg, A. 2012, ApJ, 748, 51

Käpylä, P. J., Korpi, M. J., Brandenburg, A., Mitra, D., & Tavakol, R. 2010, Astron. Nachr., 331, 73

Käpylä, P. J., Korpi, M. J., & Tuominen, I. 2006, Astron. Nachr., 327, 884

Käpylä, P. J., Mantere, M. J., & Brandenburg, A. 2011a, Astron. Nachr., 332, 883

—. 2012, ApJ, 755, L22

Käpylä, P. J., Mantere, M. J., Cole, E., Warnecke, J., & Brandenburg, A. 2013, ApJ submitted, arXiv:1301.2595

Käpylä, P. J., Mantere, M. J., Guerrero, G., Brandenburg, A., & Chatterjee, P. 2011b, A&A, 531, A162

Karak, B. B. 2010, ApJ, 724, 1021

Kitchatinov, L. L., & Olemskoy, S. V. 2012, Sol. Phys., 276, 3

Kitchatinov, L. L., & Rüdiger, G. 1995, A&A, 299, 446

Köhler, H. 1970, Sol. Phys., 13, 3

Krause, F., & Rädler, K.-H. 1980, Mean-field Magnetohydrodynamics and Dynamo Theory (Oxford: Pergamon Press)

Miesch, M. S., Brun, A. S., & Toomre, J. 2006, ApJ, 641, 618

Mitra, D., Tavakol, R., Brandenburg, A., & Moss, D. 2009, ApJ, 697, 923

Nelson, N. J., Brown, B. P., Brun, A. S., Miesch, M. S., & Toomre, J. 2013, ApJ, 762, 73

Racine, É., Charbonneau, P., Ghizaru, M., Bouchat, A., & Smolarkiewicz, P. K. 2011, ApJ, 735, 46

Rempel, M. 2005, ApJ, 622, 1320

Rüdiger, G. 1980, Reynolds stresses and differential rotation. I - On recent calculations of zonal fluxes in slowly rotating stars, Vol. 16, 239–261

—. 1989, Differential Rotation and Stellar Convection. Sun and Solar-type Stars (Berlin: Akademie Verlag)

Schrinner, M., Rädler, K.-H., Schmitt, D., Rheinhardt, M., & Christensen, U. R. 2007, Geophys. Astrophys. Fluid Dyn., 101, 81

Spiegel, E. A., & Weiss, N. O. 1980, Nature, 287, 616

Stix, M. 2002, The sun: an introduction (Springer, Berlin)

Warnecke, J., & Brandenburg, A. 2010, A&A, 523, A19

Warnecke, J., Brandenburg, A., & Mitra, D. 2011, A&A, 534, A11

—. 2012a, J. Spa. Weather Spa. Clim., 2, A11

Warnecke, J., Käpylä, P. J., Mantere, M. J., & Brandenburg, A. 2012b, Sol. Phys., 280, 299

—. 2012c, arXiv:1211.0452

Weiss, N. O. 1965, The Observatory, 85, 37

Zhao, J., Bogart, R. S., Kosovichev, A. G., & Duvall, Jr., T. L. 2012, in American Astronomical Society Meeting Abstracts, Vol. 220, 109

Zhao, J., & Kosovichev, A. G. 2004, ApJ, 603, 776

VI

DRAFT VERSION APRIL 22, 2013
Preprint typeset using LATEX style emulateapj v. 08/22/09

EFFECTS OF STRONG STRATIFICATION ON EQUATORWARD DYNAMO WAVE PROPAGATION

PETRI J. KÄPYLÄ[1,2], MAARIT J. MANTERE[1,3], ELIZABETH COLE[1], JÖRN WARNECKE[2,4] AND AXEL BRANDENBURG[2,4]
[1]Physics Department, Gustaf Hällströmin katu 2a, PO Box 64, FI-00014 University of Helsinki, Finland
[2]NORDITA, KTH Royal Institute of Technology and Stockholm University, Roslagstullsbacken 23, SE-10691 Stockholm, Sweden
[3]Aalto University, Department of Information and Computer Science, PO Box 15400, FI-00076 Aalto, Finland
[4]Department of Astronomy, AlbaNova University Center, Stockholm University, SE-10691 Stockholm, Sweden

Draft version April 22, 2013

ABSTRACT

We present results from simulations of rotating magnetized turbulent convection in spherical wedge geometry representing parts of the latitudinal and longitudinal extents of a star. Here we consider a set of runs for which the density stratification is varied, keeping the Reynolds and Coriolis numbers at similar values. In the case of weak stratification we find quasi-steady solutions for moderate rotation and oscillatory dynamos with poleward migration of activity belts for more rapid rotation. For stronger stratification, the growth rate tends to become smaller. Furthermore, a transition from quasi-steady to oscillatory dynamos is found as the Coriolis number is increased, but now there is an equatorward migrating branch near the equator. We test the domain size dependence of our results for a rapidly rotating run with equatorward migration by varying the longitudinal extent of our wedge. The energy of the axisymmetric mean magnetic field decreases as the domain size increases and we find that an $m = 1$ mode is excited for a full 2π ϕ-extent, reminiscent of the field configurations deduced from observations of rapidly rotating late-type stars.

Subject headings: Magnetohydrodynamics – convection – turbulence – Sun: dynamo, rotation, activity

1. INTRODUCTION

The large-scale magnetic field of the Sun, manifested by the 11 year sunspot cycle, is generally believed to be generated within or just below the turbulent convection zone (e.g. Ossendrijver 2003, and references therein). The latter concept is based on the idea that strong shear in the tachocline just beneath the convection zone amplifies the toroidal magnetic field which then becomes buoyantly unstable and erupts to the surface (e.g. Parker 1955b). This process has been adopted in many mean-field models of the solar cycle in the form of a non-local α-effect (e.g. Kitchatinov & Olemskoy 2012), which is based on early ideas of Babcock (1961) and Leighton (1969) that the source term for poloidal field can be explained through the tilt of active regions. Such models assume a reduced turbulent diffusivity within the convection zone and a single cell anti-clockwise meridional circulation which acts as a conveyor belt for the magnetic field. These so-called flux transport models (e.g. Dikpati & Charbonneau 1999) are now widely used to study the solar cycle and to predict its future course (Dikpati & Gilman 2006; Choudhuri et al. 2007).

The flux transport paradigm is, however, facing several theoretical challenges: 10^5 gauss magnetic fields are expected to reside in the tachocline (D'Silva & Choudhuri 1993), but such fields are difficult to explain with dynamo theory (Guerrero & Käpylä 2011) and may have become unstable at much lower field strengths (Arlt et al. 2005). Furthermore, flux transport dynamos require a rather low value of the turbulent diffusivity within the convection zone (several $10^{11}\,\mathrm{cm}^2\,\mathrm{s}^{-1}$; see Bonanno et al. 2002), which is much less than the standard estimate of several $10^{12}\,\mathrm{cm}^2\,\mathrm{s}^{-1}$ based on mixing length theory, which, in turn, is also verified numerically (e.g. Käpylä et al. 2009). Several other issues have already been addressed within this paradigm, for example the parity of the dynamo (Bonanno et al. 2002; Chatterjee et al. 2004; Dikpati et al. 2004) and the possibility of a multicellular structure of the meridional circulation (Jouve & Brun 2007), which may be more complicated than that required in the flux transport models (Hathaway 2011; Miesch et al. 2012). These difficulties have led to a revival of the distributed dynamo (e.g. Brandenburg 2005; Pipin 2012) in which magnetic fields are generated throughout the convection zone due to turbulent effects (e.g. Krause & Rädler 1980; Käpylä et al. 2006; Pipin & Seehafer 2009).

Early studies of self-consistent three-dimensional magnetohydrodynamic (MHD) simulations of convection in spherical coordinates produced oscillatory large-scale dynamos (Gilman 1983; Glatzmaier 1985), but the dynamo wave was found to propagate towards the poles rather than the equator—as in the Sun. More recent anelastic large-eddy simulations (LES) with rotation rates somewhat higher than that of the Sun have produced non-oscillatory (Brown et al. 2010) and oscillatory (Brown et al. 2011; Nelson et al. 2013) large-scale magnetic fields, depending essentially on the rotation rate and the vigor of the turbulence. However, similar models with the solar rotation rate have either failed to produce an appreciable large-scale component (Brun et al. 2004) or, more recently, oscillatory solutions with almost no latitudinal propagation of the activity belts (Ghizaru et al. 2010; Racine et al. 2011). These simulations covered a full spherical shell and used realistic values for solar luminosity and rotation rate, necessitating the use of anelastic solvers and spherical harmonics (e.g. Brun et al. 2004) or implicit methods (e.g. Ghizaru et al. 2010). Here we exploit an alternative approach by modeling fully compressible convection in wedge geometry (see also Robinson & Chan 2001) with a finite-difference method. We omit the polar regions and cover usually only a part of the longitudinal extent, e.g. 90° instead of the full 360°. At the cost of omitting connecting flows across the poles and introducing artificial boundaries there, the gain is that higher spatial resolution can be achieved. Furthermore, retaining the sound waves can be beneficial when considering possible helio- or

Electronic address: petri.kapyla@helsinki.fi (Revision: 1.189)

asteroseismic applications. Recent hydrodynamic (Käpylä et al. 2011a,b) and MHD (Käpylä et al. 2010) studies with this method have shown that this approach produces results that are in accordance with fully spherical models. Moreover, the first turbulent dynamo solution with solar-like migration properties of the magnetic field was recently obtained using this type of setup (Käpylä et al. 2013). Extended setups that include a coronal layer as a more realistic upper radial boundary have been successful in producing dynamo-driven coronal ejections (Warnecke et al. 2012). As we show in a companion paper (Warnecke et al. 2013), a solar-like differential rotation pattern might be another consequence of including an outer coronal layer.

Here we concentrate on exploring further the recent discovery of equatorward migration in spherical wedge simulations (Käpylä et al. 2013). In particular, we examine a set of runs for which the rotational influence on the fluid, measured by the Coriolis number, which is also called the inverse Rossby number, is kept approximately constant while the density stratification of the simulations is gradually increased.

2. THE MODEL

Our model is the same as that in Käpylä et al. (2012). We model a wedge in spherical polar coordinates, where (r, θ, ϕ) denote radius, colatitude, and longitude. The radial, latitudinal, and longitudinal extents of the wedge are $r_0 \le r \le R$, $\theta_0 \le \theta \le \pi - \theta_0$, and $0 \le \phi \le \phi_0$, respectively, where R is the radius of the star and $r_0 = 0.7\,R$ denotes the position of the bottom of the convection zone. Here we take $\theta_0 = \pi/12$ and in most of our models we use $\phi_0 = \pi/2$, so we cover a quarter of the azimuthal extent between ±75° latitude. We solve the compressible hydromagnetic equations[1],

$$\frac{\partial \boldsymbol{A}}{\partial t} = \boldsymbol{u} \times \boldsymbol{B} - \eta\mu_0 \boldsymbol{J}, \tag{1}$$

$$\frac{D\ln\rho}{Dt} = -\boldsymbol{\nabla}\cdot\boldsymbol{u}, \tag{2}$$

$$\frac{D\boldsymbol{u}}{Dt} = \boldsymbol{g} - 2\boldsymbol{\Omega}_0 \times \boldsymbol{u} + \frac{1}{\rho}\left(\boldsymbol{J}\times\boldsymbol{B} - \boldsymbol{\nabla}p + \boldsymbol{\nabla}\cdot 2\nu\rho\mathsf{S}\right), \tag{3}$$

$$T\frac{Ds}{Dt} = \frac{1}{\rho}\left[-\boldsymbol{\nabla}\cdot\left(\boldsymbol{F}^{\rm rad} + \boldsymbol{F}^{\rm SGS}\right) + \mu_0\eta\boldsymbol{J}^2\right] + 2\nu\mathsf{S}^2, \tag{4}$$

where $\boldsymbol{A}$ is the magnetic vector potential, $\boldsymbol{u}$ is the velocity, $\boldsymbol{B} = \boldsymbol{\nabla}\times\boldsymbol{A}$ is the magnetic field, $\boldsymbol{J} = \mu_0^{-1}\boldsymbol{\nabla}\times\boldsymbol{B}$ is the current density, η is the magnetic diffusivity, μ_0 is the vacuum permeability, $D/Dt = \partial/\partial t + \boldsymbol{u}\cdot\boldsymbol{\nabla}$ is the advective time derivative, ν is the kinematic viscosity, ρ is the density,

$$\boldsymbol{F}^{\rm rad} = -K\boldsymbol{\nabla}T \quad \text{and} \quad \boldsymbol{F}^{\rm SGS} = -\chi_{\rm SGS}\rho T\boldsymbol{\nabla}s \tag{5}$$

are the radiative and subgrid scale (SGS) heat fluxes, where K is the radiative heat conductivity and $\chi_{\rm SGS}$ is the turbulent heat conductivity, which represents the unresolved convective transport of heat and was referred to as $\chi_{\rm t}$ in Käpylä et al. (2012), s is the specific entropy, T is the temperature, and p is the pressure. The fluid obeys the ideal gas law with $p = (\gamma - 1)\rho e$, where $\gamma = c_{\rm P}/c_{\rm V} = 5/3$ is the ratio of specific heats at constant pressure and volume, respectively, and $e = c_{\rm V}T$ is the internal energy. The rate of strain tensor S is given by

$$\mathsf{S}_{ij} = \tfrac{1}{2}(u_{i;j} + u_{j;i}) - \tfrac{1}{3}\delta_{ij}\boldsymbol{\nabla}\cdot\boldsymbol{u}, \tag{6}$$

where the semicolons denote covariant differentiation (Mitra et al. 2009).

The gravitational acceleration is given by $\boldsymbol{g} = -GM\hat{\boldsymbol{r}}/r^2$, where G is the gravitational constant, M is the mass of the star, and $\hat{\boldsymbol{r}}$ is the unit vector in the radial direction. In simulations, the maximum possible Rayleigh number is much smaller than in real stars, which implies a larger Mach number (Brandenburg et al. 2005). The rotation vector $\boldsymbol{\Omega}_0$ is given by $\boldsymbol{\Omega}_0 = (\cos\theta, -\sin\theta, 0)\Omega_0$. However, to have realistic Coriolis numbers, the angular velocity in the Coriolis force is increased correspondingly, but that in the centrifugal force is omitted, as it would otherwise be unrealistically large (cf. Käpylä et al. 2011b). We recall that dropping the centrifugal force is connected with the fact that the Rayleigh number is much less than in the Sun and the Mach number therefore larger. To have realistic Coriolis numbers the Coriolis force has to be larger by the same amount that the turbulent velocity is larger, but without significantly altering the hydrostatic balance that is determined by gravity and centrifugal forces.

2.1. *Initial and boundary conditions*

The initial state is isentropic and the hydrostatic temperature gradient is given by

$$\frac{\partial T}{\partial r} = -\frac{GM/r^2}{c_{\rm V}(\gamma-1)(n_{\rm ad}+1)}, \tag{7}$$

where $n_{\rm ad} = 1.5$ is the polytropic index for an adiabatic stratification. We fix the value of $\partial T/\partial r$ on the lower boundary. The density profile follows from hydrostatic equilibrium. The heat conduction profile is chosen so that radiative diffusion is responsible for supplying the energy flux in the system, with K decreasing more than two orders of magnitude from bottom to top (Käpylä et al. 2011a). We do this by choosing a variable polytropic index $n = 2.5\,(r/r_0)^{-15} - 1$, which is 1.5 at the bottom of the convection zone and approaches -1 closer to the surface. This means that $K = (n+1)K_0$ decreases toward the surface like r^{-15} such that most of the flux is carried by convection (Brandenburg et al. 2005). Here, K_0 is a constant to be defined below. A weak random small-scale seed magnetic field is taken as initial condition (see below).

The radial and latitudinal boundaries are assumed to be impenetrable and stress free, i.e.,

$$u_r = 0, \quad \frac{\partial u_\theta}{\partial r} = \frac{u_\theta}{r}, \quad \frac{\partial u_\phi}{\partial r} = \frac{u_\phi}{r} \quad (r = r_0, R), \tag{8}$$

$$\frac{\partial u_r}{\partial \theta} = u_\theta = 0, \quad \frac{\partial u_\phi}{\partial \theta} = u_\phi \cot\theta \quad (\theta = \theta_0, \pi - \theta_0). \tag{9}$$

For the magnetic field we assume perfect conductors at the lower radial and latitudinal boundaries, and radial field at the outer radial boundary. In terms of the magnetic vector potential these translate to

$$\frac{\partial A_r}{\partial r} = A_\theta = A_\phi = 0 \quad (r = r_0), \tag{10}$$

$$A_r = 0, \quad \frac{\partial A_\theta}{\partial r} = -\frac{A_\theta}{r}, \quad \frac{\partial A_\phi}{\partial r} = -\frac{A_\phi}{r} \quad (r = R), \tag{11}$$

$$A_r = \frac{\partial A_\theta}{\partial \theta} = A_\phi = 0 \quad (\theta = \theta_0, \pi - \theta_0). \tag{12}$$

---

[1] Note that in Equation (4) of Käpylä et al. (2013) the Ohmic heating term $\mu_0\eta\boldsymbol{J}^2$ and a factor ρ in the viscous dissipation term $2\nu\mathsf{S}^2$ were omitted, but they were actually included in the calculations.

We use small-scale low amplitude Gaussian noise as initial condition for the magnetic field. On the latitudinal boundaries we assume that the thermodynamic quantities have vanishing first derivatives, thus suppressing heat fluxes through the boundaries.

On the upper boundary we apply a black body condition

$$\sigma T^4 = -K\frac{\partial T}{\partial r} - \chi_{\rm SGS}\rho T\frac{\partial s}{\partial r}, \tag{13}$$

where σ is the Stefan–Boltzmann constant. We use a modified value for σ that takes into account that our Reynolds and Rayleigh numbers are much smaller than in reality, so K and therefore the energy flux through the domain are much larger than in the Sun.

2.2. *Dimensionless parameters*

To facilitate comparison with other work using different normalizations, we present our results in this paper by normalizing with physically meaningful quantities. We note, however, that in the code we used non-dimensional quantities by choosing

$$R = GM = \rho_0 = c_{\rm P} = \mu_0 = 1, \tag{14}$$

where ρ_0 is the initial density at $r = r_0$. The units of length, time, velocity, density, entropy, and magnetic field are therefore

$$[x] = R,\ \ [t] = \sqrt{R^3/GM},\ \ [u] = \sqrt{GM/R},$$
$$\rho = \rho_0,\ \ [s] = c_{\rm P},\ \ [B] = \sqrt{\rho_0\mu_0 GM/R}. \tag{15}$$

Our simulations are defined by the energy flux imposed at the bottom boundary, $F_{\rm b} = -(K\partial T/\partial r)|_{r=r_0}$, the temperature at the top boundary, $T_1 = T(r = R)$, as well as the values of Ω_0, ν, η, and $\overline{\chi}_{\rm SGS} = \chi_{\rm SGS}(r_{\rm m} = 0.85\,R)$. The radiative conductivity is proportional to $K_0 = (\mathcal{L}/4\pi)c_{\rm V}(\gamma - 1)\rho_0\sqrt{GMR}$, where $\mathcal{L}$ is the non-dimensional luminosity, given below. Furthermore, the radial profile of $\chi_{\rm SGS}$ is piecewise constant above $r > 0.75R$ with $\chi_{\rm SGS} = \overline{\chi}_{\rm SGS}$ at $0.75 < r < 0.98$, and $\chi_{\rm SGS} = 12.5\overline{\chi}_{\rm SGS}$ above $r = 0.98R$. Below $r = 0.75R$, $\chi_{\rm SGS}$ tends smoothly to zero; see Fig. 1 of (Käpylä et al. 2011a). The corresponding nondimensional input parameters are the luminosity parameter

$$\mathcal{L} = \frac{L_0}{\rho_0(GM)^{3/2}R^{1/2}}, \tag{16}$$

the normalized pressure scale height at the surface,

$$\xi = \frac{(\gamma-1)c_{\rm V}T_1}{GM/R}, \tag{17}$$

the Taylor number

$$\mathrm{Ta} = (2\Omega_0 R^2/\nu)^2, \tag{18}$$

the fluid and magnetic Prandtl numbers

$$\mathrm{Pr} = \frac{\nu}{\overline{\chi}_{\rm SGS}},\quad \mathrm{Pm} = \frac{\nu}{\eta}, \tag{19}$$

and the non-dimensional viscosity

$$\tilde{\nu} = \frac{\nu}{\sqrt{GMR}}. \tag{20}$$

Instead of ξ, we often quote the resulting density contrast, $\Gamma_\rho \equiv \rho(r_0)/\rho(R)$.

We note that we intend to use low values of $\mathcal{L}$ so that the Mach number is sufficiently below unity near the surface. This is particularly important when the stratification is high. In our current formulation the unresolved turbulent heat conductivity, $\chi_{\rm SGS}$, acts on the total entropy and thus contributes to the radial heat flux. Using values of Pr close to unity would lead to a greater contribution due to the SGS-flux. To minimize the effects of the SGS-flux within the convection zone, we use the smallest possible value of $\chi_{\rm SGS}$ that is still compatible with numerical stability.

Other useful diagnostic parameters are the fluid and magnetic Reynolds numbers

$$\mathrm{Re} = \frac{u_{\rm rms}}{\nu k_{\rm f}},\quad \mathrm{Rm} = \frac{u_{\rm rms}}{\eta k_{\rm f}}, \tag{21}$$

and the Coriolis number

$$\mathrm{Co} = \frac{2\Omega_0}{u_{\rm rms}k_{\rm f}}, \tag{22}$$

where $u_{\rm rms} = \sqrt{(3/2)\langle u_r^2 + u_\theta^2\rangle_{r\theta\phi t}}$ is the rms velocity and the subscripts indicate averaging over θ, ϕ, and a time interval during which the turbulence is statistically stationary. Note that for $u_{\rm rms}$ we omit the contribution from the azimuthal velocity, because its value is dominated by effects from the differential rotation (Käpylä et al. 2011b). The Taylor number can also be written as $\mathrm{Ta} = \mathrm{Co}^2\mathrm{Re}^2(k_{\rm f}R)^4$, with $k_{\rm f}R \approx 21$. Due to the fact that the initial stratification is isentropic, we quote the turbulent Rayleigh number $\mathrm{Ra_t}$ from the thermally relaxed state of the run,

$$\mathrm{Ra_t} = \frac{GM(\Delta r)^4}{\nu\overline{\chi}_{\rm SGS}R^2}\left(-\frac{1}{c_{\rm P}}\frac{{\rm d}\langle s\rangle_{\theta\phi t}}{{\rm d}r}\right)_{r_{\rm m}}, \tag{23}$$

where $k_{\rm f} = 2\pi/\Delta r$ is an estimate of the wavenumber of the largest eddies, and $\Delta r = R - r_0 = 0.3R$ is the thickness of the layer. We also quote the value of $k_\omega = \omega_{\rm rms}/u_{\rm rms}$, where $\boldsymbol{\omega} = \boldsymbol{\nabla}\times\boldsymbol{u}$ and $\omega_{\rm rms}$, is the volume averaged rms value of $\boldsymbol{\omega}$. The magnetic field is expressed in equipartition field strengths, $B_{\rm eq}(r) = \langle\mu_0\rho\boldsymbol{u}^2\rangle^{1/2}_{\theta\phi t}$, where all three components of $\boldsymbol{u}$ are included. We define mean quantities as averages over the ϕ-coordinate and denote them by overbars. However, as we will see, there can also be significant power in low-order spherical harmonic modes with azimuthal order $m = 1$ and 2, which will be discussed at the end of the paper.

The simulations were performed with the PENCIL CODE[2], which uses a high-order finite difference method for solving the compressible equations of magnetohydrodynamics.

3. RESULTS

We perform runs for four values of ξ, corresponding to initial density stratifications $\Gamma_\rho = 2, 5, 30$, and 100. These runs are referred to as series A–D. In series E we use $\Gamma = 30$ and vary ϕ_0 with all other parameters being kept the same as in Run C1. For each series we consider different values of Co and Re. The hydrodynamic progenitors of the Runs B1, C1, and D1 correspond to Runs A4, B4, and C4 from Käpylä et al. (2011a). The rest of the simulations were run from the initial conditions described in Section 2.1.

Earlier studies applying fully spherical simulations have shown that organized large-scale magnetic fields appear provided the rotation of the star is rapid enough (Brown et al.

---

[2] http://code.google.com/p/pencil-code/

TABLE 1
SUMMARY OF THE RUNS.

Run	grid	Pr	Pm	Ta	ξ	Γ_ρ	$\tilde{\nu}$	$\mathcal{L}$	$\mathrm{Ra_t}$	Re	Rm	Co
A1	$128 \times 256 \times 128$	1.5	1.0	10^{10}	0.29	2	$1.7 \cdot 10^{-5}$	$3.8 \cdot 10^{-5}$	$8.3 \cdot 10^{5}$	26	26	8.6
A2	$128 \times 256 \times 128$	1.5	1.0	$1.8 \cdot 10^{10}$	0.29	2	$1.7 \cdot 10^{-5}$	$3.8 \cdot 10^{-5}$	$1.1 \cdot 10^{5}$	24	24	12.8
B1	$128 \times 256 \times 128$	2.5	1.0	$6.4 \cdot 10^{9}$	0.09	5	$2.9 \cdot 10^{-5}$	$3.8 \cdot 10^{-5}$	$1.1 \cdot 10^{6}$	22	22	8.1
B2	$128 \times 256 \times 128$	2.5	1.0	$1.4 \cdot 10^{10}$	0.09	5	$2.9 \cdot 10^{-5}$	$3.8 \cdot 10^{-5}$	$1.1 \cdot 10^{6}$	20	20	13.7
C1	$128 \times 256 \times 128$	2.5	1.0	$1.4 \cdot 10^{10}$	0.02	30	$2.9 \cdot 10^{-5}$	$3.8 \cdot 10^{-5}$	$2.1 \cdot 10^{6}$	35	35	7.8
C2	$128 \times 256 \times 128$	2.5	1.0	$4.0 \cdot 10^{10}$	0.02	30	$2.9 \cdot 10^{-5}$	$3.8 \cdot 10^{-5}$	$2.7 \cdot 10^{6}$	31	31	14.8
D1	$128 \times 256 \times 128$	7.5	3.0	$1.6 \cdot 10^{9}$	0.008	100	$4.7 \cdot 10^{-5}$	$6.3 \cdot 10^{-6}$	$1.2 \cdot 10^{6}$	11	34	8.0
D2	$256 \times 512 \times 256$	4.0	2.0	10^{10}	0.008	100	$2.5 \cdot 10^{-5}$	$6.3 \cdot 10^{-6}$	$2.4 \cdot 10^{6}$	25	50	9.1
E1	$128 \times 256 \times 64$	2.5	1.0	$1.4 \cdot 10^{10}$	0.02	30	$2.9 \cdot 10^{-5}$	$3.8 \cdot 10^{-5}$	$2.1 \cdot 10^{6}$	34	34	7.9
E2	$128 \times 256 \times 128$	2.5	1.0	$1.4 \cdot 10^{10}$	0.02	30	$2.9 \cdot 10^{-5}$	$3.8 \cdot 10^{-5}$	$2.1 \cdot 10^{6}$	35	35	7.8
E3	$128 \times 256 \times 256$	2.5	1.0	$1.4 \cdot 10^{10}$	0.02	30	$2.9 \cdot 10^{-5}$	$3.8 \cdot 10^{-5}$	$2.4 \cdot 10^{6}$	35	35	7.9
E4	$128 \times 256 \times 512$	2.5	1.0	$1.4 \cdot 10^{10}$	0.02	30	$3.5 \cdot 10^{-5}$	$3.8 \cdot 10^{-5}$	$2.2 \cdot 10^{6}$	28	28	8.1

NOTE. — The second to ninth columns show quantities which are input parameters to the models whereas the quantities in the last four columns are results of the simulations computed from the saturated state. Here we use $\phi_0 = \pi/2$ in Sets A–D. In Set E we use $\phi_0 = \pi/4$ (Run E1), $\phi_0 = \pi/2$ (E2), $\phi_0 = \pi$ (E3), and $\phi_0 = 2\pi$ (E4). Runs C1 and E2 are the same model, and is also the same as Run B4m of Käpylä et al. (2012).

TABLE 2
SUMMARY OF DIAGNOSTIC VARIABLES.

Run	$\tilde{\lambda}$	$\tilde{u}_{\mathrm{rms}}$	$E_{\mathrm{mer}}/E_{\mathrm{kin}}$	$E_{\mathrm{rot}}/E_{\mathrm{kin}}$	$E_{\mathrm{mag}}/E_{\mathrm{kin}}$	$E_{\mathrm{pol}}/E_{\mathrm{mag}}$	$E_{\mathrm{tor}}/E_{\mathrm{mag}}$	$\Delta_\Omega^{(r)}$	$\Delta_\Omega^{(\theta)}$	k_ω
A1	0.084	0.010	0.000	0.580	0.418	0.045	0.396	0.013	0.089	62
A2	0.095	0.009	0.000	0.490	0.553	0.068	0.338	0.009	0.050	62
B1	0.028	0.013	0.000	0.705	0.345	0.038	0.487	0.034	0.142	68
B2	0.098	0.012	0.000	0.757	0.222	0.056	0.427	0.023	0.072	72
C1	0.006	0.021	0.001	0.440	0.346	0.138	0.203	0.047	0.068	93
C2	0.105	0.019	0.001	0.326	0.706	0.198	0.238	0.016	0.030	94
D1	0.003	0.011	0.002	0.222	0.472	0.166	0.135	0.011	-0.000	89
D2	0.003	0.013	0.000	0.617	0.222	0.133	0.190	0.045	0.058	116
E1	0.007	0.021	0.001	0.478	0.393	0.133	0.328	0.048	0.069	92
E2	0.006	0.021	0.001	0.440	0.346	0.138	0.203	0.047	0.068	93
E3	0.005	0.021	0.001	0.375	0.380	0.120	0.172	0.037	0.055	92
E4	0.024	0.020	0.001	0.363	0.470	0.065	0.114	0.035	0.050	91

NOTE. — Here $\tilde{\lambda} = \lambda/(u_{\mathrm{rms}} k_{\mathrm{f}})$ is the normalized growth rate of the magnetic field and $\tilde{u}_{\mathrm{rms}} = u_{\mathrm{rms}}/\sqrt{GM/R}$ is the non-dimensional rms velocity. $E_{\mathrm{kin}} = \frac{1}{2}\langle\rho\boldsymbol{u}^2\rangle$ is the volume averaged kinetic energy. $E_{\mathrm{mer}} = \frac{1}{2}\langle\rho(\overline{u}_r^2 + \overline{u}_\theta^2)\rangle$ and $E_{\mathrm{rot}} = \frac{1}{2}\langle\rho\overline{u}_\theta^2\rangle$ denote the volume averaged energies of the azimuthally averaged meridional circulation and differential rotation. Analogously $E_{\mathrm{mag}} = \frac{1}{2}\langle\boldsymbol{B}^2\rangle$ is the total volume averaged magnetic energy while $E_{\mathrm{pol}} = \frac{1}{2}\langle(\overline{B}_r^2 + \overline{B}_\theta^2)\rangle$ and $E_{\mathrm{tor}} = \frac{1}{2}\langle\overline{B}_\theta^2\rangle$ are the energies in the axisymmetric part of the poloidal and toroidal magnetic fields.

2010) and that at even higher rotation rates, cyclic solutions with poleward migration are obtained (Brown et al. 2011). A similar transition has been observed in spherical wedge models of Käpylä et al. (2010) and Käpylä et al. (2012). However, in the former case the oscillatory mode showed poleward migration of the activity belts whereas in the latter an equatorward branch appears near the equator. Furthermore, in the runs of Käpylä et al. (2012) the dynamo mode changes from one showing a high frequency cycle with poleward migration near the equator to another mode with lower frequency and equatorward migration when the magnetic field becomes dynamically important.

There are several differences between the models of Käpylä et al. (2010) and Käpylä et al. (2012): the amount of density stratification (a density contrast of 3 in comparison to 30), efficiency of convective energy transport (20 per cent versus close to 100 per cent in the majority of the domain), and the top boundary condition for entropy (constant temperature versus black body radiation). Here we concentrate on studying the influence of the density stratification on models similar to those presented in Käpylä et al. (2012).

3.1. *Thermal boundary effects and energy balance*

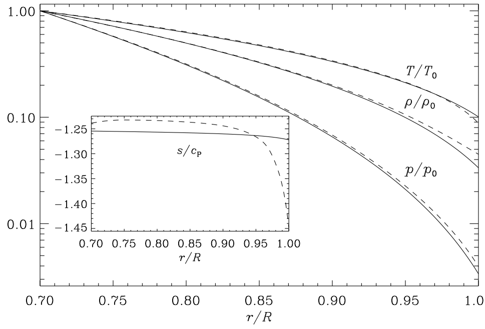

FIG. 1.— Initial (solid lines) and saturated (dashed) radial profiles of temperature T, density ρ, and pressure p, normalized by their respective values at the bottom of the domain from Run C1 (indicated by subscript zero). The inset shows the specific entropy s/c_P from the same run.

In Käpylä et al. (2011a) we started to apply the black body boundary condition, Equation (13), that has previously been used in mean-field models with thermodynamics (Brandenburg et al. 1992). Instead of using the physical value for the

Stefan–Boltzmann constant, we estimate the value of σ so that the flux at the upper boundary is approximately that needed to transport the total luminosity of the star through the surface. However, the final thermally relaxed state of the simulation can significantly deviate from the initial state. In combination with the nonlinearity of Equation (13), the final stratification is usually somewhat different from the initial one; see Figure 1 for an illustrative example from Run C1. The final density stratification in this case is around 22, down from 30 in the initial state.

The main advantage of the black body condition is that it allows the temperature at the surface more freedom than in our previous models where a constant temperature is imposed (Käpylä et al. 2010, 2011b). Furthermore, as the temperature is allowed to vary at the surface, this can be used as a diagnostic for possible irradiance variations. These are discussed further in Section 3.6.

Considering the energy balance, we show the energy fluxes for Run E4 in Figure 2. We find that the simulation is thermally relaxed and that the total luminosity is close to the input luminosity, i.e. $L_{\rm tot} - L_0 \sim 0$. The fluxes are defined as:

$$\overline{F}_{\rm rad} = -K \frac{\partial \langle T \rangle}{\partial r}, \tag{24}$$

$$\overline{F}_{\rm conv} = c_{\rm P} \langle (\rho u_r)' T' \rangle, \tag{25}$$

$$\overline{F}_{\rm kin} = \tfrac{1}{2} \left\langle (\rho u_r)' \boldsymbol{u}'^2 \right\rangle, \tag{26}$$

$$\overline{F}_{\rm visc} = -2\nu \left\langle (\rho u_i)' S_{ir} \right\rangle, \tag{27}$$

$$\overline{F}_{\rm turb} = -\chi_{\rm SGS} \langle \rho \rangle \langle T \rangle \frac{\partial \langle s \rangle}{\partial r}, \tag{28}$$

$$\overline{F}_{\rm Poyn} = \langle E_\theta B_\phi - E_\phi B_\theta \rangle / \mu_0, \tag{29}$$

where $\boldsymbol{E} = \eta\mu_0 \boldsymbol{J} - \boldsymbol{u}\times\boldsymbol{B}$, the primes denote fluctuations, and angle brackets averaging over θ, ϕ, and a time interval over which the turbulence is statistically stationary. The radiative flux carries energy into the convection zone and drops steeply as a function of radius so that it contributes only a few per cent in the middle of the convection zone. The resolved convection is responsible for transporting the energy through the majority of the layer, whereas the unresolved turbulent transport carries energy through the outer surface. The other contributions are much smaller. The flux of kinetic energy is also very small in the rapid rotation regime considered here (see also Augustson et al. 2012).

3.2. *Dynamo excitation and large-scale magnetic fields*

The azimuthally averaged toroidal magnetic fields from all runs listed in Table 1 are shown in Figures 3–6. The full time evolution from the introduction of the seed magnetic field to the final saturated state is shown for each run. Although the magnitude of the seed field in terms of the equipartition strength is different in each set, already a visual inspection suggests that the growth rate of the dynamo is greater in the cases with low stratification. The measured average growth rates over the kinematic stage,

$$\lambda = \langle d \ln B_{\rm rms} / dt \rangle_t, \tag{30}$$

support this conjecture; see the second column of Table 2. Comparing Runs A1, B1, C1, and D2 with roughly comparable Reynolds and Coriolis number shows that the normalized growth rate decreases monotonically from 0.084 in Run A1 to just 0.003 in Run D2. Another striking feature is that λ increases by a factor of nearly 20 from Run C1 to C2 where the only difference between the runs is that the latter has a roughly two times higher Coriolis number. It turns out that in all of the cases (Runs A1, A2, B1, B2, C2, and E4) with the highest growth rates, a poleward migrating dynamo mode at low latitudes is excited first. In some of the runs this mode is later overcome by another one that can be quasi-stationary (Runs A1 and B1) or oscillatory with equatorward migration and a much longer cycle period (Runs C2 and E4).

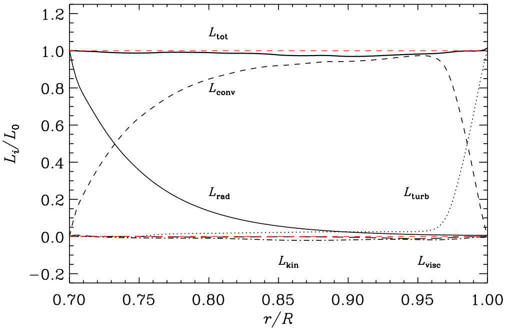

FIG. 2.— Luminosity of the energy fluxes from Run E4: radiative conduction (thin solid line), enthalpy (dashed), kinetic energy (dot-dashed), viscous (long dashed), and unresolved subgrid scale (dotted) fluxes. The thick solid line is the sum of all contributions. The two dashed red lines indicate the zero and unity line.

Table 2 shows that, even though the growth rates decrease dramatically with increasing stratification, many properties of the saturated stage quantities are similar. In particular the ratio of magnetic to kinetic energy does not seem to depend systematically on stratification, but rather on the Coriolis number, which varies only little between different runs.

In Figure 3 we show the azimuthally averaged toroidal magnetic field $\overline{B}_\phi$ near the surface of the computational domain ($r = 0.98\,R$) for two runs (A1 and A2; see Table 1) with $\Gamma_\rho = 2$ (Set A). We find that in Run A1 with ${\rm Co} \approx 8.7$ the mean magnetic field is initially oscillatory with poleward propagation of the activity belts. At $tu_{\rm rms}k_{\rm f} \approx 400$ the dynamo mode changes to a quasi-steady configuration. In Run A2 a poleward mode persists throughout the simulation, although the oscillation period is irregular and significant hemispherical asymmetry exists. This behavior is similar to the runs presented in Käpylä et al. (2010) which are comparable in terms of stratification, Coriolis and Reynolds numbers.

In Set B with $\Gamma_\rho = 5$ the situation is similar: in Run B1 with ${\rm Co} \approx 8.1$ there is a poleward mode with a short cycle period near the equator which is visible from early times, see Figure 4. However, after around $tu_{\rm rms}k_{\rm f} = 1200$ there is a dominating non-oscillatory mode which is especially clear at high latitudes. There are still hints of the poleward mode near the equator. In Run B2 with ${\rm Co} \approx 13.7$, however, the poleward mode prevails also at late times. As in Run A2, the cycles show significant variability and hemispheric asymmetry. The runs in Sets A and B also show signs of non-axisymmetric 'nests' of convection (cf. Busse 2002; Brown et al. 2008) in the hydrodynamical and kinematic stages. Once the magnetic field is strong enough these modes either vanish or they are significantly damped.

Increasing the stratification further to $\Gamma_\rho = 30$ (Set C) the dynamo solutions at lower rotation rates, ${\rm Co} \lesssim 5$, are still quasi-steady; see Figure 2 of Käpylä et al. (2012). However, a watershed regarding the oscillatory modes at higher Co seems

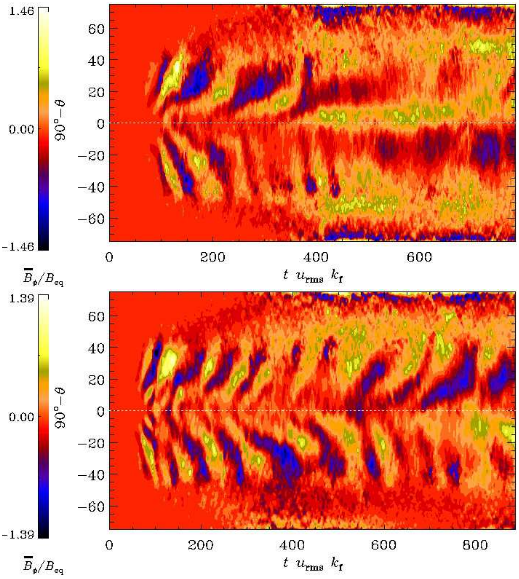

FIG. 3.— $\overline{B}_\phi$ near the surface of the star at $r = 0.98\,R$ as a function of latitude ($= 90^\circ - \theta$) for Runs A1 (top) and A2 (bottom). The white dotted line denotes the equator $90^\circ - \theta = 0$.

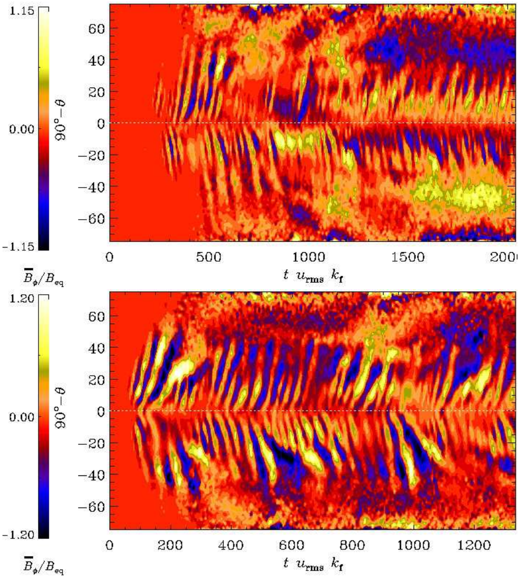

FIG. 4.— Same as Figure 3 but for Runs B1 (top) and B2 (bottom).

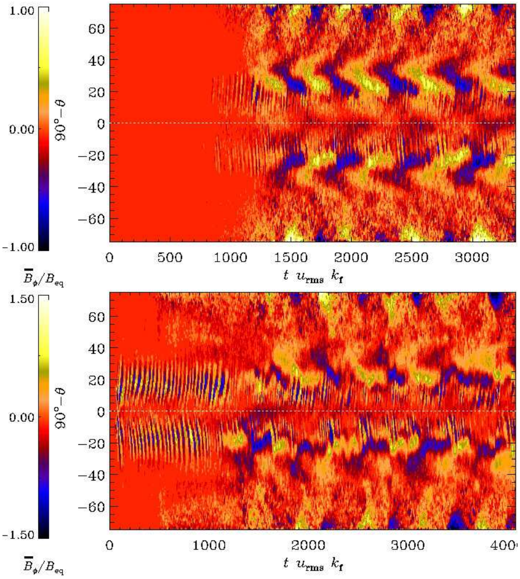

FIG. 5.— Same as Figure 3 but for Runs C1 (top panel) and C2 (bottom). Note the difference in cycle frequency between early times when the frequency is similar to that of Run B2 (Figure 4) and late times.

to have been reached so that the irregular poleward migration seen in Sets A and B is replaced by more regular equatorward patterns. In Run C1 with $\mathrm{Co} \approx 8.7$ the poleward migration near the equator is secondary to the equatorward mode—even in the kinematic stage; see Figure 5. The poleward mode near the equator is more prominent in the early stages of Run C2 with $\mathrm{Co} \approx 14.7$, but subdominant at late times.

For $\Gamma_\rho = 100$ (Set D) the general picture is similar to that in Set C. Quasi-steady configurations at lower rotation change into equatorward migrating solutions at sufficiently high values of Co. We find this transition to occur between $\mathrm{Co} = 5$ and 8, similarly as in Set C. For Set D the equatorward mode is visible for both runs; see Figure 6. In Run D1 no poleward migration at low latitudes is seen in the kinematic stage. Also the poleward migrating branch at high latitudes is missing in the non-linear stage. Both of these features are present in Run D2. The apparently slower growth of the magnetic field in Run D1 is due to a two orders of magnitude lower initial seed magnetic field than in Run D2.

To connect our results with observations of magnetically active stars we compute the ratio of the dynamo cycle frequency and the rotation rate, $\omega_{\rm cyc}/\Omega_0$. Plotting this ratio as a function of the Coriolis number for stars exhibiting chromospheric activity has shown that stars tend to group along inactive and active branches (Brandenburg et al. 1998), and for higher Coriolis numbers along a super-active branch (Saar & Brandenburg 1999). Six of our simulations (Runs A2, B2, C1, C2, D1, and D2), excluding the runs in Set E which are very similar to each other and Run C1 in this respect, show cycles and can be thus used in this analysis. For Runs C1, C2, D1, and D2 the cycle frequency was measured from a few latitudes on both hemispheres and for all available cycles individually. The final result is an average over the individually computed values. In two of our models (Runs A2 and B2) the cycle periods vary irregularly. There the cycle frequency is computed from the highest peak of a temporal Fourier transformation of the time series for $\overline{B}_\phi$ at low latitudes near the surface. The results are shown in the upper panel of Figure 7.

The association with real branches in Figure 7 is clearly

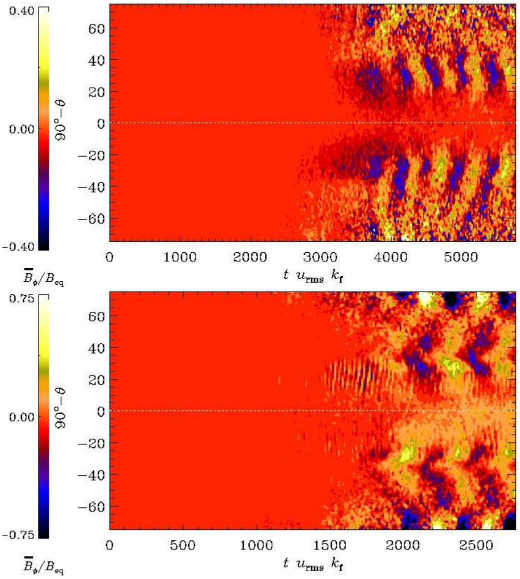

FIG. 6.— Same as Figure 3 but for Runs D1 (top panel) and D2 (bottom).

premature, because we cannot be sure that there are no stars connecting the group of Runs C1, D1, D2 with that of A2 and B2 through a single line with a larger slope. Nevertheless, this plot allows us to see that, while the separation in the ratio $\omega_{\rm cyc}/\Omega_0$ is slightly less for the two groups of runs, compared with active and inactive stars, their relative ordering in the value of $\rm Co$ is actually the other way around. One would therefore not have referred to Runs A2 and B2 as inactive just because their $\omega_{\rm cyc}/\Omega_0$ ratio agrees with that of inactive stars. In fact, their $E_{\rm mag}/E_{\rm kin}$ ratios in Table 2 are typically larger than for Runs C1, D1, D2.

As is clear from the inset of the upper panel of Figure 7, there is no clear relation between $\rm Co$ and $E_{\rm mag}/E_{\rm kin}$, which is different from stars for which there is a clear relation between $\rm Co$ (referred to as inverse Rossby number in that context) and stellar activity (a measure of $E_{\rm mag}/E_{\rm kin}$); see Brandenburg et al. (1998) for details and references. Furthermore, there is also no clear indication of two branches in the graph of $\omega_{\rm cyc}/\Omega_0$ versus $E_{\rm mag}/E_{\rm kin}$; see the lower panel of Figure 7. Instead, there might just be one group in it, possibly with a positive correlation, i.e., $\omega_{\rm cyc}/\Omega_0$ might increase with $E_{\rm mag}/E_{\rm kin}$. As discussed by Brandenburg et al. (1998), a positive slope is not easily explained in the framework of standard mean-field dynamo theory, where the frequency ratio is usually a decreasing function of normalized rotation rate and activity parameter.

In conclusion, we can say that the quantity $\omega_{\rm cyc}/\Omega_0$ is an important and robust property of any cyclic dynamo model and its dependence on other properties of the model should therefore be a useful characteristics that can be compared with other models and ultimately with actual stars. Here we have just make a first attempt in classifying model results in this sense.

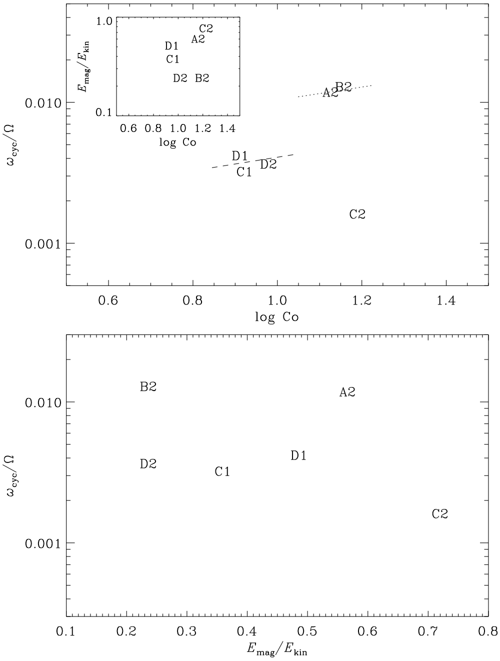

FIG. 7.— Ratio of the dynamo cycle and rotation frequencies from six runs which show cyclic activity as functions of rotation (upper panel) and the ratio of magnetic to kinetic energy (lower panel). The dotted and dashed lines in the upper are given by $c_i{\rm Co}^{\sigma_i}$, where the σ_i correspond to those in Brandenburg et al. (1998), and c_i are used as fit parameters. The inset in the top panel show the ratio $E_{\rm mag}/E_{\rm kin}$ as a function of $\rm Co$.

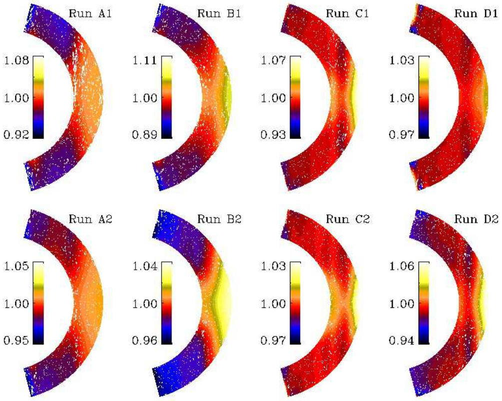

FIG. 8.— Mean rotation profile $\overline{\Omega}/\Omega_0$ (gray/color scale) and meridional circulation $\overline{\boldsymbol{u}}_{\rm m}=(\overline{u}_r,\overline{u}_\theta,0)$ (arrows) from Sets A, B, C, and D.

We note that in the geodynamo literature it has become popular to consider the Elsasser number as a measure of the magnetic energy. It correlates well with $\rm Rm$ (Christensen & Aubert 2006), but this is partially explained by the fact that $\rm Rm$ itself enters in the definition of the Elsasser number. Those models are mostly dominated by a strong dipolar component. Gastine et al. (2012) have shown that such solutions fall on a branch that is distinct from the cyclic solutions studied here, and that the latter become favored once density stratification is large, and rotation sufficiently rapid so that large-scale non-axisymmetric fields become dominant (see also Nelson et al. 2013).

3.3. *Differential rotation and meridional circulation*

Non-uniform rotation of the convection zone of the Sun is an important ingredient in maintaining the large-scale magnetic field. Furthermore, the sign of the radial gradient of the mean angular velocity plays a crucial role in deciding whether the dynamo wave propagates towards the pole or the equator in mean-field models (e.g. Parker 1955a, 1987). In the following we use the local angular velocity defined as $\overline{\Omega} = \overline{u_\phi}/r\sin\theta + \Omega_0$. Azimuthally averaged rotation profiles from the runs in Sets A to D are shown in Figure 8. The rotation profiles of Runs E1, E3, and E4 are very similar to that of Run C1. We quantify the radial and latitudinal differential rotation by

$$\Delta_\Omega^{(r)} = \frac{\overline{\Omega}_{\rm eq} - \overline{\Omega}_{\rm bot}}{\overline{\Omega}_{\rm eq}}, \tag{31}$$

$$\Delta_\Omega^{(\theta)} = \frac{\overline{\Omega}_{\rm eq} - \overline{\Omega}_{\rm pole}}{\overline{\Omega}_{\rm eq}}, \tag{32}$$

where $\overline{\Omega}_{\rm eq} = \overline{\Omega}(R,\pi/2)$ and $\overline{\Omega}_{\rm bot} = \overline{\Omega}(r_0,\pi/2)$ are the angular velocities at the top and bottom at the equator, respectively, and $\overline{\Omega}_{\rm pole} = \frac{1}{2}[\overline{\Omega}(R,\theta_0) + \overline{\Omega}(R,\pi-\theta_0)]$.

It has long been recognized that dynamo-generated magnetic fields can have an important effect on the angular velocity (Gilman 1983; Glatzmaier 1985, 1987). Indeed, magnetic fields affect the turbulence that gives rise to Reynolds stress and turbulent convective heat flux (e.g. Kitchatinov et al. 1994; Käpylä et al. 2004). Furthermore, the large-scale flows are directly influenced by the Lorentz force when the magnetic field is strong enough (e.g. Malkus & Proctor 1975). A decrease of $\Delta_\Omega^{(\theta)}$ has also been observed in LES models (e.g. Brun et al. 2004). Comparing the latitudinal differential rotation in Run B1 with that of otherwise identical hydrodynamic Run A4 of Käpylä et al. (2011a), we find that $\Delta_\Omega^{(\theta)}$ decreases only slightly from 0.15 to 0.14. For $\Delta_\Omega^{(r)}$ the change is more dramatic from 0.079 to 0.034. The fraction of kinetic energy contained in the differential rotation drops from 0.91 to 0.71. A similar decrease is observed in Run C1 in comparison to its hydrodynamical parent Run B4 of Käpylä et al. (2011a) with $\Delta_\Omega^{(\theta)}$ changing from 0.08 to 0,07, $\Delta_\Omega^{(r)}$ from 0.066 to 0.047, and $E_{\rm rot}/E_{\rm kin}$ dropping from 0.58 to 0.44. These changes in the flow are not surprising. Similar changes have been seen in dynamos both from forced turbulence in Cartesian domains (Brandenburg 2001) and convective turbulence in spherical shells (Brun et al. 2004).

We see a rapidly spinning equator with a positive radial gradient of $\overline{\Omega}$ in all cases; see Figure 8. The latitudinal variation of angular velocity is however not always monotonic and there can be local minima at mid-latitudes, as is seen for example in Run C1. Similar features have been seen before (see, e.g., Miesch et al. 2000; Käpylä et al. 2011b) and might be related to the lack of small-scale turbulence. Especially at larger stratification one would expect smaller-scale turbulent structures to emerge, but this requires sufficient resolution and thus large enough Reynolds numbers, which is not currently possible.

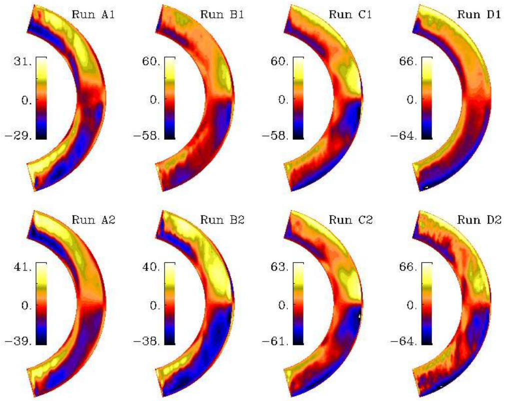

FIG. 9.— Dynamo number C_α from Sets A, B, C, and D.

The amount of latitudinal differential rotation is clearly less than in the Sun where $\Delta_\Omega^{(\theta)} \approx 0.2$ between the equator and latitude 60° (e.g. Schou et al. 1998). Furthermore, $\Delta_\Omega^{(\theta)}$ generally decreases within each set of runs as Co increases with the exception of Runs D1 and D2. However, in Run D1 the lower Reynolds number possibly contributes to the weak differential rotation in comparison to Run D2 with comparable Co. The rotation profiles appear to be dominated by the Taylor-Proudman balance except at very low latitudes where the baroclinic term is significant. In a companion paper (Warnecke et al. 2013), we show that an outer coronal layer seems to favor a solar-like rotation, which shows even radially outward pointing contours of constant rotation. Such 'spoke-like' rotation profiles have so far been obtained only in mean-field models involving anisotropic heat transport (e.g. Brandenburg et al. 1992) or a subadiabatic tachocline (Rempel 2005), and in LES models where a latitudinal entropy gradient is enforced at the lower boundary (Miesch et al. 2006).

The meridional circulation is weak in all cases and typically shows multiple cells in radius. The circulations are mostly concentrated in the equatorial regions outside the inner tangent cylinder. This is similar to earlier results by Käpylä et al. (2012) where the meridional circulation pattern was shown in larger magnification. In addition, as we will show below, the strength of meridional circulation relative to the turbulent magnetic diffusivity is rather low, which is another reason why it cannot play an important role in our models.

3.4. *Estimates of dynamo numbers*

We estimate the dynamo numbers related to the α-effect, radial differential rotation, and the meridional circulation by

$$C_\alpha = \frac{\alpha\Delta R}{\eta_{\rm t0}}, \quad C_\Omega = \frac{\partial\overline{\Omega}/\partial r(\Delta R)^3}{\eta_{\rm t0}}, \quad C_U = \frac{\overline{u}_{\rm mer}^{\rm rms}\Delta R}{\eta_{\rm t0}}, \tag{33}$$

where $\partial\overline{\Omega}/\partial r$ is the r- and θ-dependent radial gradient of $\overline{\Omega}$ and α is a proxy of the α-effect (Pouquet et al. 1976)

$$\alpha = -\tfrac{1}{3}\tau(\overline{\boldsymbol{\omega}\cdot\boldsymbol{u}} - \overline{\boldsymbol{j}\cdot\boldsymbol{b}}/\overline{\rho}), \tag{34}$$

with $\tau = \alpha_{\rm MLT}H_{\rm P}/u_{\rm rms}(r,\theta)$ being the convective turnover time and $\alpha_{\rm MLT}$ the mixing length parameter. We use $\alpha_{\rm MLT} = 5/3$ in this work. We estimate the turbulent diffusivity

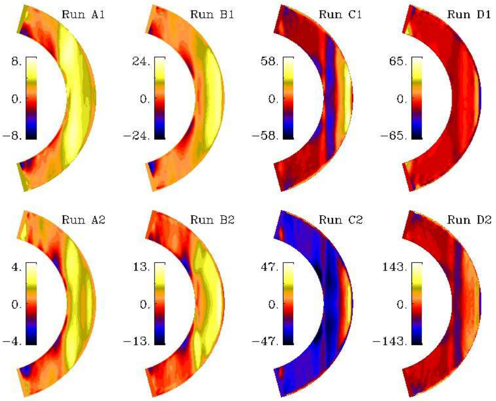

FIG. 10.— Dynamo number C_Ω from Sets A, B, C, and D. We omit regions closer to $2.5°$ from the latitudinal boundaries.

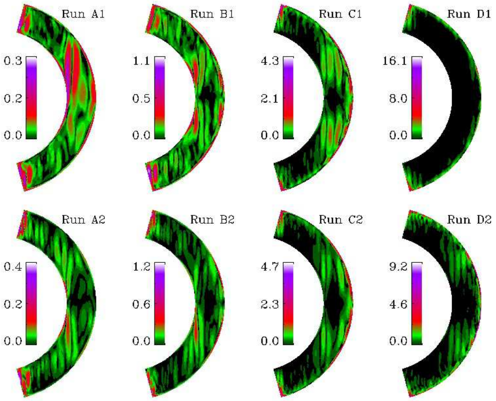

FIG. 11.— Dynamo parameter C_U from Sets A, B, C, and D.

by $\eta_{t0} = \frac{1}{3}u_{\rm rms}(r,\theta)\alpha_{\rm MLT}H_{\rm P}$. Furthermore, $\overline{u}_{\rm mer}^{\rm rms} = \sqrt{\overline{u}_r^2 + \overline{u}_\theta^2}$ is the rms value of the meridional circulation.

The results for the dynamo numbers are shown in Figures 9–11. Generally, the values of C_α are fairly large, and those of C_Ω surprisingly small, suggesting that the dynamos might mainly be of α^2 type. In the following, however, we focus on relative changes between different runs. It turns out that there is a weak tendency for C_α to increase as a function of Γ_ρ and Co. In Set B, however, C_α decreases by a third from Run B1 to B2. The spatial distribution of C_α becomes more concentrated near the boundaries as Γ_ρ increases.

We find that the effect of the differential rotation is strongest near the equator in all cases. In Sets A and B the absolute values of C_Ω are clearly smaller that those of C_α. This is surprising given the fact that the energy of the toroidal mean field is greater than that of the poloidal field by a significant factor which would be expected if differential rotation dominates over the α-effect in maintaining the field. In Runs C1, C2, and D1, C_α and C_Ω have comparable magnitudes whereas in Run D2 the maximum of C_Ω is roughly twice that of C_α. However, in these cases the toroidal and poloidal field energies are roughly comparable.

We find that C_U is always small in comparison to both C_α and C_Ω. Figure 11 also shows the concentration of coherent meridional circulation cells in the equatorial regions with a multi-cell structure.

3.5. *Effect of domain size*

We recently reported equatorward migration of activity belts in a spherical wedge simulation (Käpylä et al. 2012). There we gave results from simulations with a ϕ-extent of $\pi/2$. However, at large values of the Coriolis number, the α effect becomes sufficiently anisotropic and differential rotation weak so that non-axisymmetric solutions become possible; see Moss & Brandenburg (1995) for corresponding mean-field models with dominant $m = 1$ modes in the limit of rapid rotation. To allow for such modes, we now choose a ϕ-extent of up to 2π. In the present case, we find that for ${\rm Co} \approx 7.8$ it is possible that non-axisymmetric dynamo modes of low azimuthal order ($m = 1$ or 2) can be excited. This would not be possible in the simulations of Käpylä et al. (2012). The same applies to non-axisymmetric modes excited in hydrodynamic convection (e.g. Busse 2002; Brown et al. 2008; Käpylä et al. 2011b; Augustson et al. 2012).

We test the robustness of this result by performing runs with $\Delta\phi = \pi/4, \pi/2, \pi$, and 2π with otherwise identical parameters. We find that the same dynamo mode producing equatorward migration is ultimately excited in all of these runs. The only qualitatively different run is that with $\phi_0 = 2\pi$ where the poleward mode near the equator grows much faster than in the other cases. However, after $tu_{\rm rms}k_{\rm f} \approx 1500$ the equatorward mode takes over similarly as in the runs with a smaller ϕ_0.

The velocity field shows no marked evidence of non-axisymmetry, but there are indications of $m = 1$ structures in the instantaneous magnetic field; see Figure 12, see also http://www.helsinki.fi/∼kapyla/movies.html for a movie of the toroidal magnetic field. This is also reflected by the fraction of the axisymmetric component of the total magnetic energy, see the 5th and 6th columns of Table 2. We find that the energy of the mean toroidal field decreases monotonically when ϕ_0 is increased so that there is a factor of three difference between the extreme cases of Runs E1 and E4. The axisymmetric component still exhibits an oscillatory mode with equatorward migration in all runs in Set E.

We compute power spectra of the toroidal component of the magnetic field from the Run E4 over three $10°$ latitude strips from each hemisphere, centered around latitudes $\pm25°$, $\pm45°$ and $\pm65°$. The results for the three lowest modes are shown in Figure 13. We find that at low ($\pm25°$) and high ($\pm65°$) latitudes the axisymmetric ($m = 0$) mode begins to dominate after around 1000 turnover times and shows a cyclic pattern consistent with that seen in the time-latitude diagram of the azimuthally averaged field. After $tu_{\rm rms}k_{\rm f} \approx 1600$, however, the $m = 1$ mode becomes stronger in the southern hemisphere. This coincides with the growth of the $m = 1$ mode at mid-latitudes where it dominates already earlier in both hemispheres. This is in rough agreement with some observational results of rapid rotators, which show the most prominent non-axisymmetric temperature (e.g. Hackman et al. 2001; Korhonen et al. 2007; Lindborg et al. 2011) and magnetic structures (Kochukhov et al. 2013) at the latitudinal range around 60–80°, while the equatorial and polar regions are more axisymmetric; some temperature inversions even show almost completely axisymmetric distributions in the polar regions and

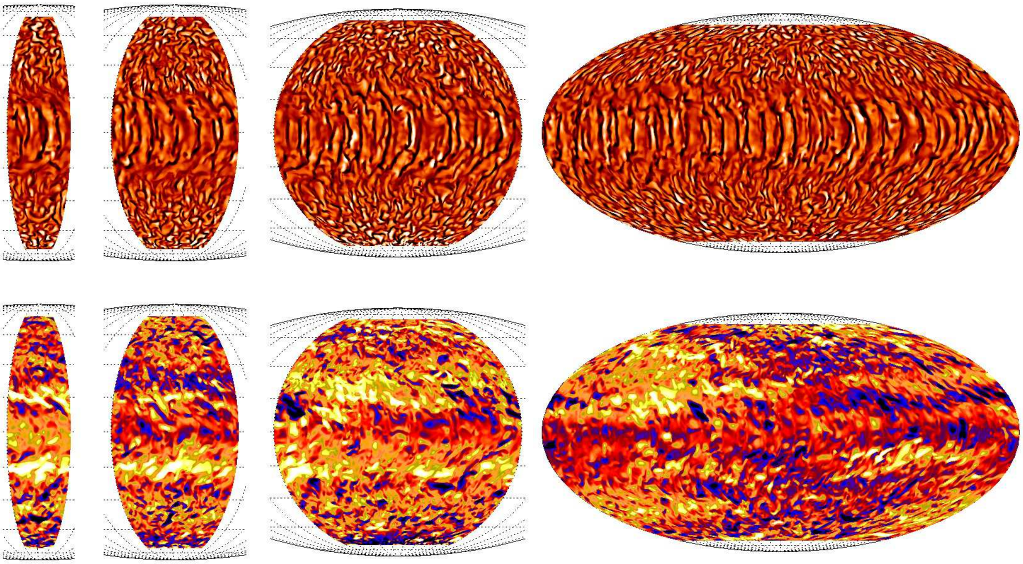

FIG. 12.— Radial velocity u_r (top row) and toroidal magnetic field (bottom) near the surface of the star $r = 0.98\,R$ in Mollweide projection from a Runs E1 (left), E2, E3, and E4 (right).

rings of azimuthal field at low latitudes (e.g. Donati et al. 2003). The strength of the axisymmetric versus the non-axisymmetric component has also been reported to vary over time with a time scale of a few years (Kochukhov et al. 2013).

3.6. *Irradiance variations*

The black body boundary condition (13) allows the temperature to vary at the surface of the star and thus enables the study of irradiance variations due to the magnetic cycle (Spruit 2000). Such variations might even be responsible for driving torsional oscillations in the Sun (Spruit 2003; Rempel 2006). In Figure 14 we show for Run C1 the difference between the azimuthally averaged temperature and its temporal average for the saturated state of the dynamo. There are many instances where enhanced magnetic activity leads to a local decrease in temperature. The signal is strongest for the poleward branch at high latitudes and is also visible for the equatorward branch near the equator. The peak values at high latitudes are up to 20 per cent of the surface temperature. This is relatively large compared with earlier work using mean-field models (Brandenburg et al. 1992), which showed remarkably little relative variation of the order of 10^{-3} in the bulk of the convection zone and even less at the surface. This difference is probably related to the importance of latitudinal variations that were also present in the mean-field model of Brandenburg et al. (1992) and referred to as thermal shadows (Parker 1987).

4. CONCLUSIONS

We have studied the effects of density stratification on the dynamo solutions found in simulations of rotating turbulent convection in spherical wedge geometry. For the four values of Γ_ρ, which is the ratio of the densities at the bottom and at the surface of the convection zone. In addition, we vary the rotation rate for each value of Γ_ρ. For all stratifications we find quasi-steady large-scale dynamos for lower rotation and oscillatory solutions when rotation is rapid enough. The transition from quasi-steady to oscillatory modes seems to occur at a lower Co for higher stratification. Furthermore, for low values of Γ_ρ the oscillatory solutions show only poleward propagation of the activity belts whereas in higher Γ_ρ an equatorward branch appears at low latitudes.

The equatorward branch was first noticed by Käpylä et al. (2012) using a wedge with $\Delta\phi = 90^\circ$ longitude extent. Here we test the robustness of this result by varying $\Delta\phi$ from 45° to full 360°. We find a very similar pattern of the axisymmetric component of the field in all cases. However, the energy of the axisymmetric magnetic field decreases with increasing $\Delta\phi$. In the simulation with the full 2π ϕ-extent we observe an $m = 1$ mode which is visible even by visual inspection of the simulation data (see Figure 12). Such field configurations have been observed in rapidly rotating late-type stars (see e.g. Kochukhov et al. 2013) and our simulation is the first time such features have been seen in direct numerical simulations. We are currently investigating the rapid rotation regime with more targeted runs which will be reported in a separate publication (Cole et al. 2013, in preparation).

The ratio between cycle to rotation frequency, $\omega_{\rm cyc}/\Omega_0$, is argued to be an important non-dimensional output parameter of a cycle dynamo. For the Sun and other relatively inactive stars, this ratio is around 0.01, while for the more active stars it is around 0.002. For our models we find values in the range 0.002–0.01, but for most of the runs it is around 0.004. Although it is premature to make detailed comparisons with other stars and even the Sun, it is important to emphasize that kinematic mean-field dynamos produce the correct cycle frequency only for values of the turbulent magnetic diffusivity that are at least 10 times smaller than what is suggested

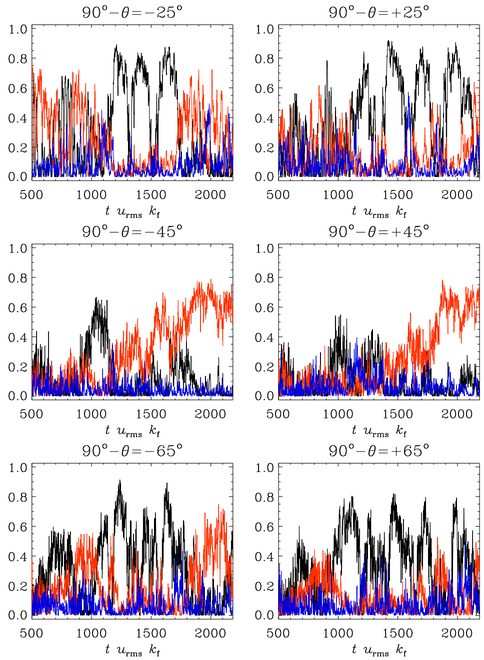

FIG. 13.— Energies of the $m = 0$ (black lines), 1 (red), and 2 (blue) modes of the toroidal magnetic field as functions of time near the surface of the star ($r = 0.98\,R$) in Run E4. The data is averaged over 10° latitude strips centered at latitudes $90^\circ - \theta = \pm 25$ (top panels), ± 45 (middle), and ± 65 (bottom) degrees and normalized by the total energy within each strip. The left and right columns refer to positive and negative latitudes, respectively.

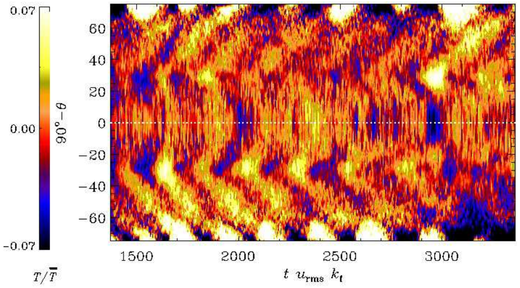

FIG. 14.— Temperature fluctuation at the surface from Run C1. The values are saturated at 7 per cent of the mean, whereas the maxima at high latitudes are around 20 per cent. The white dotted line denotes the equator.

by standard estimates (Choudhuri 1990). In our case, these longer cycle periods (or smaller cycle frequencies) are a result of nonlinearity and are only obtained in the saturated regime of the dynamo. The detailed reason for this is unclear, but it has been speculated that it is connected with a slow magnetic helicity evolution (Brandenburg 2005). On the other hand, magnetic helicity effects are expected to become important only at values of Rm between 100 and 1000 (Del Sordo et al. 2013), which is much larger than what has been reached in the present work. Equally unclear is the reason for equatorward migration, which, as we have seen, is a consequence of nonlinearity, too. It will therefore be important to provide an accurate determination of all the relevant turbulent transport coefficients.

We thank the referee for making a number of useful suggestions. The simulations were performed using the supercomputers hosted by CSC – IT Center for Science Ltd. in Espoo, Finland, who are administered by the Finnish Ministry of Education. Financial support from the Academy of Finland grants No. 136189, 140970 (PJK) and 218159, 141017 (MJM), as well as the Swedish Research Council grant 621-2007-4064, and the European Research Council under the AstroDyn Research Project 227952 are acknowledged as well as the HPC-Europa2 project, funded by the European Commission - DG Research in the Seventh Framework Programme under grant agreement No. 228398. The authors thank NORDITA for hospitality during their visits.

REFERENCES

Arlt, R., Sule, A., & Rüdiger, G. 2005, A&A, 441, 1171
Augustson, K. C., Brown, B. P., Brun, A. S., Miesch, M. S., & Toomre, J. 2012, ApJ, 756, 169
Babcock, H. W. 1961, ApJ, 133, 572
Bonanno, A., Elstner, D., Rüdiger, G., & Belvedere, G. 2002, A&A, 390, 673
Brandenburg, A. 2001, ApJ, 550, 824
—. 2005, ApJ, 625, 539
Brandenburg, A., Chan, K. L., Nordlund, Å., & Stein, R. F. 2005, Astron. Nachr., 326, 681
Brandenburg, A., Moss, D., & Tuominen, I. 1992, A&A, 265, 328
Brandenburg, A., Saar, S. H., & Turpin, C. R. 1998, ApJ, 498, L51
Brown, B. P., Browning, M. K., Brun, A. S., Miesch, M. S., & Toomre, J. 2008, ApJ, 689, 1354
—. 2010, ApJ, 711, 424
Brown, B. P., Miesch, M. S., Browning, M. K., Brun, A. S., & Toomre, J. 2011, ApJ, 731, 69
Brun, A. S., Miesch, M. S., & Toomre, J. 2004, ApJ, 614, 1073
Busse, F. H. 2002, Physics of Fluids, 14, 1301
Chatterjee, P., Nandy, D., & Choudhuri, A. R. 2004, A&A, 427, 1019
Choudhuri, A. R. 1990, ApJ, 355, 733

Choudhuri, A. R., Chatterjee, P., & Jiang, J. 2007, Physical Review Letters, 98, 131103

Christensen, U. R., & Aubert, J. 2006, Geophys. J. Int., 166, 97

Del Sordo, F., Guerrero, G., & Brandenburg, A. 2013, MNRAS, 429, 1686

Dikpati, M., & Charbonneau, P. 1999, ApJ, 518, 508

Dikpati, M., de Toma, G., Gilman, P. A., Arge, C. N., & White, O. R. 2004, ApJ, 601, 1136

Dikpati, M., & Gilman, P. A. 2006, ApJ, 649, 498

Donati, J.-F., et al. 2003, MNRAS, 345, 1145

D'Silva, S., & Choudhuri, A. R. 1993, A&A, 272, 621

Gastine, T., Duarte, L., & Wicht, J. 2012, A&A, 546, A19

Ghizaru, M., Charbonneau, P., & Smolarkiewicz, P. K. 2010, ApJ, 715, L133

Gilman, P. A. 1983, ApJS, 53, 243

Glatzmaier, G. A. 1985, ApJ, 291, 300

—. 1987, 137, 263

Guerrero, G., & Käpylä, P. J. 2011, A&A, 533, A40

Hackman, T., Jetsu, L., & Tuominen, I. 2001, A&A, 374, 171

Hathaway, D. H. 2011, arXiv:1103.1561

Jouve, L., & Brun, A. S. 2007, A&A, 474, 239

Käpylä, P. J., Korpi, M. J., & Brandenburg, A. 2009, A&A, 500, 633

Käpylä, P. J., Korpi, M. J., Brandenburg, A., Mitra, D., & Tavakol, R. 2010, Astron. Nachr., 331, 73

Käpylä, P. J., Korpi, M. J., & Tuominen, I. 2004, A&A, 422, 793

—. 2006, Astron. Nachr., 327, 884

Käpylä, P. J., Mantere, M. J., & Brandenburg, A. 2011a, Astron. Nachr., 332, 883

—. 2012, ApJ, 755, L22

—. 2013, Geophysical and Astrophysical Fluid Dynamics, 107, 244

Käpylä, P. J., Mantere, M. J., Guerrero, G., Brandenburg, A., & Chatterjee, P. 2011b, A&A, 531, A162

Kitchatinov, L. L., & Olemskoy, S. V. 2012, Sol. Phys., 276, 3

Kitchatinov, L. L., Pipin, V. V., & Rüdiger, G. 1994, Astron. Nachr., 315, 157

Kochukhov, O., Mantere, M. J., Hackman, T., & Ilyin, I. 2013, A&A, 550, A84

Korhonen, H., Berdyugina, S. V., Hackman, T., Ilyin, I. V., Strassmeier, K. G., & Tuominen, I. 2007, A&A, 476, 881

Krause, F., & Rädler, K.-H. 1980, Mean-field Magnetohydrodynamics and Dynamo Theory (Oxford: Pergamon Press)

Leighton, R. B. 1969, ApJ, 156, 1

Lindborg, M., Korpi, M. J., Hackman, T., Tuominen, I., Ilyin, I., & Piskunov, N. 2011, A&A, 526, A44

Malkus, W. V. R., & Proctor, M. R. E. 1975, J. Fluid Mech., 67, 417

Miesch, M. S., Brun, A. S., & Toomre, J. 2006, ApJ, 641, 618

Miesch, M. S., Elliott, J. R., Toomre, J., Clune, T. L., Glatzmaier, G. A., & Gilman, P. A. 2000, ApJ, 532, 593

Miesch, M. S., Featherstone, N. A., Rempel, M., & Trampedach, R. 2012, ApJ, 757, 128

Mitra, D., Tavakol, R., Brandenburg, A., & Moss, D. 2009, ApJ, 697, 923

Moss, D., & Brandenburg, A. 1995, Geophys. Astrophys. Fluid Dyn., 80, 229

Nelson, N. J., Brown, B. P., Brun, A. S., Miesch, M. S., & Toomre, J. 2013, ApJ, 762, 73

Ossendrijver, M. 2003, A&A Rev., 11, 287

Parker, E. N. 1955a, ApJ, 122, 293

—. 1955b, ApJ, 121, 491

—. 1987, ApJ, 321, 984

Pipin, V. V. 2012, IAU 294 proceedings, arXiv:1211.2426

Pipin, V. V., & Seehafer, N. 2009, A&A, 493, 819

Pouquet, A., Frisch, U., & Léorat, J. 1976, J. Fluid Mech., 77, 321

Racine, É., Charbonneau, P., Ghizaru, M., Bouchat, A., & Smolarkiewicz, P. K. 2011, ApJ, 735, 46

Rempel, M. 2005, ApJ, 622, 1320

—. 2006, ApJ, 647, 662

Robinson, F. J., & Chan, K. L. 2001, MNRAS, 321, 723

Saar, S. H., & Brandenburg, A. 1999, ApJ, 524, 295

Schou, J., et al. 1998, ApJ, 505, 390

Spruit, H. C. 2000, Space Sci. Rev., 94, 113

—. 2003, Sol. Phys., 213, 1

Warnecke, J., Käpylä, P. J., Mantere, M. J., & Brandenburg, A. 2012, Sol. Phys., 280, 299

—. 2013, ApJ, submitted, arXiv:1301.2248